Liquid Crystals : Surfaces, Nanostructures, and Chirality

Ian Robert Nemitz

Université Pierre et Marie Curie

Case Western Reserve University

Ecole doctorale 397

Institut des NanoSciences de Paris/Physico-Chimie des Surfaces Fonctionnelles

Cristaux Liquides : Surfaces, Nanostructures, et Chiralité

Liquid Crystals : Surfaces, Nanostructures, and Chirality

Par : Ian Robert Nemitz

Thèse de doctorat de physique

Dirigée par Mme. Emmanuelle Lacaze et M. Charles Rosenblatt

Présentée et soutenue publiquement le 4 novembre 2016

Devant un jury composé de :

Lacaze, Emmanuelle (Directrice de Recherche) ; Rosenblatt, Charles ; Tin, Padetha (Rapporteur); Selinger ; Robin (Rapporteur) ; Petschek, Rolfe G. ; Peshek, Timothy ; Carlès, Pierre ; DiLisi, Gregory

“The most exciting phrase to hear in science, the one that heralds new discoveries, is not ’Eureka!’ but ’That’s funny...’ ”

-Isaac Asimov

Remerciements/Acknowledgements

If I were to thank all of those that helped get me to where I am today, the length of this dissertation would increase by at least two-fold. It is no exaggeration to say that I have been extraordinarily lucky to have the support of so many family, friends, and mentors. With such a support base, it's no wonder I've been able to accomplish my goal of becoming Dr. Ian Robert Nemitz.

I would first like to express my deepest appreciation to my advisors; Dr. Charles Rosenblatt and Dr. Emmanuelle Lacaze. They stuck with me when nothing seemed to work, through the frustration of failed experiments, and finally through my final successes as a graduate student. Their advice, guidance, and knowledge were indispensable.

I would especially like to thank my committee members, Dr. Rolfe Petschek, Dr. Timothy Peshek, Dr. Robin Selinger, Dr. Padetha Tin, Dr. Gregory DiLisi, and Dr. Pierre Carlès. Their input on my dissertation and their participation in my defense - even with all the complicated requirements of my dual degree - were much appreciated.

There are a number of other people that I've had the support of throughout the years who I would like to thank: Dr. Jeffrey Wilson for giving me the chance to intern at NASA, Dr. Fulcher for encouraging me to stick with physics, and Dr. Mikhail Zamkov for giving me my first real taste of research. I would also like to thank the those made sure everything was on track throughout the past six years, and made Case a welcoming place for me: Betty Gaffney, Kathleen Kjaglien, Lori Morton, and Georgia Wilkins.

In addition, there are a number of lab members that I would like to recognize for their input and assistance: Rajratan Basu, Tzu-Chieh Lin, James Scheuermann, Joel Pendery, Andrew Ferris, Bryce Murray, Catherine Areklett, and Emily Shelton.

I would also like to thank my friends, those in the US and abroad. To the Case lunch crew, your truth and honesty kept me sane through most of this. To my friends at UPMC - especially Laurent, Mattia, and Iryna - thank you for showing me the ropes, as well as how to enjoy Paris. Lastly, to my long time friends from St. Marks, thanks for putting up with me.

I would like to thank Kate, who was there for me when all I had time for was my work. Her patience and understanding were exceptional, especially when I had none for myself.

Finally, I want to thank my family. You have always made jokes about not understanding what I do, or how I became so interested in the sciences. Luckily, what you do understand is how to support someone. You, more than anyone, are why I've been able to accomplish so much. Dad, you brought the fun. Mom, you brought the brains. Grandma, you brought the curiosity.

Sommaire

Dans cette thèse, je présente les résultats de diverses expériences qui explorent les interactions de cristaux liquides chiraux avec des surfaces et des nanostructures de cristal liquide. Les approches prises pour étudier ces propriétés de cristaux liquides sont discutées, et une attention particulière est portée à l'effet électrooptique lié à la chiralité, aussi connu sous le nom d'effet électroclinique. Dans celui-ci, un champ électrique E appliqué induit une rotation proportionnelle du vecteur directeur suivant un angle θ. Sont explorés aussi par microscopie optique les effets de la chiralité sur la nanostructure smectique-A et sur une nouvelle structure en phase smectique-C.

Les cellules nématiques torsadées sont de puissants instruments pour à la fois détecter et créer de la chiralité dans les systèmes de cristaux liquides. En remplissant une cellule nématique torsadée avec un cristal liquide de configuration achirale, la torsion macroscopique imposée par les conditions de limites planaires tournées vont causer une déracémisation partielle du cristal liquide. Lors de l'application d'un champ électrique au travers de la cellule, il est possible d'observer un effet électroclinique. En utilisant une cellule torsadée avec un gradient d'épasseur et remplie d'un cristal liquide dopé de faon chirale, il est montré que l'effet électroclinique disparait dans les régions où le dopant chiral compense exactement la torsion imposée. Ces résultats indiquent que, dans un système utilisant un cristal liquide déracémisable en conformation, un effet électroclinique existe toujours près des surfaces d'alignement planaire de la cellule torsadée. En outre, cette méthode apparait comme une mesure efficace de la capacité de torsion hélicodale de dopants chiraux dans les cristaux liquides.

Ensuite sont étudiées les propriétés d'induction chirale d'organosilicates mésoporeux périodiques (OMP) chiraux. Dans des travaux précédents, il avait été montré que la chiralité était transférée dans le massif d'un cristal liquide par l'intermédiaire du cristal liquide déracémisé dans les pores des OMP. Dans un tel système, il est une fois de plus possible d'observer un effet électroclinique. Lors du refroidissement vers la température de transition smectique$A$ – smectique-C, cet effet électroclinique se ralentit et augmente en intensité. En comparant la réponse en fréquence de l'effet électroclinique dans une structure de cristal liquide dopée avec des OMP par rapport à celle dopée avec une molécule chirale, il est possible de distinguer la contribution du cristal liquide au sein des pores à travers la signature électro-optique globale. Le résultat central est que la source dominante de la réponse électro-optique provient de

l'extérieur des OMP et que la contribution de cristal liquide dans les pores des OMP est beaucoup plus faible, inférieure au niveau de bruit.

Alors que l'existence de l'effet électroclinique a été montrée en phases smectique et nématique, il y a relativement peu d'information sur son existence dans la phase isotrope. Des cellules contenant l'un des deux types de cristaux liquides chiraux ont été préparées et réchauffées au-delà de leurs températures respectives de transition nématique – isotrope. Lorsqu'un champ électrique est appliqué au travers des cellules, l'existence d'un effet électroclinique est mise en évidence dans la phase isotrope chirale des deux cristaux liquides. L'amplitude de la réponse électroclinique près de la température de transition de phase isotrope – nématique chirale est montrée comme étant comparable à celle observée dans le massif d'une phase nématique chirale et à celle de la région parasmectique au-dessus de la transition smectique-A – isotrope. Cependant, la réponse électroclinique dans la région paranématique varie beaucoup plus lentement avec la température que dans la région parasmectique. En outre, le temps de relaxation de l'effet électroclinique dans la région paranématique est plus lent, de plus de trois ordres de grandeur, que celui de l'effet électroclinique nématique chiral dans le massif.

Nous nous sommes éloignés des effets optoélectriques pour étudier le vaste domaine des structures de cristal liquide. Lorsque des films minces de smectique-A de quelques centaines de nanomètres d'épaisseur sont soumis à des conditions aux limites différentes, ils peuvent former diverses nanostructures. L'une d'entre elles, connue sous le nom de "strie huileuse", se forme lorsque de telles conditions aux limites forcent le cristal liquide à adopter une structure en réseaux linéaires d'hémicylindres aplatis. Lors de son observation sous polariseur et analyseur croisés ces structures apparaissent comme des alternances de stries claires et sombres perpendiculaires à l'axe facile. Afin d'étudier les effets de la chiralité sur ce système, un cristal liquide achiral est dopé avec une molécule chirale et déposé sur une couche d'alignement planaire. Lorsqu'elles sont dopées, les stries huileuses tournent avec un angle ϕ dépendant de la température qui est maximum juste en-dessous de la température de transition nématique – smectique-A et qui augmente de faon monotone avec la concentration. Lorsque la température se réduit, ϕ se relche vers un état stable orienté ($\phi = 0$) pour $T \leq T_{NA} - 1\mathrm{C}$, où T_{NA} est la température de transition nématique – smectique-A. L'origine de cette rotation vient de la rotation des couches smectiques sur le substrat. Cette rotation des couches est supposée venir d'un effet électroclinique de surface combiné à un adoucissement du paramètre d'ordre smectique et une augmentation correspondante de la susceptibilité de l'inclinaison du directeur, près de la transition. En outre sont présentées des données préliminaires liées à la relation entre les périodes des stries huileuses avec la température.

Enfin, l'existence d'une nouvelle structure smectique de film mince est explorée. Un cristal liquide possédant une transition de phase smectique-A – smectique-C est déposé en rotation sur une couche d'alignement planaire et est placé dans un four de haute précision. En phase smectique-A, le cristal liquide présente des stries huileuses. En revanche, lors du refroidissement dans la phase smectique-C, la formation d'une nouvelle structure est observée. Cette structure apparait comme des lignes périodiques claires et obscures alignées perpendiculairement aux stries huileuses, et

n'apparait jamais complètement noire sous polariseur et analyseur croisés. Ces "stries savonneuses" se forment de faon discontinue, s'étendant d'un point limite sur une strie huileuse vers un autre point limite sur la suivante, détruisant les traves physiques des stries huileuses. A des températures plus basses encore, les stries savonneuses commencent à onduler suivant un schéma chiral bidimensionnel. En prenant en compte les données de rayons X et l'observation optique, nous suggérons un modèle de base pour la formation et la structure des stries savonneuses.

Summary

In this dissertation, I present results from a variety of experiments that explore chiral liquid crystal interactions with surfaces and liquid crystal nanostructures. Approaches to studying these liquid crystal properties are discussed. Specific attention is focused on the the chirality dependent electrooptic effect known as the electroclinic effect, in which an applied electric field E induces a proportional rotation of the director by an angle θ. Also, the effects of chirality on smectic-A nanostructure and a novel structure in the smectic-C phase are explored through optical microscopy.

Nematic twist cells are powerful instruments for both detecting and inducing chirality in liquid crystal systems. By filling a nematic twist cell with a configurationally achiral liquid crystal, the macroscopic twist imposed by the rotated planar boundary conditions partially deracemizes the liquid crystal. On application of an electric field across the cell, it is possible to observe an electroclinic effect. Utilizing a twist cell with a thickness gradient and filled with a chiral doped liquid crystal, the electroclinic effect is shown to disappear in regions where the chiral dopant exactly compensates for the imposed twist. These results indicate that, in a system utilizing a conformationally deracemizable liquid crystal, an electroclinic effect always exists near the twist cell's planar alignment surfaces. In addition, this method is shown to be an effective measure of the helical twisting power for chiral dopants in liquid crystals.

Next, the chiral induction properties of chiral periodic mesoporous organosilica (PMO) are probed. In previous work, chirality was shown to be transferred into the bulk of a liquid crystal *via* deracemized liquid crystal in the PMO pores. In such a system, electroclinic effect can be observed. On cooling toward the smectic-A – smectic-C transition temperature, the electroclinic effect increases in magnitude and begins to slow. By comparing the frequency dependence of the electroclinic response in a liquid crystal system doped with PMO to a system doped with a chiral molecule, the contribution of the liquid crystal within the pores can be separated from the overall electrooptical signature. The main result is that the primary source of the electrooptic response emanates from outside the PMO, and the contribution from the liquid crystal in the PMO pores is far smaller, below the level of noise.

While the electroclinic effect has been shown to exist in smectic and nematic phases, there is relatively little information about the existence of an electroclinic effect in the isotropic phase. Cells containing one of two types of chiral liquid crystal are prepared, and heated above their respective chiral nematic - isotropic phase

transitions. When an electric field is applied across the cells, an electroclinic effect is shown to exist in the chiral isotropic phase of both liquid crystals. This electrooptic response appears to exist in the extremely thin paranematic regions that are created by the planar surface alignment layers. The magnitude of the electroclinic response near the isotropic - chiral nematic transition is shown to be comparable to that observed in a bulk chiral nematic phase, and to that in the parasmectic region above a chiral smectic-A - isotropic transition. However, the electroclinic response in the paranematic region varies much more slowly with temperature than in the parasmectic region. Additionally, the relaxation time of the electroclinic effect in the paranematic region is more than three orders of magnitude slower than that of the bulk chiral nematic electroclinic effect.

Moving away from optoelectric effects, the rich subject of liquid crystal structures is explored. When thin smectic-A films of only a few hundred nanometers are subjected to competing boundary conditions, they can form in a variety of nanostructures. One such structure, known as the "oily streak", forms when competing boundary conditions force the liquid crystal into linear arrays of flattened hemicylinders. When imaged under crossed polarizers, these structure appear as alternating light and dark stripes perpendicular to the easy axis. In order to explore the effects of chirality on this system, an achiral liquid crystal is doped with a chiral molecule and spin coated onto a planar alignment layer. When doped, the oily streaks rotate by a temperature dependent angle ϕ that is strongest just below the nematic – smectic-A transition temperature, which increases monotonically with concentration. As the temperature is lowered, ϕ relaxes to a steady-state oriented near 0° for $T \leq T_{NA} - 1$℃, where T_{NA} is the nematic – smectic-A transition temperature. The origin of this rotation is due to a rotation of the smectic layers at the substrate. This layer rotation is believed to come about from a surface electroclinic effect in conjunction with a softening of the smectic order parameter, and a corresponding increase in the director tilt susceptibility, near the transition. Additionally, preliminary data pertaining to the dependence of oily streak periods on temperature is presented.

Finally, the existence of a novel thin film smectic structure is explored. A liquid crystal possessing a smectic-A smectic-C phase transition is spin coated onto a planar alignment layer, and is placed in a highly accurate heater. In the smectic-A phase the liquid crystal presents with oily streaks. However, on cooling into the smectic-C phase, the formation of a new structure is observed. This structure appears as periodic dark and light lines running perpendicular to the oily streaks, and never appears completely dark when imaged between crossed polarizers. These "soapy streaks" form discontinuously, extending from a termination point at one oily streak to a new termination point at the next oily streak, destroying optical evidence of the oily streaks in the process. At still lower temperatures the soapy streaks begin to undulate in a chiral 2D pattern. Taking into account x-ray data, and optical observation, a basic model for the formation and structure of soapy streaks is suggested.

Table des matiéres

Chapitre 1

Introduction

Liquid crystals were first observed at Karl-Ferdinands-Universität in 1888 by Friedrick Reinitzer. While studying the properties of cholesterols that had been extracted from carrots, Reinitzer noted some strange properties. Unlike other materials, cholesteryl benzoate presented with not one, but two, clearing (melting) points that were associated with vivid color changes. Conferring with the physicist Otto Lehmann, it was determined that the intermediate state was actually crystalline-like in nature. Reinitzer summarized his results in the first recognized publication on liquid crystals "Beiträge zur Kenntniss des Cholesterins" [1]. While Reinitzer did not pursue further research in liquid crystals, Lehmann decided to continue the work. Using a polarized microscope and a temperature controlled heating stage, he studied the process by which these novel materials changed states, and the properties they exhibited [2]. Lehmann soon went on to publish a series of papers on liquid crystals, starting with "Über fließende Krystalle" (On flowing Crystals). In this first publication, Lehmann presented evidence that this new intermediate phase had crystalline properties, but was still capable of flow [3]. From there on research into liquid crystals rapidly expanded.

For years, the popularity of liquid crystals waxed and waned. Due to their novel

nature, they were originally thought of as only a peculiarity with little application. There was even a great deal of controversy as to whether they actually exhibited new phases of matter, or were just a combination of liquid and crystalline components [2], but that was put to rest relatively early on. With the advent of liquid crystals for use in display technology – which they have revolutionized – liquid crystals became mainstream [4, 5, 6].

In 1991 Pierre-Gilles de Gennes, a physicist working at Collège de France in Paris, was awarded the Nobel Prize in physics for his work in "discovering that methods developed for studying order phenomena in simple systems can be generalized to more complex forms of matter, in particular to liquid crystals and polymers" [7]. To date, this is the only Nobel Prize awarded for work involving liquid crystals. This was a great milestone for a branch of research into materials that only had been discovered 100 years earlier and which has become a broad interdisciplinary field of research. Today we know liquid crystals mainly for their use in display technology, but this is far from their only application. From lasers [8] to photovoltaics [9, 10], to liquid crystal thermometers [11], liquid crystals are widely used in current (and future) technology. For this reason, and many more, liquid crystal are still a rich and viable source of research.

1.1 Liquid Crystals

In general, liquid crystals are any material that presents with a phase of matter – a "mesophase" – that exists somewhere between that of a solid and a liquid. They have a fluid-like nature similar to liquids, but possess varying degrees of order on the molecular level akin to a solid crystal (though weaker). The types of materials that exhibit these sorts of phases all have one thing in common: an anisotropic structure. This anisotropy is the root of nearly all liquid crystalline properties.

1.1.1 Structure

There are a variety of anisotropic materials and structure that can be classified as liquid crystalline. Examples of these include: soaps [12], DNA [13], suspended clay particles [14], tobacco mosaic virus [15], cell membranes [16], many polymers [11], and most notably the molecules that make up the display of LCD TVs or new cellular phones. However, the most often utilized liquid crystalline materials are the molecular liquid crystals, with over several thousand having been found/synthesized.

The structure of molecular liquid crystals tends to follow a template. The majority of a molecular liquid crystals are made of elongated (calamitic) or disk-like (discotic) structures. These structures are usually based around a flat, mesogen that is commonly a series of benzene or aromatic rings. This core is what gives the molecule its basic anisotropic structure [17, 11]. The aromatic units are joined to each other by short linking groups containing one or multiple bonds that increase the length of the molecules, modify their electric polarization, and add anisotropy [11]. These cores make up the rigid backbone of molecule. Attached to this backbone are less rigid polar or apolar chains that give the molecule a degree of flexibility and, sometimes, a longitudinal dipole. These components can be arranged in a variety of structures that include, but are not be limited to: calamitic, bent-core, and discotic, with a variety of subtypes [17, 12].

Calamitics are the most commonly utilized form of liquid crystals, the constituent molecules of which are rod or cylinder shaped. The molecules are generally linear with two or three aromatic rings forming a central mesogenic core, which terminate on both sides with aliphatic chains or polar groups. 5CB and MBBA are two examples of calamitic liquid crystals, shown in Fig. 1.1a and b respectively. On the opposite end of the aspect ratio are discotic liquid crystals, which from their namesake suggest a disk-like molecular structure. These disks are generally formed around a central planar core of aromatic rings, with radial protrusions of aliphatic chains. An example

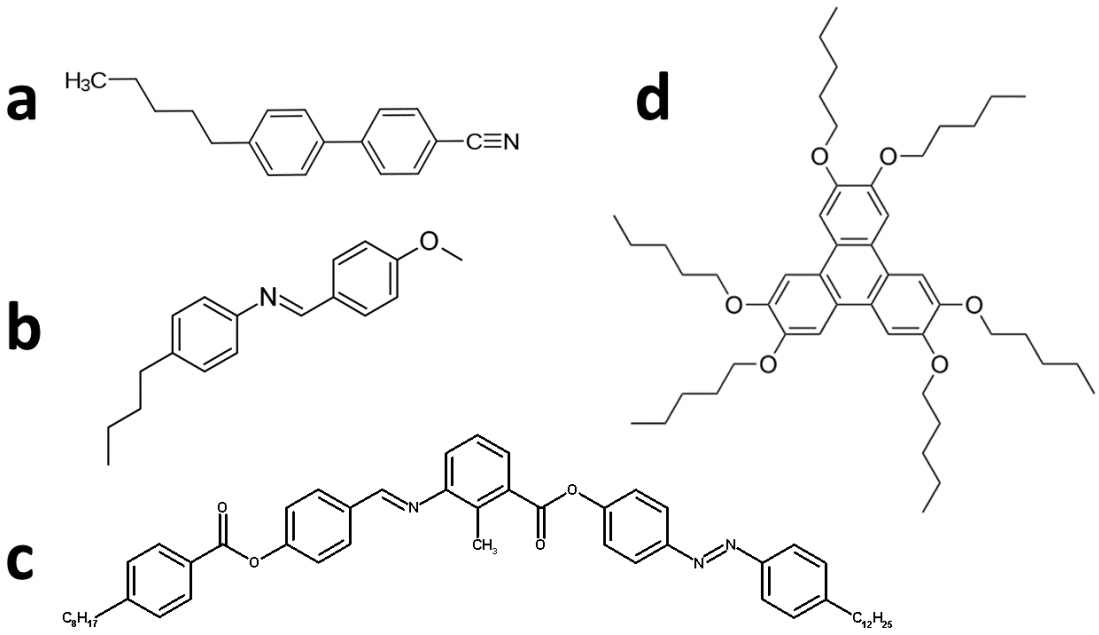

Figure 1.1: Examples of liquid crystal structures for a) the calamitic *4-n-pentyl-4- cyanobiphenyl* (5CB), b) the calamitic *N-(4-methoxybenzylidene)-4-butylaniline* (MBBA) c) the bent core *phenylene bis(alkoxyphenyliminomethyl) benzoate*, d) and the discotic *Hexapentyloxytriphenylene* (HAT5).

of a discotic liquid crystal can be found in Fig. 1.1d. Bent core liquid crystals bridge the gap between calamitics and discotics. Due to their "banana" or "boomerang-like" structure, bent core liquid crystals are biaxial (calamitics and discotics are uniaxial), forming unique liquid crystal phases with very different properties. Fig. 1.1c shows an example of a bent-core liquid crystal.

1.1.2 Chirality

Along with molecular arrangements that define their anisotropic shape, chirality is an additional characteristic common to many liquid crystals, which can be intrinsic or introduced through doping with chiral materials. In fact, the first observed liquid crystal, cholesteryl benzoate, was chiral. Chiral materials (or objects) are those that lack mirror symmetry, which can be an extremely important characteristic for liquid crystals. Lord Kelvin described it best when he said "I call any geometrical figure, or

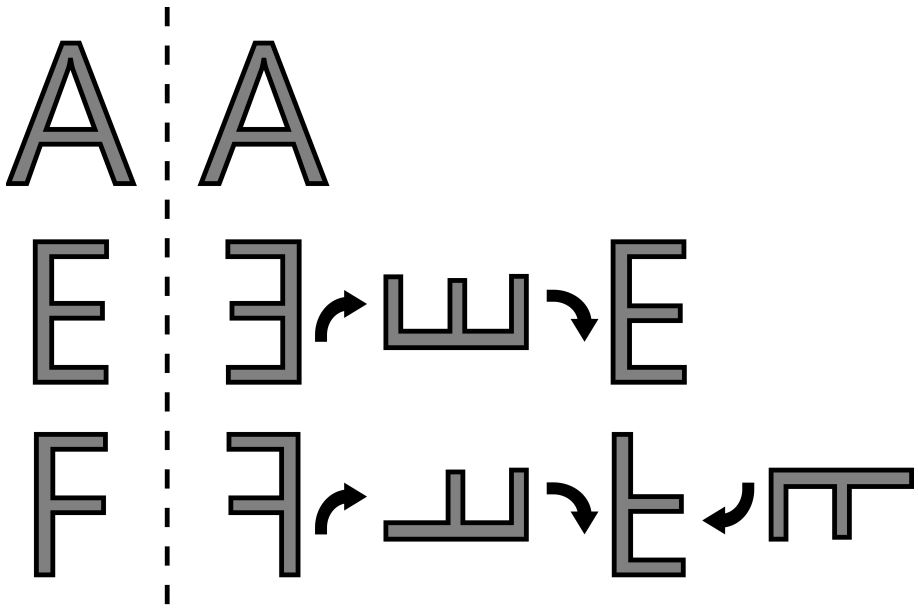

Figure 1.2: The achiral letters **A** and **E**, the chiral letter **F** and these letters' respective mirror images are shown. The dashed line represents the mirror plane, and the curved arrows represent a 90° rotation. The mirror image of **A** requires no rotation to be superimposed on its original, while the mirror image of **E** requires a 180° rotation. The mirror image of **F** can never be superimposed over its original.

group of points, and say it has chirality, if its image in a plane mirror, ideally realized, cannot be brought to coincide with itself"[18].

As a two dimensional example of chirality, we can use the letters from the Latin alphabet. Take a look at Fig. 1.2. Here the letters **A** and **E** are not chiral, while the **F** is chiral in 2D. Putting a mirror next to the letter **A** right away shows that it does have in plane mirror symmetry, and is therefore achiral. The mirror image of **E** may not be directly superimposable on the original, but after an in plane rotation of 180° it can be shown that **E** is also achiral. However, if you take the mirror image of the letter **F**, it can never perfectly be superimposed over the original no matter how it is rotated *in the plane*. Therefore, **F** is chiral in 2D (but not in 3D).

In three dimensions an example of chirality would be a helical structure (like the cholesteric helix in Sec. 1.2.3) such as a screw. Nearly every screw used today is right handed, meaning that as you turn it clockwise in the x-y plane it will travel in the +z

direction. When you line up two right handed screws, you are able to interlace the helical threading. If you attempt this with a right handed and a left handed screw, the threadings will be mirror images of one another, and the helices won't be able to interlace.

Since molecules can easily be modeled as "geometrical figures" and "groups of points", it is simple to see how this can relate to liquid crystals. Unlike the alphabet – and more like the screws – chiral molecules must be chiral in *three* dimensions. In most cases these molecules have what are known as chiral centers. These centers are usually carbon atoms that have four different functional groups attached to them in a quasi-tetrahedral structure. These different units can be arranged one of two ways that are mirror images of one another. The molecules of which these chiral centers are part are structurally identical except for the arrangement around these chiral centers [11, 19]. Chiral molecules can be identified as having either left-handed (S) or right-handed (R) cores, and it is very common for one molecule to form either handedness. If the geometry of a molecule is permanent – as in it can only form its mirror image by breaking chemical bonds – it is known as configurationally chiral. Otherwise, a molecule may have the ability to change handedness through some sort of free rotation, and is known as conformationally chiral. (In chemistry, the molecules that have the same molecular arrangement but differ in orientation are known as stereoisomers, and those that are mirror images are called enantiomers.) These different arrangements can present with very different and interesting effects. A very apparent example is limonene, the molecule that gives both oranges and lemons their distinct scents. Fig. 1.3 shows the right handed (orange) and left handed (lemon) enantiomers of limonene. The molecules are identical except for the chiral core attached to the molecules in the bottom of the image [19].

Bulk liquid crystal systems are said to be chiral if there is a net enantiomeric excess of either R or S. If there are equal concentrations of left and right handed enantiomers,

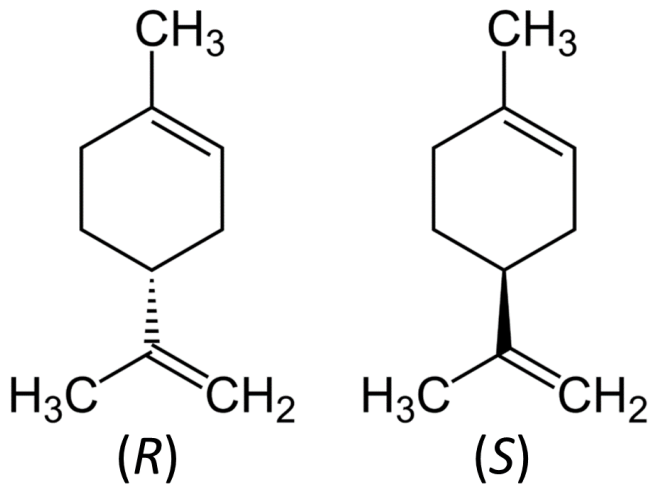

Figure 1.3: Chemical structure of the right-handed (R) and left-handed (S) limonene enantiomers.

the mixture is racemic and will not present with any bulk chiral properties. However in the cases where there is an excess, chiral liquid crystals present with a variety of properties, ranging from the optical activity of the cholesteric phase (Sec. 1.2.3) to the ferro-, antiferro-, and ferri- electric properties found in chiral smectic phases [20]. Chiral liquid crystals also exhibit the so-called "blue phases" that involve multi-dimensional twisted structures [21], are crucial for the ferroelectric properties of liquid crystals [22], and are exploited for their photonic band-gap and lasing properties [8, 23, 24, 25].

These chiral properties can be probed through a variety of experiments. In the nematic phase, the Raynes' experiment [26] can be used to measure the pitch of a chiral liquid crystal by taking the radius of bowed disclination lines. Other measurements such as circular dichroism – where light of different handedness propagates and is absorbed differently in chiral mediums [27] – or Faraday rotation – where polarized light rotates differently through a chiral medium depending on the direction the light propagates [28] – give insights into the nature of chiral materials. For the purposes of this dissertation, the most useful chiral effect is known as the electroclinic effect, and will be discussed in Sec. 1.11.

1.1.3 Classifications

In addition to their structure and symmetry, liquid crystals can be classified by their distinct types of transitional behavior. These behaviors determine how their different phases appear: lyotropic and thermotropic. In lyotropic liquid crystals, mesophases occur when a crystalline material is dissolved in a solvent. These phases occur for concentrations of liquid crystal material where there is sufficient solvent to promote fluid-like interactions, without making the mixture isotropic [11]. Unlike lyotropics, thermotropic liquid crystals transition due to temperature effects, and are usually organic substances [29]. The phases that have less order appear in systems with higher temperatures, and phases with more order appear in those at lower temperatures. The point at which these liquid crystal materials transition is known as their transition temperature. The works presented herein focus on thermotropic liquid crystal materials.

1.2 Liquid Crystal Mesophases

Different liquid crystal mesophases are easily classified by the amount of order they possess, specifically orientational and positional order. It is common for a liquid crystal to exhibit only one of these phases – 5CB only presents with a nematic phase between 18℃ and 35℃ – but there are a variety liquid crystals that present with multiple different phases at different respective temperatures. Described here are some of the more common liquid crystal phases of thermotropic calamitic liquid crystals.

1.2.1 Isotropic and Crystalline

Analogous with the liquid state seen in nature, the isotropic phase is characterized by having neither long range positional or orientational order. Like a fluid, a liquid crystal material in the isotropic phase is free to flow. In this state the molecules

are randomly oriented throughout the bulk of the material, and show few to none of the properties commonly associated with ordered liquid crystals. However, as the transition to one of the more ordered phases nears, the presence of nematic or smectic fluctuations (especially near a surface alignment layer, due to the increase in imposed order) increases [30, 31], their correlation length increases and the fluctuations become longer in duration which in turn changes the properties of the liquid crystal medium.

On the other end of the spectrum is the crystalline phase. While the isotropic phase correlates to a liquid, the crystalline phase correlates to the solid. The crystalline phase presents with the highest degree of order, both positional and orientational. As the temperature of the system in reduced from the isotropic phase or increased from the crystalline phase, the liquid crystal will transition into a phase with more or less order, respectively. These are known as the nematic and smectic phases. In addition to the phases listed here, there are a variety of other smectic and columnar phases – each with varying degrees of order – that are beyond the scope of this work.

1.2.2 Nematic

The nematic phase is the most commonly observed and utilized liquid crystal mesophase. This phase appears below the isotropic to nematic transition temperature T_{NI}, and above a nematic to smectic transition. The nematic phase is the least ordered and the most liquid-like liquid crystal phase besides the isotropic. Like a true liquid it has the ability to flow in three dimensions, and the liquid crystal molecules are free to slide past one another in each all dimensions. However, nematics are more viscous due to the anisotropic alignment of the molecules: the viscosity of a typical nematic is an order of magnitude more than that of water [12].

As can be seen in Fig. 1.4, molecules in the nematic phase have no long range order associated with their centers of mass. The average orientation of the molecules

is aligned in a preferred direction described by unitless vector called the director, $\hat{n}$. It is important to note that in the nematic phase the sign of the director is unimportant with $\hat{n} = -\hat{n}$, meaning that any molecular dipole moments would be evenly distributed [12]. While the long axis of the these molecules lines up with $\hat{n}$, the molecules themselves are free to rotate around this axis, making the nematic phase uniaxial and part of the $D_{\infty h}$ symmetry group.

The orientation of this director usually varies from location to location, but can easily be aligned or manipulated by external forces such as electric and magnetic fields. Very commonly aligning surfaces (represented here by the plane of the paper) can give the director a preferred direction, which is represented by the arrow in Fig. 1.4. Additionally, nematic liquid crystal systems can be characterized by what is known as an order parameter, which defines to what degree the molecules are aligned with this director. This will be expanded upon later in Sec. 1.3

In the nematic phase, thermal fluctuations are especially noticeable, with the scattering of light being much higher – a factor of 10^6 – than what is seen in isotropic fluids [12]. These fluctuations aren't visible to the naked eye, and can be seen best when a bulk liquid crystal is placed in a microscope between crossed polarizers.

1.2.3 Cholesteric

The cholesteric phase is the chiral analog to the nematic phase. Similar to the nematic phase, the molecules in the cholesteric phase are free to slide past one another in all dimensions and the molecules still have no long range order associated with their centers of mass. Additionally, the cholesteric phase still shows *locally* an average long range alignment with the director $\hat{n}$. However, due to the asymmetry of the chiral molecules, the director is no longer pinned constant in space. In the cholesteric phase $\hat{n}$ rotates and forms a helix with pitch P as its equilibrium state. This helix, if we assume that the helical axis is along z, can be taken as:

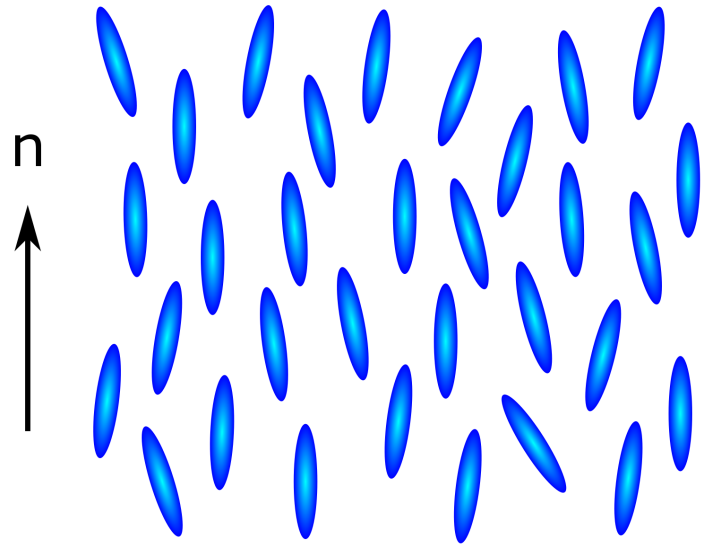

Figure 1.4: Schematic representation of the Nematic Phase. The molecules are aligned, but there is no positional order present.

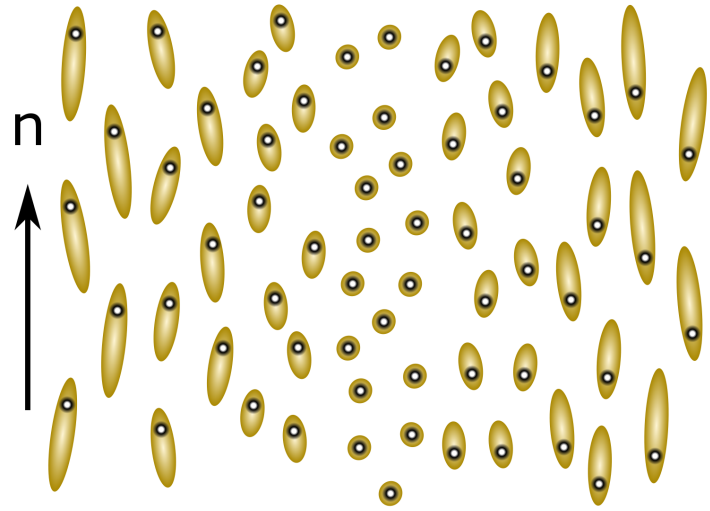

Figure 1.5: Schematic representation of the Cholesteric phase. Like a nematic, the molecules are alignment but there is no positional order. Additionally, the molecules present with a helical twist in this phase. The circles are included to distinguish the direction of director rotation.

$$
\begin{aligned}
n_x &= \cos\left(q_0 z + \phi\right) \\
n_y &= \sin\left(q_0 z + \phi\right) \\
n_z &= 0
\end{aligned}
\tag{1.1}
$$

where $q_0 = 2\pi/P$ is the wavevector, ϕ is the phase, with $\theta = q_0 + \phi$ is the relative angular orientation of the director in the xy-plane for any position in z [12]. For a positive q_0, the pitch of the helix is right-handed, and a negative q_0 gives a left-handed helical pitch. This cholesteric pitch is highly temperature sensitive, with higher temperatures giving shorter pitch length and lower temperatures giving longer ones. An interesting effect of this helical arrangement is its ability to selectively reflect wavelengths of light incident parallel to the helix's axis of rotation and equal to its pitch through Bragg scattering [12].

Another widely utilized effect of the cholesteric phase is its ability to rotate the polarization of light, also known as optical activity. The polarization will follow the rotating director orientation as it propagates through cholesterics with long pitches (of the order 10μm) when

$$
\lambda > P\Delta n \tag{1.2}
$$

where λ is the wavelength of light, and Δn is the material's birefringence (more on birefringence in Sec. 1.4.1 [32]. This optical activity is exploited for twisted nematic displays [11], used for the manufacture of wave plates [11, 28], and is an important factor in Chapter 2.

1.2.4 Smectics

Smectics are characterized by periodic layers with well defined layer spacings that are easily measured by X-ray diffraction [12]. Both nematics and smectics possess orientation order, but smectics also possess a degree of quasi-long-range positional order by nature of their layers. This means that in addition to the orientational order parameter, smectics can also be characterized by a positional order parameter (refer to 1.3). The thicknesses of these layers range between the length of the constituent molecules, to twice the length of the molecules. Generally occurring at lower temperature than the nematic phase and possessing more order, smectics – as a result of this order – are more viscous than nematics. Inside these layers the liquid crystal acts like a two dimensional fluid, with the molecules' centers of mass having no long range positional order (like a nematic). There are a variety of smectic phases - smectic-A, B, C, F, I, E, G, H, J, and K – but here we will focus on some of the most common; the smectic-A (Sm-A) and smectic-C (Sm-C), as well as their chiral analogs.

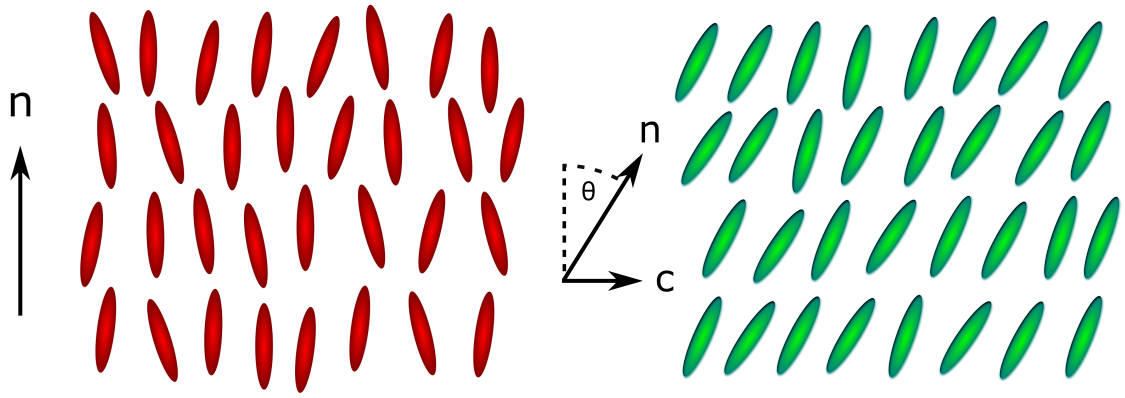

(a) Sm-A (b) Sm-C

Figure 1.6: Schematic representation of a) the smectic-A phase and the b) smectic-C phase. Both phases present with orientational order well as quasi long range positional order. While the molecules in the smectic-A are perpendicular to the smectic layers, molecules in the smectic-C are tilted by and able θ with respect to the smectic layers.

Figure 1.6a shows schematically the Sm-A phase. In both the Sm-A and the chiral smectic-A (Sm-A*) the molecules are, on average, oriented parallel to the layer

normal, have a C_∞ rotation about this axis just like in a nematic, and show director invariance ($\hat{n} = -\hat{n}$). Even though molecules in the Sm-A^* phase may have an electric dipole moment, this director invariance doesn't allow for a net polarization in the bulk material. Under an applied electric field the dipoles will align until the field is removed, making the Sm-A^* phase a paraelectric phase [33]. Because of layer constraints, there is no analogous cholesteric twist in the Sm-A^*, so both the Sm-A and Sm-A^* phases are members of the D_∞ symmetry group. However, for sufficiently strong chirality, the Sm-A^* phase can break into regions in which the layer normal rotates about an axis from one region to the next; this is the "twist grain boundary" phase [34, 35].

Figure 1.6b is a representation of a liquid crystal in the Sm-C phase. The Sm-C phase typically occurs at temperatures below a Sm-A phase, though this isn't necessary. Unlike the ordinary Sm-A phase (non-de Vries [36]), the molecules in the Sm-C phase are tilted on average with respect to the layer normal, making it optically biaxial and part of the C_{2h} symmetry group. In addition to the director $\hat{n}$, the Sm-C phase has a unit vector, $\hat{c}$, which is the projection of the director tilt onto the layer plane. The plane in which both $\hat{n}$ and $\hat{c}$ are included is known as the tilt plane.

The chiral smectic-C (Sm-C^*) is one of the more interesting liquid crystal phases. In this phase the director is also tilted with respect to the layer normal, but mirror symmetry is broken due to the chiral component. Therefore, the Sm-C^* is a member of the C_2 symmetry group, where the only symmetry operator is a two-fold rotation axis perpendicular to the tilt plane. In the absence of surface stabilization the tilt in the Sm-C^* phase azimuthally rotates from layer to layer, creating a helical structure (like that of in a cholesteric) parallel to the layer normal. Due to their chiral structure, the liquid crystal Sm-C^* phase possesses local electric polarization [37]. However, due to the helical structure of this phase the *bulk* net polarization is zero. If this rotation from layer to layer can be inhibited by an external force, a net bulk polarization can

occur [33, 37]. For these reasons this phase presents with ferroelectric properties and is known as the ferroelectric Sm-C^* phase. The (Sm-C^*) can also present with other phases: the antiferroelectric phase where $\hat{c}$ alternates from layer to layer to make a zigzag molecular alignment structure, and the ferrielectric phase where the $\hat{c}$ varies but more often in one direction than another [38, 39]. These interesting phases have a great many properties that can be exploited by applying an electric field to bias the director – such as in fast switching displays [20] – and even extends into the paraelectric Sm-A^* phase where the electric field can induce a tilt in the director (Sec. 1.11 will expand on this).

1.3 Order Parameters

As mentioned in 1.2.2, an "order parameter" characterizes the degree of order in the various phases of a liquid crystal system. The scalar nematic order parameter S for a uniaxial molecule is represented by the second Legendre polynomial:

$$S =< P_2(cos\theta) >= \frac{1}{2} < 3\cos^2(\theta) - 1 >= \frac{\int f(\theta)(\frac{1}{2})(3\cos^2(\theta) - 1)d\Omega}{\int f(\theta)d\Omega} \tag{1.3}$$

where $f(\theta)$ is the orientational distribution function for molecular deviation from the local director, and the system can be both temporally and spatially averaged [40]. The values for the orientational order parameter can be from $S = -1/2$ when the director deviation lies in the xy-plane (and the average director is in the $\hat{z}$), to $S = 0$ for a completely disordered system, to $S = 1$ for a perfectly ordered system. Experimentally these values range from 0.3 to 0.8 – generally decreasing with increasing temperature – and can be measured through a number of means such as diamagnetism, birefringence, and nuclear magnetic resonance [11]. While it is possible to use higher order even Legendre polynomials such as $P_4(\cos\theta)$ to obtain

additional information, these higher order terms are often unnecessary and difficult to obtain. It is important to note that due to the condition $\hat{n} = -\hat{n}$ all odd Legendre polynomials average to zero [12].

In addition to the orientational order parameter, it is possible to define a complex order parameter for position. Since liquid crystals in smectic phases (specifically the Sm-A phase) generally form layered structures that depend on their molecular length, and molecules tend to stay in the layers more often than between them, the density, ρ, of their centers of mass can be used. Treating the center of mass density as an oscillating wave along the z-axis we can approximate ρ to be

$$\rho(z) = \rho_0(1 + \Psi \cos(\frac{2\pi z}{d})) \tag{1.4}$$

where ρ_0 is the average density, d is the layer spacing, and Ψ is the complex order parameter which defines the amplitude and phase of the osculation in density. While it is possible to include higher harmonic sinusoidal terms in this approximation, it usually unnecessary as they are relatively small.

1.4 Dielectric anisotropy

Anisotropy is one of the most important and distinguishing characteristic of liquid crystals, and manifests itself in a number of their properties, one of the most apparent being dielectric anisotropy.

When an electric field is applied to a dielectric, it induces a dipole moment per unit volume, which is known as the polarization [41]. In an isotropic medium where the electric permittivity ϵ can be represented by a scalar, such as glass, the strength of this polarization is dependent only on the field. In anisotropic media, the strength of the polarization also is dependent on the direction of the field in relation to the alignment of the medium. For anisotropic media – such as a liquid crystal – the

electric permittivity is represented by a diagonalizable 3×3 matrix, where the eigenvalues correspond to different orthogonal axes. In a uniaxial liquid crystal the electric permittivity has one component parallel to the long axis of the liquid crystal, $\epsilon_{\parallel}$, and two equal components for the permittivity perpendicular to the long axis, $\epsilon_{\perp}$. Eq. 1.5 gives the electric permittivity matrix of a uniaxial liquid crystal where the average liquid crystal director is oriented arbitrarily with respect to the lab frame. If, however,the molecules' long axis is oriented along the $\vec{z}$ axis, Eq. 1.5 can simply be represented by the diagonalized matrix shown in Eq. 1.6. If the liquid crystal material were biaxial – such as a bent core liquid crystal – all three of the eigenvectors in the matrix would be different. Additionally, many liquid crystal molecules have a permanent dipole moment that can couple with an electric field and contribute to the polarization.

$$\epsilon_{ij} = \epsilon_{\perp} + (\epsilon_{\parallel} - \epsilon_{\perp}) n_i n_j \tag{1.5}$$

$$\epsilon = \begin{pmatrix} \epsilon_{\perp} & 0 & 0 \\ 0 & \epsilon_{\perp} & 0 \\ 0 & 0 & \epsilon_{\parallel} \end{pmatrix} \tag{1.6}$$

If $\epsilon_{\parallel} > \epsilon_{\perp}$ the molecules have a dipole moment that is relatively parallel to the long axis of the molecule. Since $\Delta\epsilon = \epsilon_{\parallel} - \epsilon_{\perp}$ is positive, these liquid crystals and are known as positive dielectric materials. One application of an electric field $\vec{E}$, the molecule will attempt to reorient so that the dipole moment is parallel to $\vec{E}$. On the other hand if $\epsilon_{\parallel} < \epsilon_{\perp}$ the molecular dipole moment is oriented perpendicular to the long axis, and these are called negative dielectric materials. In this situation, $\vec{E}$ couples with the dipole moment and reorients the molecule so that its long axis is perpendicular to $\vec{E}$.

It is important to note that the dielectric permittivity is frequency dependent.

At high frequencies – such as optical frequencies – liquid crystals are always positive dielectric materials [11], owing to the mostly delocalized electronic response along the liquid crystal's length.

1.4.1 Optical Anisotropy

As an extension of their dielectric anisotropy, liquid crystals also present with an optical anisotropy known as birefringence. When light enters a material, its wavelength and velocity decrease by a factor called the index of refraction, n. This index is equal to the square root of the electric permittivity [42]. There are two indices of refraction in a uniaxial medium (such as liquid crystals): the ordinary refractive index, $n_0 = \sqrt{\epsilon_\perp}$, and the extraordinary refractive index, $n_e = \sqrt{\epsilon_\parallel}$. Here, the ordinary index of refraction interacts with light that is polarized perpendicular to the optical axis of a liquid crystal molecule (the director), while the extraordinary index interacts with light polarized parallel to the optical axis. The difference between these indices, $\Delta n = n_e - n_0$, is the definition of birefringence. [42]. As with many liquid crystal properties birefringence is temperature dependent, decreasing with increasing temperature [11].

One of the most apparent and important effects of birefringence in liquid crystals is known as retardation. Due to retardation, if light incident in a birefringent medium is polarized in such a way as to interact with both indices of refraction, the components of the light travel through the medium with different velocities. When the light exits the birefringent material the ordinary and extraordinary components are out of phase with one another by an angle $\phi = k_0(n_e - n_o)d$, proportional to the distance d traveled through the material. This has the effect of changing the incident light's polarization [42].

When a liquid crystal is imaged between crossed polarizers, the light incident on the liquid crystal is linearly polarized. If the light is polarized parallel or perpendicular

to the optical axis, there will be no optical retardation and therefore no light will be transmitted through the second polarizer. If, however, the light propagates through the material at an angle $\theta \neq 0$ *or* 90 with respect to the optical axis, the ensuing retardation makes it so a portion of the light will be visible through the second polarizer. By this effect, it is possible to study the orientational order of liquid crystals.

1.5 Elastic Distortions

As stated in the section on the Order Parameter, we cannot assume that liquid crystal director $\hat{n}$ is always uniform. Be it from external fields – electric fields – or imposed boundary conditions – alignment layers – liquid crystals will often undergo some sort of director distortion. These elastic distortions can be seen as analogous to a spring system, with variations being energetically proportional to the square of the deviations , *i.e.* they are Hookean. In an achiral nematic liquid crystal system, there are typically three elastic distortions that describe how the liquid crystal molecules can be aligned: splay, twist, and bend as shown in Fig. 1.7 [12].

For an achiral nematic liquid crystal the free energy per unit volume associated with these distortions is given as:

$$F_v = \frac{1}{2}K_{11}[\nabla \cdot \hat{n}]^2 + \frac{1}{2}K_{22}[\hat{n} \cdot (\nabla \times \hat{n})]^2 + \frac{1}{2}K_{33}|\hat{n} \times (\nabla \times \hat{n})|^2 \qquad (1.7)$$

where the terms K_{11}, K_{22}, and K_{33} are the elastic constants that respectively correspond to the splay, twist, and bend distortions [12]. Like in the equation for a spring these elastic constants are the expression of how "stiff" or how much the liquid crystal material will resist being distorted, and have the units of force. When distorted, the liquid crystal will try to reduce the energy. Typical values for these constants are of the order of magnitude 10^{-6} dynes (10^{-11} newtons), with $K_{11} \approx K_{33}$ and 2 or 3 times

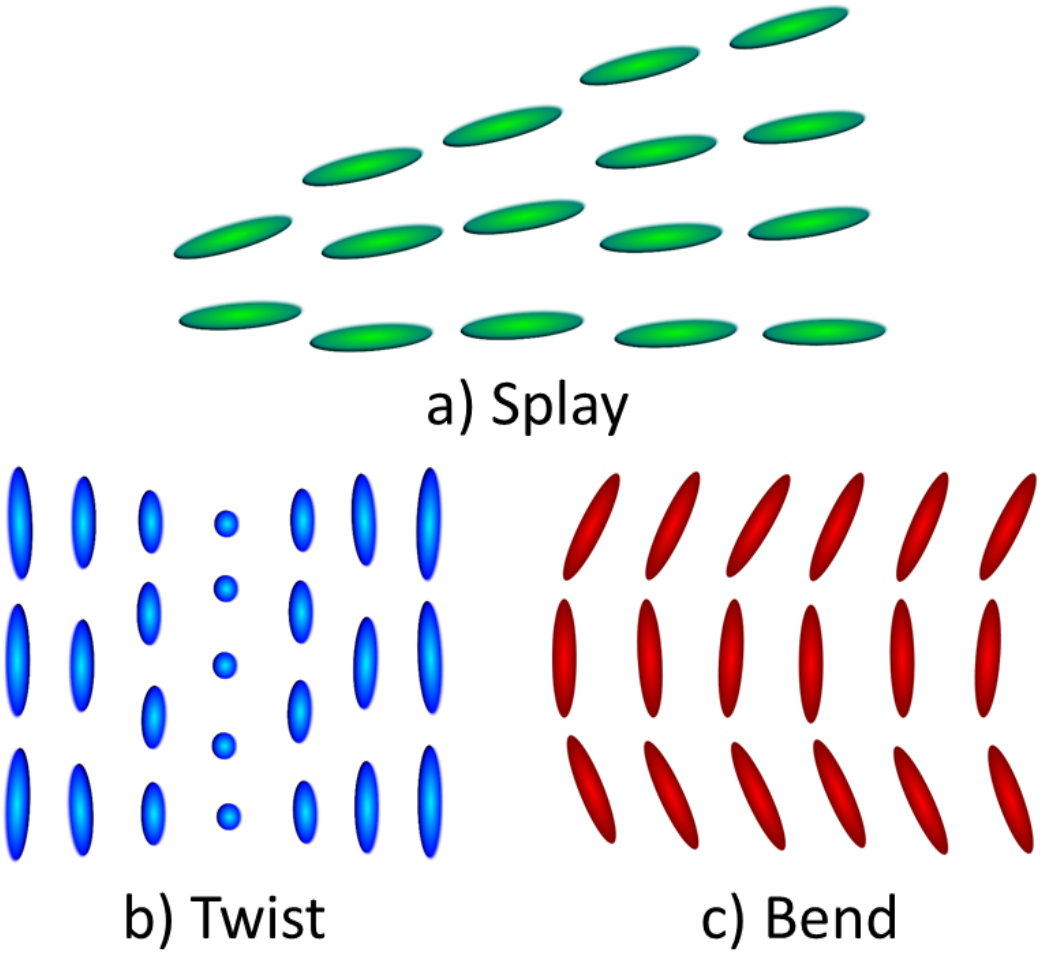

Figure 1.7: The (a) splay, (b) twist, and (c) bend elastic distortions.

larger than K_{22} [11].

While there are situations where only one distortion is present, it is possible to have any combination of these distortions in a single liquid crystal system. This can complicate the situation and make calculations too difficult to be practical. In these situations it often is prudent to make the approximation $K_{11} = K_{22} = K_{33} = K$, which simplifies the free energy equation to:

$$F_v = \frac{1}{2}K[(\nabla \cdot \hat{n})^2 + (\nabla \times \hat{n})^2] \tag{1.8}$$

When chirality is present – such as in the cholesteric phase – another linear term

may be added to the free energy:

$$F_{v\ chiral} = k_2[\hat{n} \cdot (\nabla \times \hat{n})] \tag{1.9}$$

where k_2 is another constant with units of dynes/cm [11]. In a system with chirality, the equilibrium state would be that of a helix, like that in Sec. 1.2.3.

While Eq. 1.7 does a reasonably good job on the macroscopic scale where distortions in the director are slow on the microscopic scale, it doesn't well account for regions where $\hat{n}$ is not well defined [11]. To deal with these undefined regions, additional equations describing distortions in the liquid crystal director – beyond the scope of this introduction – may be utilized [12].

1.6 Surfaces Effects

1.6.1 Surface Alignment

In order to obtain a uniform orientation in bulk liquid crystal systems, an aligning agent at a surface can be used to impose well defined boundary conditions. The primary methods used to obtain these uniformly orientation alignment layers are chemical and mechanical. These alignment layers give the liquid crystal molecules a preferred azimuthal or polar orientation known as an "easy axis" ($\hat{e}$), which is commonly parallel to the director. Depending on the type of surface or surface treatment, there are a number of different possibilities, two of which are shown in Fig. 1.8.

As shown in Fig. 1.8, the most common alignments are homeotropic – where ϕ_0, the angle between the surface and the director is 90° – and planar – where $\phi = 0$. A surface can also be treated to have an alignment such that $0° < \phi < 90°$, which is known as a "pretilt". Certain polyimides and polymers (such as RN1175 [43] and polyvinyl alcohol (PVA) [44]) can promote planar alignment when used as

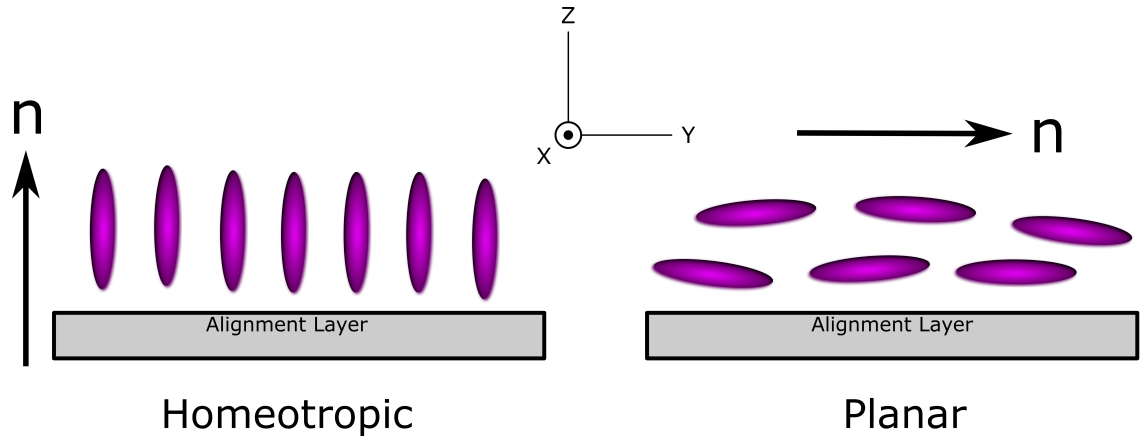

Figure 1.8: Examples of the homeotropic (left) and planar (right) liquid crystal alignment due to different surface treatments.

a surface treatment on glass. The rubbing generates grooves in the substrate as well as aligns the long polymer chains, creating a single easy axis θ_0 along which the liquid crystals orient. It is possible to attain planar alignments with two or more easy axes, such as crystals such as NaCl [12] and MoS_2 [45], or degenerate planar alignments – where there is a 2π variation with no special easy axis – through the use of poly(methyl methacrylate) (PMMA) [46]. Homeotropic alignment can be promoted through surface treatments with detergents such as hexadecyltrimethylammonium bromide (HTAB) [47] or certain lipids [12], and interfaces with isotropic media such as air [48]. By placing a liquid crystal between two different alignment layer it is possible to obtain what is known as a hybrid alignment layer, with one side planar and the other homeotropic.

1.6.2 Surface Anchoring

As with the elastic distortions, there is a free energy associated with the surface alignments. When liquid crystal molecules at a liquid crystal / alignment layer interface are oriented at an angle with respect to the easy axis, it costs energy. To first order, this "anchoring energy" depends on the square of the displacement from θ_0 and ϕ_0, the polar and azimuthal angles associated with the easy axis in an equilibrium state.

The lowest order approximation of the free energy due to surface anchoring is:

$$F_s = \frac{1}{2}W_2^{\theta}\sin^2(\theta - \theta_0) + \frac{1}{2}W_2^{\phi}\sin^2(\phi - \phi_0) + ... \tag{1.10}$$

where θ is the polar deviation from a planar anchoring, ϕ is the azimuthal deviation from a homeotropic anchoring, W_2^{θ} is the polar anchoring coefficient, and W_2^{ϕ} is the azimuthal anchoring coefficient which can depend on ϕ. While it is possible to use higher order even terms such as W_4^{θ} and W_4^{ϕ}, this is usually only necessary for when the deviations are large. Anchoring coefficients are always positive, and those on the order of $\sim 10^{-4}$ J/m^2 are considered "strong" anchoring those on the order of $\sim 10^{-6}$ J/m^2 are considered "weak". When chirality is added into the system it is possible to add in linear and cubic terms.

1.7 Electroclinic Effect

First demonstrated by Garroff and Meyer [49], the so-called electroclinic effect (ECE) is a powerful test of the chirality of liquid crystalline materials. In the bulk Sm-A^* phase the application of an external electric field $\vec{E}$ parallel to the smectic layer planes couples to the liquid crystals' molecular dipole moment. This coupling in turn induces a tilt in the director θ proportional to $\vec{E}$. This is only possible due to the chiral symmetry breaking, and a C_2 axis which lies parallel to the smectic layer plane [49]. Application of an electric field $\vec{E}$ breaks the $D_{\infty h}$ symmetry, and establishes a C_2 axis and results in a director rotation by an angle $\theta \propto E$ about that axis. The strength of this response can be described through the electroclinic coefficient $e_c = d\theta/dE$. As the temperature of such a system is decreased towards the Sm-A^* to Sm-C^* transition, the strength of this effect will increase rapidly and shows divergent behavior due to increasing Sm-C^* like fluctuations [49]. This effects is seen mostly in negative dielectric anisotropic liquid crystals.

It has also been shown that an electroclinic effect can be obtained in the chiral nematic phase [50, 51]. While the nematic phase is not characterized by smectic layers, there are still smectic like fluctuations present throughout the bulk liquid crystal material. It is these fluctuations that allow for an ECE, with the molecular dipole moments coupling to $\vec{E}$ in a similar fashion. Also similar to the Sm-A^* electroclinic effect, upon nearing the N* to Sm-A^* transition temperature the strength of this effect increases due to an increase in smectic like fluctuations in the bulk.

1.7.1 Surface Electroclinic Effect

In addition to the bulk effects seen in the Sm-A^* and N* phases, there also exists a surface effect that presents with a rotation proportional to an applied field. [52, 53, 54, 55]. For this effect to occur two requirements must be met: i) a chiral environment due to a chiral liquid crystal, a chiral surface, or both, as well as ii) some form of planar easy axis to reduce the rotational symmetry from C_∞ to a C_2 at the liquid crystal / surface interface. [56, 54]. Systems that take advantage of these requirements have been shown to exhibit a surface ECE chiral surfaces and an achiral liquid crystal [56, 57, 58], and for an achiral surface with an easy axis and a chiral liquid crystal [55]. By applying $\vec{E}$ perpendicular to the substrate, a torque on the director is created. This results in a rotation of the director at the substrate, which propagates as into the bulk as a twist. The amount of this tilt is dependent on the makeup of the liquid crystal and alignment layer, as well as their degree of chiral coupling.

1.7.2 Experimental Setup

The experimental setup to probe a bulk electroclinic effect is relatively straightforward. The most widely used geometry for it was first described by Andersson *et al* [59], and allows for easier detection than previous arrangements. The basic setup is shown in Fig. 1.9. A transparent capacitive cell with antiparallel planar alignment

layers is filled with a chiral liquid crystal material (usually a negative dielectric) in the Sm-A^* or chiral nematic phases. A collimated light source – such as a laser – is used to probe the sample. This light travels through a polarizer set at 22.5° with respect to the easy axis of the liquid crystal sample, through the sample, through another polarizer (the analyzer) which is set at 90° with respect to the first polarizer, and finally into a detector.

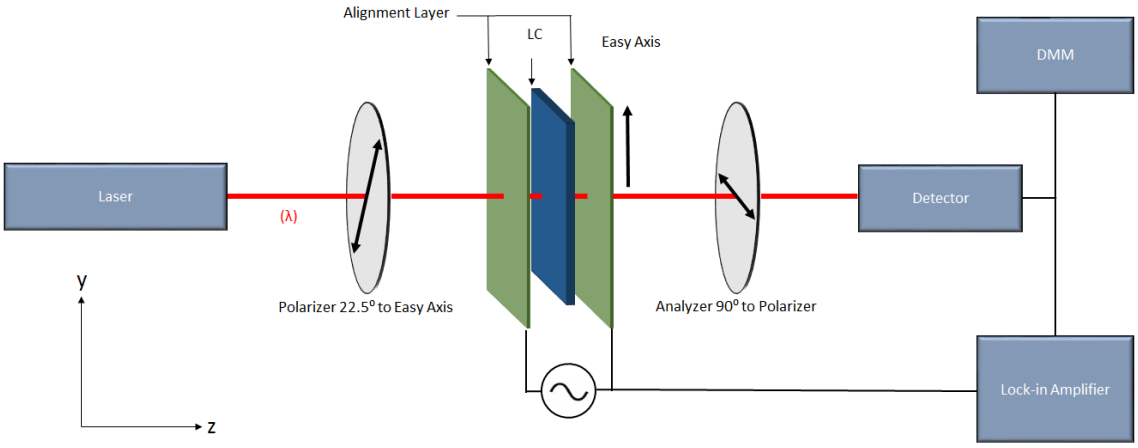

Figure 1.9: Schematic representation of the classical electroclinic setup [59].

The capacitive cell containing the liquid crystal is connected to a waveform generator which creates an oscillating electric field E in the cell, normal to the alignment layer surface. This electric field couples to the polarization of the liquid crystal, and forces it to tilt with the oscillating field which in turn induces a rotation of the director. For the geometry shown here, the induced tilt in the director θ is given by:

$$\theta = \frac{I_{ac}}{4I_{dc}} \tag{1.11}$$

where I_{ac} is the variation in light intensity due to the electric field induced tilt, and I_{dc} is the background intensity. This is derived from the geometry for the crossed polarizers set at 22.5° with respect to the system's easy axis. At this angle the response in is linearly proportional to E, and allows for the maximum possible variation in

intensity.

For a *surface* electroclinic effect, there can be a slight modification to the setup. If the surface electroclinic effect occurs on both sides of the sample, like in Chapter 4, no modification is necessary. If instead only one surface presents with an electroclinic effect – only one chiral substrate with an achiral liquid crystal – changes to the geometry of the polarizer, analyzer, and sample are necessary. The polarizer is rotated to be parallel or perpendicular to the easy axis in the cell – rather than at 22.5° – and the analyzer is no longer set perpendicular, but at 45° with respect to the polarizer. The sample cell must now be oriented so that the light source is incident on the side with no optoelectric effect. This allows the polarization of light to follow the director rotation adiabatically.

1.8 Oily Streaks

In systems where a liquid crystal is subjected to similar boundary conditions at two liquid crystal interfaces, *e.g.* planar alignment, the liquid crystal will maintain a uniform director alignment throughout the system. If, however, the liquid crystal is subjected to antagonistic boundaries, the director is forced to vary in such a way as to satisfy these conditions. For example, if a liquid crystal in a nematic phase is placed between two different alignment layers, such as one planar and one homeotropic, the liquid crystal director is forced to gradually transition from one alignment to another through a combination of bend and splay. While such a transition in alignment is easily accomplished in the nematic phase, this is not the case for more highly order phases.

In the layered smectic phases the elastic distortions twist and bend are expelled [12]. Because of this, periodic microstructures often occur in smectic films when the films are subjected to competing boundary conditions. One such structure is

known as the "oily streak", which occurs in the Sm-A phase for films of liquid crystal less than $\sim$ 500 nm in thickness. Oily streaks form as linear arrays of flattened hemicylinders due to the competition between a homeotropic alignment at a liquid crystal / air interface and a unidirectional planar alignment at a liquid crystal / substrate interface. When imaged in an optical microscope under crossed polarizers, the oily streaks appear as a linear array of lighter and darker stripes perpendicular to the easy axis (Fig. 1.10) [60, 61, 62, 48].

Figure 1.10: Photomicrograph of oily streaks, oriented at 45° between crossed polarizers. The scale bar is oriented parallel to the easy axis.

Due to the high energy cost of maintaining a transition from planar alignment to homeotropic in the Sm-A phase, these oily streaks contain a number of deformations to maintain their structure [61, 63, 60, 64, 48]. Fig. 1.11 shows a cartoon representing a generic oily streak, supported by x-ray and ellipsometry data [60, 48], and highlights a number of features characteristic to these structures. The region marked **A** represents a rotating grain boundary (RGB) which defines a transition from the curvature walls (item **C**) to a central homeotropic region (item **D**), and is characterized as being a series of edge dislocations. Item **B** denotes a 2D defect that connects the central homeotropic layers to the planar transition region near the substrate (item **E**). The exact structure of the transition layer may vary, from covering the entire

alignment layer surface to only covering the areas not immediately under the central homeotropic region [48, 65]. The appearance of this transition layer depend on many factors, including but not limited to: the liquid crystal, the alignment layer, and the liquid crystal film's thickness [48]. The 2D defect may also vary depending on these same factors, and could either be a grain boundary or a melted nematic [48]. These structures will be gone into with more detail in Chapters 5 and 6.

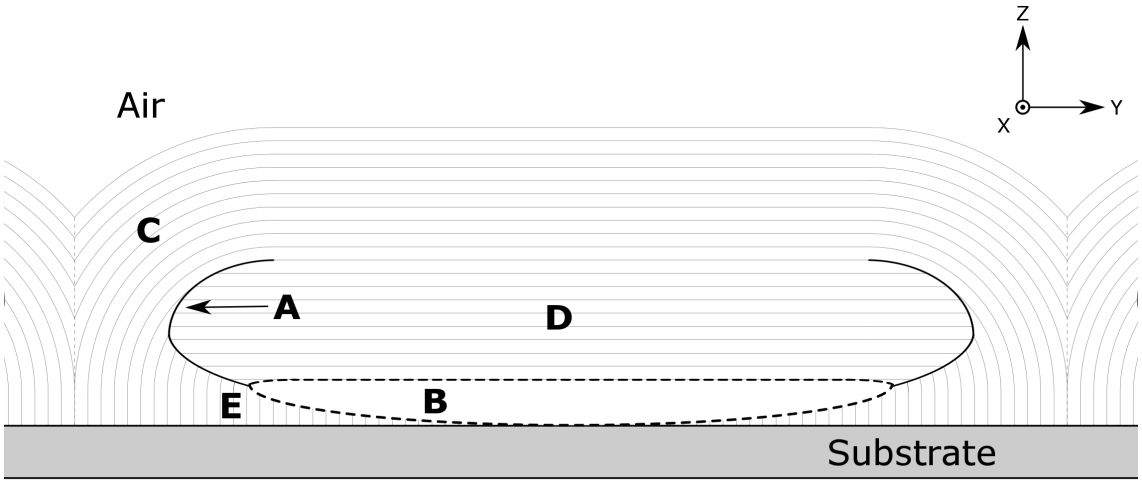

Figure 1.11: Easy axis along $\hat{y}$. Structure of Sm-A oily streaks where the thin lines represent smectic layers, **A** represents the rotating grain boundary, **B** the 2D defect, **C** the curvature walls, **D** the central homeotropic region, and **E** the planar transition region near the alignment layer.

1.9 Outline of Experiments

The focus of this dissertation is split between two different topics. The experiments in Chapters 2-4 focus on the chiral electroclinic effect due to surface interactions and microparticles. Chapter 5 is a transitional chapter dealing with both chirality and the characterization of nanostructures. The experiments in Chapter 6 focus on the characterization of nanostructures that arise from hybrid smectic liquid crystal alignments. In these chapters a number of novel properties and effects are investigated.

In Chapter 2, nematic twist cells are doped with chiral agents to compensate for the imposed twist and probed with the electroclinic effect. The results demonstrate that (i) the electroclinic effect in twist cells is localized at the surface and (ii) the electroclinic effect vanishes when the twist is perfectly compensated. Additionally, this method is shown to be an effective measure of helical twisting power of liquid crystal / chiral dopant mixtures.

In Chapter 3, the electroclinic effect in a chiral periodic mesoporous organosilica (PMO) doped liquid crystal near the Sm-A – Sm-C transition is investigated. It has been shown that the chiral pores of the PMO are the source of the chiral induction in the system. The purpose is to probe whether the liquid crystal inside or outside of the pores are the source of the electrooptic effect in the system. The results of the PMO doped system are compared with that of a system doped with the chiral molecule CB15. The results suggest that the overwhelming source of the optical signal comes from just outside of the PMO pores, and that the contribution from inside the pores is negligible.

In Chapter 4 the electroclinic effect above the nematic – isotropic transition temperature is explored in systems with planar alignment layers. Evidence that the electroclinic effect does in fact exist in this temperature regime, and that it occurs in the thin aligned layer near the alignment layers, is presented. The results show that this effect occurs due to the presence of nematic – not smectic – ordering induced by the surface. Additionally, the fact that this effect is comparable in magnitude to its bulk nematic counterpart is shown.

In Chapter 5 there is a transition from experiments that utilize the electroclinic effect to those that explore liquid crystal structures. Using a mixture of the liquid crystal 8CB doped with CB15, open cells are coated with thin films of the doped liquid crystal to make Sm-A oily streaks. Just below the nematic - Sm-A transition temperature a rotation of the oily streaks that decreases with temperature is observed.

The rotation just below T_{NA} is explained by the smectic surface electroclinic effect. It is also noted that oily streaks have a temperature dependent periodicity near the same transition.

Chapter 6 reports on a novel liquid crystal structure that we dub "soapy streaks". These soapy streak occur below the Sm-A – Sm-C transition temperature, and have a number of interesting characteristics. The new structures form parallel to the easy axis, and seen to destroy optical evidence of the Sm-A oily streaks that preceded them at higher temperature. Methods of fabrication and characterization are mentioned, and a possible model explaining the appearance of the soapy streaks is suggested.

Chapitre 2

Nematic twist cell: Strong chirality induced at the surfaces[1]

2.1 Introduction

Of great interest in liquid crystal research is the ability to induce a net chirality in configurationally achiral liquid crystals. It is well known that by doping an achiral liquid crystal with a chiral agent, a helical twist in the director is the result [12]. By inducing chirality in a liquid crystal system, it is possible to see a variety of effects. These effects range from the selective reflection of different wavelengths of light or the rotation of polarized light due to the (temperature dependent) pitch [11] in cholesterics to ferroelectric properties such as the electroclinic effect in the Sm-A^* phase [49, 59]. Even fast switching of director orientations in the Sm-C^* [20] can be explored.

Doping is not the only method of chiral induction in liquid crystal media, and many of these other methods have been thoroughly studied. One example is the work done by Ferjani *et al* [57] and Pendery *et al* [58]. They demonstrated that by scribing a surface alignment layer with a chiral pattern (using an atomic force microscope), it is

[1]This chapter is based on one of my articles in: Applied Physics Letters.
T. C. Lin, I. R. Nemitz, J. S. Pendery, C. P. J. Schubert, R. P. Lemieux, and C. Rosenblatt "Nematic twist cell: Strong chirality induced at the surfaces," *Applied Physics Letters* 102, no. 13 (2013):1134101.

possible to induce varying degrees of chirality and probe a surface electroclinic effect. Other work, dealing with molybdenum di-sulphide and graphene [66] show chiral molecular arrangements at the materials surface, and there is evidence that these can even be transferred into the bulk [67]. One such method of chiral induction recently published is induced conformal deracemization through a macroscopic torsional strain [68, 56, 69].

2.1.1 Twist Cells

By assembling a surface stabilized cell in such a way that the easy axis of the two alignment layers are rotated with respect to one another by an angle θ_0 (rather than parallel or antiparallel), an achiral nematic liquid crystal can be conformationally deracemized [68, 69]. According to the model proposed by Basu *et al* [68] this chiral environment provides its strongest effect near the surface, where the competition between the imposed twist and the surface anchoring rotate the director slightly away from the easy axis. The data showed this deracemization is proportional to the imposed inverse helical pitch P^{-1}. Later it was also shown that the deracemization is proportional to strength of the symmetry breaking at the surface (rubbing strength) [56]. The liquid crystal used in these experiments – 9OO4, shown in Fig. 2.1 – is configurationally achiral and conformationally racemic, with equal measures of both left-handed and right handed molecular conformer present at room temperature (the energy separating the two lowest energy conformational states is $\sim 0.8 k_b T$, therefore the energy barrier is small enough that each molecule is switching between right and left handed conformations). The enantiomeric excess – which is proportional to and created by the twist – now has an average molecular polarization capable of coupling to an electric field. Using a special optical geometry that compensates for this macroscopic helical twist [68], it is possible to measure this chiral effect. Applying a sinusoidal ac electric field $\vec{E}$ across the sample creates a rotation of the

director $\Delta\theta \propto E$, an electroclinic effect. The frequency response of this system, which shows a swiftly decreasing signal with an increasing in frequency, indicates that this effect is localized near the surface, and is a *surface nematic* electroclinic effect [68].

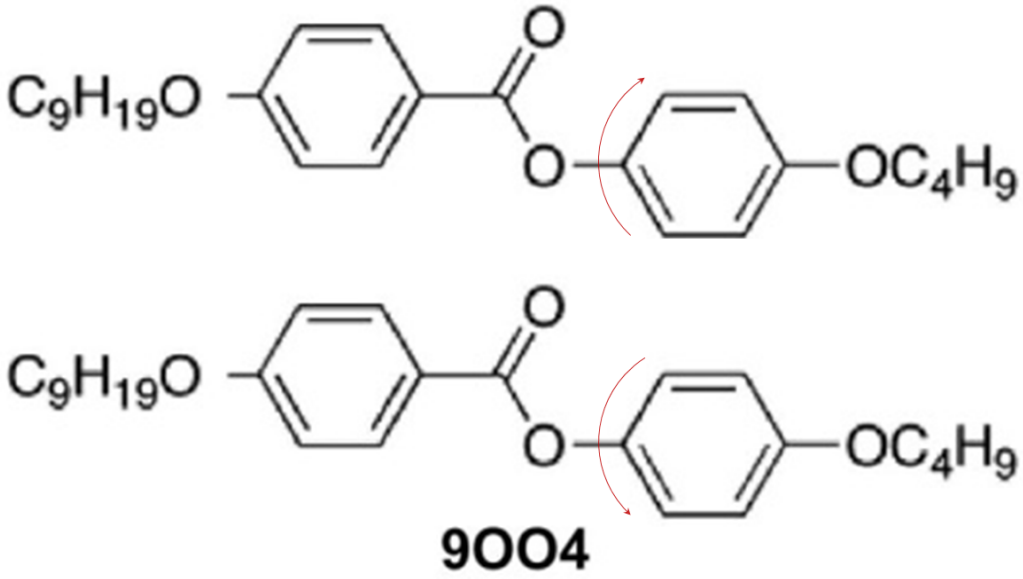

Figure 2.1: The liquid crystal 9OO4 (phase sequence Iso – 83° – N – 70° – Sm-A – 62° –Sm-C – 50° – Sm-B – 35° – Cryst.) is an achiral liquid crystal. It can adopt a chiral conformation in the ground state by adjusting the dihedryl angle between the aromatic rings. There is an equal probability distribution between the left and right handed twist fluctuations; which makes it a dynamically racemic LC.

This chapter describes a series of experiments in nematic twist cells, in which the achiral liquid crystal 9OO4 is doped with a chiral molecule. This purpose of this chiral molecule is to compensate approximately for the imposed twist in these systems. These experiments demonstrate that the electroclinic effect observed in previous work occurs most strongly at the azimuthally rotated alignment layers. The data indicate that this effect diminishes and vanishes as the thickness of a cell gap nears and becomes equal to that of the imposed twist, *i.e.* the 20°variation of the easy axis between the alignment layers. Additionally, it is shown that the helical twisting power of a dopant / liquid crystal combination can be deduced by determining the thickness of the cell where the mixtures natural rotation equals the imposed twist,

i.e., $\theta = \theta_0$.

2.2 Experimental Methods

2.2.1 Sample Preparation

Two cells with an imposed twist were prepared using indium-tin-oxide (ITO) coated glass substrates that were spin coated with the planar-alignment agent RN-1175 polyamic acid (Nissan Chemical Industries) at 2000 rpm for 20 seconds. The polyimide coated substrates were baked for 5 minutes at 80°C creating an easy axis on the substrates for alignment of the director. The rubbing cloth was attached to the cylindrical roller of an Optron rubbing machine. The cell needed to be assembled in such a way that the two substrates' easy axes were rotated by an angle $\theta_o = (20 \pm 1)^\circ = (0.35 \pm 0.02)$ rad with respect to one another. To ensure accurate assembly and reproducibility of the cells, alignment aids were machined and utilized as shown in Fig. 2.2.

The cells' thickness d was varied (a so called "wedge cell") by inserting an 8μ mylar between the substrates on only one side of the cell, while the other side was etched with acid to remove the ITO to avoid any contact between the electrodes even though the glass was touching. The final geometry is shown in Fig. 2.3. The cells were held together by a metal clip (rather than cemented, in case further modification was required), and the resulting empty cell had a thickness varying linearly across the width of the cell from 3 μm to 8 μm (from left to right in Fig. 2.3) as measured by optical interferometry. Electrical leads were attached individually to both substrates with indium tin solder, and the well was filled in the isotropic phase with a $c = (0.00144 \pm 0.00005)$ weight fraction mixture of right-handed chiral dopant CB15 in the liquid crystal 9OO4.

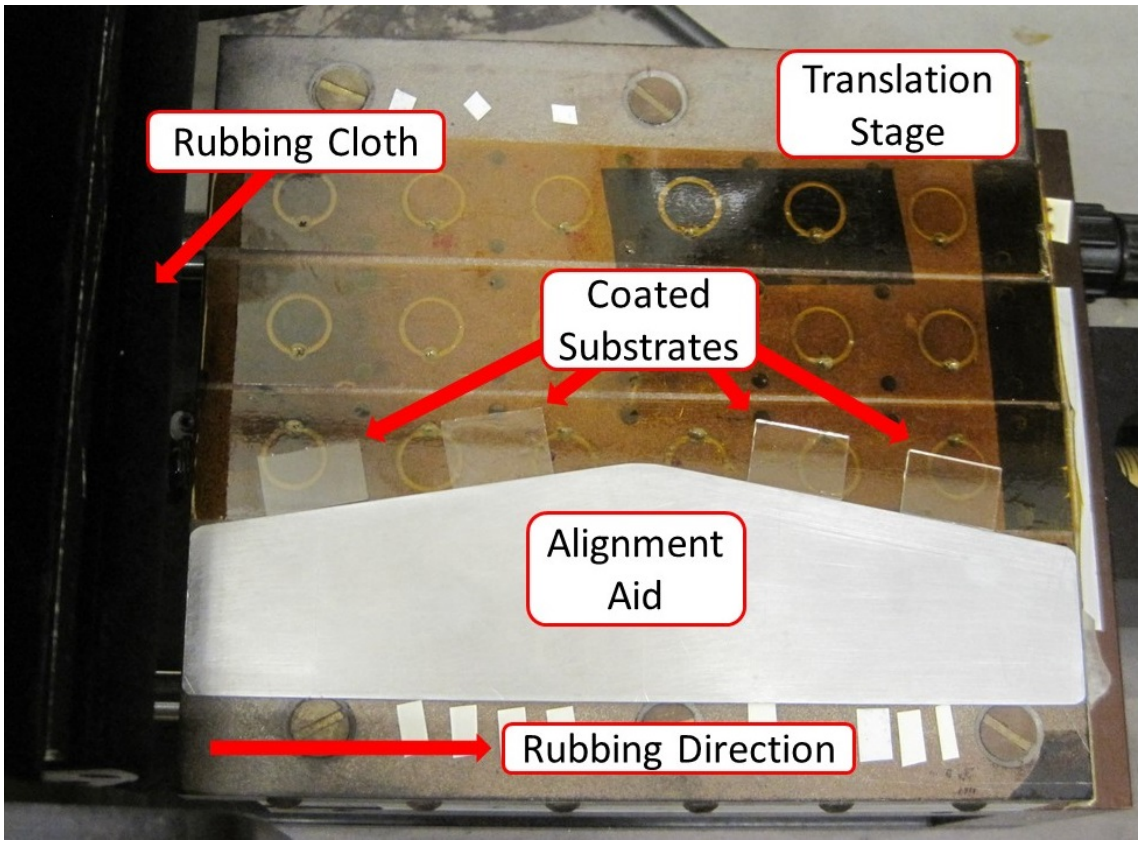

Figure 2.2: Image of the rubbing setup used in this experiment. The aluminum alignment aid is placed on the translation stage so that the long end is parallel with the intended rubbing direction. The aids are angled by 10°. When the cells are assembled they will have a 20° rotation.

2.2.2 Experimental Setup

The experimental setup was a modification of the classical optical geometry generally used for electroclinic experiments shown in Section 1.7.2 [59]. By rotating the polarizer and analyzer by approximately the same amount as the twist imposed on the cells, it is possible to compensate for the change in polarization of the light, as shown in Fig. 2.4. Specifically, in a right handed twist cell the incoming polarizer was set to an angle of $\pi/8$ counter clockwise (looking from the front to the rear of the setup) with respect to the easy axis of the first substrate. The analyzer was then oriented at an angle of $-\pi/2-\theta_0$ relative to the polarizer (for a left handed twist the polarizer would have been rotated clockwise, and the analyzer would have been adjusted by $+\theta$). θ_0

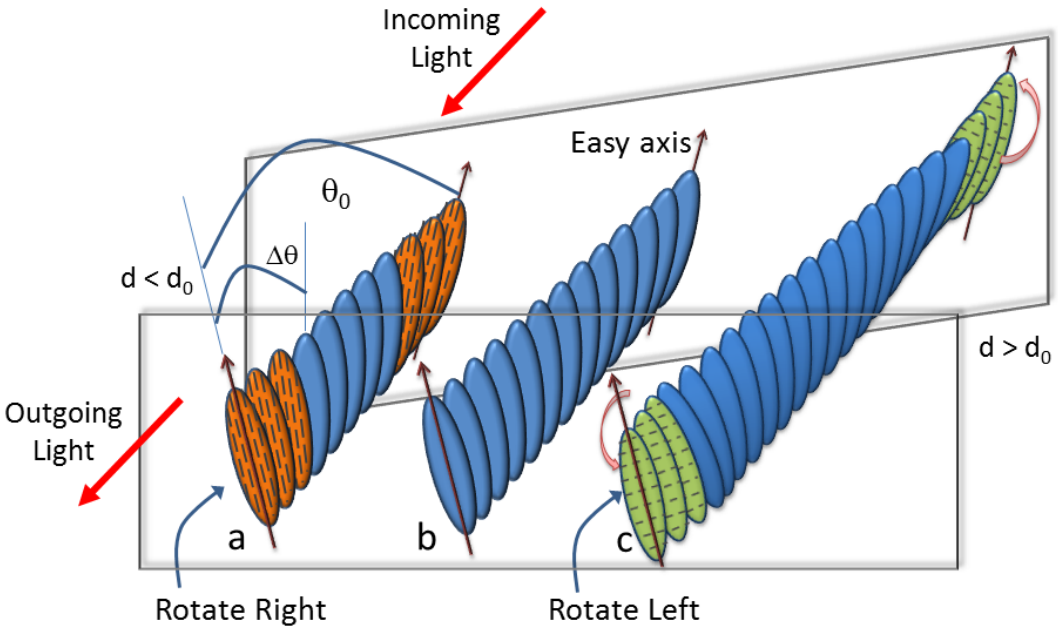

Figure 2.3: Schematic representation of experiment. The easy axes are rotated by $\theta_0 = 20^\circ$ respect to each other. For $d < d_0$ (panel a), the chirally doped liquid crystal rotates, through the bulk of the cell (solid blue "molecules"), but there is a sharp right-handed twist by angle $\Delta\theta$ over a very narrow region of a few molecules (orange, with stripes) near the surfaces. For $d = d_0$ (panel b), the bulk helical rotation is equal to θ_0 and, therefore, $\Delta\theta = 0$. For $d > d_0$ (panel c), the bulk helical rotation overshoots the easy axes, and there is a sharp left-handed twist by angle $-\Delta\theta$ over a few molecules (green, with stripes) near the surfaces. Note that "a few molecules" is not well defined.

would be zero if there were no imposed twist, and the optical arrangement would correspond to the classical electroclinic geometry [59]. For $\theta_0 \neq 0$ the polarization of the light through the samples approximately follows the weak director twist due to adiabatic following, such that the ordinary and extraordinary components of the light incident on the sample are rotated $\pm\theta_0$, where the sign of the rotation depends on the handedness of the twist: positive for a right handed twist, and negative for a left handed twist. Using this arrangement, the rotation of the analyzer and polarizer compensates for the twist of the cell, and effectively maintains a geometry similar a classical electroclinic setup.

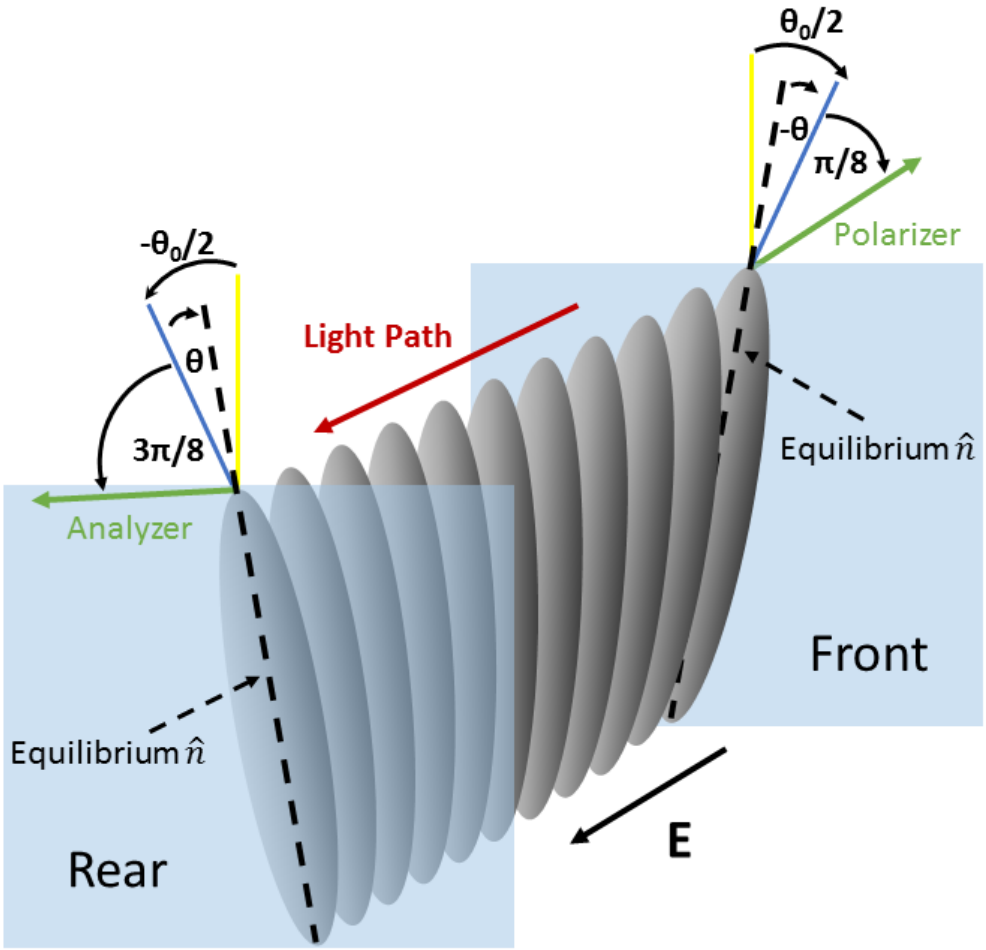

Figure 2.4: Schematic diagram of the modified electroclinic geometry used for a right handed twist cell. θ_0 represents the angle by which the substrates are rotated with respect to one another, while θ represents the director orientation $\hat{n}$ at equilibrium with respect to the easy axis at the alignment layer. $\vec{E}$ represents the electric field. Image courtesy Basu *et al* [68]

To probe this system, a He-Ne laser of wavelength $\lambda = 633$ was used as a light source, with the light passing through the polarizer, the cell, the analyzer, and finally into the detector. The cell was placed into an enclosed temperature stabilized heater (Instec Mk1), and kept at 77°C in the nematic phase for the entirety of the experiment. An ac voltage at frequency f was applied across the cells by a Stanford Research Systems DS345 waveform generator, and ramped from 0 to 6 V in ~ 0.15 V increments over 150 s. The output from the detector was fed into a Keithley 2001 dc voltmeter as well as a Stanford Research System 830 lock-in amplifier referenced to the waveform

generator's output. Four frequencies on a logarithmic scale were examined $f = 31$, 100, 310, and 1000 Hz. The ac optical intensity I_{ac}, its phase relative to the applied voltage V_{rms}, and the dc optical intensity I_{dc} were recorded.

Using the computer program known as Igor, the waveform generator and the DMM's were controlled, and data was recorded, through a program that allowed remote management of the setup's electronic components. The code used for this experiment can be found in Appendix A.

2.2.3 Compensation

Because the thickness d_{PI} of each of the two polyimide alignment layers was ~ 0.16 to 0.18 μm, which is of order of only one magnitude smaller than the liquid crystal thickness d, the data needed to be corrected to account for the voltage drop across the two polyimide layer [70]. At the frequencies used, the cell behaved a LC resistor with polyimide capacitors in series rather than resistors in series, where the total capacitance $C = \epsilon_0 A(2d_{PI}/\epsilon_{PI} + d_{test}/\epsilon_{test})^{-1}$. Here ϵ_0 is the permittivity of free space, A the area of the capacitor, ϵ_{PI} the dielectric constant (~ 3.0 [71]) of the polyimide, and ϵ_{test} is the dielectric constant of the test material (air or LC) filling the gap d_{test} between the polyimide layers. Thus, an empty test cell of uniform thickness $d_{test} = 5.2$ μm and having and ITO overlap area $A = 75$ mm^2 was constructed. The capacitance of the empty cell was then measured at temperature $T = 77$°C – the temperature for all data presented in this work – using an Andeen-Hagerling 2500 capacitance bridge, finding $C = 125$ pF, and thus $2d_{PI}/\epsilon_{PI} = (0.10 \pm 0.01)$ μm. The cell was then filled with 9OO4 in the planar alignment and obtained $C = 550$ pF, from which $\epsilon_{LC} \equiv \epsilon_{test} = 4.7$, *i.e.*, the dielectric constant of the 9OO4 perpendicular to the director, was deduced. Having these values, it is easy to determine the rms voltage V_{rms}^{LC} across *only* the LC (of thickness d) in the experimental cell: $V_{rms}^{LC} = V_{rms}(2\frac{d_{PI}}{\epsilon_{PI}}\frac{\epsilon_{LC}}{d} + 1)^{-1}$. Thus V_{rms}^{LC} was smaller than the applied V_{rms} by approximately

14% in the thinnest regions of the wedged cell, and about 6% in the thickest regions. This confirms that compensattion for the polyimide layer was indeed necessary, and that the method presented here can be used.

2.3 Results and Analysis

2.3.1 Doped Twist Cells

Shown in Figure 2.5 is the electroclinic coefficients plotted *vs* cell spacing d for four different frequencies. These correspond to the slopes $d(I_{ac}/4I_{dc})/dV_{rms}$ in Fig. 2.6 multiplied by the thickness d, and corrected for the voltage drop across the LC only, as described in Sec. 2.2.3, *i.e.*, $e_c = d(I_{ac}/4I_{dc})/dE^{LC}_{rms}$. Figures 2.6 and 2.5 clearly show that the electroclinic response changes sign at a cell thickness $d = d_0 = (4.8 \pm 0.1)$ μm, which was obtained by averaging the zero crossings of e_c for the four sets of frequency data.

As mentioned earlier, Basu *et al* (Ref. [68]) proposed a simple model in which the 9OO4 partially deracemizes conformationally so as to relax the energy cost of the imposed twist; this deracemization, in turn, has an entropic energy cost. The result was a small conformational enantiomer excess in the bulk nematic LC, but which was calculated to be insufficient to produce the e_c magnitudes observed. However, because of the competition between the twist elasticity, which promotes a uniform director profile through the cell, and the surface anchoring energy, which promotes a surface orientation along the easy axes, there is an equilibrium deviation $\Delta\theta$ of the director at the surfaces from the two easy axes. In a pure (undoped) achiral LC, this results in a very sharp twist, *i.e.*, a very tight effective helical pitch, within a few molecular widths of the surface. It is this tight pitch that causes a much larger deracemization in the vicinity of the surface, sufficient to give rise to the observed electroclinic response. But if the LC is doped with an appropriate concentration of

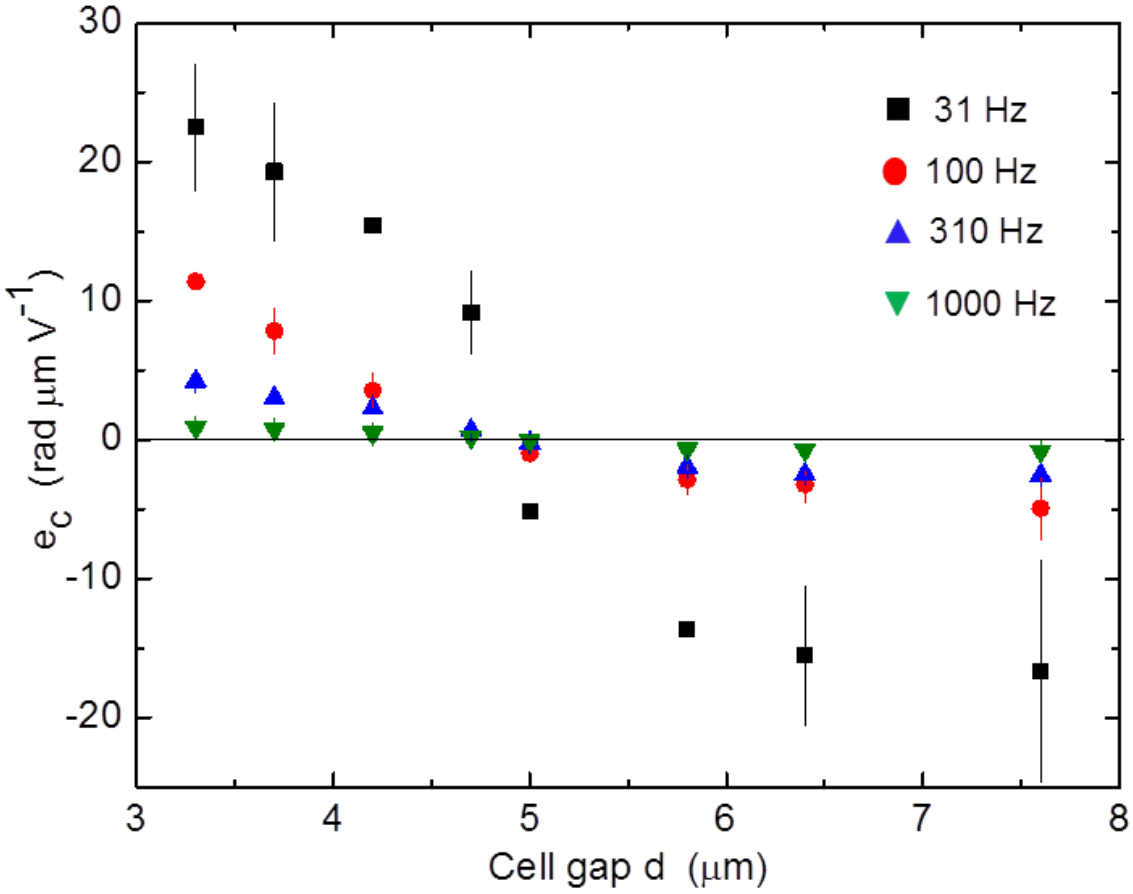

Figure 2.5: The electroclinic coefficient e_c vs. the cell gap d at four different frequencies. The horizontal line corresponds to the zero crossing of e_c.

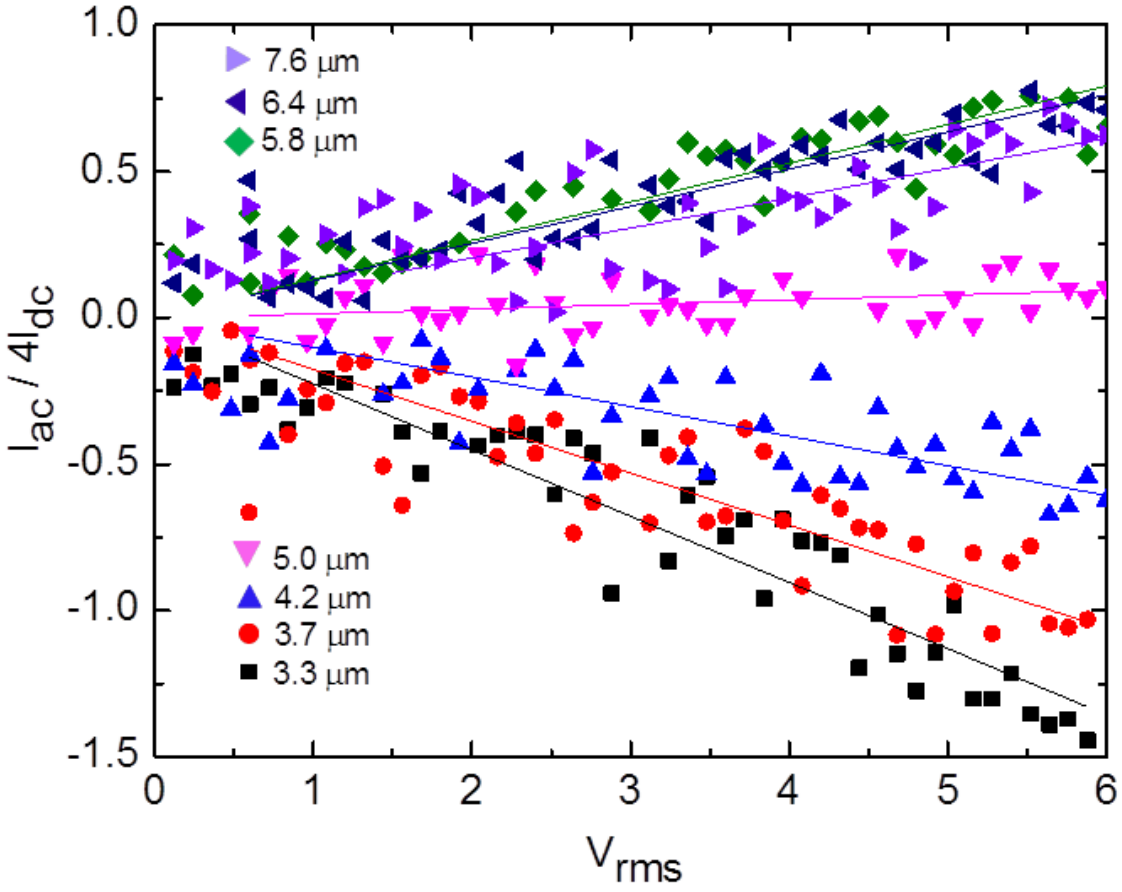

Figure 2.6: $I_{ac}/4I_{dc}$ measured at seven different gap thicknesses d, vs. the rms voltage at $f = 1000$ Hz applied across the entire cell. The uncertainty in $d(I_{ac}/4I_{dc})/dV_{rms}$ can be large, especially for large d.

chiral agent, as is the case presented herein, $\Delta\theta$ would be smaller, zero, or even change sign, the latter resulting in a sign change of the electroclinic effect. From Ref. [68] one can show that the form of the electroclinic coefficient due to deracemization at the surface for a chirally-doped cell of thickness $d \sin d_0$ becomes:

$$e_c \propto (\theta_0 - 2\pi d/P)/(2K_{22} + Wd), \tag{2.1}$$

where K_{22} is the twist elastic constant, P is the pitch of the doped liquid crystal, and W is the azimuthal anchoring strength coefficient. Thus, in the thin regions of the cell ($d < d_0$), the chiral dopant was insufficient to completely compensate the imposed rotation angle θ_0 between the easy axes, as shown schematically in Fig. 2.3a. Here there remains a moderately sharp twist very close to the two surfaces, having the same handedness as the bulk twist. This surface twist is smaller than that of an undoped cell, and thus the observed electroclinic effect is smaller than that in Ref. [68]. Then from Eq. 2.1, the dopant-induced bulk pitch P is seen to exactly match the imposed pitch at one particular thickness $d_0 = \theta_0 P/2\pi$, no sharp twist occurs at the surfaces; see Fig. 2.3b. To be sure, the bulk remains twisted and, in principle, causes an electroclinic effect, but e_c is too small to measure because of this long bulk pitch. In thicker regions of the cell ($d > d_0$) the bulk LC pitch P remains unchanged, but the director overshoots the easy axes, as shown in Fig. 2.3c. As a result $\Delta\theta$ changes sign, with a tight twist at the surface having a handedness opposite that of the bulk. Thus the electroclinic effect also changes sign and increases in magnitude with increasing d (Eq. 2.1). Overall, two important results arise from Figs. 2.6 and 2.5. First, the observed electroclinic effect must be a surface phenomenon. As noted in Ref. [68] and seen in Fig. 2.5, the rapid decrease of e_c with increasing frequency suggests that the electric field drives the electroclinic behavior at the surface, and the surface director rotation propagates slowly into the bulk, *via* elastic effects. That e_c changes sign in the doped sample as the thickness passes d_0 conclusively demonstrates

that the observed electrooptic effect is due to a tight twist localized near the surface for $d \neq d_0$. But perhaps more importantly, these results show that a significant chiral electrooptic signature should exist in *every* nematic twist cell that is not completely pitch compensated. Although the bulk LC exhibits chiral symmetry in all twist cells, the bulk twist generally is insufficient to produce an observable effect; the sharp twist at the surface, however, is easily observable.

2.3.2 Helical Twisting Power

The observed electrooptic response can be exploited as a method to extract the helical twisting power (HTP) of a chiral dopant in a liquid crystal, especially negative dielectric anisotropy liquid crystals. Here the HTP due to the chiral dopant is defined as (P_c^{-1}) The average thickness d_0 for which $e_c = 0$ corresponds to an average pitch $\langle P \rangle = 2\pi d_0/\theta_0 = (86 \pm 2)$ μm for the sample, from which $HTP = (8.1 \pm 0.4)$ μm^{-1} is obtained. This is compared to an alternative approach for measuring the helical pitch that was demonstrated by Raynes [26]. A 90° planar twist cell using 10 μm spacer beads was prepared and filled with a $c = (0.00031 \pm 0.00002)$ CB15 mixture in 9OO4. Both left and right-handed twist domains appeared in the cell, with domain wall terminating at the spacer beads (Fig. 2.7).

Because the right-handed domains are favored due to the CB15 additive, the domain walls have curvature radius R. The curvature of these domain walls – also known as disclination lines – comes from the chiral dopant favoring one sense of twist with the inability to form single twist domains by the domain walls being pinned by the spacer beads. The domain walls increase in length – forming the curvature – until a stable state is reached. In the absence of a chiral dopant, these domain walls would be straight, indicating an infinite pitch [26]. Raynes showed that the pitch $P = 2R$ within the context of a single elastic constant and the neglect of pretilt [26]. Using polarized photomicrograph (Figs. 2.7) a radius of $R = (174 \pm 8)$ μm was

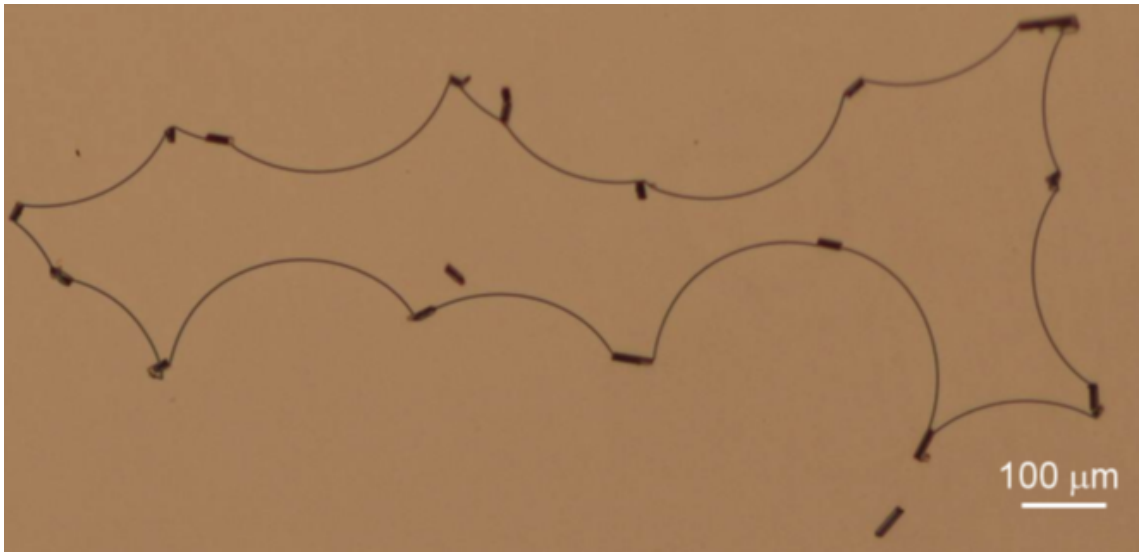

Figure 2.7: Polarized micrograph of disclination lines running between the 10 μm spacers in a 90° nematic twist cell of 9OO4 doped with $c = 0.00031$ weight-fraction CB15.

obtained, corresponding to a pitch $P = 348 \pm 16)$ μm and an $HTP = (9.3 \pm 1.1)$ μm^{-1}. This is in reasonable agreement with the value of HTP obtained above, but without the approximations needed by Ranynes's approach. As an aside, it should be noted that the measurement of the HTP *via* the surface electroclinic effect requires only a measurement of the gap d between the alignment layers, without having to account for the voltage drop across these layer. The magnitudes of e_c would be slightly in error, but their zero crossing would still occur at d_0, if one were not to use a correction for the voltage drop due to the alignment layers.

2.4 Summary

To conclude, here it has been shown that the electroclinic effect in a nematic twist cell *via* surface modification of chirality at or near the surface is due to the highly twisted environment very close to the surfaces for all twisted cells. By compensating for the imposed helical pitch in the cell by doping the liquid crystal with a chiral molecule, the electroclinic coefficient vanishes as when the cell gap equals the imposed twist.

Also, it has been shown that this can be used as an accurate method to determine the helical twisting power of a chiral dopant / liquid crystal mixture.

2.5 Future Work

While a great deal of work has now been done on this form of chiral induction, there are still a few outstanding questions. For all publications to date, the temperature has been held constant in the liquid crystal's nematic phase. In a normal nematic electroclinic effect, e_c increases with decreasing temperature approaching the nematic – Sm-A transition temperature [72]. This is due to an increase in smectic-like fluctuations in the nematic liquid crystal upon nearing the transition. This may not be the case for a twisted cell, since the electroclinic response for this system is proportional to the strength of the symmetry breaking [56].

In addition to maintaining a constant temperature, each publication involving twist cells to date has reported experiments exclusively on the nematic phase. While the director in the bulk nematic phase follows the induced pitch in a cell, this is not the case in the Sm-A phase. The presence of smectic order expels bend and twist [12]; therefore smectic layers in a twist cell would likely break up into localized domains of partially rotated layers, similar to that seen in the twist grain boundary phase [73]. These layers would likely vary along the twist axis throughout the sample from alignment layer to alignment layer. With the use of a confocal microscope it would be possible to see just how, and where, these domains occur.

Chapitre 3

Chiral periodic mesoporous organosilica in a smectic-*A* liquid crystal: source of the electrooptic response[1]

3.1 Introduction

Infiltration of liquid crystals into porous materials has provided insight into phase transitions in confined geometries [74]. Recently, such systems have presented a variety of potential applications, including electrooptics (such as controllable photonic band-gap materials) [75] and energy harvesting [76, 77]. The developments during the past decade of periodic mesoporous organosilicas (PMOs, Figure 3.1) has caused a stir in the scientific community [78, 79, 80, 81, 82, 83, 84, 85].

3.1.1 PMO

PMO microparticles are prepared by the surfactant-templated condensation of bridged organosilosesquioxane monomers [84, 85]. Surfactants with a long hydrophobic tail

[1]This chapter is based on one of my articles in: Liquid Crystals.
I. R. Nemitz, K. McEleney, C. M. Crudden, R. P. Lemieux, R. G. Petschek, and C. Rosenblatt "Chiral Periodic Mesoporous Organosilica in a Smectic-*A* Liquid Crystal: Source of the Electrooptic Response," *Liquid Crystals* 43, no. 4 (January 8, 2016):497-504.

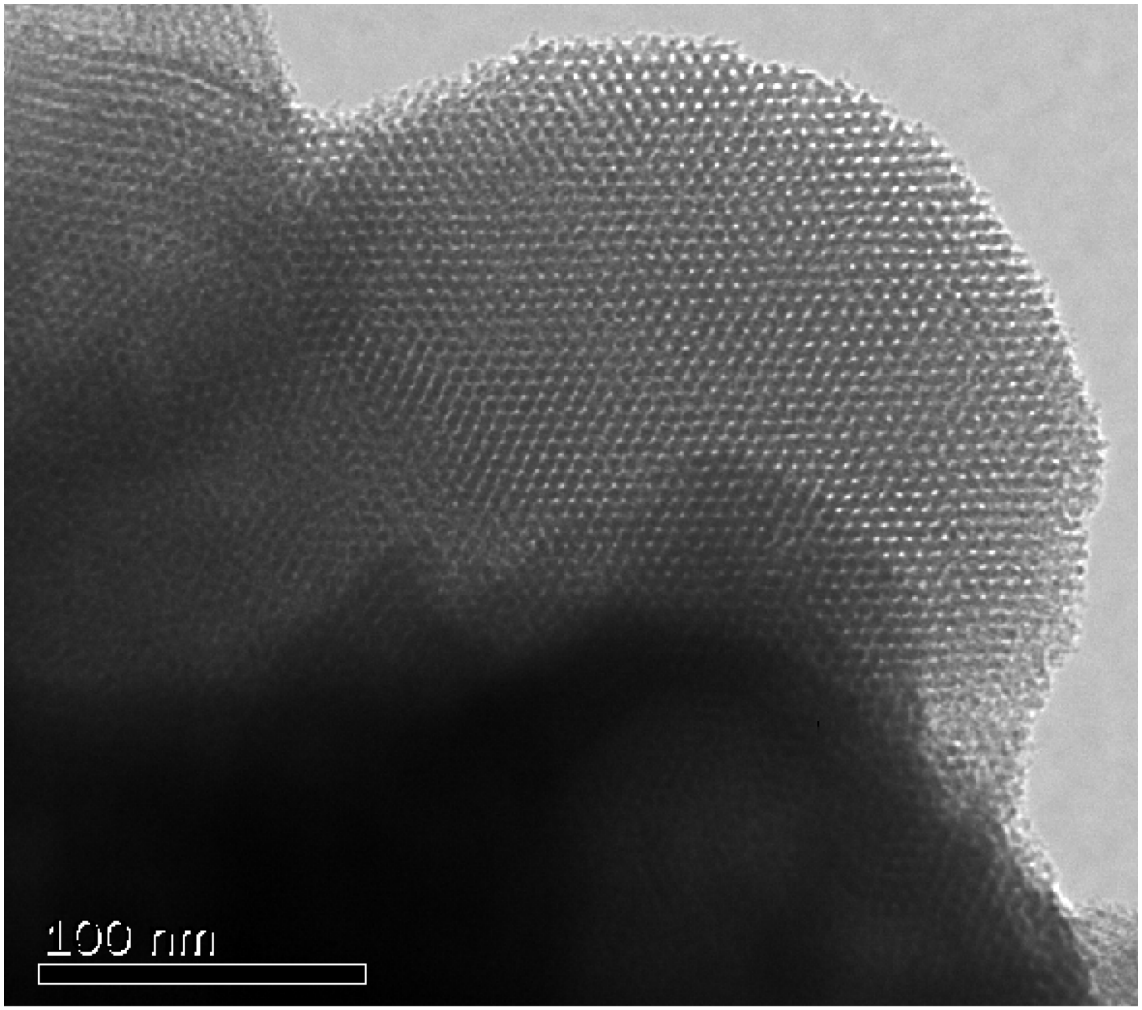

Figure 3.1: TEM image of PMO, showing the 2D hexagonally ordered porous mesostructure.

and hydrophilic head self assemble into groups of rod shaped nanostructures: a lyotropic columnar phase. These rods pack into hexagonal lattices that form a template for the final porous structures. When bridged organosilosesquioxane monomers are added to the system, they fill the interstices between these rods, and are subsequently polymerized. Once the initial surfactant is extracted – *via* a solvent – the final PMO structure is left. PMOs thus are unique among other silica-based porous materials since the inclusion of other organic units directly within the walls of the material provides the opportunity to exert significant control over the structure and properties of the resulting composition material. In addition, by judicious choice of surfactant and condensation conditions, the PMO can be tailored to have an extensive range of chemical and physical properties, including nanometer sized pores and controlled spacing of the highly ordered porous channels [85].

3.1.2 Chiral PMO

The use of bridging *chiral* monomers provides the unique opportunity to impart chirality into the backbone of the material, including within the PMO pores. This facilitates possible applications in chiral chromatography and non-linear optics [85]. While it is possible to make PMO with only chiral precursors, the fact that these precursors are bridged by large flexible organic groups means they usually generate low quality materials on their own [86, 85]. There are three strategies used to ameliorate these structures: (i) by grafting monofunctional chiral precursors to the silica particles after condensation has occurred, (ii) by incorporating or "co-condensing" monofunctional chiral precursors with more structurally sound achiral precursor, and (iii) by co-condensing bifunctional chiral precursors with more structural precursors. For the purposes of the research presented here, method (iii) was used. By varying the amounts of the condensible silane precursors (achiral and chiral) it is possible to fine-tune the physical properties of the resulting organosilica material, with the structural

material having little effect on the chirality and improving the quality of the materials [85]. Using this method facilitates possible applications in chiral chromatography and non-linear optics [85].

To date, only a few reports have appeared that characterize the chirality of pore structures in these materials. Characterization of chirality has been achieved by methods including polarimetry [87, 88], solid-state circular dichroism [89], interactions with chiral gases [90], and interactions of chiral PMOs with liquid crystalline solvents [84]. In particular, suspension of micrometer-sized chiral PMO particles in a configurationally achiral liquid crystal matrix, and the resulting infiltration of the liquid crystal into the PMO pores, has been shown to induce measurable chiral properties in the nematic and smectic-*A* (Sm-*A*) phases of liquid crystals [84]. For example a 90° nematic twist cell filled with the configurationally achiral liquid crystal 4-cyano-4'-pentylbiphenyl (5CB), doped with chiral PMO particles displays bowed disclination lines in the bulk liquid crystal [84]. This behavior indicates that the liquid crystal has been partially deracemized conformationally, so that domains having the same imposed handedness of twist as the deracemized liquid crystal are favored at the expense of the opposite sense of twist [26]. Importantly, this result also shows that the chiral pores induce chirality in the liquid crystal *outside* the PMO. In the same paper [84] it was shown that a cell containing a mixture of the conformationally racemic liquid crystal **9OO4** (**1**, Figure 3.2) in its Sm-*A* phase and chiral PMO microparticles exhibits an electroclinic effect (ECE).

The appearance of these chiral signatures in the nematic cell clearly demonstrates that chiral PMO induces chirality – directly or indirectly – in the interparticle region of the liquid crystal, outside the PMO pores. Importantly Jayalakshmi *et al*, showed that the chiral electroclinic signature vanishes if the PMO pores are plugged with an achiral surfactant that prevents pore infiltration by the liquid crystal [84]. From this result it was concluded that the chirality transfer to the bulk achiral liquid crystal

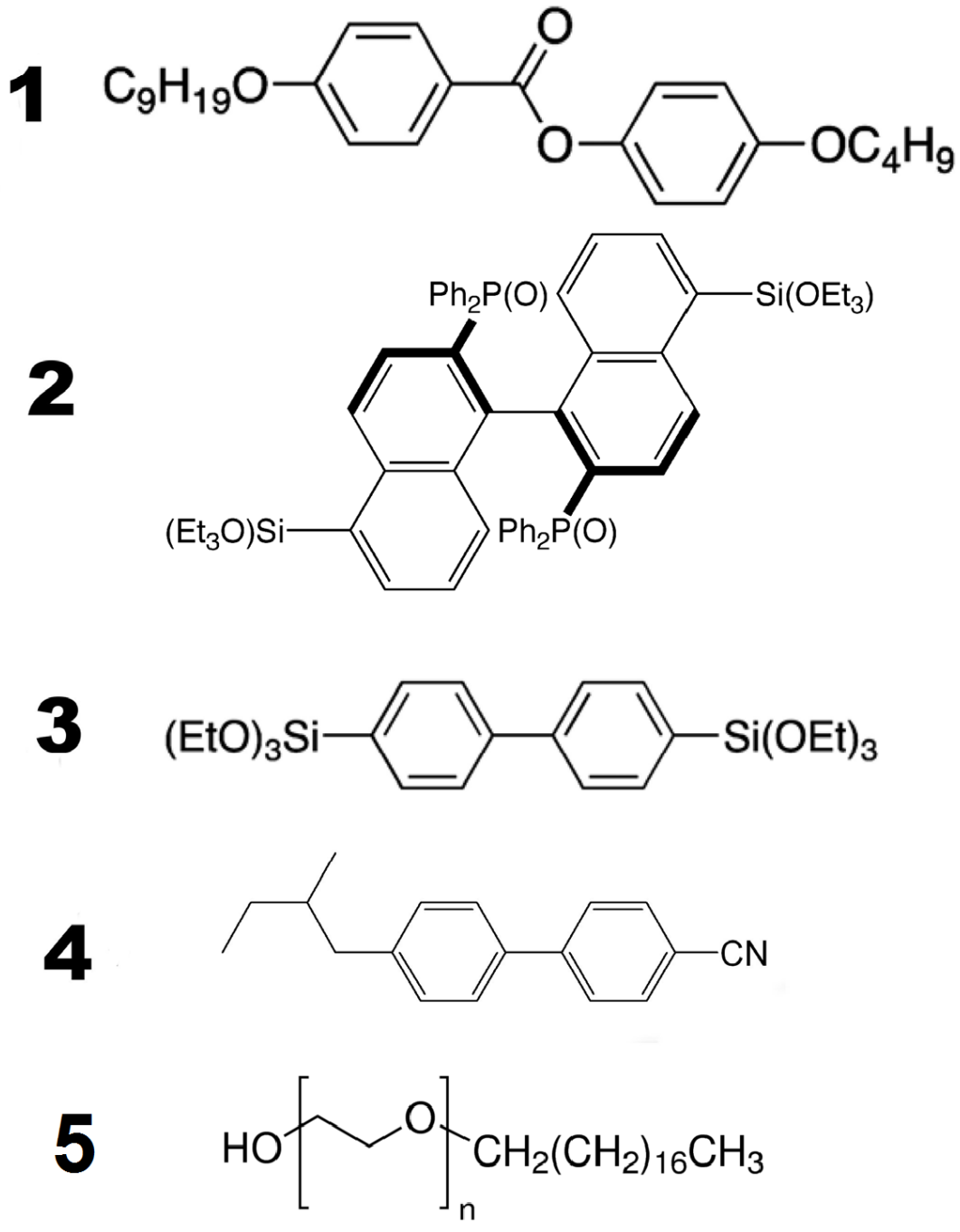

Figure 3.2: Chemical structures of (1) liquid crystal 9OO4, (2) (S) chiral binaphthyl monomer, (3) 4,4-bis-(triethoxysilyl)biphenyl, (4) chiral dopant CB15, and (5) the surfactant Brij 76 (n = 10)(Polyoxyethylene (10) Stearyl Ether).

originates predominantly from within the pores. These results suggest that the chiral pores deracemize the liquid crystal in the pores, and that chirality is transferred to the bulk of the liquid crystal though interactions at the mouth of the pores. However, in previous work, the contribution of the liquid crystal within the pores to the overall electooptical signature was not separated from that attributed to the bulk phase. Thus, in this chapter I present electroclinic measurements in the Sm-A phase of **9OO4** doped with the chiral PMO particles as a function of angular frequency ω of the applied electric field and of temperature T above the Sm-A – Sm-C phase transition temperature T_{AC}, which allows me to separate the effect of the encapsulated liquid crystal from that of the bulk exterior liquid crystal.

3.2 Experimental

3.2.1 Chiral PMO Fabrication

The fabrication of the PMO used in this experiment was done in the laboratory of Professor C. Crudden at Queens University in Ontario, Canada. The optically pure (S) chiral binaphthyl monomer **2** (Fig. 3.2) – the PMO used herein is similar, but not identical to, the binaphthyl-based monomer used in [84] – and the bulk monomer 4,4'-bis-(triethoxysilyl)biphenyl (monomer **3**, Fig. 3.2) were prepared in a 15 : 85 (weight/weight) ratio to prepare the chiral PMO material. Both materials are bi-functional monomers, therefore the chiral binaphthyl will become part of the pores' walls rather than being grafted to the interior of the pores. The nonionic, alkly-polyther surfactant Brij 76 **5** was allowed to self assemble into a periodic hexagonal packed series of rods, making the template for the porous final structure [91, 85]. The 15 : 85 (w/w) ratio mixtures of bridged monomers was added to the self assembled Brij 76, and allowed to co-condense. The templating surfactant was removed after co-condensation by Soxhlet in acidic ethanol, leaving mesoporous particles of (S)-**15**-

QPMO1-ex having a range of aspect rations, but a characteristic size $d \sim 1\mu$m. The particles contain well-ordered pores of diameter $\sim$ 2.5 nm in a hexagonal lattice with spacing $\sim$ 6 nm. Details of the synthesis – beyond the scope of the work presented here – are described elsewhere [92, 84].

3.2.2 Cell Fabrication

The liquid crystal **9OO4**, whose phase sequence for this batch was measured to be Crystal – 34℃ – Smectic B – 44℃ – Smectic C – 57.5℃ – Smectic A – 70℃ – Nematic – 85.5℃ – Isotropic, was mixed with the PMO particles in toluene. A small amount of PMO was measured out ($\sim$ 1 mg), and placed into its own vial. In order to obtain an extremely accurate value for the amount of LC needed, 50 mg of 9OO4 was first dissolved into 5 ml of toluene. An amount of this toluene / 9OO4 mixture was added to the vial containing the PMO, such that the solution would contain a final concentration of 1.0 wt.-% PMO in liquid crystal. The vial containing the PMO, LC, and toluene was stirred using a vortex mixer for 5 minutes, and then sonicated for $\sim$1 hour. Once the PMO and LC were sufficiently dispersed in the toluene, the vial was rapidly moved to an enclosed oven that was maintained at 100℃, just below the boiling point of toluene. This temperature was chosen to evaporate the solvent, but avoid the actual boiling process, which may disperse the LC into the air and change the ratio of LC to PMO. The enclosed oven was used instead of a hot plate, so that there would be an even distribution of heat over the entire vial containing the mixture, preventing any condensation of the solvent near which would retard the evaporation process. The mixture was held at this temperature until the entirety of the solvent was removed, $\sim$10 minutes. The resulting LC / PMO mixture was used to fill a closed cell immediately after removal from the oven, while the 9OO4 was still in its isotropic phase. This method rendered a very uniformly distribution of PMO in LC.

The closed cells were constructed using a pair of semi-transparent, electrically-conducting indium-tin-oxide (ITO) coated glass substrates. The ITO was spin-coated with the polyamic acid RN-1175 (Nissan Chemical Industries), baked according to the manufacturer's specifications, *i.e.*, 5 minutes at 80℃ then 1 hour at 250℃ to imidize. It was then rubbed unidirectionally with a cotton pile cloth (YA-20-R, Yoshikawa Chemical Co.) to create an easy axis for planar liquid crystal director alignment. The substrates were placed together with the rubbing directions oriented antiparallel, separated by Mylar spacers, and cemented with a high temperature epoxy that was stable up to 120℃ . Previous experiments using **9OO4** have shown that the high temperatures required to transition into the isotropic phase cause rapid deterioration of epoxy cements rated for 120℃ which is $\sim$ 30℃ higher than the nematic – isotropic transition. The finished cell was housed inside an Instec 402 hot stage controlled by an Instec mk1000 temperature controller with stability of a few millikelvin. The cell was filled in the bulk isotropic phase with the (*S*)-**15-QPMO1-ex** / **9OO4** mixture.

For comparison purposes, a second cell was constructed and filled with a 0.56 wt.-% mixture of the chiral molecular dopant **CB15** (**4**, Merck, Figure 3.2) in **9OO4**, which was dispersed in the liquid crystal in an identical manner as the PMO. This chiral dopant facilitated an ECE without the imposition of micron-sized PMO inclusions. The thickness d of each cell cavity was determined by optical interference before the cell was filled. Here d was found to be (10.0 $\pm$ 0.1) μm for the PMO-containing cell and (3.9 $\pm$ 0.2) μm for the **CB15** containing cell.

3.2.3 Data Acquisition

Similar measurements described here were performed separately on each of the two samples. Each cell was slowly cooled from the isotropic phase and the temperature was stabilized deep in the Sm-*A* phase. I used the classical electroclinic geometry [59] (described in Sec. 1.7.2) to measure an effective electroclinic coefficient $e_c = d\theta/dE$ vs.

frequency and temperature. Light from a He-Ne laser passed consecutively through a Glan – Thompson polarizer oriented at 22.5° with respect to the cell's rubbing direction, the cell, and then through a crossed polarizer (also a Glan – Thompson) before passing into a fast photodiode detector (refer to Fig. 1.9). The detector's output was fed into a high speed low attenuation preamplifier and then into a Stanford Research Systems model 830 lock-in amplifier that was referenced to the angular frequency ω of the electric field applied across the cell by a Stanford Research Systems DS345 waveform generator. (The waveform generator, detector, and preamplifier's responses were flat to well over 6.28 x 10^5 s^{-1}, *i.e.*, 100 kHz.) Measurements were made in the lock in amplifier's $R - \theta$ mode, *i.e.*, the amplitude and phase of the signal with respect to the reference input. In this geometry it can be shown [49] that the effective induced director rotation $\theta = I_{ac}/4I_{dc}$, where I_{ac} is the measured amplitude of that intensity at frequency ω and I_{dc} is the dc intensity. θ corresponds to the actual director rotation for a well-aligned Sm-A cell, such as the cell containing **CB15**: however, here θ corresponds to an effective director rotation averaged over the 1 mm diameter laser spot for a cell that contains PMO microparticles with not-well-defined-director boundary conditions at the PMO surface. This will be discussed in more detail later. All measurement devices were connected through GPIB connections and controlled using Matlab programs that can be found in Appendix B.

First I verified that the experimental setup was working properly by examining the **CB15 / 9OO4** sample at three temperatures in the Sm-A phase: $T = 59°\,60°$ and 62°C. An ac voltage at $\omega = 628$ s^{-1} (100 Hz) was applied to the cell and increased step-wise from zero to 10 V rms over 1200 s, with a dwell time of 15 s at each applied voltage setting. Because of the relatively weak signal-to-noise ratio, the lock-in amplifier's time constant was set at 3 s. I found that $\theta = I_{ac}/4I_{dc}$ is linear in voltage V, as shown in Figure 3.3; moreover, no hydrodynamic instabilities were observed at these voltages when the sample was viewed in an optical microscope.

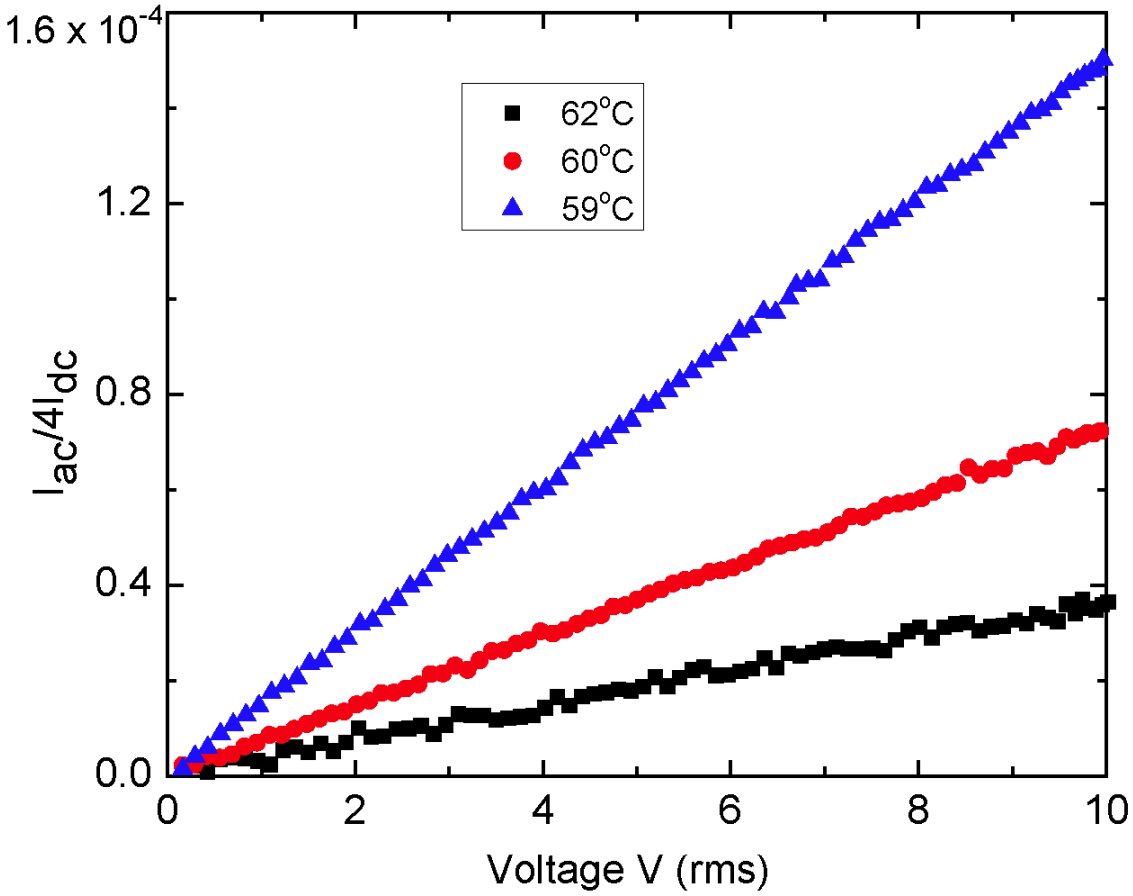

Figure 3.3: Electroclinic response $I_{ac}/4I_{dc}$ *vs.* applied voltage for the **CB15** / **9OO4** sample at three temperatures in the Sm-A phase.

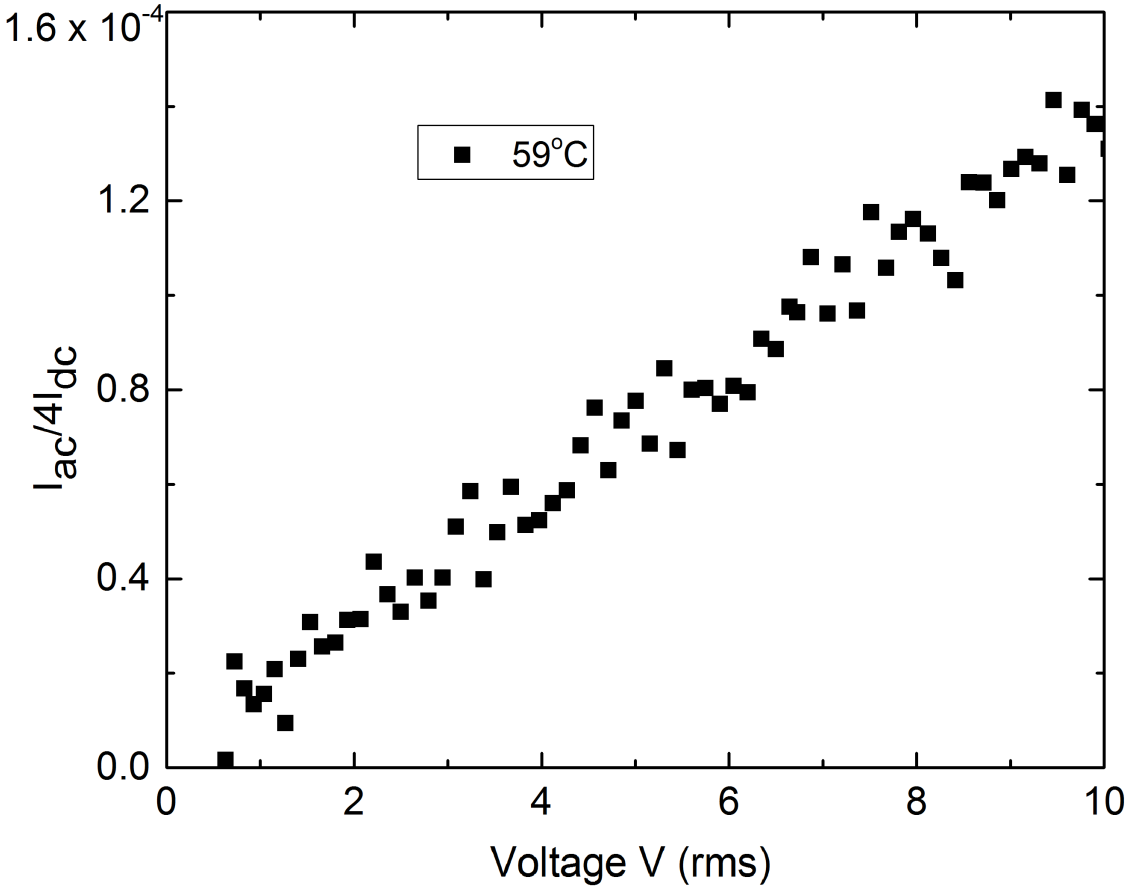

Figure 3.4: Electroclinic response $I_{ac}/4I_{dc}$ *vs.* applied voltage for the *S*)-**15-QPMO1-ex** sample at 59℃ in the Sm-*A* phase.

With the setup working properly, I repeated this examination at $T = 59$℃ with the (S)-**15-QPMO1-ex** sample. I was able to ensure a linear electroclinic response similar to that presented in previous work [84], as shown in Fig. 3.4. Once again there were no hydrodynamic instabilities, though the signal was approximately an order of magnitude smaller than the **CB15 / 9OO4** sample at comparable voltage and temperature. The magnitude difference is due to the different cell thicknesses used in each sample, as well as the differing chiral induction strength between the two materials.

Given the linear responses, I then fixed the applied voltage at 7 V rms and measured $\theta[= I_{ac}/4I_{dc}]$ for the **CB15 / 9OO4** sample as a function of frequency ω over the range $250 \leq \omega \leq 6.28x10^5$ s^{-1}. (Measurements at $\omega \leq 250$ s^{-1} were found to be noisy and less reliable, particularly for the $\Delta T[= T - T_{AC}] > 1$℃, and therefore will not be used in the analysis and discussion. While the electroclinic effect can ideally be observed at $\omega \sim 0$, in practice hydrodynamic instabilities render this difficult.) Data were collected in intervals of approximately 50 mK above the Sm-A – Sm-C transition. Figure 3.5 shows θ, *i.e.* $I_{ac}/4I_{dc}$, vs. ω with 7 V rms applied at several representative temperatures ΔT in the Sm-A phase close to T_{AC}. The transition temperature $T_{AC} = (57.52 \pm 0.02)$℃ was taken to be the temperature at which $d\theta/dE$ saturates at $\omega = 628$ s^{-1}. The experiment was then repeated using the (S)-**15-QPMO1-ex** (PMO) / **9OO4** mixture, and representative results are shown in Figure 3.6.

3.3 Results and Discussion

3.3.1 CB15 / 9OO4

First I will consider the **CB15 / 9OO4** data in Fig. 3.5, which correspond to a bulk, electroclinic effect in the Sm-A phase. In the equal elastic constant approximation,

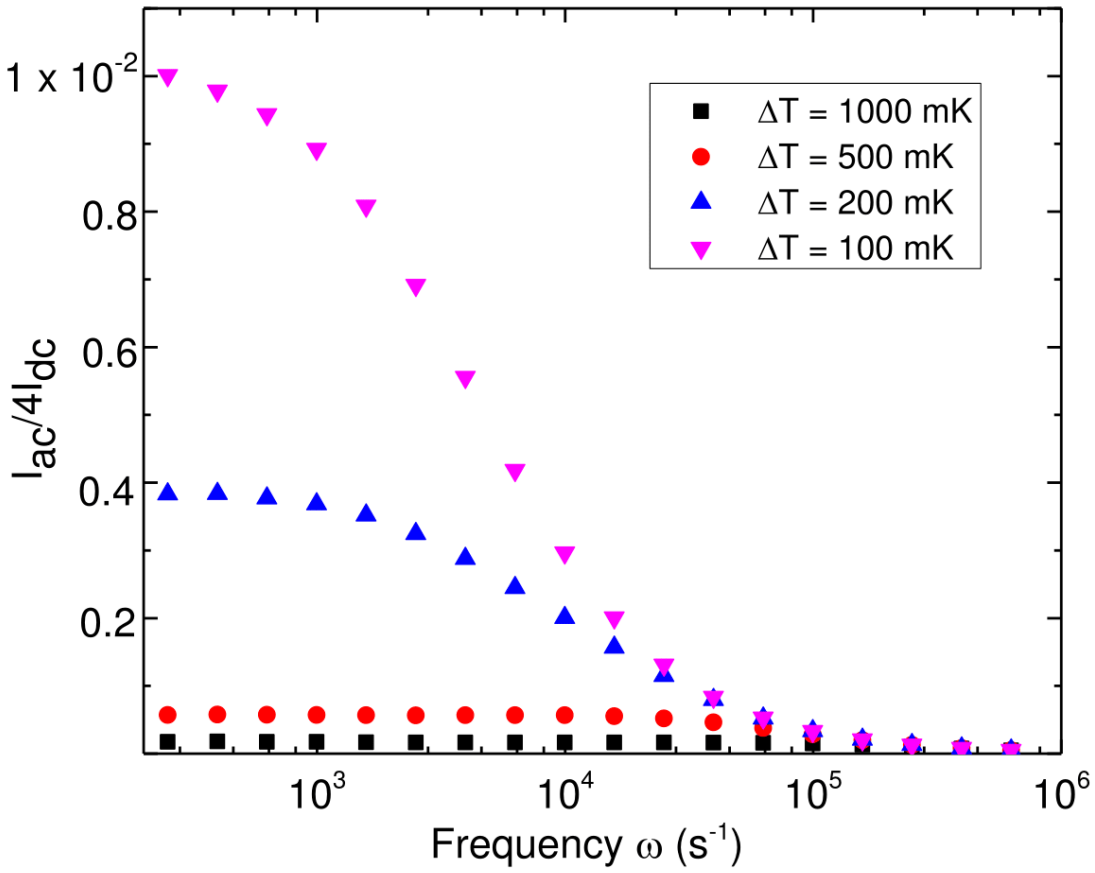

Figure 3.5: Electroclinic response $I_{ac}/4I_{dc}$ *vs.* angular frequency ω for the **CB15** / **9OO4** sample at four different values of ΔT. Here the applied voltage was fixed at 7 V.

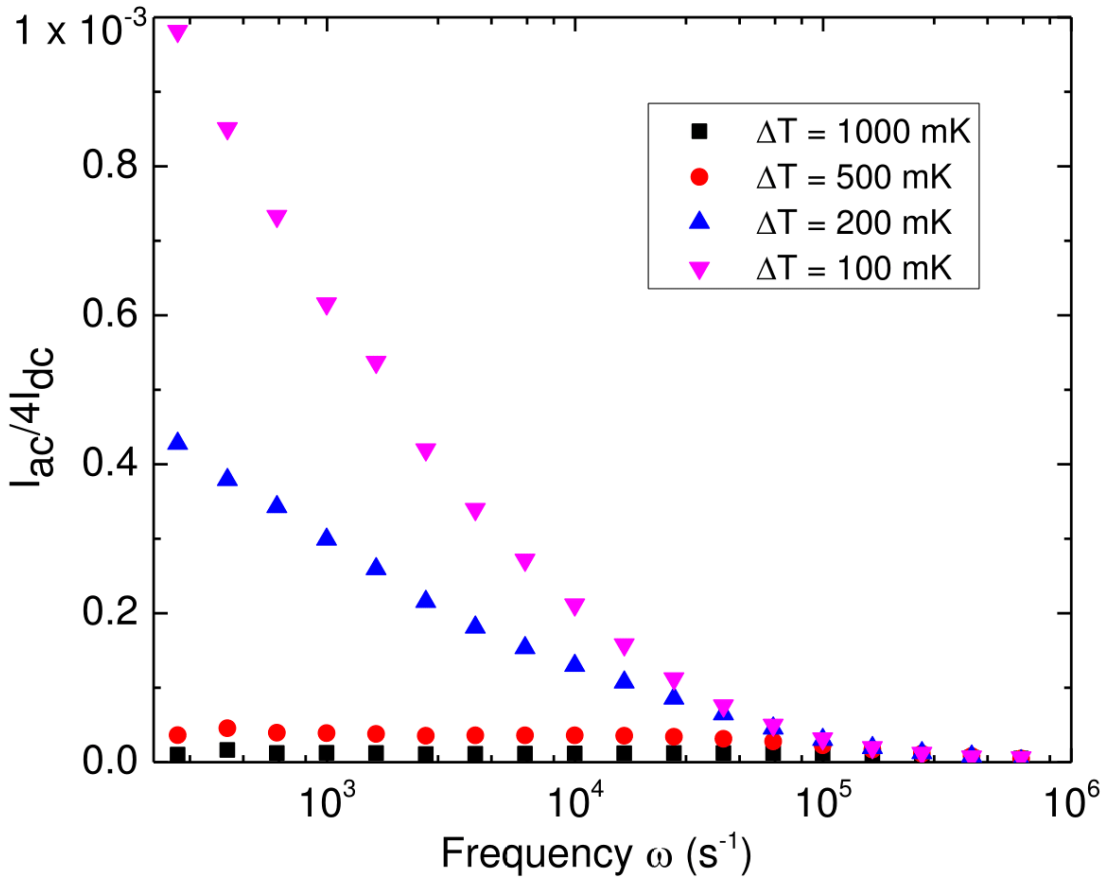

Figure 3.6: Electroclinic response $I_{ac}/4I_{dc}$ *vs.* angular frequency ω for the **PMO** / **9OO4** sample at four different values of ΔT. Here the applied voltage was fixed at 7 V.

the free energy density F in the Sm-A phase can be written

$$F = \frac{1}{2}K(\nabla\theta)^2 + \frac{1}{2}D\theta^2 - cE\theta \tag{3.1}$$

where D is the inverse tilt susceptibility of the director in the Sm-A phase and which vanishes as $T \longrightarrow T_{AC}$, c is the coupling constant between θ and E in the free energy, and K is an elastic constant in the Sm-A phase that tends to inhibit spatial variations in the director. On spatially Fourier transforming Eq. 3.1 and using the dynamical equation for θ_q, *viz.*, $\nu\partial\theta_q/\partial t = -\partial F/\partial\theta_q$, where ν is viscosity, θ_q is the spatial Fourier component of the rotation angle, and q is the wavevector, I obtain

$$\nu\frac{d\theta_q}{dt} + D\theta_q + Kq^2\theta_q = cE \tag{3.2}$$

Whence the magnitude of the Fourier component of the field-induced director rotation at frequency ω is

$$\theta_q = cE/[(D + Kq^2)^2 + \omega^2\nu^2]^{1/2} \tag{3.3}$$

For the **CB15/9OO4** cell the importance of the different terms can be estimated by using $\nu \sim 0.1$ kg m^{-1} s^{-1}, $K \sim 10^{11}$ N [12], and $q \sim 10^6$ m^{-1}, *i.e.*, π divided by the cell thickness. (This value for q assumes a director orientation that is fixed along the easy axes at the cell's walls. This is unlikely to occur, and q is likely to be smaller than 10^6 m^{-1}). Well above the T_{AC}, the *inverse* tilt susceptibility term D is large [93] and totally dominates the denominator up to frequencies $\omega \sim 10^5$ s^{-1}. Close to T_{AC} the D term becomes small and vanishes at T_{AC}. In this region the K^2q^4 term needs to be compared with the $\omega^2\nu^2$ term. Even at a low frequency $\omega \sim 300$ s^{-1} the elastic term is calculated to be $\ll$ the viscous damping term. From these comparisons, it can be seen that the q-dependent term in Eq. 3.3 can be neglected entirely for the **CB15/9OO4** cell. Thus, for this mixture the simple model predicts

that $\theta_q \approx cE/(D^2+\omega^2\nu^2)^{1/2}$ at all frequencies and temperatures studied in this work.

Using this Debye form, the data in Fig. 3.5 can be fitted using two fitting parameters, D/c and ν/c; the results from the two fits are shown in Figs. 3.7a and 3.7b. The fits are very good close to T_{AC} but as the temperature is increased, the experimental data become slightly stretched along the frequency axis relative to the Debye form. Using the ferroelectric mixture SCE12 (Merck), Li *et al.*, observed an anomalous relaxation time at higher temperatures in the Sm-A phase [94]. They proposed that the ECE can be described by *two* coupled dynamical equations, the dynamical equation above involving θ and another involving the induced polarization P, *viz.*, $\nu\partial P_q/\partial F = -\partial F/\partial P_q$. This produces an eigenvalue equation whose solution has a slow and a fast mode. The ECE experiment probes a combination of the two modes, such that $d\theta/dE$ is a linear combination of the slow and fast mode Debye-like responses. [I remark that dP/dE is a (different) linear combination of the same slow and fast processes.] Close to T_{AC}, the slow response dominates $d\theta/dE$ with only a negligible contribution from the fast process; thus the fit to a single Debye process is quite good in this temperature regime. At higher temperature, however, Li *et al* suggested [94] that the fast mode comes to play a more important role in $d\theta/dE$, thereby explaining the observed stretch of the measured ECE along the frequency axis. Thus, absent a much more detailed model, I will focus the measurements and discussion on the temperature region within $\Delta T = \sim 1$℃ of T_{AC}.[2]

3.3.2 PMO / 9OO4

Now consider Fig. 3.6, which shows the data from the PMO-containing sample, *i.e.*, the (*S*)-**15-QPMO1-ex** (PMO) / **9OO4** mixture. The data, which are much more stretched along the ω than the **CB15** / **9OO4** data at comparable values of

[2]I also note that a very weak and slow decay process at $\omega \sim 10^3$ s^{-1} was observed at temperatures $> T_{AC} + 2$℃. Closer to T_{AC} this was overwhelmed by the much larger (and growing) mode corresponding to $d\theta/dE$ This very weak process is beyond the scope of this chapter, and I concentrate on the dominant processes close to T_{AC}.

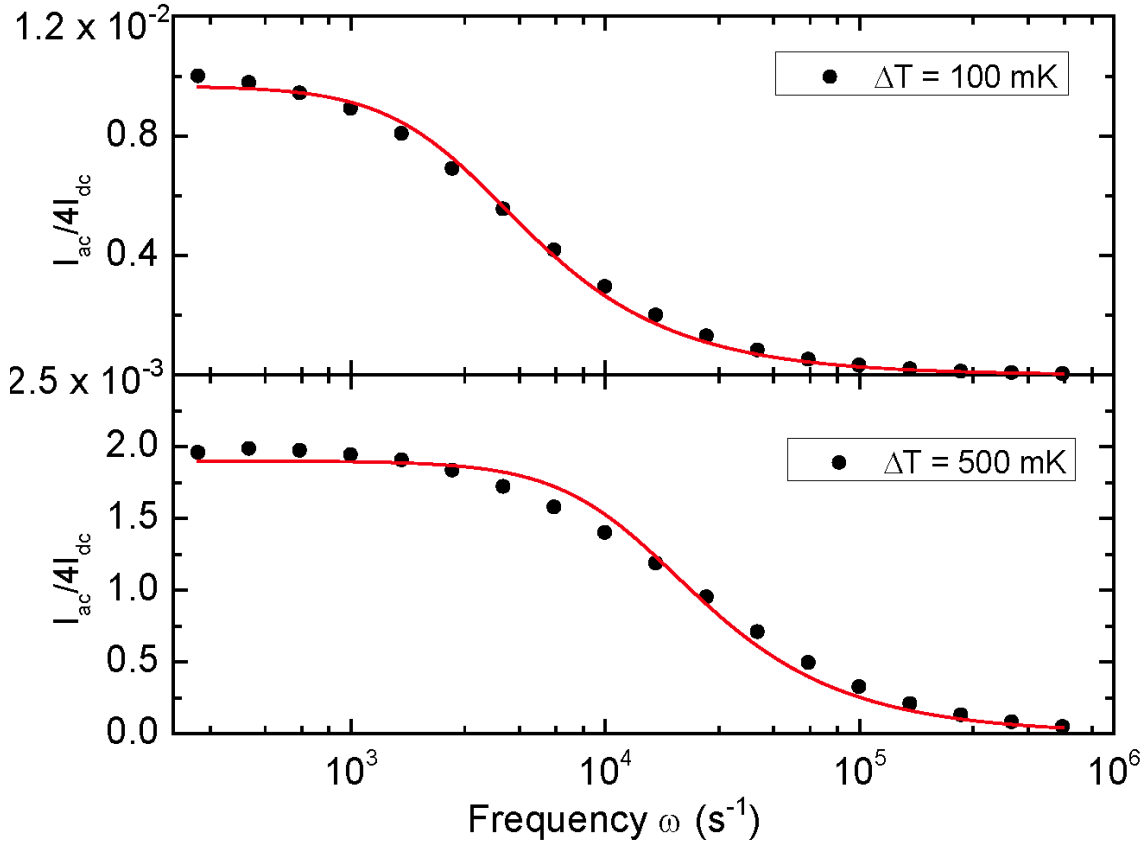

Figure 3.7: Electroclinic response $I_{ac}/4I_{dc}$ *vs.* angular frequency ω for the **CB15** / **9OO4** sample at two different values of ΔT with a two-parameter fit to Equation 3.3 and neglecting the Kq^2 term.

ΔT, clearly are inconsistent with the Debye form of 3.3, even at small ΔT. Several sources need to be examined for the observed chiral electroclinic signature. Previously I noted that a (*S*)-**15-QPMO1-ex** (PMO) / **9OO4** mixture in a 90° twist nematic cell exhibits bowed disclination lines, from which the effective chiral pitch can be extracted [84]. This result suggests that one source of the ECE may occur in the bulk liquid crystal, outside the PMO pores. Earlier measurements, in which the PMO pores are plugged with an achiral surfactant before mixing the PMO particles into the liquid crystal, showed no signs of induced liquid crystalline chirality [84]. This means that the chiral induction outside the silica particle is not being caused by the silica surface, but rather the induction emanates from the liquid crystal-filled chiral pores over some distance L – perhaps 5 or 10 nm [95] – into the bulk **9OO4**. The behavior can be modeled in real space by assuming that the liquid crystal outside the PMO becomes chiral in a thin region of thickness L where the pores exit from the silica. On application of an electric field, the liquid crystal director in this region undergoes a rotation and elastically induces a rotation of the bulk liquid crystal further away from the PMO. The free energy density $F_{achiral}$ in the *bulk* liquid crystal is

$$F_{achiral} = \frac{1}{2}K(\nabla\theta)^2 + \frac{1}{2}D\theta^2 \tag{3.4}$$

Note that here, there is no chiral coupling term containing the applied field in the bulk liquid crystal. Applying Euler's equation to $F_{achiral}$ and reintroducing a viscous term, I obtain

$$\nu\frac{\partial\theta}{\partial t} = K\nabla^2\theta - D\theta \tag{3.5}$$

On performing a time Fourier transform of Eq. 3.5 and assuming that $\theta \longrightarrow 0$ far from the chiral surface, I find the general solution $\theta = A\exp(-z\sqrt{\frac{i\omega\nu+D}{K}})$, where A is

a constant that is determined by the boundary condition when the director is normal to the silica surface is given by

$$-K(\frac{\partial\theta}{\partial z})_{surf} + DL\theta_{surf} = cLE \tag{3.6}$$

where θ_{surf} is the director rotation at the pore-exit boundary and L is the thickness of the chiral layer. For other director orientations the effective value of D would need to be adjusted accordingly. For an applied electric field at frequency ω, *viz.*, $E = E_0 e^{i\omega t}$, I obtain a solution for $\theta(z, \omega)$

$$\theta(z,t) = \frac{cLE_0}{DL + K\sqrt{\frac{i\omega\nu+D}{K}}} e^{-z\sqrt{\frac{i\omega\nu+D}{K}}} e^{i\omega t} \tag{3.7}$$

If the magnitude of $\theta(z, \omega)$ is examined at the PMO surface, *i.e.*, $\theta_{surf}(\omega)$ at $z = 0$, similar behavior, but not identical, to that of the Debye behavior used to model the **CB15/9OO4** mixture in Fig. 3.7 and Eq. 3.3 can be found.

There are two primary differences. First, the surface-driven process in Eq. 3.7 has a longer tail at high frequencies than does Eq. 3.3. This is to be expected because the surface-driven behavior involves not only modes near $q = 0$, but also the entire range of wavevectors, with the larger wavevector components having a faster response. Qualitatively, this behavior is observed in a high frequency tail for the (*S*)-**15-QPMO1-ex** (PMO) / **9OO4** mixture in Fig. 3.6. The optics for the **CB15/9OO4** mixture geometry probes the actual rotation angle θ in the bulk sample when q is small. For the PMO sample in which θ can vary with position in the liquid crystal, however, the experimental data in Fig. 3.6 do not correspond to the magnitude of θ_{surf} but rather to some sample-averaged rotation that is approximately proportional to the rotation near the PMO surface. But there is yet another complication for the PMO cell: the elastic constant K – generally this would be the twist modulus K_{22} – takes on different values depending on the direction of z relative to the

cell's easy axis direction and the PMO surface. This will have the effect of further broadening the frequency response. A full three-dimensional calculation is beyond the scope of this dissertation. Nevertheless, the main point is that the chiral-induced liquid crystal near the pores exiting from the PMO surface responds to the applied electric field and the rotation elastically propagates into the bulk, resulting in a more spread out frequency response than a bulk Debye process.

I will now examine the low frequency behavior of the PMO sample, Fig 3.6. That the electroclinic response of the (*S*)-**15-QPMO1-ex** (PMO) / **9OO4** mixture does not yet saturate at the lower frequencies suggests that there is a significant relaxation process that is even slower than the $q \sim 0$ electroclinic effect, which is approximated by the **CB15/9OO4** mixture. What might this be? One possibility is that there is a dissipative process that occurs in the induced chiral liquid crystal layer immediately at the surface of the PMO, but which is not reflected in Eqs. 3.5-3.7; this corresponds to the region of the liquid crystal that couples to the applied electric field in Eq. 3.6. In the next chapter (Chapter 4), I will examine the electroclinic effect in the thin ($\sim 10-20$ nm) "paranematic" region at a planar-orienting substrate in at temperatures above the bulk isotropic to chiral nematic phase transition temperature T_{NI}. The results indicate a relaxation time of ~ 1 ms at approximately $T = T_{NI}+500$ mK [30], suggesting a viscous interaction of the thin paranematic layer with the substrate on one side of the layer and/or the bulk isotropic liquid crystal on the other. Nevertheless this is still considerably faster than the observed slow relaxations reported herein, and I do not believe that this behavior is responsible for the observed slow process.

Turning to effects directly related to the PMO, it is important to realize that the PMO pores are not arranged radially from the particle's center, nor are they always oriented perpendicular to the surface of the PMO. Rather, the pores are templated by the lyotropic columnar phase that forms from the surfactant, resulting in long columns

over length scales of $< 1\mu$m. Thus, the particles are not only anisometric in shape, but also anisotropic both optically and electrically [96], with the anisotropies arising from the shape birefringence of the aligned pores, the alignment of the birefringent monomers that for the PMO, and the liquid crystal molecules within the pores. It is likely that the pores' optical shape birefringence is relatively small due to the reasonably close refractive index match between the liquid crystal and silica. For an order of magnitude estimate of the PMO rotational contribution, I make the simple assumption that the PMO particles are uniaxial; thus the free rotational diffusion time $\tau_{free} = 1/6D_{rot}$ is the rotational diffusion constant [97]. Even though there is a distribution of PMO particle shapes, in the spirit of this order of magnitude estimate I take $D_{rot} = k_B T/\pi\mu d^3$, where k_B is Boltzmann's constant and μ is the shear viscosity. Here $d \sim 1$ μm. The shear viscosity μ is unknown owing to the likelihood of disordered smectic layers in contact with, at least, parts of the PMO surface. (I note, in fact, that the breaking and reconstruction of the smectic layers as a result of the electric field itself and/or the rotation of the PMO also may contribute to the measured signal, with its own relaxation time.) Nevertheless, it can be assumed that $\mu \sim 0.1$ kg m^{-1} s^{-1} [11], I obtain a rotational random walk time $\tau_{free} \sim 10$ s. This suggests the presence of a slow process that may be observed optically due to the optical anisotropy of the PMO particles. Now, one considers an *electrically-driven rotation* with a relaxation time $\tau_{driven} = 2k_b T/\epsilon_0 \Delta\epsilon_{PMO} E^2 d^3 D_{rot}$, where ϵ_0 is the permittivity of free space and $\Delta\epsilon_{PMO}$ is the anisotropy of the relative dielectric constants of the PMO particles, this driven process could be considerably faster, of order hundreds or even tens of milliseconds. In principle, one may be able to separate this direct rotational relaxation (which has an E^2 behavior) from the electroclinic process (which is linear in E), but two factors work against this. First, the available voltage range is limited due to the onset of electro-hydrodynamic instabilities of the liquid crystal at higher voltages [92] and the much smaller signal-to-noise ratio

at the lower frequencies where rotational diffusion could come into play. Second, PMO rotation can result in smectic layer breaking, thereby coupling processes at ω and 2ω and confounding the analysis. Nevertheless, I believe that the observed low frequency behavior is not a true electroclinic effect associated with the chirality of the PMO, but rather involves a very low frequency artifact of the PMO's shape and pore arrangement. Earlier measurements [84] in which the chirality was removed by plugging the pores with a surfactant were performed at much higher frequencies and would not have been sensitive to this low frequency artifact.

I now consider the role played by the liquid crystal-filled chiral pores in the electroclinic signal. Owing to the small pore diameter, ~ 2.5 nm, the liquid crystal molecules in the pores would conformationally deracemize, and the chiral strength of the liquid crystal would be expected to be approximately uniform inside the pores [93]. In this case I return to Eq. 3.3, and note that the wavevector q would be of order 10^9 m^{-1} for the small pore diameter. Here the Kq^2 term can be comparable to D even far above T_{AC}, where D is large. But as before, close to the T_{AC} the Kq^2 term would be much larger than D, resulting in the relaxation process having a characteristic frequency Kq^2/ν which is of order 10^9 to 10^8 s^{-1} for $\nu \sim 0.01$ to 0.1 kg m^{-1} s^{-1}. Although these frequencies are well beyond the capabilities of the experimental equipment, the data in Fig. 3.6 show almost a complete decay of signal for $\omega \sim 10^6$ sec^{-1} close to the bulk Sm-A – Sm-C transition, which suggests that the liquid crystal-infiltrated pores' contribution to the observed electroclinic signal are small compared to the bulk liquid crystal contribution in this temperature range. That is, the electrooptic effect apparently is dominated by the behavior of the bulk liquid crystal *outside* the pore, such that the chiral pores induce a conformational deracemization of the liquid crystal inside the pores, which in turn causes a deracemization of the liquid crystal in the region at which the pores terminates at the PMO / bulk liquid crystal boundary. It is this region, when driven by an electric field, that couples elastically to the bulk

liquid crystal. I should remark that the pores' tiny diameter also suppress the Sm-A to Sm-C transition within the pores, and thus suppresses the pretransitional behavior associated with Eq. 3.3 [1].

3.4 Summary

In this chapter I presented results that reveal a complex electrooptic response when the PMO is mixed with a liquid crystal. Not only do I observe the apparent absence of a high frequency relaxation that would be characteristic of an electroclinic response within the PMO's pores, but I also observe a low frequency response that I believe is an artifact of the electric field coupling to the PMO colloids themselves. These suggest that the observed electroclinic response comes overwhelmingly from the chiral-induced region outside the chiral pores and the subsequent viscoelastic response of the bulk liquid crystal outside of the region, and is templated by the liquid crystal within the chiral pores of the PMO materials.

Chapitre 4

Electroclinic effect in a chiral paranematic liquid crystal layer above the bulk nematic to isotropic transition temperature[1]

4.1 Introduction

Expanding on previous theoretical work [98, 99], Miyano, and then Tarczon and Miyano, explored the surface-induced orientational order above the isotropic to nematic transition temperature, T_{IN} [100, 101, 102]. Using a Pockels cell they measured the optical phase retardation of the liquid crystals 5CB and MBBA (molecular structures in Fig. 1.1). Their experiments were done in the isotropic phase for several alignment layers, as the temperature was reduced toward the transition. The central result of their work was, even though the liquid crystals were in the isotropic phase, they still presented with a surprising degree of orientational order at the substrates. They observed that this order was apparent up to 7°C above T_{IN}, and was dependent on the surface order parameter S for the different alignment layers. Alignment layers

[1]This chapter is based on one of my articles in: Physical Review E.
I.R. Nemitz, E. Lacaze, and C. Rosenblatt "Electroclinic effect in a chiral paranematic liquid crystal layer above the bulk nematic to isotropic transition temperature," *Physical Review E* 93, no. 2 (January 2, 2016):022701.

with larger order parameters correspond to a larger birefringence at the substrates, which indicates a larger degree of liquid crystalline order. This order comes from the so-called "paranematic region", near the substrates in the isotropic phase.

It had been known for quite some time random fluctuations of order in the bulk are present in the isotropic phase, and that they increase upon nearing T_{IN} [103, 104, 105, 106, 107, 108, 109]. But since the original experiments by Miyano and Tarczon, there has been tremendous amount of work aimed at measuring and understanding the growth of this orientational order near a substrate [110, 111, 112, 113, 114, 115, 116, 117, 118, 119, 120, 121, 122, 123, 123, 124, 125, 126, 127, 128, 129, 130, 131, 132]. In nearly all cases it had been assumed that the potential is localized near, *i.e.*, within a few nanometers of, the liquid crystal / alignment layer interface [110, 112, 116, 117, 118]. If the interaction is weak, only partial wetting of the nematic phase occurs. On the other hand, for sufficiently strong interaction, the nematic phase completely wets the surface and the integrated orientational scalar order parameter S diverges logarithmically on cooling toward T_{IN} [100, 101, 102, 110, 119]. Here $S = \langle \frac{3}{2}\cos^2\phi - \frac{1}{2} \rangle$, where ϕ is the orientation of the liquid crystal molecule. Other effects, such as capillary condensation in which a localized boundary layer transitions to the nematic phase [111, 118, 120, 121, 125, 126, 127], and a prewetting transition in which the orientational order parameter increases discontinuously at a temperature just above T_{IN} [112, 130], have been predicted theoretically and observed experimentally. Recently, Lee, *et al* immersed a highly tapered optical fiber into a thin paranematic layer above T_{IN} and determined the surface-induced orientational order parameter $S(z)$ as a function of temperature and height z above the substrate [131]. Their analysis was model-free, *i.e.*, it did not require a specific functional form for the spatial decay of the order. They found that S initially decays weakly with z into the bulk $z < 10$ nm, after which it falls off rapidly with increasing z. Pikina and Rosenblatt explained the results theoretically in terms of the small isotropic – nematic

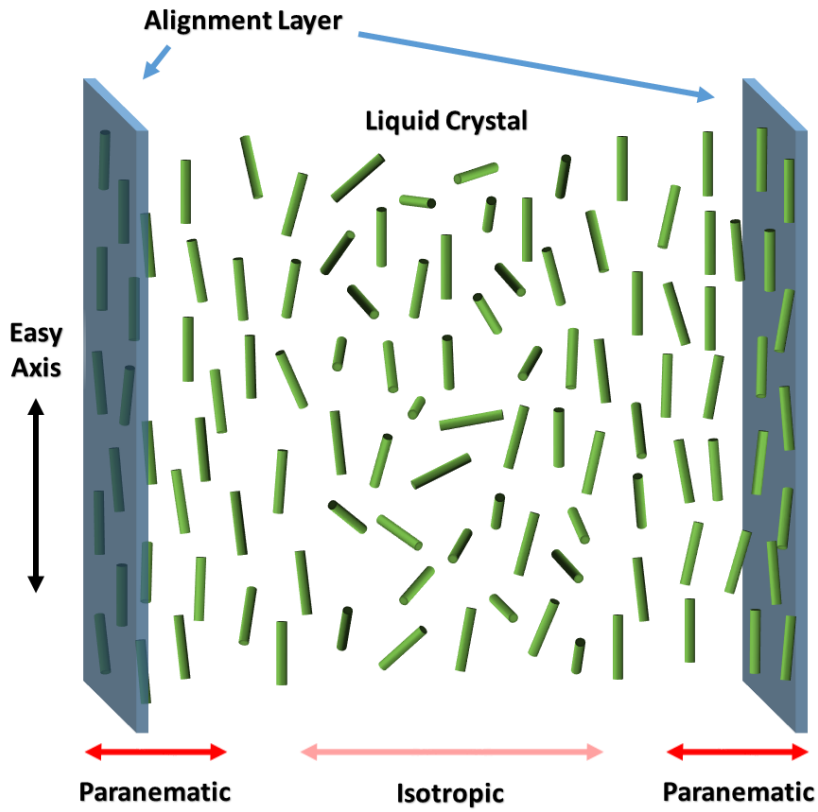

Figure 4.1: A pictorial representation of paranematic order in a typical liquid crystal cell treated for planar alignment above T_{IN}

(IN) interfacial tension and a resulting renormalization of the repulsive interactions from the fluctuations of the IN interface [131].

As noted in Sec. 1.7, the electroclinic effect (ECE) was first found to occur in the bulk chiral smectic-A (Sm-A^*) phase in which mirror symmetry is broken and a C_2 (two-fold rotation) axis lies parallel to the smectic layer plane [49]. When an electric field E is applied to a Sm-A^* liquid crystal, E couples to the chiral molecular polarization p, which results in a director rotation by angle $\theta[\propto E]$ about that axis. This effect also has been observed in the bulk chiral nematic phase (N*) [50, 51], where the required symmetry comes from smectic layer fluctuations that occur in the bulk [72]. These experiments seem to indicate that the ECE required smectic symmetry, but experiments involving the surface electroclinic effect indicated this is not the case. As long as there is chiral environment (from the liquid crystal [55], or the substrate [56, 57, 58]) and there is a reduction of symmetry from C_∞ to C_2 due to the existence of a planar aligning easy axis [56], a rotation θ proportional to an applied field can be observed [52, 53, 54, 55].

4.1.1 The Isotropic Electroclinic Effect

While the smectic and nematic ECE have been explored in detail, research into an isotropic ECE has been sparse. This makes sense. Though the bulk isotropic phase of a chiral liquid crystal presents with only small fluctuations in orientational order, the thin orientationally ordered layer in close proximity to the alignment layer observed by Miyano and Tarczon possesses the characteristic necessary for an ECE. [100, 101, 102]. The first reported research into the isotropic ECE was done over 20 years ago by Lee, Patel, and Goodby [133]. For their experiments they used the liquid crystal S-1-methylpentyl 4-n-decyloxybenzoyloxybiphenyl-4'-carboxylate, a material that presents with a direct Sm-A^* – isotropic phase transition, with no chiral nematic phase in between. Lee, *et al* examined this liquid crystal above the bulk Sm-A^* –

isotropic transition temperature in a cell with planar alignment surface treatments. As the sample was cooled toward the isotropic – Sm-A^* (IA) transition, they observed a weak ECE – with a director tilt proportional to the applied electric field E – in a thin region of surface-induced smectic order (of the order a few nanometers). That a surface region of smectic can exist even at bulk isotropic temperature is not surprising, and has been shown explicitly by several groups [126, 134, 135]. Owing to temperature fluctuations in their system, they were only able to approach to within 0.2℃ of the Sm-A^* – isotropic phase transition temperature (T_{IA}) from above. Nevertheless, they were able to observe an ECE response that increased by nearly 3 orders of magnitude over 1℃ between $T_{IA} + 1.2$℃ to $T_{IA} + 0.2$℃ as the system was cooled. This reported temperature dependence is by far much stronger than shown in previous work for materials near the chiral nematic – Sm-A^* transition [50, 51, 136]. Coupled with the observation that upon doubling the thickness of their samples from 5 to 10 μm they saw only a 5% difference in signal at each temperature, they noted that these facts indicate the appearance of incipient smectic layers at the substrate in an otherwise bulk isotropic phase [133]. Moreover, they explicitly *excluded* the possibility of only nematic order in this thin surface region close to T_{IA}, citing that for symmetry and temperature dependence reasons smectic order is the most likely origin.

The purpose of this chapter is to show that it is possible to observe an electroclinic effect *above* the bulk isotropic – chiral nematic phase transition temperature, T_{IN}. This isotropic ECE occurs without the presence of smectic fluctuations, in a thin layer of nematic-like oriented liquid crystal. The thickness of this region is known to be perhaps $h = 10 - 20$ nm near the alignment layer [131], where h depends on surface treatment, liquid crystal, and $T - T_{IN}$ [101, 102, 100]. Moreover, the profile of the order parameter S *vs.* z tends not to be a decaying exponential, but exhibits a shoulder [131], thus facilitating the simple approximation of a uniformly-oriented paranematic region of thickness h extending a short distance $h(T - T_{IN})$ from the

surface, beyond which the liquid crystal can be considered as isotropic. Included here are the results obtained for temperature- and frequency-dependent measurements of an ECE in this thin paranematic region of a chiral liquid crystal, above the bulk isotropic to chiral nematic phase transition temperature T_{IN}. The data show an ECE above the first order phase transition that is temperature dependent, and that increases with decreasing temperature. This effect does not vary as rapidly with temperature as observed shown by Lee, *et al*; the magnitude of the paranematic signal falls over 10℃ or more, rather than only 1℃ in the parasmectic signal [133]. Also, I show that the relaxation frequency of this chiral isotropic electroclinic effect is on the order of 100 Hz, and varies relatively little with changing temperature; this is by far slower than a bulk chiral nematic ECE, but faster than a surface nematic electroclinic effect [137].

4.2 Experimental Methods

4.2.1 Sample Preparation

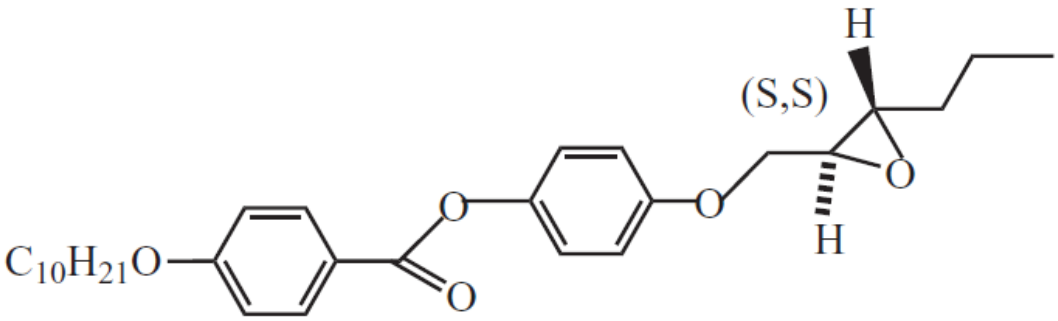

Figure 4.2: The structure of W46 (Displaytech, Inc), phase sequence Isotropic – 97℃ – Nem* – 81℃ – Sm-A* – 80℃ – Sm-C* – 75℃ – Crystal.

Capacitive cells were prepared using indium-tin-oxide (ITO) coated glass substrates that were spin coated with the planar alignment layer RN-1175 polyamic acid

(Nissan Chemical Industries). The coated substrates were baked and prepared in the same manner as in Chapters 2 and 3. The rubbed substrates were placed together in an antiparallel geometry, separated by Mylar spacers, and cemented to form cells of thickness of several micrometers. The empty-cell thicknesses d were measured by interferometry, as d is required to determine the electric field magnitude E from the applied voltage V. Conducting leads were attached to the ITO and the cells were filled in the isotropic phase *via* capillary action with negative dielectric anisotropy chiral LCs. One liquid crystal was the single component (s,s) enantiomer of W46 (Displaytech, Inc), for which the manufacturer specifies the phase sequence Isotropic – 97℃ – Nem* – 81℃ – Sm-A* – 80℃ – Sm-C* – 75℃ – Crystal and is shown in Fig. 4.2. Here the asterisks signify that the liquid crystalline phases are chiral. W46 shows virtually no biphasic region around the IN transition temperature T_{IN} and has a 16 to 17 K wide Nem* phase. The other material was the chiral mixture SCE12 (Merck, formerly BDH Ltd), which has a manufacturer-specified phase sequence Isotropic – 118℃ – Nem* – 81℃ –Sm-A* – 66℃ – Sm-C*. This material, although having a biphasic region, has an extremely wide Nem* range of some 37 K. Moreover, there is a large amount of literature for its bulk chiral ECE with which the results can be compared.

4.2.2 Experimental Setup

The cells were inserted into an oven that was temperature-stabilized to 2 mK, which was placed in a classic electroclinic optical setup shown in Sec. 1.7.2 [59]. Collimated light from diode laser ($\lambda = 532$ nm) was passed through a power stabilizer, a polarizer oriented at 22.5° with respect to the cell's rubbing easy axis, through the cell, and then through a crossed polarizer. Since this experiment was done in the isotropic phase, there was relatively little light passing through the crossed polarizers. Without a power stabilizer, minor changes and oscillations in the laser intensity – insignificant

for higher intensity experiments – had the ability to overwhelm the ECE signal. The light intensity was detected with a photodiode detector, for which I previously had measured a calibration curve $C(f)$ for the detector and lock-in amplifier combination. $C(f)$ was determined by exposing the detector and downstream electronics to light from a light emitting diode over the frequency range used in these experiments. For consistency, all intensities in this experiment were scaled by $C(f)$, which gave a signal variation of only a few percent at high frequencies ($>$ 30000 Hz). The cells' temperatures were raised by at least 30℃ above their respective T_{IN}, and the optics were adjusted to extinguish nearly the total intensity of the laser light passing through the crossed polarizers. A small remnant signal was due to the weak paranematic region near the substrates, as well as to the small strain birefringence in the optics. The consequence of this background will be discussed later. Due to the extreme thinness of the paranematic region relative to the pitch of the chiral nematic helix, the director orientation in the paranematic region can be treated as being nearly uniform.

4.2.3 Data Collection

The electroclinic coefficient $e_c = d\theta/dE$ was measured for the single-component W46 liquid crystal as a function of temperature at fixed frequency f = 1000 Hz, and also as a function of frequency at several temperatures above the bulk nematic – isotropic transition temperature $T_{IN} \sim 95.2 \pm 0.2$℃ which is slightly different than the manufacturer's specifications. I determined the transition temperature from texture measurements, as well as the extremely sharp increase of the optical signal (see below). For all measurements, an ac electric field was applied across the cells, and the detector output was fed into both a dc voltmeter and a lock-in amplifier that was referenced to the ac driving frequency f = 1000 Hz. For the first set of scans, the W46 cell was brought deep into the isotropic phase ($>$ 11 K above the IN transition) and an electric field was applied across the cell at f = 1000 Hz. The rms voltage V

was stepped upward from 0 to 5 V over 400 s with a 4 s dwell time between each measurement, the intensity scaled by $C(f)$ and both the scaled ac intensity I_{ac} and scaled dc intensity I_{dc} were recorded. Here I_{ac} is the intensity at the detector measured by the lock-in amplifier at driving frequency f and I_{dc} is the dc component of the intensity measured by a digital voltmeter. The temperature T was then reduced and another voltage scan was made, with temperature increments becoming smaller at T approached T_{IN}. All devices used to record data for these experiments were connected using GPIB connections. Through these connections, the devices were controlled remotely by program that can be found in Appendix B.

Figure 4.3 shows the quantity $I_{ac}/4I_{dc}$, which corresponds to the effective rotation angle θ in the surface paranematic regions [59], *vs.* applied field at several temperatures. I say "effective" in defining the rotation angle because the orientational order parameter S is not completely uniform through the paranematic region, and therefore θ may vary with position. Figure 4.4 shows the derivative with respect to electric field E of the data in Fig. 4.3, which is defined as an effective electroclinic coefficient $e_c = d\theta/dE = d(I_{ac}/4I_{dc})/dE$. (The inset shows $1/e_c$ *vs.* temperature.) Similar measurements also were performed on cells containing the chiral liquid crystal mixture SCE12, with the results shown in Fig. 4.5. Because of the phase separation at the isotropic to nematic transition in SCE12, I do not attempt to identify a transition temperature T_{IN}. Instead, I simply show the SCE12 results for e_c *vs.* temperature in Fig. 4.5. Additionally, Table 4.1 is a compilation of the e_c for all temperatures in both the SCE12 and W46 systems.

For the second scan, the temperature of the W46 liquid crystal was fixed at four different values ΔT $[= T - T_{IN}]$ relative to T_{IN}: ΔT = 0.7 K, 1.2 K, 1.7 K, and 2.2 K. A constant ac electric field E = 4.8 V m^{-1} was applied as the frequency was varied over 3000 s from 40 Hz to 40 kHz in logarithmic steps, with a 12 s dwell time at each

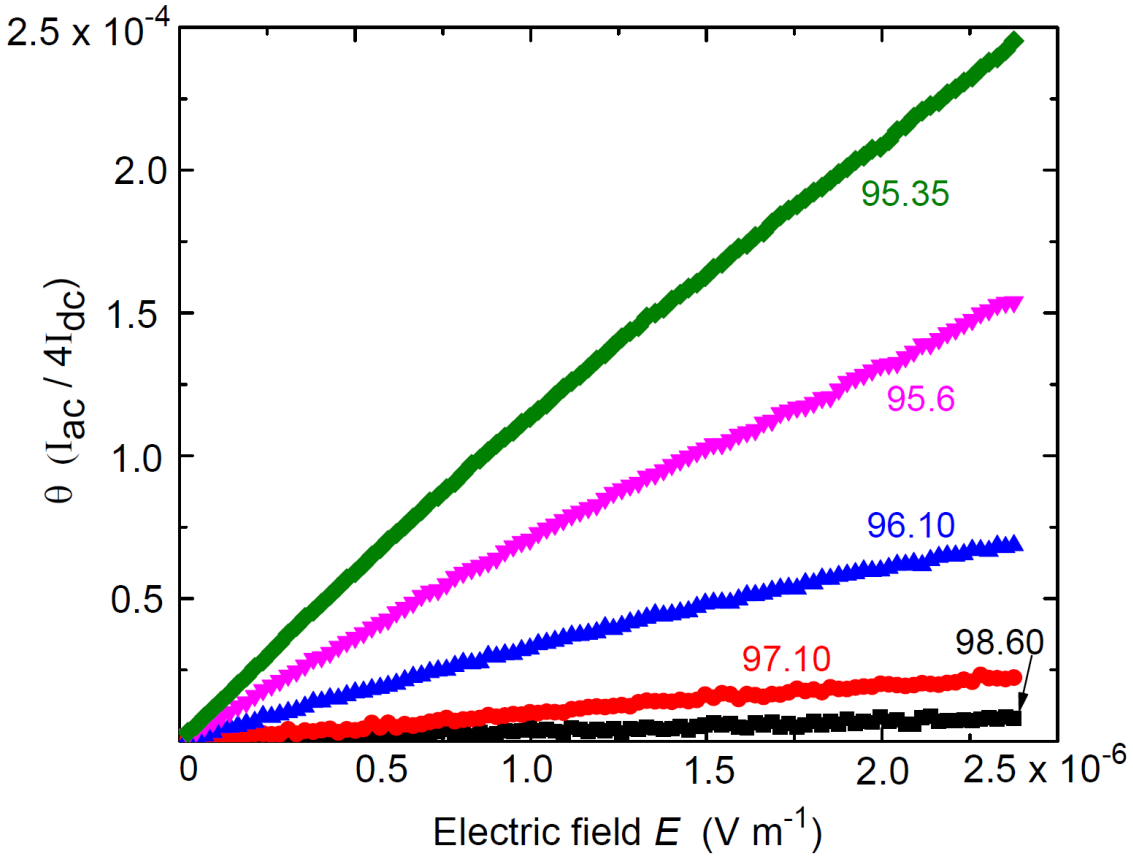

Figure 4.3: $I_{ac}/4I_{dc}$, which is defined as the effective rotation angle θ, *vs.* applied electric field E for the liquid crystal W46 (shown) at several temperatures above the bulk nematic isotropic transition temperature.

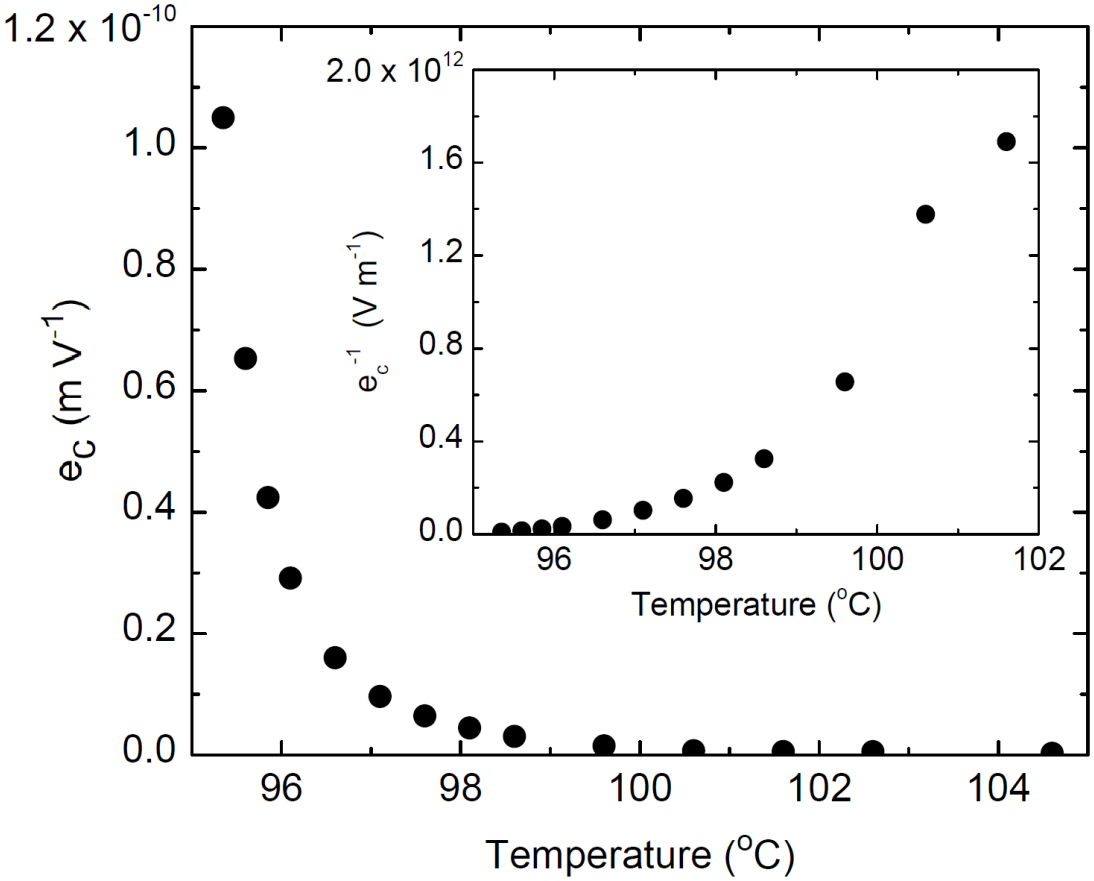

Figure 4.4: The effective electroclinic coefficient e_c *vs.* temperature for W46. The inset shows the inverse electroclinic coefficient e_c^{-1} vs. temperature.

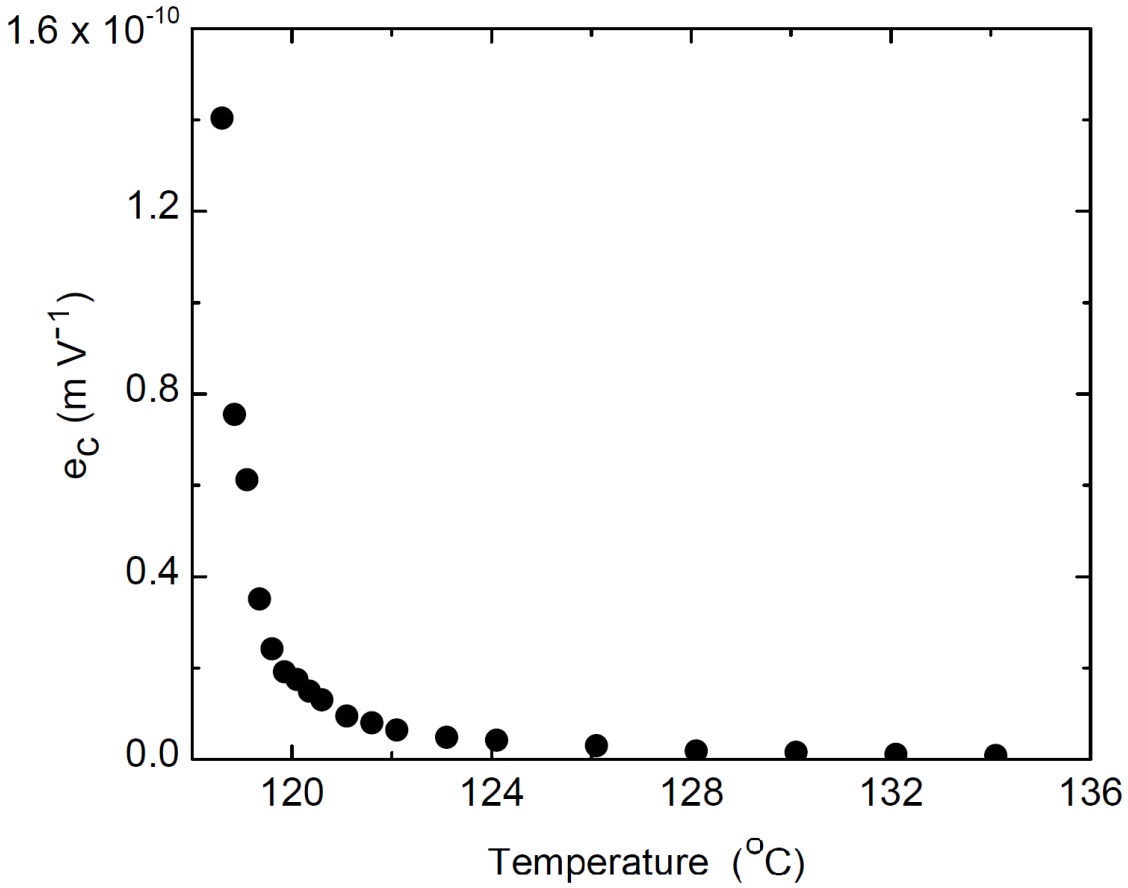

Figure 4.5: The effective electroclinic coefficient e_c *vs.* temperature for SCE12.

Table 4.1: The effective electroclinic coefficient e_c for each temperature for Figs. 4.4 and 4.5.

W46		SCE12	
Temperature (℃)	$e_c * 10^{-11}$ (mV^{-1})	Temperature (℃)	$e_c * 10^{-11}$ (mV^{-1})
104.6	0.029	134.10	0.088
102.6	0.058	132.10	0.112
101.6	0.059	130.10	0.158
100.6	0.073	128.10	0.185
99.06	0.152	126.10	0.302
98.60	0.307	124.10	0.422
98.10	0.447	123.10	0.485
97.60	0.646	122.10	0.644
97.10	0.965	121.60	0.803
96.60	1.603	121.10	0.951
96.10	2.914	120.60	1.309
95.85	4.241	120.35	1.496
95.60	6.531	120.10	1.752
95.35	10.50	119.85	1.920
		119.06	2.422
		119.35	3.512
		119.10	6.112
		118.85	7.553
		118.60	14.03

data point. Figure 4.6 shows e_c *vs.* f using a linear vertical scale in Fig. 4.6a and a logarithmic scale in Fig. 4.6b. As mentioned earlier, because of the extraordinarily small integrated birefringence in the ultra-thin paranematic region, I had to contend with a (possibly temperature-dependent) small offset values of I_{dc} from the inherent birefringence in the optics. The offset resulted in a systematic error in e_c (generally downward) of a few percent within a quarter degree of the transition temperature T_{IN}, of $\sim 20\%$ within a degree of T_{IN}, and considerably more several degrees above T_{IN}. At $T > T_{IN} + 4$ K the (unwanted) background in I_{dc} was comparable to the (desired) component from the integrated birefringence in the paranematic layer, indicating that e_c could be in error by a factor of 2. Nevertheless, despite this systematic error, the general trends observed in the data permits me to make string conclusions about the physics, especially close to T_{IN}.

4.3 Results and Discussion

First I will examine the $f = 1000$ Hz electroclinic data for the single component liquid crystal W46, as shown in Fig. 4.4 and Table 4.1. Here $T_{IN} = (95.2 \pm 0.2)$℃ and occurs approximately 16 K above the Nem* – Sm-A* phase transition temperature and 17 K above the Sm-A* – Sm- C* transition temperature. As noted above, the data at higher temperatures have larger relative uncertainties and systematic errors than those close to T_{IN} due to the very small values of both I_{ac} and I_{dc} far above T_{IN}. As is evident in Fig. 4.4, e_c increases smoothly with decreasing temperature, with the magnitude of e_c close to T_{IN} being similar to that of Ref. [133] close to the Sm-A* – isotropic transition. This increase of e_c with decreasing temperature the transition comes primarily from the increasing order parameter S on approaching T_{IN}. However, there may be other effects that also come into play. First, the thickness h of the paranematic region near the surface increases as the liquid crystal is cooled

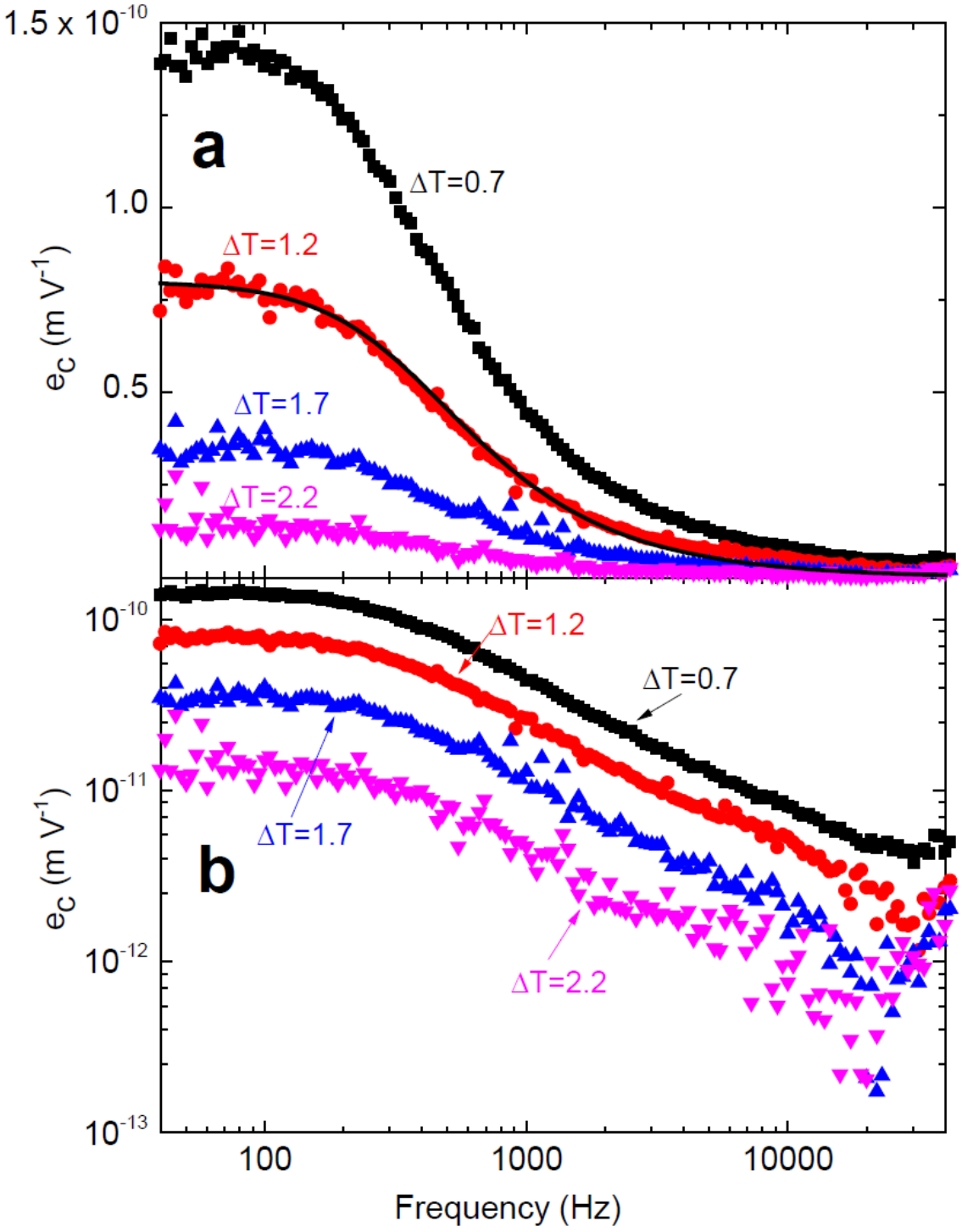

Figure 4.6: a) The electroclinic coefficient measured of W46 as a function of frequency f at four temperatures ΔT above T_{IN}. A fit to the Debye form is shown for $\Delta T = 1.2K$. b) Same as Fig. 4.6a but using a logarithmic scale for e_c.

toward T_{IN} [101, 102, 131]. This growth of h increases *both* I_{ac} and I_{dc} by the same total optical retardation factor. Because of this, $e_c = d(I_{ac}/4I_{dc})/dE$ should be little affected by the temperature-dependent width h of the paranematic region, except insofar as the order parameter S and coupling to the symmetry-breaking surface depend more strongly on z when h becomes larger close to the IN transition. Second, the frequency dependence of the ECE is quite strong, as is apparent in Figs. 4.6a and 4.6b. I chose to collect data in Fig. 4.4 at frequency $f = 1000$ Hz – this frequency is the same used by Lee, Patel, and Goodby [133] – because the signal-to-noise ratio is considerably better than it is at lower frequencies. But my choice of $f = 1000$ Hz, which is well above the quasi-dc region that extends out to several hundred Hz (Fig. 4.6), could possibly confound the interpretation of e_c *vs.* T in Fig. 4.4: *If* the measured e_c profile (Figs. 4.6a and 4.6b)) were temperature dependent in ways beyond a simple multiplicative factor, *e.g.*, if there were a critical slowing down near T_{IN}, then the shape of the measured e_c *vs.* T curve would depend on frequency. However the e_c *vs.* temperature measurements in Fig. 4.6 (and especially in the logarithmic plot Fig. 4.6b) indicate that all e_c *vs.* T curves are nearly identical, aside from a multiplicative factor associated with the rotation susceptibility *vs.* temperature. This suggests that there is little or no slowing down near the transition temperature, and thus the shape of the e_c *vs.* T curve in Fig. 4.4 is approximately independent of frequency, aside from a scaling factor that decreases with increasing f, as in in Figs. 4.6a and 4.6b. This in itself is an important difference between these results and those of the parasmectic effect in Ref. [133]: Whereas the parasmectic data shows a nearly three orders of magnitude increase in the ECE on decreasing the temperature from $T = T_{IA} + 1.2$ K to $T = T_{IA} + 0.2$ K, for these samples the corresponding increase above T_{IN} is only one order of magnitude (Fig. 4.4). Lee, *et al* ascribed [133] their very rapid variation of e_c with temperature in the parasmectic region to the strong temperature dependence of the smectic order parameter, even if an ultra-thin layer

of only nematic order resided immediately at the interface. To be sure, the liquid crystals used here and in Ref. [133] are not the same. Nevertheless, the very large difference in their respective temperature profiles is quite remarkable, and shows a very different sort of qualitative behavior between a paranematic and a parasmectic region.

Another observation can be made based on the data in Fig. 4.4. The inset in Fig. 4.4 shows the inverse response, *i.e.*, e_c^{-1}, *vs.* temperature. The IN transition generally exhibits mean-field-like behavior in quantities such as the Kerr [105, 106] or Cotton-Mouton [107] coefficient above T_{IN}, where the relevant response function at wavevector $q = 0$ varies as $(T - T_{NI})^{-1}$. There can be small variations from this very close to the transition, generally involving a small downward deviation of the inverse susceptibility. However, the inset in Fig. 4.4 clearly shows a deviation opposite from those found elsewhere [105, 106, 107]. Although the induced order parameter S at the surface has been shown to increase in a mean-field-like manner [131], the chiral coupling with the substrate and the anchoring strength coefficient both play a role in the surface ECE response [56]. Therefore, these results suggest that the evolution of the ECE with temperature goes beyond the evolution of S and also involves the evolution of the chiral coupling with the substrate and/or the anchoring strength coefficient. The temperature dependences of these quantities, which are beyond the scope of this dissertation, have not yet been determined.

I now consider Figs. 4.6a and 4.6b, the frequency response of W46 above T_{IN} The behavior is very close to that of a single relaxation process having a Debye-like response:

$$\theta = kE/[D(1 + \nu^2\omega^2/D^2)^{1/2}] \tag{4.1}$$

Here, k is the coupling constant between θ and E in the free energy, which can depend on the anchoring strength coefficient W_2^{ϕ} [56]; ν is a viscosity; $\omega = 2\pi f$; and

D is an inverse tilt susceptibility with respect to the easy axis and is proportional to W_2^{ϕ}. (Note that D would correspond to an inverse tilt susceptibility relative to the layer normal for a bulk liquid crystal above the Sm-A^* to Sm-C^* transition temperature.) Upon fitting the data in Fig. 4.6a at $\Delta T = 1.2$ K, as shown by the black line, a relaxation time of $\tau = (2\pi f)^{-1} = (4.5 \pm 0.4) * 10^{-4}$ s was found. The same relaxation time τ is obtained when fitting data at the other temperatures, and can been seen in the log-log plot shown in Fig. 4.6b, where the curves are identical except for a vertical translation. Because of this, I conclude that τ shows no significant temperature dependence over the vertical temperature range studied.

Single relaxation Debye behavior often is observed in a bulk ECE in the Sm-A^* and chiral nematic phases [49, 137]. The relaxation time τ_{bulk} for the bulk chiral nematic ECEs is fast, typically $\tau_{bulk} < 10^{-6}$ s. However, surface nematic electroclinic effects due to chirality localized at a surface tend to be *much* slower [138, 68]. In particular, the e_c *vs.* frequency data in Ref. [68] corresponds to a bulk *achiral* nematic liquid crystal that becomes deracemized immediately adjacent to the polymer alignment layer. An electric field drives a rotation of the director at the surface, which in turn is transmitted by elastic forces into the bulk. Thus the frequency response in that experiment is related to dissipation at the liquid crystal – polymer interface, but also (and importantly) to the viscosity for twist-like elastic distortions in the bulk liquid crystal. It is interesting that the e_c *vs.* f data shown in Figs. 4.6a and 4.6b are much slower than τ_{bulk}, but much faster than nematic ECEs driven by the surface [138, 68]. I believe that the relaxation process in Figs. 4.6a and 4.6b is due primarily to dissipation from the director rotation at the surface, but is not slowed further by elastic coupling to the (now nonexistent) bulk nematic region.

I now turn to the data for SCE12, shown in Fig. 4.5 as well as in Table 4.1. SCE12 is a (proprietary) mixture and therefore phase separates at the isotropic –chiral nematic transition, rendering it less ideal for the main point of this study. Each time

T_{IN} was approached from above, different areas of the system would transition at different temperatures, making reproducibility near the transition relatively difficult. Nevertheless, I examined SCE12 for two important reasons: i) SCE12 has a very large nematic phase range – $T_{IN} \sim T_{NA} + 37$ K – so that smectic fluctuations at temperatures above T_{IN} are virtually nonexistent, and ii) comparisons can be made with the large amount of literature for its bulk chiral nematic and Sm-A^* ECEs. I note that it was easily verified that measurements were performed in the isotropic phase rather than the biphasic region by monitoring I_{dc}, which jumped immediately by several orders of magnitude on cooling into the biphasic region. I first compare the approximate magnitude of the surface ECE with that of Lee, *et al* [133] at temperatures a few hundred millikelvins above their respective phase transition temperatures, *viz.*, T_{IN} and T_{IA}. Note that Ref. [133] reports results for I_{ac}/I_{dc}, which is a factor of 4 larger than my definition of $\theta = I_{ac}/4I_{dc}$. Accounting for this difference, in Fig. 4.5 I find values for $e_c \sim 10^{-11}$ to 10^{-10} rad V^{-1} m at a temperature a few hundred millikelvins above T_{IN} for SCE12. This is smaller than – but of the same order of magnitude as – the data reported in Ref. [133] at comparable temperatures above T_{IA}. That the surface ECE is a bit smaller above the Nem* – isotropic transition [133] is not surprising: The "strength" of the symmetry breaking due to the substrate's easy axis in the former case, and the strength of the induced smectic order in the latter, both depend critically on the surface preparation and choice of liquid crystals. Next, I compare the *surface* ECE data in Fig. 4.5 for the liquid crystal SCE12 with previous measurements of the ECE for SCE12 in the *bulk* nematic phase [51]. In Fig. 4.5 I find a value of $e_c \sim 10^{-10}$ rad V^{-1}m for SCE12 in the paranematic region just above T_{IN}. This is the same order of magnitude that was found in its bulk ECE nearly 37 K lower in temperature, deep into the *bulk* nematic phase [51]. This suggests that smectic order is extremely unlikely to be the source of the *surface* ECE above T_{IN} presented herein because $T_{IN} = T_{NA} + 37$ K. In fact at $T_{NA} + 9$ K, corresponding

to $\sim$ 28 K below T_{IN} – this is the highest temperature examined in Ref. [51] – the bulk nematic e_c for SCE12 is more than an order of magnitude smaller than the value reported herein for the surface ECE just above the IN phase transition temperature T_{IN}, and would likely decrease further with increasing temperature [51].

4.4 Summary

In this chapter, I presented data showing that it is possible to observe an electroclinic effect in a chiral liquid crystal above the bulk chiral nematic – isotropic transition temperature. My reasoning is based upon the understanding that a chiral electroclinic effect is obtainable on a substrate having an easy axis for orientation and symmetry breaking, and does *not* require smectic layering [56]. Additionally, I have shown that this effect occurs in the thin paranematic layer above this same transition. I find that the magnitude of this response near the transition temperature is comparable to that of the parasmectic region seen just above bulk Sm-A^* – isotropic transition temperature [133]. However, unlike the response in the parasmectic region – which shows an electroclinic effect that nearly vanishes $\sim$ 1°C above the Sm-A^* to isotropic transition – the electroclinic effect in the paranematic region falls off much more gradually with temperature, and can be observed nearly 10°C above the chiral nematic – isotropic transition with the liquid crystal W46, and nearly 15°C with SCE12. Also, I show that the magnitude of this effect in the paranematic layer is similar to that in the bulk chiral nematic phase, just above the transition to the Sm-A^* phase. But unlike the bulk nematic phase, the electroclinic effect in the paranematic phase has a relaxation time that is two to three orders of magnitude slower. Lastly, I find that the frequency dependence of this surface electroclinic effect has little to no temperature dependence, and has a Debye-like response.

Chapitre 5

Oily streaks in a chiral smectic-A liquid crystal[1]

5.1 Introduction

Liquid crystals are a fertile source of defect structures [139, 140], both in the nematic and the layered smectic phases. Depending on the system's parameters – this includes the composition of the substrate(s), film thickness, applied fields (electric, magnetic, strain), the temperature-dependent elastic moduli, and chirality – the smectic-A (Sm-A) phase can be deformed into a variety of one- and two-dimensional ordered defect patterns [141, 142, 60, 143, 144, 61, 62, 45, 145, 48]. These structures provide insights into the physical behavior of the liquid crystal, such as anchoring properties, phase transition, and grain boundaries, and are studied for possible applications.

A defect that is particularly rich in a variety of physics properties, and in consequence has been garnering increasing attention, is the Sm-A oily streak, first introduced in Sec. 1.8. These oily streaks occur in ultra-thin ($100 < h < 500$ nm, where h is the film thickness) smectic films that reside at the interface between a substrate treated for uniform planar anchoring of the director $\hat{n}$ and an isotropic medium (such

[1]This chapter is based on one of my articles in: Physical Review E.
I.R. Nemitz, A. J. Ferris, E. Lacaze, and C. Rosenblatt "Chiral oily streaks in a smectic-A liquid crystal," *Physical Review E* 12, no. 21 (July 13, 2016):6662-6668.

as air) that imposes vertical alignment of the director [60, 61, 62, 48]. In order to match the competing boundary conditions: i) $\hat{n}$ is parallel to the "easy axis" $\hat{e}$ immediately at the substrate over most or all of the alignment layer (except for the very thinnest liquid crystal films); see Fig. 5.1b for a generic representation, and ii) the smectic layers deform into a series of hemicylinders Fig. 5.1b, resulting in the texture observed under a polarizing microscope seen in Fig. 5.1a. For example, it has been shown that for thin films ($\sim$120–230 nm) of the liquid crystal octylcyanobiphenyl (8CB) on a polyvinyl alcohol (PVA) alignment layer, the director's planar alignment results in a very narrow region of smectic layers close to the substrate that are perpendicular to the substrate plane [48]. On polyimide, I can expect the presence of a similar transition region for smectic films that exhibit oily streaks, with layer oriented perpendicular to the substrate covering part, most, or the entirety of the substrate (region B in Fig. 5.1b). The exact structure will depend on the choice of liquid crystal, the alignment layer preparation, and most importantly, the thickness of the liquid crystal film [48]. it is this smectic transition region that will be responsible for the rotation of the oily streaks when the liquid crystal is doped with a chiral molecule. Additionally, I note that there is a region (Region A) that could be either a grain boundary or a melted nematic if the director discontinuity is sufficiently large [48, 146].

In this chapter I report on oily streaks, which involve rotation smectic layers that can be observed as stripes under crossed polarizers (Fig. 5.1), and which are composed of the liquid crystal 8CB (Fig. 5.2a) mixed with small quantities (up to 4 wt.-%) of the right-handed chiral dopant CB15 (Fig. 5.2b). On cooling below the nematic – Sm-A phase transition temperature T_{NA}, oily streaks without chiral dopant are oriented an angle $\phi = 0°$, *i.e.*, *perpendicular* to the easy axis $\hat{e}$, as is usual [48]. This orientation remains fixed as the temperature is lowered further into the Sm-A phase. With the addition of chiral dopant, however, $\phi(T = T_{NA}) \neq 0$, but decreases toward

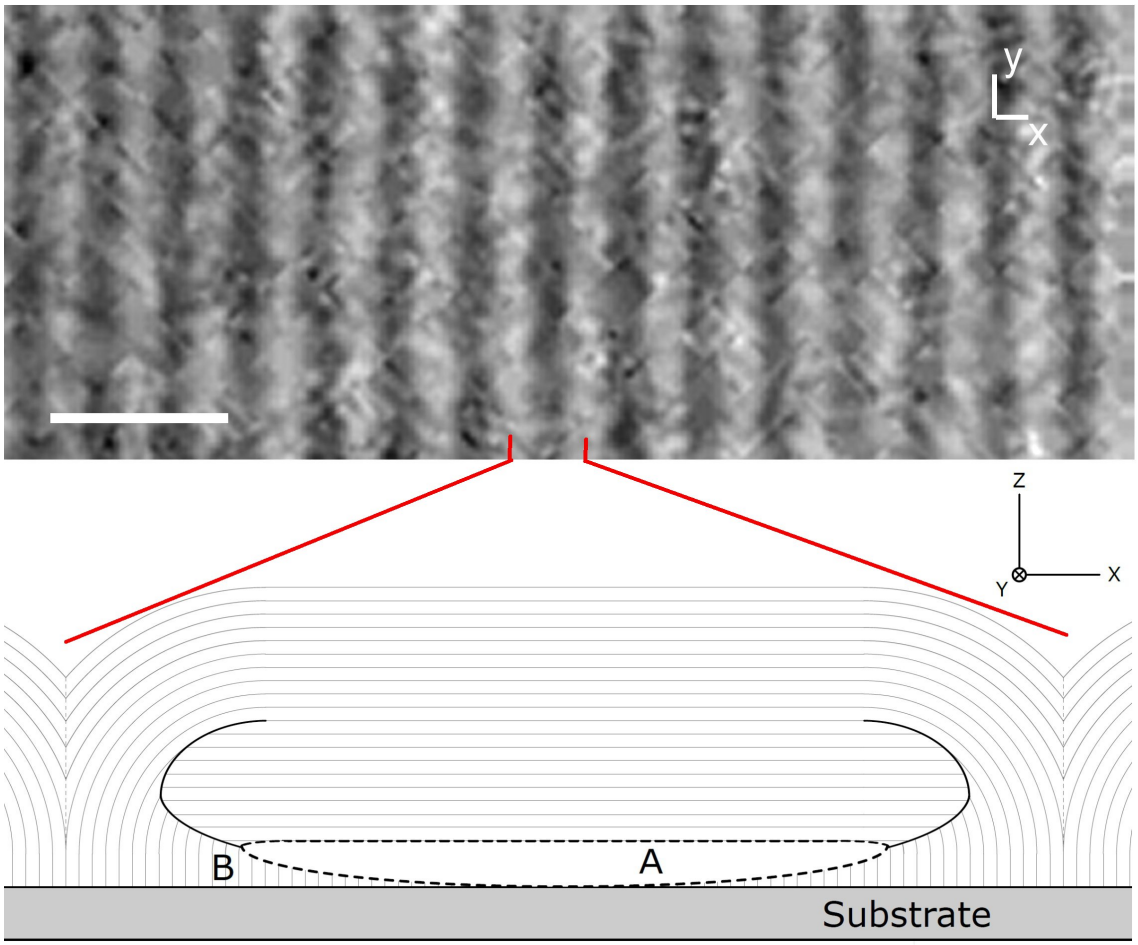

Figure 5.1: a) Photomicrograph of oily streaks looking downward along the z-axis for undoped liquid crystal at temperature $T_{NA} - T = 0.38$℃. Polarizers and analyzer are crossed and are at an angle of 45° with respect to the easy axis orientation. The horizontal bar corresponds to 2μm and is parallel to the easy axis. b) Generic schematic diagram of and end-on view of the liquid crystal structure that forms oily streaks. The red lines indicate the portion of (a) shown schematically in (b). The precise structure depends on the elastic constants, $T_{NA} - T$, and the film thickness h. For this chapter the most important feature is the orientation of the smectic layers (Region B) at substrate.

zero as the temperature is reduced. ϕ eventually reaches a steady-state value very close to 0° at a temperature $T_{NA} - T \equiv \Delta T \sim 1$℃. I ascribe this result to a surface electroclinic effect (ECE), *i.e.*, an ECE in a region very close to the interface, for a chiral Sm-A liquid crystal in the bookshelf geometry. The surface ECE for a chiral Sm-A liquid crystal was first observed by Xue and Clark using a bookshelf liquid crystal geometry [53]. This is an effect in which the director near the substrates tilts by an angle θ with respect to the smectic layer normal, where θ is proportional to the polar coupling between the liquid crystal and the substrate – in essence, this polar coupling corresponds to a spontaneous electric polarization localized at, and normal to, the surface. The surface ECE requires sufficiently low symmetry, including the absence of mirror symmetry; in other words, chirality is a required ingredient. More recently Shao, *et al* observed [147] a giant surface ECE in a 3.5 μm closed smectic cell having a bookshelf geometry, where they found a chiral-induced rotation of dark lines (parallel to the smectic layer normal) below the isotropic – Sm-A phase transition temperature. It is important to note that these dark lines do *not* correspond to oily streaks, which are perpendicular to the smectic layer normal in a much thinner open cell [48]. For the cases examined in Refs. [53] and [147], the director's tilt angle θ was due to the large susceptibility of the director close to the Sm-A to smectic-C phase transition temperature T_{AC}. On the other hand, for the smectic oily streaks I find that the largest oily streak rotation ϕ occurs immediately below the second-order nematic – Sm-A transition temperature T_{NA}, and falls rapidly toward zero on cooling. I discuss this behavior in the context of the temperature dependence of the smectic order parameter Ψ and the director's tilt elastic constant $D[\propto |\Psi|^2]$ with respect to the smectic layer normal below the second-order nematic – Sm-A phase transition temperature.

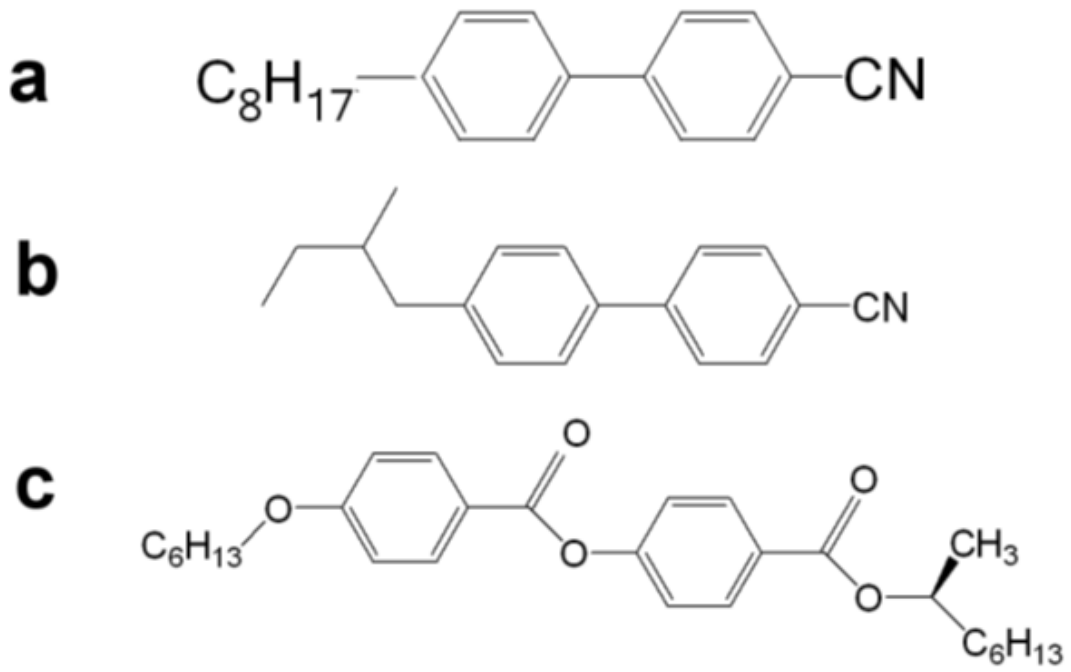

Figure 5.2: Molecules used in this work: a) the liquid crystal 8CB, b) the right-twisting chiral dopant CB15, c) the left-twisting chiral dopant ZLI-811.

5.2 Experimental Methods

5.2.1 Sample Preparation

The liquid crystal 8CB, which has the phase sequence: isotropic – 40.5℃ – nematic – 33.5℃ – Sm-A – 21.5℃ – crystal, was mixed with the right-handed chiral dopant CB15 shown in Fig. 5.2b. Concentrations of $c = 0, 1.0, 2.0, 3.4, 4.0(\pm 0.1)$ wt.-% were investigated. A 5 wt.-% mixture of 8CB with the left-handed chiral dopant ZLI-811 (Fig. 5.2c) was also made to determine whether the sense of the oily streak rotation would be reversed from that of the right-handed dopant.

An aluminum front-surface mirror (Edmund Optics Worldwide, flatness 4-6λ, coated with a $\lambda/2$ film of Silicon Monoxide (SiO), a wavelength range between 400 and 700 nm, and a reflectivity near 100% in the visible spectrum) was cut and then cleaned in detergent, distilled water, acetone, and ethanol. The reflecting surfaces were spin-coated at 2000 rpm for 20 s with the polyamic acid RN-1175 (Nissan Chemical In-

dustries) and baked at 80℃ for 5 minutes and then 250℃ for one hour, according to manufacturer's specifications. The resulting polyimide alignment layers were rubbed with a commercial rubbing cloth (YA-20-R, Yoshikawa Chemical Co.) on a Optron rubbing machine with a roller radius of $r = 4$ cm rotating at ∼1000 rpm while the sample is translated underneath it at ~ 1 mm s^{-1}, to obtain an easy axis $\hat{e}$ for planar liquid crystal alignment. Each liquid crystal/chiral dopant composite was mixed as a 0.2 M solution in chloroform, 40 μL of which was applied to the polyimide-coated substrate, and was spin coated at a spinning speed 1750 rpm for 30 s. The goal was to obtain liquid crystal films of approximately uniform thickness after the solvent evaporated.

In addition to polyimide, samples also were constructed using polyvinyl alcohol or MoS_2 as alignment layers. For the PVA, a 0.5% by weight PVA (average molecular weight M_w = 85000 – 124000) in water solution was spin coated onto a mirrored substrates at 3000 rpm for 30 seconds. The PVA coated substrates then were baked at 120℃ for 120 minutes, and allowed to cool. The resulting samples were rubbed, and coated with liquid crystal in a similar fashion as the polyimide alignment layers. For MoS_2, atomically smooth samples of crystalline MoS_2 were coated with ~ 1 mg pure 8CB through simple deposition. The samples were raised into the isotropic phase in order to wet the substrate, covering it with a thin film of liquid crystal. MoS_2 samples were never coated with doped liquid crystal, and were simply used as a control.

5.2.2 Imaging

Each sample was observed using an Olympus BX60 polarizing microscope in reflection mode. The use of a mirrored substrate, rather than a transparent microscope slide, greatly enhanced the visibility and definition of the oily streaks. The sample was heated into, and then cooled down from, the isotropic phase, through the nematic phase, and into the Sm-A phase just below T_{NA}. The approximate film thickness $h \sim$

320 ± 50 nm was determined through interference color. When observing the samples in reflection mode through crossed or parallel polarizers, different film thicknesses correspond to different colors. When the polarizers are crossed, the colors come from interference between the ordinary and extraordinary rays emerging from the LC films. When the polarizers are parallel, the light reflecting off of the LC / air interface and light reflecting off of the LC / mirror interface creates the different colors through constructive or destructive interference, depending on the difference in their phase (which depends on the thickness of the LC film). [48, 148, 149]. The data reported here correspond to a slightly thicker film regime than the one investigated in Ref. [48].

After T_{NA} was reached, the temperature was reduced in 50 mK steps, allowed to equilibrate, and high resolution (23 megapixels) images (Fig. 5.1a) were taken at each temperature with a 50x objective. Here the easy axis of the sample was oriented at an angle 45° with respect to the crossed polarizer and analyzer. Note that the reflected intensity goes to zero uniformly when the polarizer/analyzer is parallel or perpendicular to the oily streaks, in agreement with the picture in Fig. 5.1b in which the director near the substrate, and therefore the hemicylinders above, rotate in a plane parallel to the surface.

5.3 Results and Analysis

5.3.1 Streak Rotation vs. Temperature

I will first examine the results qualitatively. Figure 5.1a shows an image of the oily streaks for the $c = 0$ wt.-% sample, *i.e.*, no chiral dopant, at a temperature $\Delta T = 0.38$ ℃. As is obvious, the streaks are at an angle $\phi = 0°$ with respect to the normal to the easy axis, which corresponds to the horizontal 2 μm length scale bar. It is important to note that the orientation ϕ of the $c = 0$ oily streaks remained unchanged as the

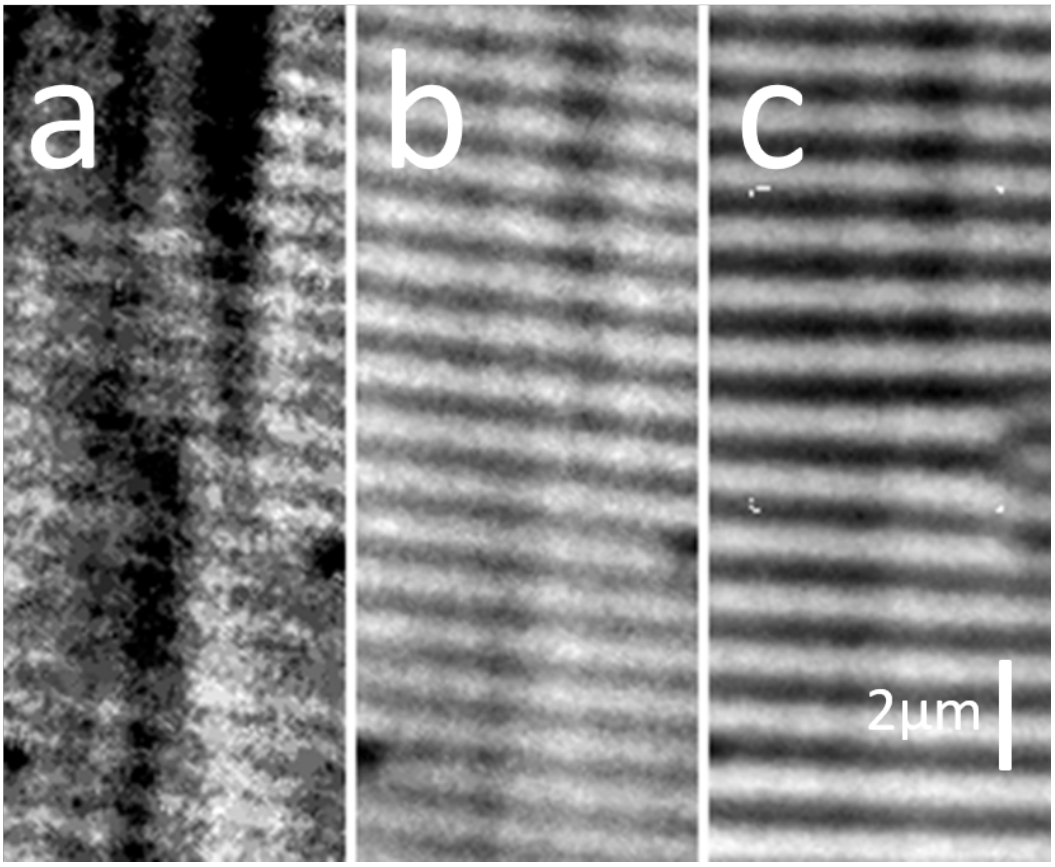

Figure 5.3: a) Photomicrograph of oily streaks for $c = 4$ wt.-% at temperatures ΔT =0.2 (a), 0.4 (b), and 1.3 (c) ℃. Note the first image (a) has been contrast-enhanced in order to make visible the rotated oily streaks, as the optical contrast close to T_{NA} is particularly weak. The bar represents 2 μm and is parallel to the easy axis. The dashed rectangle corresponds to the area in Fig. 5.4.

temperature was reduced.

In Fig. 5.3 I show oily streak images for the $c = 4.0$ wt.-% samples at three temperatures ΔT below T_{NA}. Several features can be observed. First and foremost is that the oily streak orientation $\phi \neq 0$; ϕ is large just below T_{NA} (Fig. 5.3a) and decreases toward zero with increasing ΔT (*i.e.*, decreasing temperature) in the Sm-A phase. Second, rather than the entire length of the streaks rotating with decreasing temperature, the process occurs by rotation of individual – or a group of – streak *segments*. The ends of the segments are manifested as streak discontinuities (dislocations), which are especially evident in Fig. 5.4, where the images corresponding to

the boxed area in Fig. 5.3c were collected every 2 s as the sample was cooled at a rate of 1.7 mK s^{-1}. As the temperature was lowered the segments broke and fused repeatedly, giving the appearance of an "unzipping" and "zipping" process. Third, I found qualitatively similar results using the left-handed chiral dopant ZLI-811, except that the sense of the oily streak rotation was reversed, *i.e.*, $\phi < 0$; see Fig. 5.6. This is an important check to verify that the effect is, indeed chiral. Fourth, the average periodicity $\langle p \rangle$ of the oily streaks was found to increase with decreasing temperature for all chiral dopant concentrations (including $c = 0$), eventually reaching a stable periodicity at $\Delta T \sim 1$℃. The change in $\langle p \rangle$ appears to occur by means of edge dislocations, similar to those seen in Fig.5.4 and especially in Fig. 5.5. This will be discussed in Section 5.3.2.

To analyze these images and extract the rotation angle, the software package, Image-J® was used. Image-J is a powerful free software available online, and has a multitude of uses for the extraction of information from micrographs.

All images for each individual concentrations were imported sequentially as a stack into Image-J. This allowed for consistent reproducible analysis from image to image. Once imported, the stacks were cropped to a size of 1536 pixels by 1536 pixels – previous work on this microscope using an optical grating showed that 1μm corresponded to 15.625 pixels, meaning 1536 pixels $\propto$ 100μm – so that the same area of uniform thickness and minimal imperfections would be analyzed for every temperature. A rolling ball background subtraction with a radius of between 50 and 100 μm was performed to reduce noise in the images. (This size rolling ball was used since it was up to 2 orders of magnitude larger than the structures I am investigating). Using the FFT (Fast Fourier Transform) function the image stacks were converted into q-space. Because the period of the oily steaks is only slightly larger than optical wavelengths, any sharp features that may exist tend to be washed out, resulting in a near-sinusoidal real space intensity profile in a direction perpendicular to the

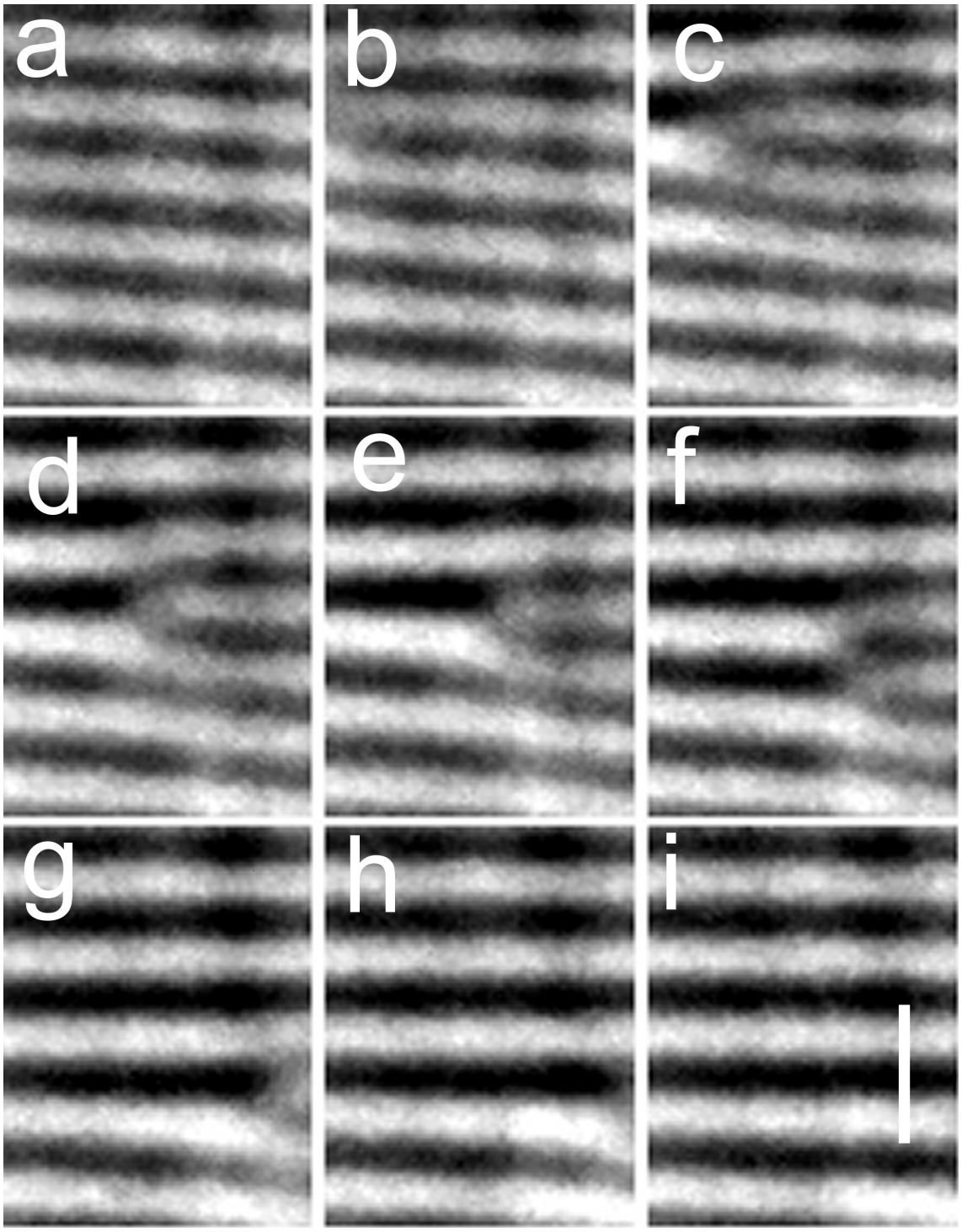

Figure 5.4: A series of photomicrographs of oily streaks for $c = 4$ wt.-% in the rectangular region of figure Fig. 5.3c. Images were taken at 2 s intervals (each with a 1 s exposure time) as the temperature was reduced at a rate of approximately 1.7 mK s^{-1} in the neighborhood of $\Delta T = 1.3$ ℃. Notice that the discontinuities in the streaks (dislocations) move downward and to the right as the sample is cooled. Bar in image i represents 2 μm and is parallel to the easy axis.

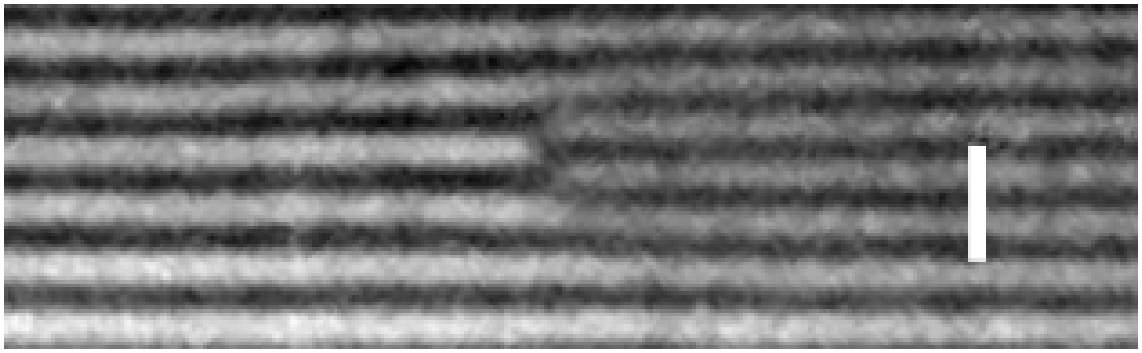

Figure 5.5: Photomicrograph of oily streaks having concentration $c = 4$ wt.-% at temperature $\Delta T = 1.3$℃, clearly showing the edge dislocations. Bar corresponds to 2 μm and is parallel to the easy axis.

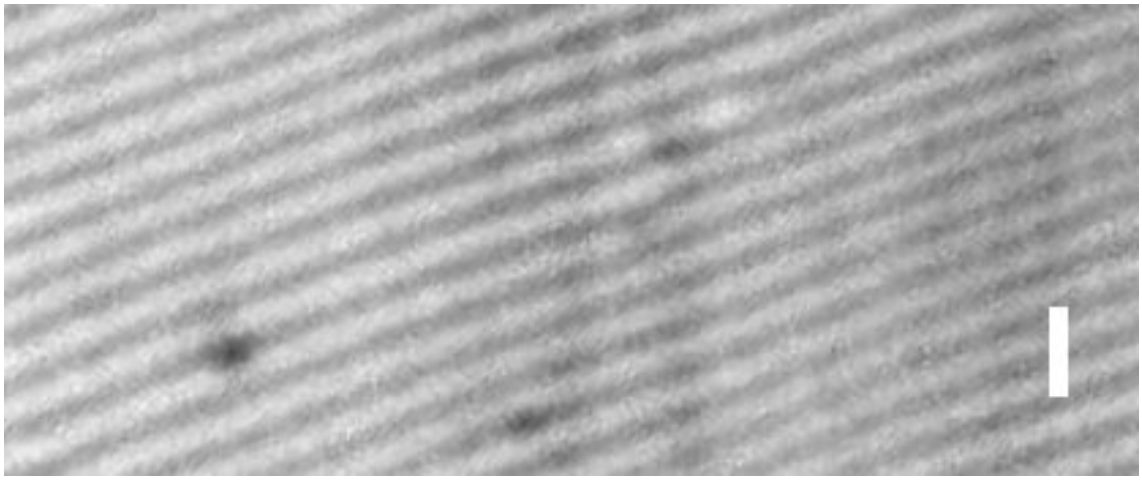

Figure 5.6: Photomicrograph of oily streaks having concentration $c = 5$ wt.-% of the *left-handed* chiral dopant ZLI-811. Notice that the rotation of the oily streaks has a sense opposite that of the right-handed dopant CB15 in Fig. 5.3 and Fig. 5.4. Bar corresponds to 2 μm and is parallel to the easy axis.

streaks. As a consequence, all higher harmonics of the fundamental Fourier peaks are suppressed; therefore I will focus solely on the fundamental. An example of a real-space image and its Fourier transform are shown in Fig. 5.7; here $c = 3.4$ wt.-% and $\Delta T = 0.35$ ℃.

For each Fourier image I used Image-J's Find Maxima tool to obtain the region at which the Bragg spot is brightest – this generally corresponds to the central part of the fundamental peak – from which I extracted their average rotation angle $\langle\phi\rangle$, as well as the average wavevector magnitude $\langle q\rangle$. That the Bragg spot is spread out in q-space suggests that: i) the film thickness is not completely uniform and there is a range of oily streak spacings, not a single periodicity p associated with each temperature and concentration (this is further explained later), ii) there is a range of rotation angles ϕ; and iii) some of the spread comes from the segments' ends (the unzipped regions), the edge dislocations, and very wide stripes (Fig. 5.7a) that tend to appear and become more numerous at lower temperature. These wide stripes are oriented perpendicular to the easy axis $\hat{e}$ to within an angle of $\pm 0.3^{\circ}$, and their orientation does not change with temperature. My initial studies of these wide stripes indicate that they have a structure different from the oily streaks, and will be the subject of future research.

Based on the Fourier analysis, Fig. 5.8 shows the average rotation angle $\langle\phi\rangle$ *vs.* ΔT with respect to the orientation of the wide stripes for all concentrations. In addition to this, Fig. 5.9 gives a sense of what the maximum average rotation (just below T_{NA}) of the oily streaks, plotted versus each sample concentration. Another measurement was also performed using a $c = 3$ wt.-% mixture on a PVA substrate. The results are shown in Fig. 5.10 for a film of 8CB having a thickness comparable to those shown in Fig. 5.8.

Several more features can be gleaned from Figs. 5.8, 5.9 and 5.10. First, on decreasing the temperature from T_{NA} there is a rapid decrease of $\langle\phi\rangle$ immediately below, *i.e.*, within 100 mK of T_{NA}. This behavior occurs not only for the polyimide

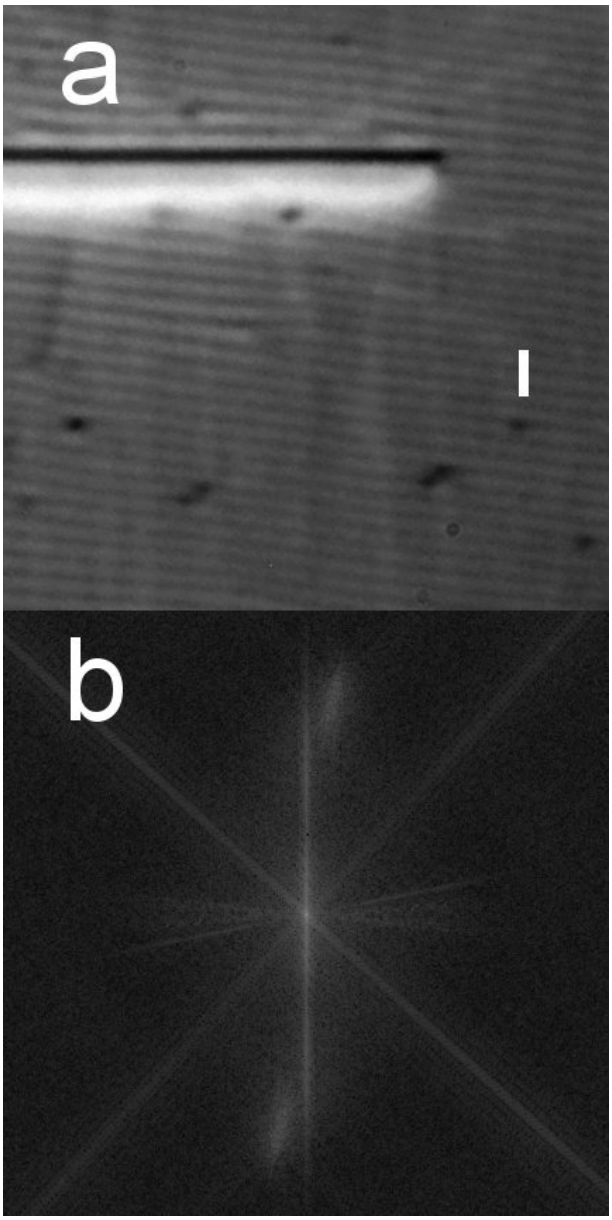

Figure 5.7: (a) Real space image of the $c = 3.4$ wt.-% sample at $\Delta T = 0.35$℃. The bar represents 2 μm and is parallel to the easy axis. The wide stripe is discussed in the text. (b) 2D Fourier transform of (a). The lines at $\pm 45^{\circ}$ are image compression artifacts, the approximately horizontal lines are an artifact of the alignment layer rubbing to create the easy axis, and the vertical lines artifact is due to the wide stripe. The relevant features, which are easy to extract are the elongated smudges in the first and third quadrants, from which I determined the average oily streak rotation angle $\langle \phi \rangle$ and average periodicity $\langle p \rangle$.

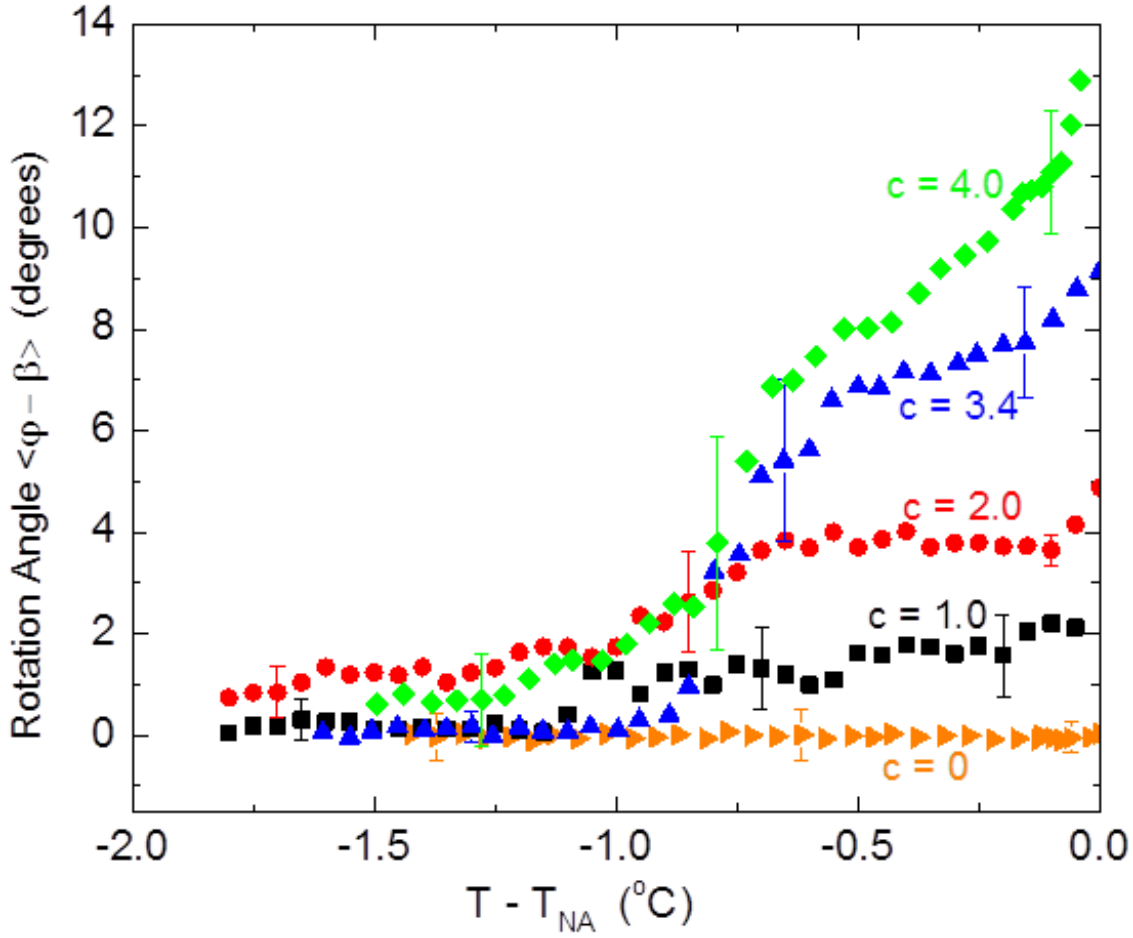

Figure 5.8: The average rotation angle (relative to the wide stripes (Fig. 5.7)) *vs.* $T - T_{NA}$ for all concentrations decreases as temperatures is reduced, approaching a limiting value that corresponds to the wide stripes (Fig. 5.7) that appear at lower temperatures and remain fixed in orientation as the temperature is further reduced. Typical error bars are shown.

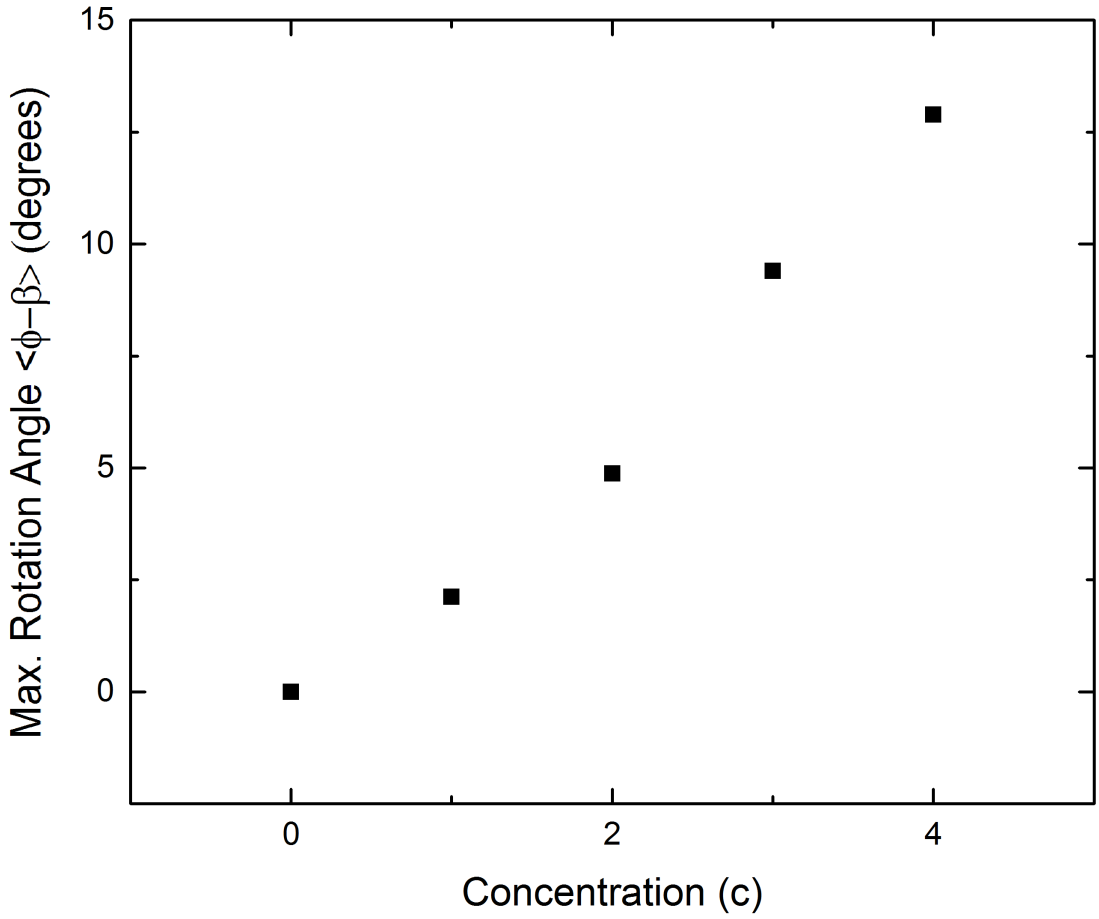

Figure 5.9: The maximum average rotation angles $\langle\phi\rangle$ from Fig. 5.8 just below T_{NA} for all concentrations (weight percents of dopant in liquid crystal). As the concentration of CB15 in 8CB is increased, the rotation (especially near T_{NA}) increases relatively monotonically.

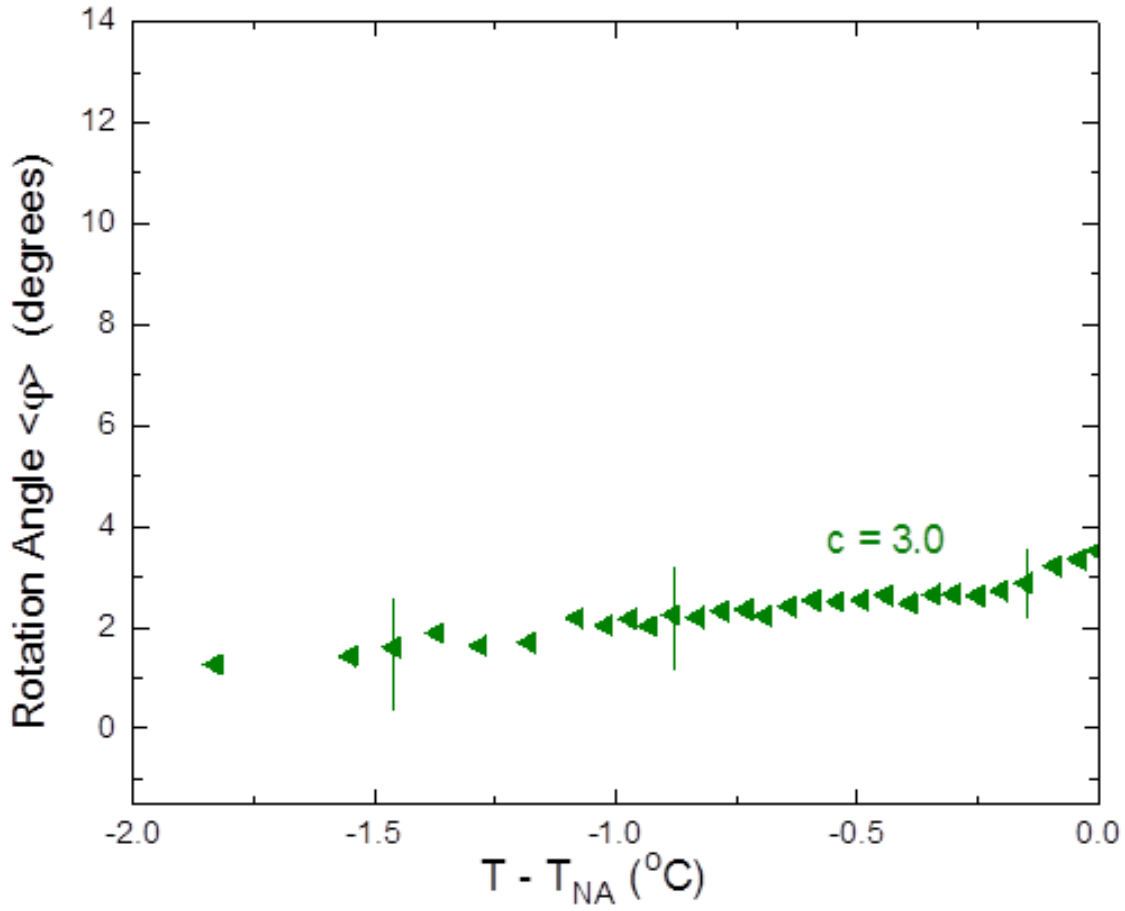

Figure 5.10: Same as Fig. 5.8, but for a PVA substrate. Concentration $c = 3$ wt.-%.

alignment layer, but also for the PVA alignment layer. The origin of this rapid variation very close to T_{NA} is not clear, although it may be due in part to a combination of temperature gradients across the sample in conjunction with a non-segregation of the chiral dopant that results from a nematic - Sm-A phase boundary. Second, on lowering the temperature further by a few hundred millikelvin, the relaxation rate (decrease) of $\langle\phi\rangle$ with decreasing temperature, *i.e.*, $d\langle\phi\rangle/dT$, becomes weaker, perhaps even vanishing for the $c = 1.0$ and 2.0 wt.-%. At still lower temperatures $\langle\phi\rangle$ relaxes smoothly toward zero. Third, the rotation for the PVA alignment layer is uniformly smaller than for the RN-1175 polyimide alignment layer: this will be discussed later. A more quantitative interpretation of these apparent trends in difficult due to the relative size of the error bars. Nevertheless, the overall trends described above are quite striking.

5.3.2 Periodicity vs. Temperature

In addition to the variation of the average rotation angle, I observed an evolution of the periodicity with temperature just below T_{NA}, reaching steady-state periodicities similar to those observed in [48]. This rapid evolution in periodicity from thinner streaks (those with a lower period) to wider streaks (those with a higher period) is first observed in Fig. 5.3. It is apparent that the streaks in the image taken at 0.2℃ below the transition temperature have a smaller period than those taken at 1.3℃ below the transition. I expand on this using Image-J® to determine the periodicity of different samples over the same temperature range as the oily streak rotations. Utilizing the same Fourier transforms as before, a plot profile was taken from the very center of the Fourier transform, through the brightest maximum in the Bragg peak (associated with the average rotation angle ϕ). Doing this for each image, I was able to obtain profiles of the Bragg peaks. These profiles were imported into Origin© as a spreadsheet, and plotted individually as scatter plots; an example of this is shown

in Fig. 5.11. These scatter plots were then fitted to a series of Gaussians (one for the zero wavevector due to noise and one for the Bragg peak). The mean of the fitted Gaussians were taken as the average wavevector $\langle q \rangle$ associated with the oily streaks which was used to determine the average periodicity $\langle p \rangle$ of the oily streaks for each temperature.

The average periodicities $\langle p \rangle$ *vs.* temperature for 8CB on a polyimide alignment layer can be seen in Fig. 5.12, and the features in this preliminary examination are very apparent. As the temperature of the system was lowered, $\langle p \rangle$ for the undoped ($c = 0$) and the doped $c = 3.4$ wt.-% samples, as well as all other dopant concentrations. Once the temperature had been lowered by $\Delta T \sim 1$°C, the change in $\langle p \rangle$ abruptly stopped and further reductions in temperature had no effect on $\langle p \rangle$, which had reached a stable state in both the doped and undoped samples.

In order to further explore this variation of periodicity with temperature, measurements were repeated for thin films of undoped 8CB on both PVA and MoS_2 alignment layers. Figs. 5.13 and 5.14 show preliminary data of the average periodicity $\langle p \rangle$ *vs.* temperature for the thin films of 8CB on PVA and MoS_2 respectively. As the temperature was reduced near T_{NA}, I observed a rapid increase in periodicity with decreasing temperature for both substrates, especially for those samples having a large equilibrium $\langle p \rangle$ value (≥ 1 μm). Unfortunately, samples with a MoS_2 alignment layer became completely filled with wide stripes at lower temperatures, rendering periodicity measurements below $T - T_{NA} \approx -0.5$°C impractical.

In all three samples, the increase in $\langle p \rangle$ happens through the formation of edge-like dislocations throughout the sample, as shown in Fig.5.4 and particularly Fig. 5.5. As the temperature was reduced near the transition, these dislocations formed, appearing as a line of dislocations perpendicular to the oily streaks, between streaks of high periodicity and those of low periodicity. It is as if the lower periodicity streaks were breaking and reconnecting as larger period streaks at this boundary.

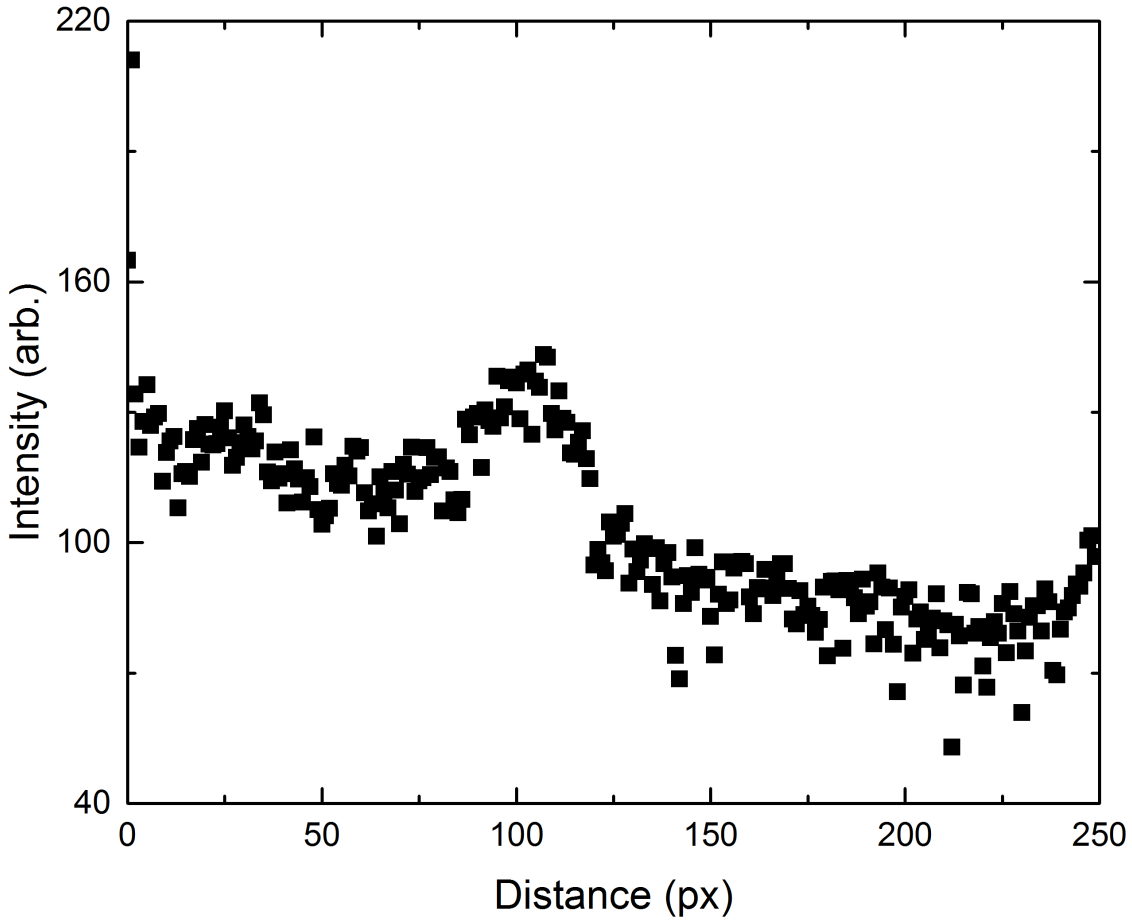

Figure 5.11: A typical scatter plot used to determine the period of 8CB oily streaks. This plot was taken from an image obtained 100 mK below T_{NA}. The peak at ∼100 pixels corresponds to Bragg peak of the Fourier transform. The average period of the oily streaks will increase when the Bragg peak moves to the left as the temperature is reduced.

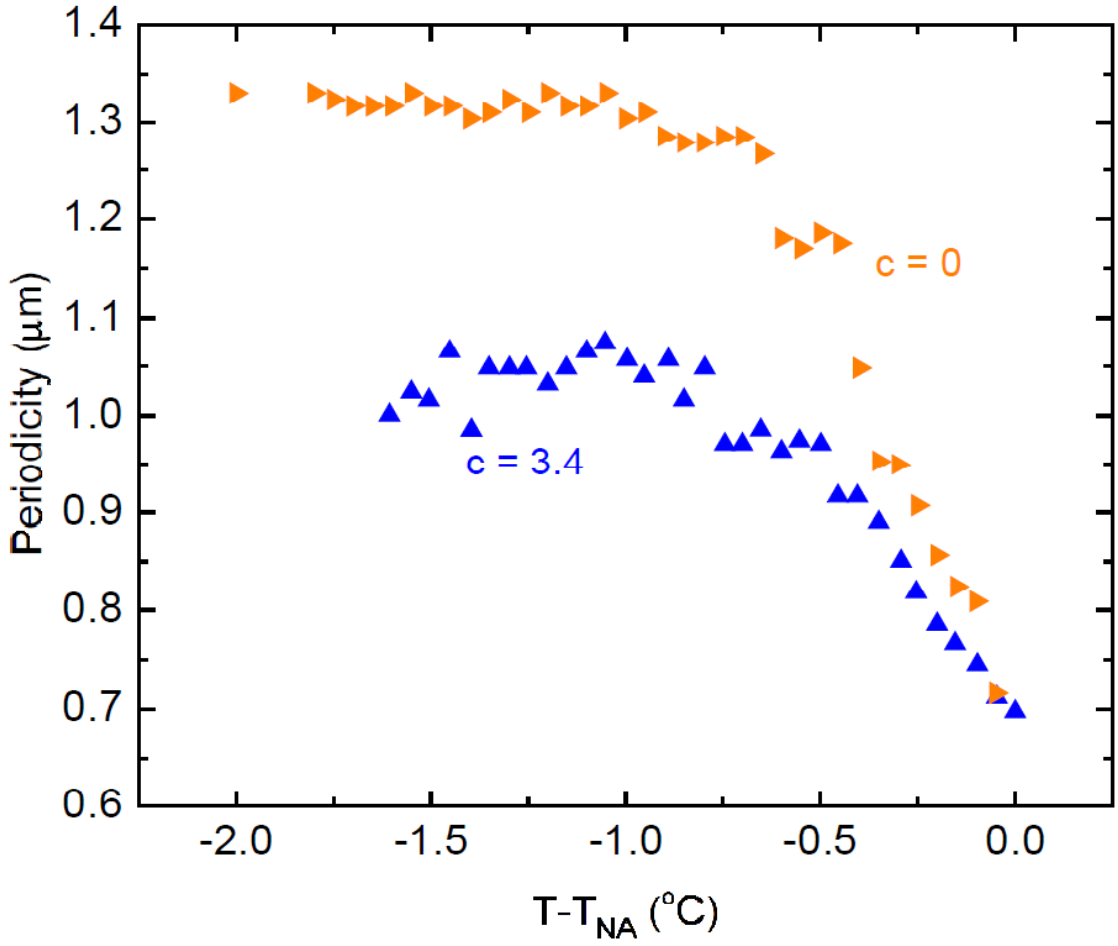

Figure 5.12: Average periodicities $\langle p \rangle$ for two concentrations, $c = 0$ and 3.4 wt-%, *vs.* temperature on polyimide.

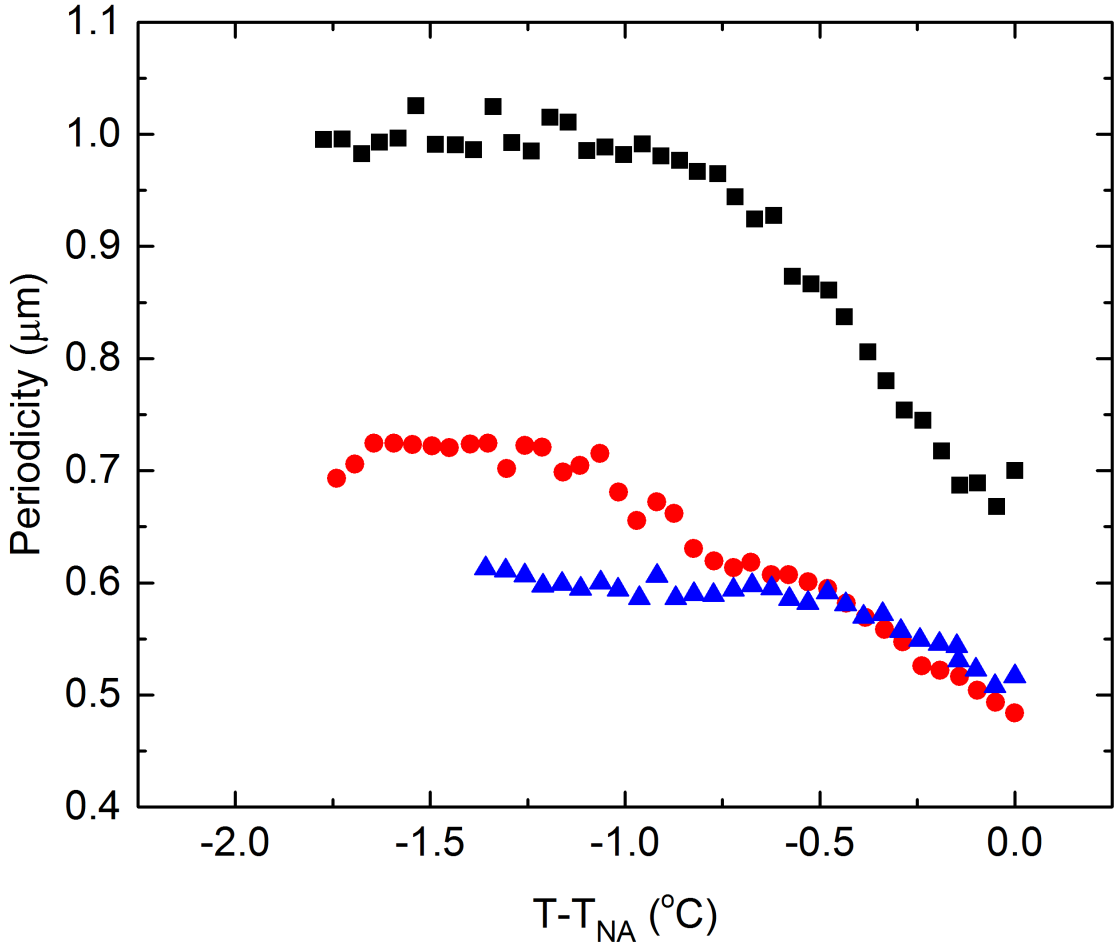

Figure 5.13: Average periodicities $\langle p \rangle$ *vs.* temperature for undoped 8CB on PVA at three different sample locations.

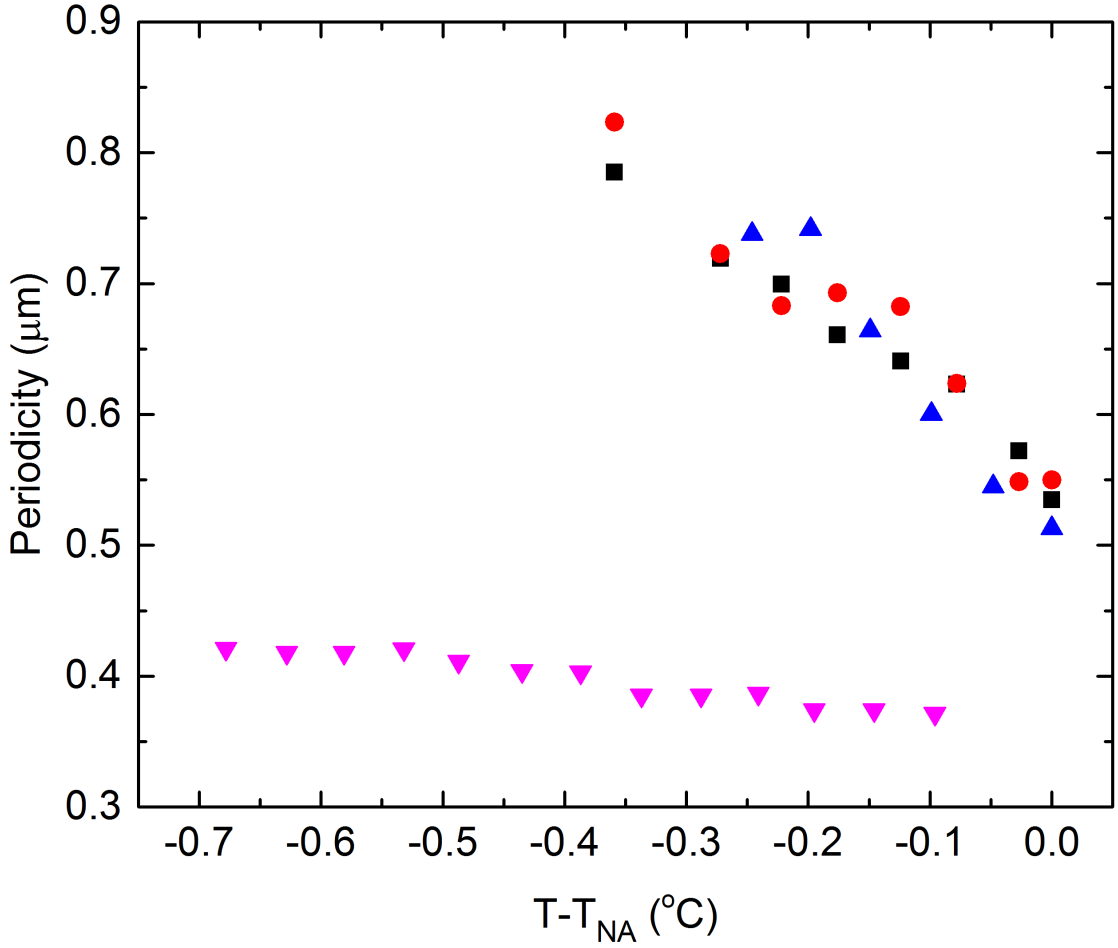

Figure 5.14: Average periodicities $\langle p \rangle$ *vs.* temperature for undoped 8CB on MoS_2 at four different sample locations.

This breaking and reconnecting traveled parallel with the reforming streaks, until an entire series of streaks had been reformed. As the temperature was reduced, this reforming continued until the sample's average periodicity had reached its stable state / highest period. Even after the sample was cooled many degrees deeper into the Sm-A phase, the period remained unaffected. Interestingly, when the oily streaks are reformed into a larger period structure, they only marginally affect the period of surrounding streaks. This gives the stretched distribution in the Bragg peak that was mentioned earlier. While this may be true for polyimide and PVA, new data show that when oily streaks on MoS_2 reform, the periodicity is redistributed evenly throughout all of the surrounding oily streaks, in turn giving a less stretched Bragg peak.

While these are preliminary measurements, a few further observations may be made. Comparing Fig. 5.12, 5.13, and 5.14 it is clear that the evolution in $\langle p \rangle$ with temperature is a property characteristic to oily streaks, and does not depend on chirality. While this not a chiral effect, it is nonetheless interesting. The differences in the evolution of $\langle p \rangle$ with temperature on the alignment layers – specifically MoS_2, which appears to have a more rapid increase in period with decreasing temperature – indicates there may be a dependence on the substrate used. Additionally, because it is known that thicker liquid crystal films present with larger period oily streaks [148], these data indicate the increase in $\langle p \rangle$ just below T_{NA} is dependent on liquid crystal film thickness as well. Just how the evolution of $\langle p \rangle$ depends on the thickness of the smectic films, and on the alignment layer used, are viable avenues of research that will be explored more thoroughly in the future.

5.4 Rotation Explained

Xue and Clark demonstrated a smectic surface electroclinic effect, which they ascribed to a polar interaction between the chiral liquid crystal and the substrate that acts like an external electric field localized at the interface [53]. The liquid crystal's molecular orientation at the interface adjusts so that an electric polarization points toward or away from the interface. This, in turn, couples to the director tilt angle θ_0 with respect to the smectic layer normal immediately at the surfaces ($z = 0$), which relaxes elastically (by an azimuthal twist) into the bulk (See Fig. 5.15). The average value of θ_0 at the surface would vanish if the liquid crystal were achiral, but θ_0 is nonzero with a particular sense of rotation (clockwise of counterclockwise) that depends on the handedness of the liquid crystal (*cf.* Figs. 5.3 and 5.6). Xue and Clark's free energy calculation [53] for $\theta(z)$ was based on that for the bulk ECE [34], but with significant modifications to account for its localization near the surface. First, there is a characteristic correlation length $\xi = (K_{22}/D)^{1/2}$ over which the director tilt with respect to the smectic layer normal, *viz.* $\theta(z) = \theta_0 exp(-z/\xi)$, relaxes from θ_0 at the surface to $\theta = 0$ in the bulk (Fig. 5.15).

Here K_{22} is the twist elastic constant and D^{-1} is an effective susceptibility for the tilt of the director relative to the layer normal, where D vanishes on approaching T_{AC}. Second, the applied electric field for the bulk ECE [34] corresponds to a localized field due to the polarization discontinuity at the interface [53] for the surface ECE. For sufficiently small ξ, Xue and Clark found that the induced director tilt at the surface θ_0 is proportional to ξ/K_{22}, where the proportionality coefficient depends on the generalized polarization susceptibility, the strength of the polar interaction at the interface, and coupling between tilt angle and polarization. Because I am doping the configurationally achiral liquid crystal with a chiral additive, the coupling in this experiment is also related to the dopant concentration c, increasing with increasing c.

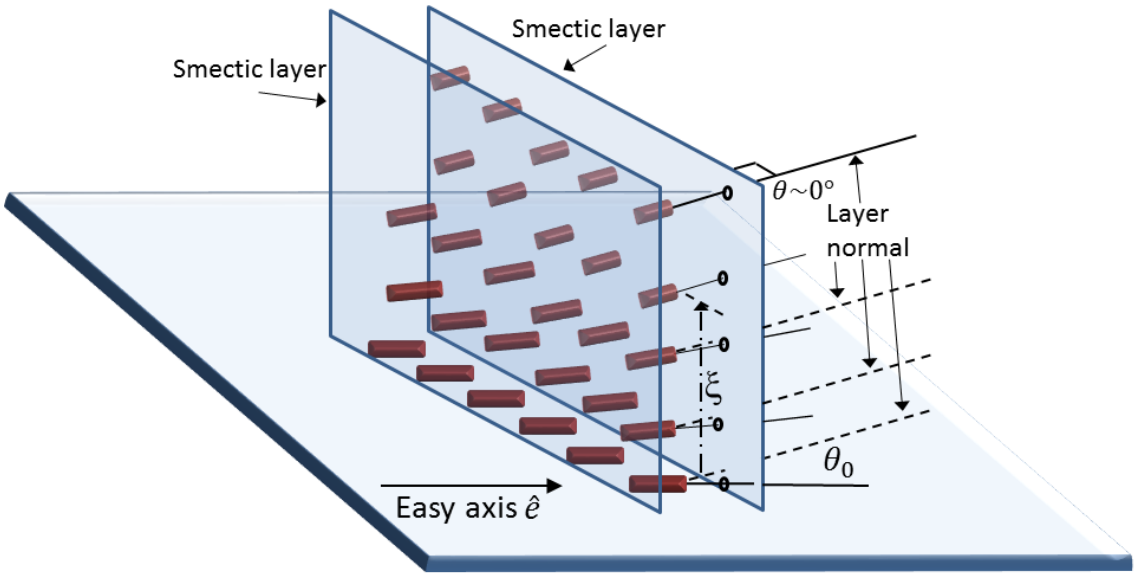

Figure 5.15: Schematic diagram of director and smectic sublayers (item B Fig. 5.1b) close to the alignment layer. director is parallel to the easy axis at the substrate ($z = 04$), where the smectic layers are rotated by an angle θ_0 with respect to the director due to the ECE. The director orientation relaxes to be parallel to the smectic layer normal over a distance $z = \xi$ from the substrate. The distance of the molecules above the substrate is represented by the darkness (color saturation), with the darkest (deepest red) being closest to the substrate and the lightest (least saturated red) being far above the substrate.

Turning to these experiments, which involve a complex layer structure (Fig. 5.1) rather than the uniform Sm-A phase studied in Ref. [53], the following physical picture emerges: The smectic layers over most of the surface (item B in Fig. 5.1b) are perpendicular, or nearly so, to the alignment layer. Because of the presence of an easy axis $\hat{e}$, the director $\hat{n}$ at the substrate is approximately parallel to $\hat{e}$. I remark that this is different from the case of Ref. [53], where the director orientation was established by shearing the cell. Then as with Ref. [49], the polar interaction between the liquid crystal and the alignment layer, *i.e.*, the effective surface field, induces a rotation of the director θ_0 with respect to the smectic layer normal at the surface (Fig. 5.15). This is the surface ECE, which can be large just below T_{NA} because the elastic constant D for director tilt is proportional to $|\Psi|^2$ [150, 12]). But owing to the easy axis, it is the director *at the surface* that remains fixed and it is the smectic layers that rotate; again, see Fig. 5.15. This is the mechanism that drives the rotation of the oily streaks, which must be perpendicular to the smectic layer normal in the sublayer corresponding to zone B in Fig. 5.1.

As one moves a small distance away from the surface and into the bulk where the effective surface field vanishes, the director orientation relaxes over a length scale ξ, so that $\hat{n}$ becomes perpendicular to the already-rotated smectic layers. Shao, *et al* noted [147] that this variation of θ with z would entail a small amount of smectic layer curvature near the surface. In addition, they noted that there must be a periodic smectic layer dislocation at the surface due to the difference in smectic layer spacing $f = d_0 cos\theta(z)$ between surface and bulk, where d_0 is the smectic layer spacing corresponding to the director being normal to the layer. These effects are likely to be small given the relatively small values of θ.

Returning to the chiral oily streaks, on reducing the temperature below T_{NA} and going more deeply into the Sm-A phase, the smectic order parameter Ψ increases. This has the effect of increasing the tilt elastic constant D and thereby decreasing θ_0

at the interface. Because the director remains parallel to the easy axis $\hat{e}$, the smectic sublayers (item B in Fig. 5.1b) and, in consequence, the oily streaks must rotate so that the oily streaks approach an orientation perpendicular to $\hat{e}$ at low temperatures. Since rotation of the long oily streaks *en masse* would involve significant defect movement at points far from the pivot, the oily streaks break into smaller segments that can rotate more easily, unzipping and zipping at the segment ends.

Xue and Clark's experiments [53] were performed near T_{AC}, and therefore the relevant correlation length was based on the tilt susceptibility D^{-1} diverging at T_{AC}. This experiment takes place in a very different region, just below the nematic – Sm-A transition temperature, where $D \propto |\Psi|^2$ and Ψ grows with decreasing temperature. Litster, *et al* used light scattering to obtain the quantity D/K_{33}^0 *vs.* temperature in the Sm-A phase for the liquid crystal octyloxycyanobiphyenyl (8OCB) [151], where K_{33}^0 is the non-divergent part of the bend elastic constant. They found that D/K_{33}^0 evolves from approximately 3 x 10^{11} cm^2 at $\Delta T \sim 30$ mK for approximately 10^{12} cm^2 at $\Delta T \sim 300$ mK to approximately 3 x 10^{12} cm^2 at $\Delta T \sim 3$ ℃. Accounting for the smaller value – by at least a factor of 3 (Ref. [12]) – of the twist elastic constant K_{22}, I would expect ξ to be of order 100 nm at $\Delta T \sim 30$ mK and of order 35 nm at $\Delta T \sim 1$℃. To be sure, 8CB and 8OCB are not identical molecules and their critical behaviors differ [151]. Moreover, these lengths already are larger than the typical 20 nm thickness of the smectic transition region at the base of the hemicylinders obtained on PVA substrates [48] (region B in Fig. 5.1b). In consequence, the decaying exponential form $\theta(z) = \theta_0 exp(-z/\xi)$ is not totally appropriate for the oily streak situation nevertheless, the qualitative features that I observe are consistent with the surface electroclinic effect: in particular, a rotation of the oily streaks just below T_{NA} that is larger with higher chiral dopant concentration c, which decreases as the temperature is reduced in the Sm-A phase.

I will briefly address the magnitudes observed for the average oily streak rotation

angle $\langle\phi\rangle$. First, the values of $\langle\phi\rangle$ measured for the PVA alignment layer are smaller than the corresponding values for the polyimide, although the general behavior with temperature is qualitatively similar. This may be expected, as the polar interactions that drive the ECE are likely to be different for the two alignment materials; it also is possible that the transition regions close to the substrates have different structure. Second, values of $\langle\phi\rangle$ observed by Xue and Clark [53], which were due to the proximity of the Sm-C phase, were relatively small. The rotation angles observed by Shao, *et al* [147], also with a nearby Sm-C phase, were considerably larger owing to their use of the compound W415, which has an enormous surface ECE. Their pure chiral liquid crystal did not possess a nematic phase and therefore there was no nematic – Sm-A transition at which the smectic order parameter Ψ would vanish. This is why no decrease of $\langle\phi\rangle$ was observed as the temperature was reduced in the Sm-A phase in Ref. [147], in contrast with the chiral oily streaks discussed herein. The relatively large rotation angles $\langle\phi\rangle$ that I observed just below T_{NA}, especially for the polyimide alignment layer (Figs. 5.8 and 5.9), occur even though the chiral dopant concentration is only a few wt.-%. I speculate that the large rotations may be due to partial segregation of the chiral dopant near the surface. This would facilitate a larger tilt of the director θ_0 relative to the layer normal than would occur if the chiral dopant concentration were uniform throughout the liquid crystal film. This conjecture requires further study.

5.5 Summary

I have shown that a chiral dopant causes a rotation by angle ϕ of smectic oily streaks relative to a direction perpendicular to the easy axis. The rotation angle is largest just below the nematic – Sm-A transition temperature, and relaxes toward zero with decreasing temperature in the Sm-A phase. The results are consistent with a surface

smectic electroclinic effect, albeit due to the large director tilt susceptibility close to T_{NA} (rather than the Sm-A – Sm-C transition temperature), where the Sm-A order parameter is small. I also demonstrated that by increasing the chiral dopant in this type of system, I increase the rotation of the oily streaks near T_{NA} monotonically. In addition, I showed preliminary data on the change in periodicity of oily streaks, where-by decreasing the temperature deeper into the Sm-A phase below T_{NA} I see an increase in the periodicity of the oily streaks that approaches a limiting value.

Similar to the oily streak rotation, I believe the increase in the average periodicity of the oily streaks – as the sample temperature is reduced below and close to T_{NA} – is due to the weak smectic order parameter Ψ. As the temperature is decreased, Ψ increases rapidly, which relates to the rapidly increased period of the oily streaks.

The controlled tilt of the oily streaks demonstrated in this work can be viewed as a potential new tool for the control of topological defect orientation, especially in light of the large number of topological defects know to be present in the oily streak structure above the thin transition region [48]. It could even allow for rotation of nanoparticle assemblies trapped in these defects [152, 153].

5.6 Future Work

In order to expand upon and add to this work, a number of avenues may be explored. The most apparent of these is continued research focusing on dependence of oily streak periodicity on temperature, relative to T_{NA}. While I did not delve deeply into this, it would be interesting to investigate what factors – other than temperature – have an effect on average period of the oily streaks.

Another interesting facet of the experiment which was not explored, was the effect of the liquid crystal film thickness on the rotation of the oily streaks. For the sake of consistency, and ease of measurement, this experiment maintained a $\sim$320 nm film.

There is some debate as to the actual structure of oily streaks [48], and there is evidence that there may be an evolution from one structure to another depending on the thickness of the film [149]. This transition is likely to occur as a shift in the liquid crystal alignment at the surface, from a planar alignment in the thinner ∼20 nm, to a homeotropic(like) alignment underneath the grain boundary / melted nematic region (region A in Fig. 5.1). If this is the case, then it is likely that the smectic surface ECE, which I purport to be the driving mechanism behind the rotation of the oily streaks, may be strengthened or weakened, in turn actually increasing or reducing the rotation of the streaks. Imaging oily streaks in these films is difficult – their width is near the optical limit –but it may be possible using a special microscope filter. This would allow visible light of the smallest wavelength for probing the structures; imaging only the shorter visible wavelengths would allow the study of smaller structures. Also, by switching the observation method, to that of a microscope such as a Near Field Scanning Optical Microscope (NSOM), it would be possible to image oily streaks on films down to the thickness of tens of nanometers.

While this rotation in itself is interesting, one most useful extensions of this project would be the addition of nanoparticles to the system. It has already been shown that when liquid crystals films that present with oily steaks are doped with nanoparticles, the nanoparticles line up and form chains in the grain boundaries of the oily streaks [152, 154]. By doping the chiral oily streaks with nanoparticles, and maintaining the temperature near the Sm-A to nematic transition temperature, it may be possible to obtain nanoparticle chains that are also rotated. In addition to this, by doping the chiral streaks with both the nanoparticles, and a polymerizing agent, such as 1,4-Bis[4-(3-acryloyloxypropyloxy)benzoyloxy) (RM25), it may also be possible to maintain these rotated nanoparticle chains even at room temperature.

Turning to the surface smectic electroclinic effect, there is more that could be done to probe this mechanism of the rotation. The papers published by Shao, *et al*

[147] and Xue and Clark [53] reference the need for a vanishingly weak smectic-C order parameter near the Sm-A – Sm-C transition. Due a weakening of the smectic order parameter near the near the nematic – Sm-A transition temperature, I see a similar effect. If a liquid crystal with both a nematic – Sm-A and Sm-A – Sm-C transition (such as 9004) were doped, it may be possible to see oily streaks rotate in the Sm-A phase near upon nearing both transition temperature. It is possible that the effect may not be identical due to changes in the oily streaks internal structure from multiple factors, but analogous behavior might be expected to occur.

Chapitre 6

Observations of a streak texture in a hybrid-aligned Smectic-C phase

6.1 Introduction

Owing to the expulsion of bend and twist distortions in a perfect smectic [12], periodic microstructures often occur in Sm-A films when the film is subjected to competing boundary conditions at the two surfaces. These can be two dimensional when there is a 2π azimuthal degeneracy of the boundary conditions [155, 156, 157, 158, 159], or one dimensional if this azimuthal degeneracy is broken for a planar-orienting substrate [61, 160, 161, 162, 163, 62]. For the latter case, the Sm-A oily streaks, smectic layers through most of the sample thickness remain parallel to the air interface (Fig. 6.1). Near the substrate however, the smectic layers tend to be normal to the substrate, such that the director lies along the easy axis direction. In order to satisfy these competing boundary conditions, there is a bending of the smectic layers into an array of flattened hemicylinders with a central defect. The result is a series of periodic stripes, *i.e.* the oily streaks, along a direction perpendicular to the substrate's easy axis. Because the director at the liquid crystal / substrate interface presents with

planar alignment along a specified easy axis, when imaged in an optical microscope under crossed polarizers the entire sample appears dark if the director is parallel to either polarizer. This oily streak texture has been researched extensively, and has been observed in liquid crystals such as octylcyanobiphenyl (8CB) on cleaved mica [164] and MoS_2 surfaces [61, 63, 60, 64], on polyvinyl alcohol (PVA) coated surfaces [48, 65], and also on polyimide coated surfaces [165, 148].

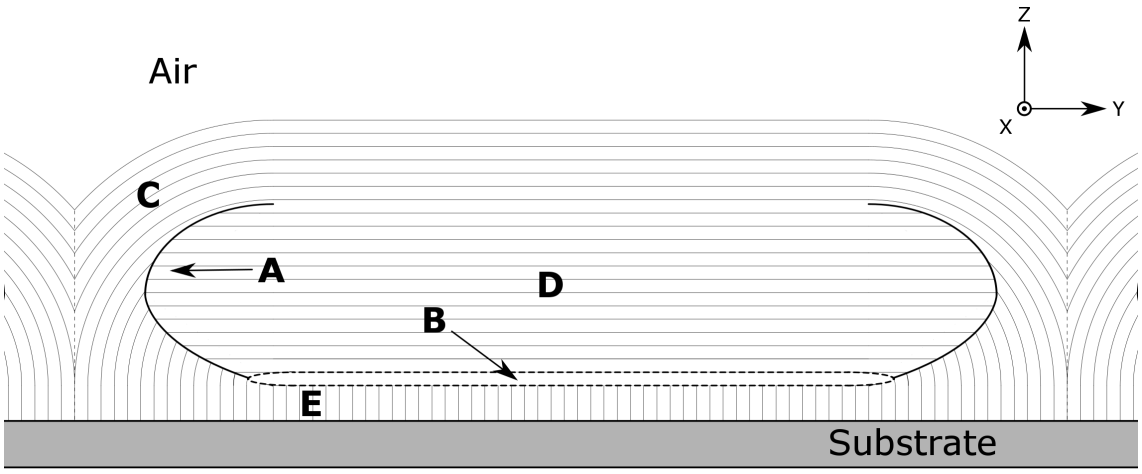

Figure 6.1: Easy axis along $\hat{y}$. Structure of Sm-A oily streaks where the thin lines represent smectic layers, **A** represents the rotating grain boundary (RGB), **B** a possibly melted nematic region, **C** the curvature walls, **D** the central homeotropic region, and **E** the planar transition region near the MoS_2 substrate.

Figure 6.1 presents a cartoon that is consistent with thin films (∼120–230 nm) of the liquid crystal octylcyanobiphenyl (8CB) on a PVA alignment layer. On this substrate, unlike the general representation Figs. 1.11 and for the polyimide alignment layers in Chapter 5, it is known that the planar transition layer covers the entire alignment layer [48]. On PVA, unlike the models in previous chapters, it is most likely that the 2D defect is a melted nematic and not a grain boundary [48]. Additionally, it is postulated that oily streaks on MoS_2 have a similar structure to those on PVA [61, 63, 64]. In Fig. 6.1 the region marked **A** is a rotating grain boundary (RGB), **B** a possibly melted nematic region, **C** the curvature walls, **D** the central homeotropic

region, and **E** the planar transition region near the substrate [48]. In this chapter, we refer to the region **B** as the central defect.

In the lower symmetry Sm-C phase, there are also reports of structures that consist of linear arrays. These undulations have been shown to occur in freely suspended films [166, 167, 168, 169] as well as in systems with competing alignment [170, 171]. In the systems with competing alignment a new competition emerges: The director not only must match the air and substrate boundary conditions, but it is no longer normal to the smectic layer. In this chapter, we present empirical evidence that this competition in the Sm-C phase results in a novel structure that appears in thin films of liquid crystal as a series of straight streaks. These steaks run perpendicular to oily streaks, and grow in a discontinuous and incremental manner. As these new streaks grow, they remove any optical evidence of the oily streaks, therefore we call them "soapy streaks"[1]. It is believed that as the temperature is decreased, the layered smectic structure of the system undergoes a rearrangement in the vicinity of the Sm-A to Sm-C phase transition. In the oily streaks, where the layers curve toward the substrates [62], an energy barrier must be overcome for the creation and propagation of the new structures. Even deeper into the Sm-C phase these straight stripes begin to undulate and become wavy, sometimes appearing to transform into an even more complicated series of sawtooth-like patterns. In this work-in-progress, we report on the appearance and characteristics of these novel structures, and speculate on their makeup and the mechanisms behind their formation in thin layers of smectic liquid crystal.

[1]The term "soapy streak" does not imply the existence of surfactants, and was chosen because they apparently cause the oily streaks to vanish optically

6.2 Experimental Methods

6.2.1 Sample Preparation

The liquid crystal 9OO4 (Fig. 6.2 , with phase sequence in the bulk :Iso – 87° – N – 73° – Sm-A – 62° – Sm-C – 50° – Sm-B – 35° – Cryst), was used for most experiments presented herein. Soapy streaks were created following procedures similar to that used to form oily streaks in open cells: a hybrid-aligned liquid crystal film with planar alignment at the substrate, and a free surface (air) at the top with a homeotropic alignment [48, 165, 148] (Chap. 5). Three different aligning substrates were used to obtain the planar surface alignment: crystalline MoS_2, rubbed PVA alignment layers, and rubbed polyimide alignment layers.

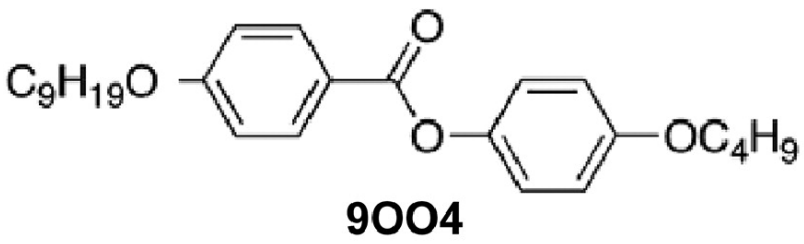

Figure 6.2: Molecular structure of the liquid crystal 9OO4.

The naturally occurring MoS_2 crystals originated in Queensland (Australia), and were supplied by The Ward company (New York). Fresh substrates – only a few microns thick and $\sim$ 1 cm^2 in area – were cleaved from the bulk crystals using Scotch^{TM} tape (similar to the scotch tape exfoliation method for fabricating graphene [172]). Because of the weak van der Waals interactions between the layers of sulfide atoms in MoS_2, it is relatively easy to separate individual layers in order to obtain large monocrystalline domains that are clean and are atomically smooth [173]. Due to the fragility of these MoS_2 substrates, they were mounted on microscope slides with either epoxy or double sided tape. Once stabilized, the fresh substrates were coated

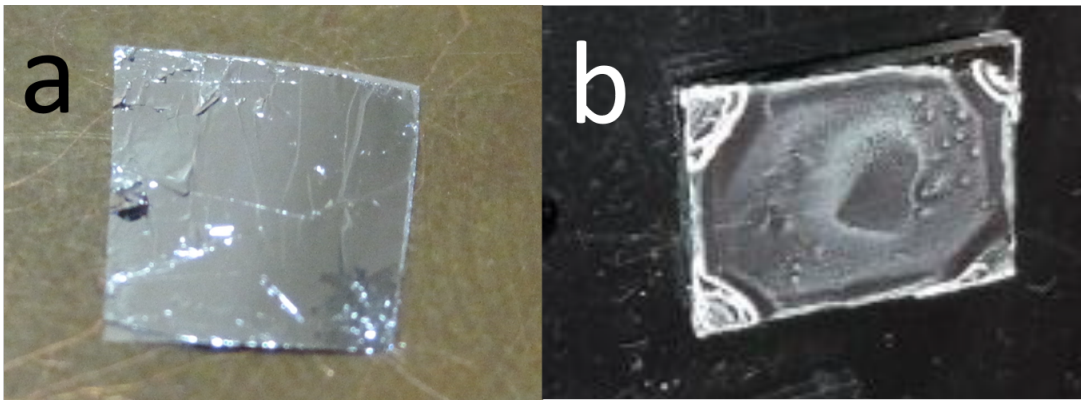

Figure 6.3: Images of a) LC distributed on fresh cleaved MoS_2 b) LC spin-coated on mirrored polyimide substrate.

with 9OO4. To coat, less than 1 mg of the liquid crystal 9OO4 was deposited on the MoS_2 substrate at a temperature above the liquid crystal's isotropic–nematic phase transition temperature, T_{NI}. The liquid crystal would transition, and over a time of 2 to 12 hours – a shorter period left thick films in small regions, while longer periods allowed for thin films over a majority of the substrate – it was left to wet the surface of the substrate. This resulted in a thin film, typically between 70 and 350 nm, over much of the MoS_2. The sample then was allowed to cool to room temperature, which corresponds to the bulk crystalline phase of 9OO4. An image of MoS_2 with a thin film of 9OO4 is shown in Fig. 6.3a.

In addition to MoS_2, experiments were performed using rubbed polyimide alignment layers and polyvinyl alcohol (PVA). Here a protected aluminum substrate (like those used in Chapter 5) was spin-coated with either the polyamic acid RN-1175 (Nissan Chemical Industries) or PVA. For certain experiments, glass slides were also coated. The RN1175 was baked and given an easy axis using the same methods as in prior chapters. For PVA substrates, a 0.5% by weight PVA in water was spin coated onto a substrate at 3000 rpm for 30 seconds. The PVA coated substrate then was baked at 120℃ for 120 minutes, allowed to cool, and then rubbed in the same manner as the RN1175 samples. Unlike the MoS_2 substrates, allowing the liquid crystal to

wet polyimide and PVA substrates was not a viable option. When liquid crystal was applied to the polyimide and PVA substrates and left in the isotropic phase, the liquid crystal tended to cohere and form droplets rather than a thin film. Therefore, in order to obtain a thin film, a solution of liquid crystal in solvent was spin coated onto the substrates. A 0.2 M solution of 9OO4 in toluene was prepared, and approximately 40 μL of this isotropic solution was deposited on a substrate at room temperature. The substrate was then spun for 30 second at rotational velocities between 1500 and 2500 rpm. This spin coating method evaporated the solvent, and left a relatively uniform layer of liquid crystal comparable to that obtained on MoS_2. In order to vary the film thicknesses with this method, the samples were spun at higher or lower velocities. While this is a feasible method for coating MoS_2 with liquid crystal, there was the possibility of a small amount of solvent being absorbed, which may have some unforeseen effect.

The thickness of the liquid crystal films for all substrates was estimated by their interference colors using polarized reflection microscopy [148]. Referring to a Newton tint table [148], we were able to estimate the local thickness to within $\pm$15 nm for the thickness range 70 to 350 nm.

6.2.2 Imaging

Using an Instec mk1000 temperature controller with a compatible 402 heat stage, the samples were brought into the isotropic phase and then cooled to the nematic phase to facilitate orientational alignment. The samples then were slowly cooled in intervals of 0.1℃ from the nematic phase into the Sm-A phase, and eventually into the Sm-C phase. The temperature was allowed to stabilize for each temperature step, after which polarized micrographs were taken at (again for each temperature step) using a high resolution camera (23 megapixels) and a Olympus BX60 polarizing microscope in reflection mode between crossed polarizers. For maximum contrast, the samples

were usually positioned with their easy axes set at $\sim 45^{\circ}$ with respect to the polarizer direction. These images were taken the same day as the samples were fabricated to minimize any possible degradation of the samples – or absorption of LC into the MoS_2 – with time.

6.3 Results and Discussion

6.3.1 MoS_2

Thin film Sm-A oily streaks [61, 62, 164] were observed on cooling the liquid crystal into the Sm-A phase, as shown on MoS_2 in Fig. 6.4a. Cooling further toward the Sm-A – Sm-C transition, the formation of fan shaped focal conic domains was observed in regions where there previously had been oily streaks. These domains appeared initially at the thickest regions ($\sim$350 nm) of the liquid crystal films, most often near boundaries or imperfections such as the "wide stripes" (mentioned in the previous chapter). The narrow end of these defects regularly pointed along the easy axis, from the thicker to the thinner regions. As the temperature was reduced, these focal conics continued to form in increasingly thinner regions of film, becoming progressively smaller in size (Fig. 6.4a and b).

In regions of thin liquid crystal film, as the temperature was further decreased, the fan defects evolved into regular arrays of streaks *parallel* to the easy axis. Fig. 6.4b shows the initial formation of these new structures, which we refer as "soapy streaks", as their formation apparently eliminates optical evidence of the oily streaks. With decreasing temperature, the soapy streaks were found to grow discontinuously into the regions where oily streaks were present in the Sm-A phase. As the temperature was lowered deeper into the film's Sm-C phase, the soapy streaks would suddenly – that is, in time not resolvable by a 30 frames per second camera – extend to the dark region of the next oily streak, growing in an incremental fashion, as is apparent in the inset of

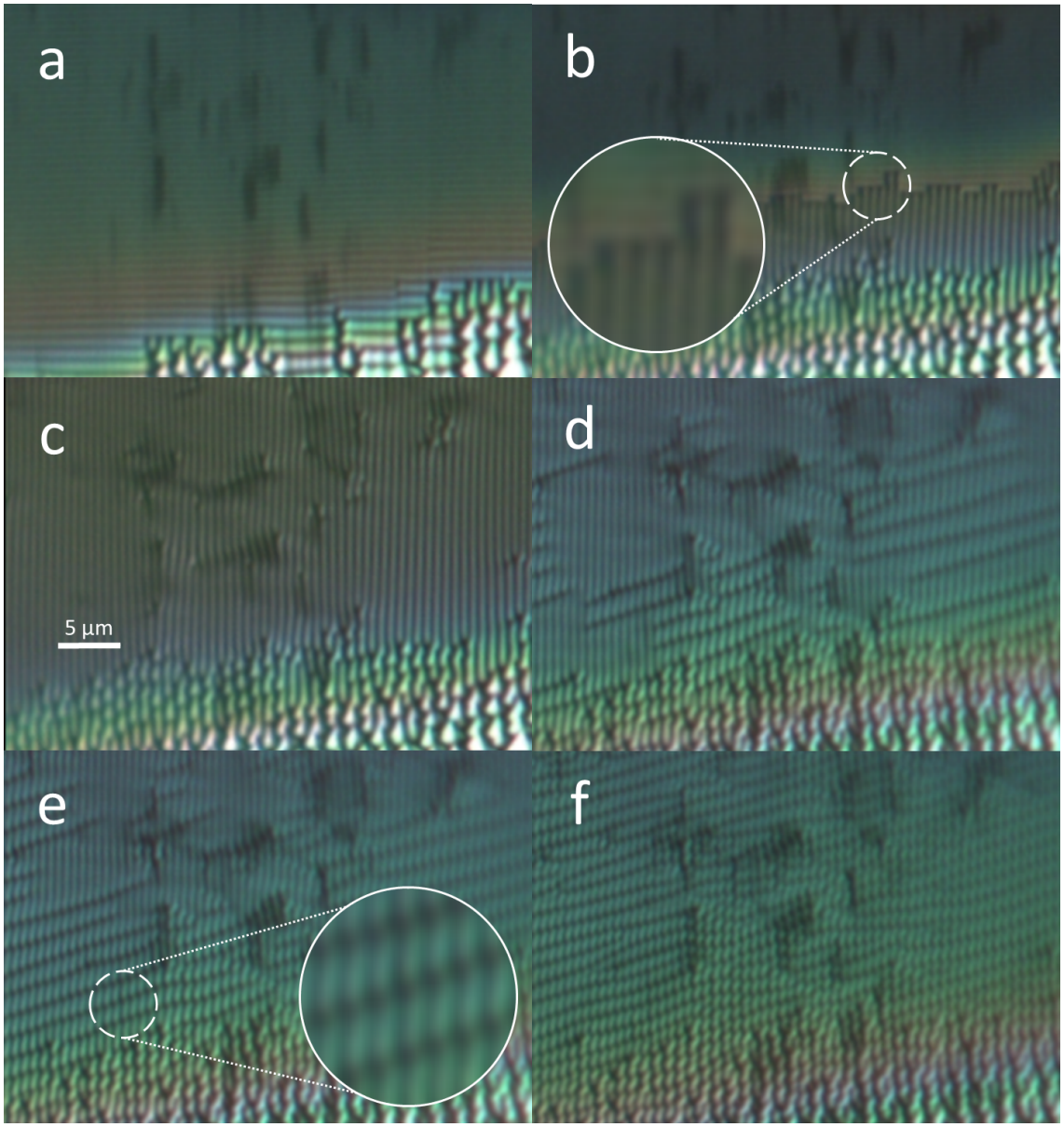

Figure 6.4: Photomicrographs of 9OO4 thin films presenting with soapy streaks on MoS_2 at a) 71.5℃ b) 71.3℃ c) 71.1℃d) 65.3℃ e) 65.0℃ and f) 63.4℃. Inset in (b) show the discrete growth of the soapy streaks, and the inset in (e) shows a magnified view of soapy streak undulations. The scale bar in (c) is oriented perpendicular to the easy axis.

Fig. 6.4b. More specifically, as the soapy streaks formed, their progress always began and terminated in the darkest region of the oily streaks. In oily streaks these darker regions are believed to be characterized by a mostly vertical director orientation [62], except near the liquid crystal / alignment layer interface. This discrete growth of soapy streaks occurred in a reversible and quantized manner, and the growth length corresponded exactly to the width of the oily streaks through which they propagated. While groups of adjacent soapy streaks generally progressed as a uniform front, they were also found to progress individually, with one or more streaks outpacing the group by multiple oily streak widths. This was more apparent in regions with a gradient in the film thickness. As the soapy streaks tended to form in the slightly thicker regions first, and spread to thinner regions, they also tended to advance furthest (*i.e.* ahead of the pack) in the thicker regions as well. Even if the layer of liquid crystal was too thin to permit optical observation of the oily streaks – the oily streaks are evident down to a film thickness on order of only tens of nanometers [148] – it still was possible to observe the presence of the soapy streaks.

During this transition from oily streaks to soapy streaks, the liquid crystal film appeared to change. In regions where the soapy streaks were most likely to form (such as near the wide stripes) the film became thicker, seemingly drawing liquid crystal away from other areas. This coarsening was evidenced by the change in the spatial period of the oily streaks, and a corresponding change in color. These alterations made it especially difficult to compare film thickness from image to image. Additionally, the appearance of the soapy streaks was not uniform. In areas where the streaks were most consistent they appeared as spatially-periodic linear arrays similar to oily streaks, but with slightly greater contrast between their light and dark regions. Nevertheless, the soapy streaks sometimes could be found to split into two distinct streaks, or two separate streaks could be seen to spread with the formation of a third between them; this sort of behavior also occurs in oily streaks as shown in prior work [62, 165]. Near

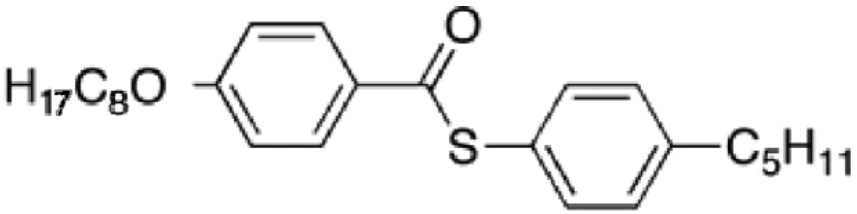

Figure 6.5: Molecular structure of the liquid crystal $\bar{8}$S5.

the thickest regions of liquid crystal film, where there was a crossover from fan-like defect to soapy streak, or from wide stripe to soapy streak, the streaks tended to be less regular. Here the soapy streaks would have non-periodic undulations, and form branches, as described above.

With a further decrease in temperature in the Sm-C phase, the field of view became completely covered with soapy streaks (Fig. 6.4c). The only evidence of pretransitional structures was the presence of the wide stripes, which served as the nucleation points for soapy streaks. Upon continued lowering of the temperate, the soapy streaks began to undulate in the plane with a periodicity larger than the width of the streaks themselves, (shown in Figs. 6.4d, e, and f). The waviness of adjacent streaks appeared to be correlated to one another as nearby streaks tended to undulate together, forming a texture of repeating waves with slightly different phases. On further cooling, the size of these wavy areas increased and the period of the undulations shortened. As the amplitude of the undulations became more pronounced, the waviness eventually transitioned into a saw-tooth pattern (figs. 6.4e and f). This pattern would spread through the entire sample, until it was observable in every soapy streak. Lowering the temperature further into the Sm-C only showed slight increases in the periodicity of this undulation.

In addition to 9OO4, it was possible to reproduce the aforementioned results with other liquid crystals. Most notably, we found similar behavior for the liquid crystal 4-n-pentylphenylthiol-4'-n-octyloxybenzoate ($\bar{8}$S5, phase sequence Iso - 86° – N – 64° – Sm-A – 56° - Sm-C - 30.6° – Sm-J – 14.6° – Cryst) for both oily and soapy streaks,

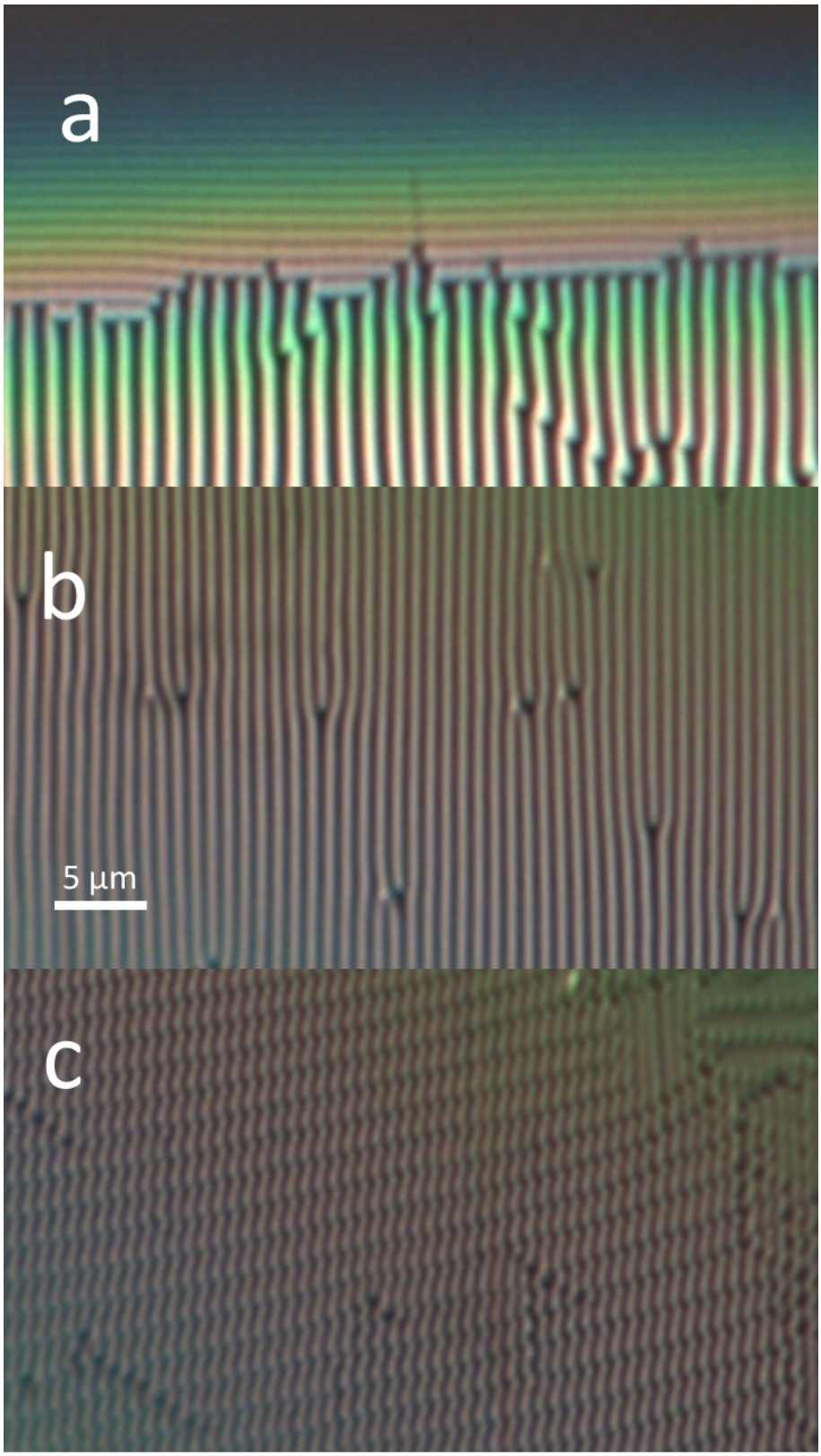

Figure 6.6: Photomicrographs of $\bar{8}$S5 soapy streaks on MoS_2 at a) 63.7℃ b) 60.7℃ and c) 55.3℃. The scale bar is oriented perpendicular to the easy axis.

as shown in Fig. 6.6. Like 9OO4, $\bar{8}$S5 has a Sm-A – Sm-C phase transition. This is unlike the observations of only oily streaks in the Sm-A phase using the liquid crystal octylcyanobiphenyl (8CB), which does not exhibit a Sm-C phase. For these reasons we believe that the soapy streaks are associated with a transition from the Sm-A to the Sm-C phase. Even though Figs. 6.4 and 6.6 occur above the Sm-A – Sm-C transition temperature *in bulk*, it is well known that the temperature of many liquid crystal phase transitions can shift upwards in tightly confined regions [174, 175, 176, 177]; we believe this to be the case here. One difference between the $\bar{8}$S5 and 9OO4 systems should be noted. For larger film thicknesses (greater than 350 nm), soapy streaks formed in thin films of 9OO4 no longer presented with soapy streaks, but transitioned directly to focal conics. This is not the case for $\bar{8}$S5, as it appeared to tolerate much thicker films of at least up to 450 nm and presented with soapy streaks of far larger periods and variations in contrast between light and dark regions.

6.3.2 Contrast Measurements

To study the evolution of reflected light intensity in the bright and dark regions of the perpendicular streaks, a sample that presented with both oily streaks and soapy streaks was imaged. Photos were taken of the streaks oriented at various angles with respect to the polarizer and crossed analyzer in reflection mode, and were imported into the photo analysis software Image-J®. Intensity profiles of the images were taken perpendicular to the same series of soapy streaks (at the same location) for each angle, and plotted *vs.* their position; the plots are shown in Fig.6.7. From the data an apparent sinusoid-like intensity dependence of contrast on position can be seen, but this is not the most interesting feature. It should be noted that while the oily streaks always go uniformly dark when they are parallel to either crossed polarizer, the soapy streaks remain visible no matter the orientation of the easy axis

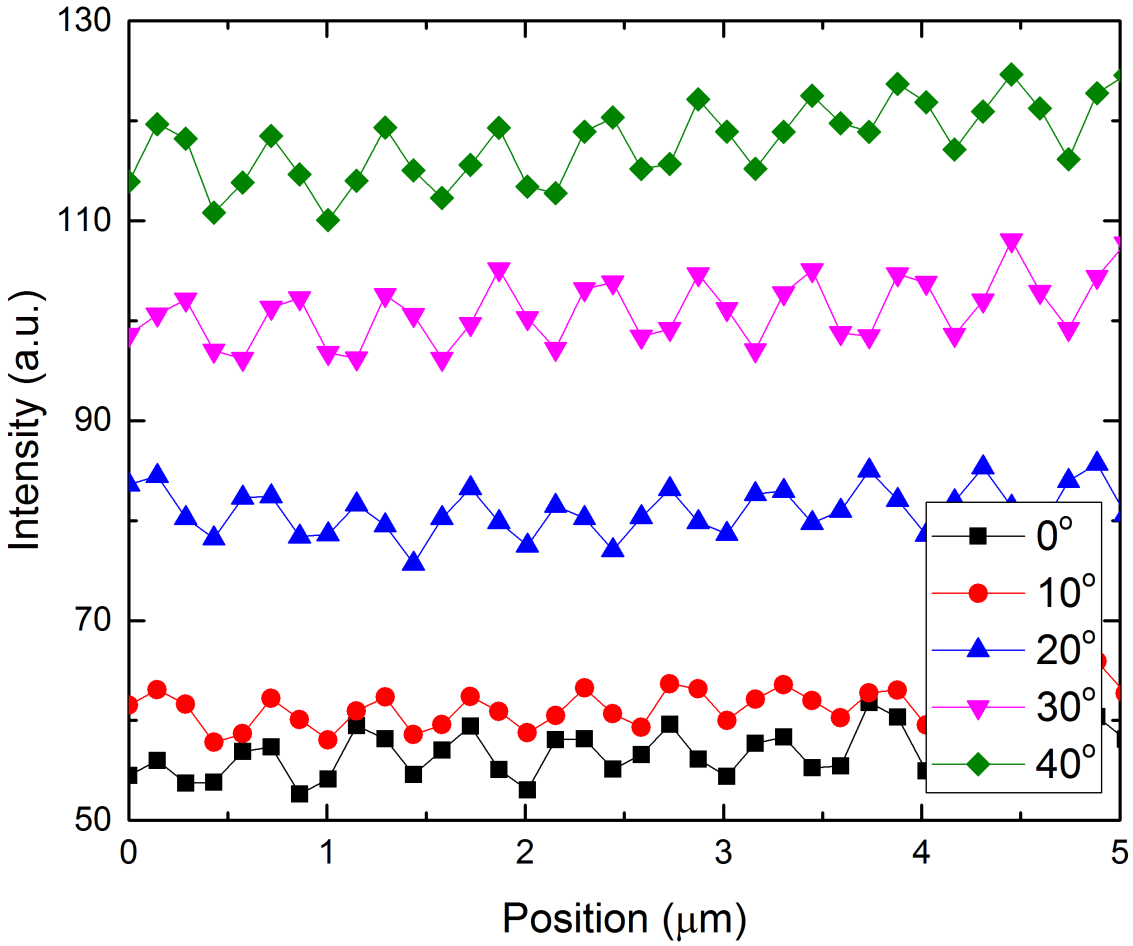

Figure 6.7: Intensity *vs.* position plot for a series of soapy streaks (9OO4 on MoS_2) at 10° intervals with respect to the crossed polarizers. Lines are meant as a guide to the eye.

with respect to the polarizers, even at 0°.

When oily streaks are imaged between crossed polarizers, it is the change from homeotropic alignment in the dark regions to a near planar alignment in the light regions that give their variations in contrast. Because the average director always lies in a plane perpendicular to the oily streaks, oily streaks present with a maximum of light extinction when the streaks are oriented parallel to either polarizer. Since this is not the case for the soapy streaks, another form of director variation having an alignment outside of this homeotropic to planar tilt plane must be the cause. Since it is believed the soapy streaks are formed in the Sm-C phase, the director variation might be attributed to the tilt of the liquid crystal molecules with respect their smectic layers. It has been shown by the Lemieux group, formerly at Queen's University in Ontario, that 9OO4 possesses a $\sim$3° polar tilt with respect to the smectic layer normal in the Sm-C phase. Taking this into account, it can be assumed that this tilt is root of contrast I see. Nevertheless, I note that the small spatial period of the soapy streaks could have resulted in diffraction effects, confounding the interpretation of the intensity vs. position results, and distorting the information about the director field distribution.

6.3.3 Polyimide and PVA

Similar to oily streaks, soapy streaks were found to form on a variety of substrates, such as PVA, RN1175, and MoS_2. However, there were some noticeable differences among the soapy streaks as they formed on these different substrates. When 9OO4 was deposited onto MoS_2, the streaks and patterns that formed tended to be relatively uniform, with regimented linear arrays formed at higher temperatures and uniform undulations and sawtooth patterns formed at lower temperatures. While some imperfections were present due to variations in the MoS_2 crystal structure and flakes, the streaks were nearly always straight and unbroken. In contrast, soapy streaks that

formed on rubbed polyimide were not always straight, and regularly had undulations directly after the transition, as shown in Figs. 6.8a and b.

The difference between the soapy streaks on different substrates was especially noticeable once the undulating patterns had formed. On MoS_2, the undulations had a uniform periodicity, giving the wavy texture a quasi-long range order (Figs. 6.4e and f). On RN-1175 – as well as on PVA – the undulations of a given soapy streak showed far less correlation with its neighbors; Fig. 6.8c shows an example of this. Additionally, the saw-tooth patterns that were present on the MoS_2 substrate at lower temperatures were relatively nonexistent on the polyimide. These differences can likely be explained by the nature of the alignment layers. While MoS_2 aligns on the atomic level and is atomically flat, polyimide alignment layers are relatively rough and rely on external rubbing to create an easy axis. This external rubbing gives a macroscopically uniform easy axis, on orders comparable to the period of oily and soapy streaks there can be some variation. The roughness and microscopic variations could very likely contribute to the formation of the less ordered soapy streaks on polyimide and soapy streaks.

6.3.4 Periodicity Measurements

While it was relatively difficult to obtain a uniform liquid crystal film on MoS_2 – and therefore in a uniform periodicity for oily and soapy streaks – the spin coating method deposits liquid crystal films of very uniform thickness. This uniform film allowed for comparisons to be made between the periodicity of oily and soapy streaks. By maintaining the liquid crystal 9OO4 at a constant temperature that presented with oily streaks (73.0℃) and soapy streaks (68.5℃), and measuring their periods in areas of comparable thickness, I was able to observe a strong relationship between the periods of the two types of streak. As shown in Fig. 6.9, both streaks show a positive linear relationship between their period and the thickness of the liquid crystal film.

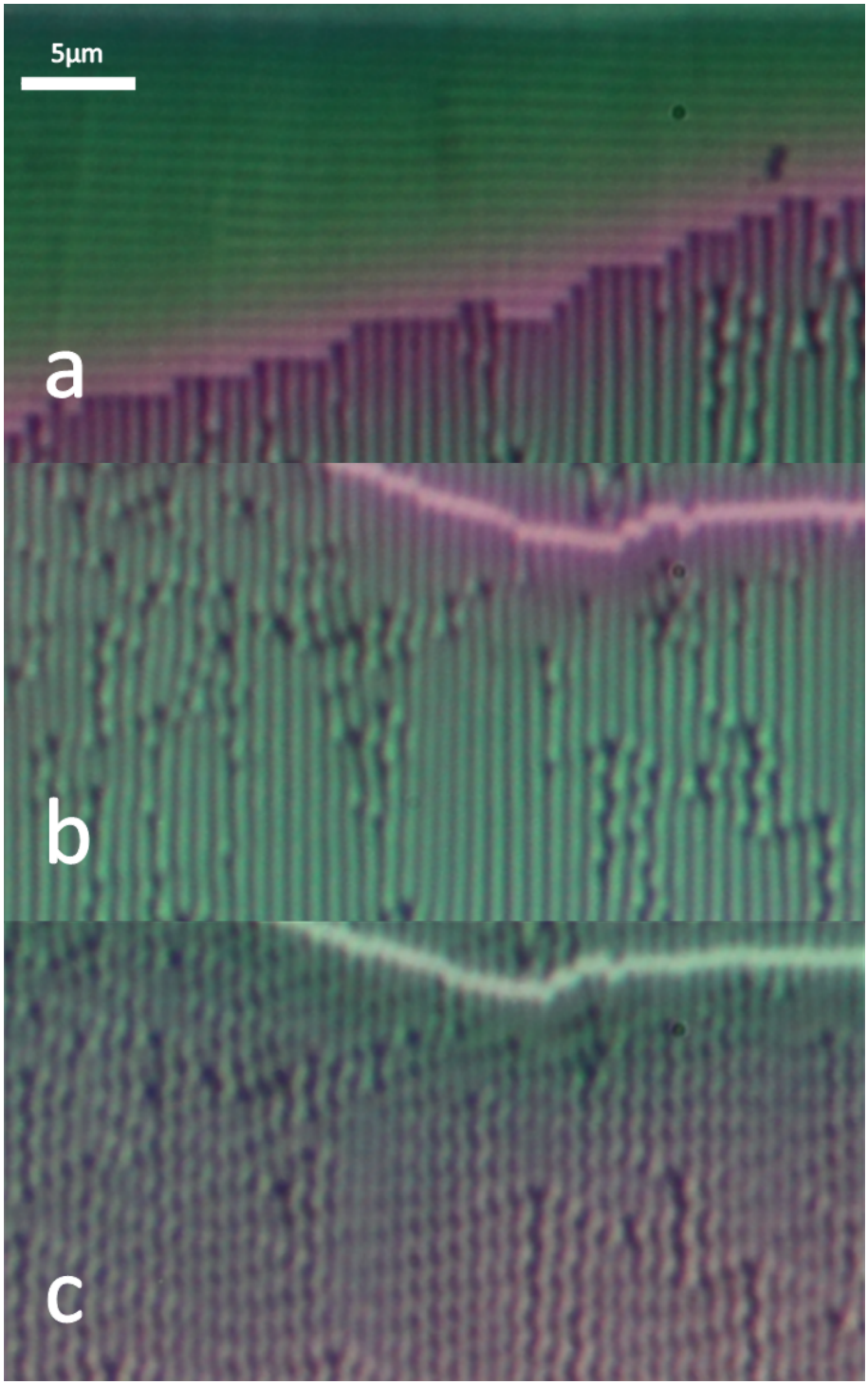

Figure 6.8: Photomicrographs of soapy streaks that formed from 9OO4 on RN1175 at a) 71.1℃ b) 66.9℃ c) 63.8℃. All images were taken at the same location. The scale bar is oriented perpendicular to the easy axis.

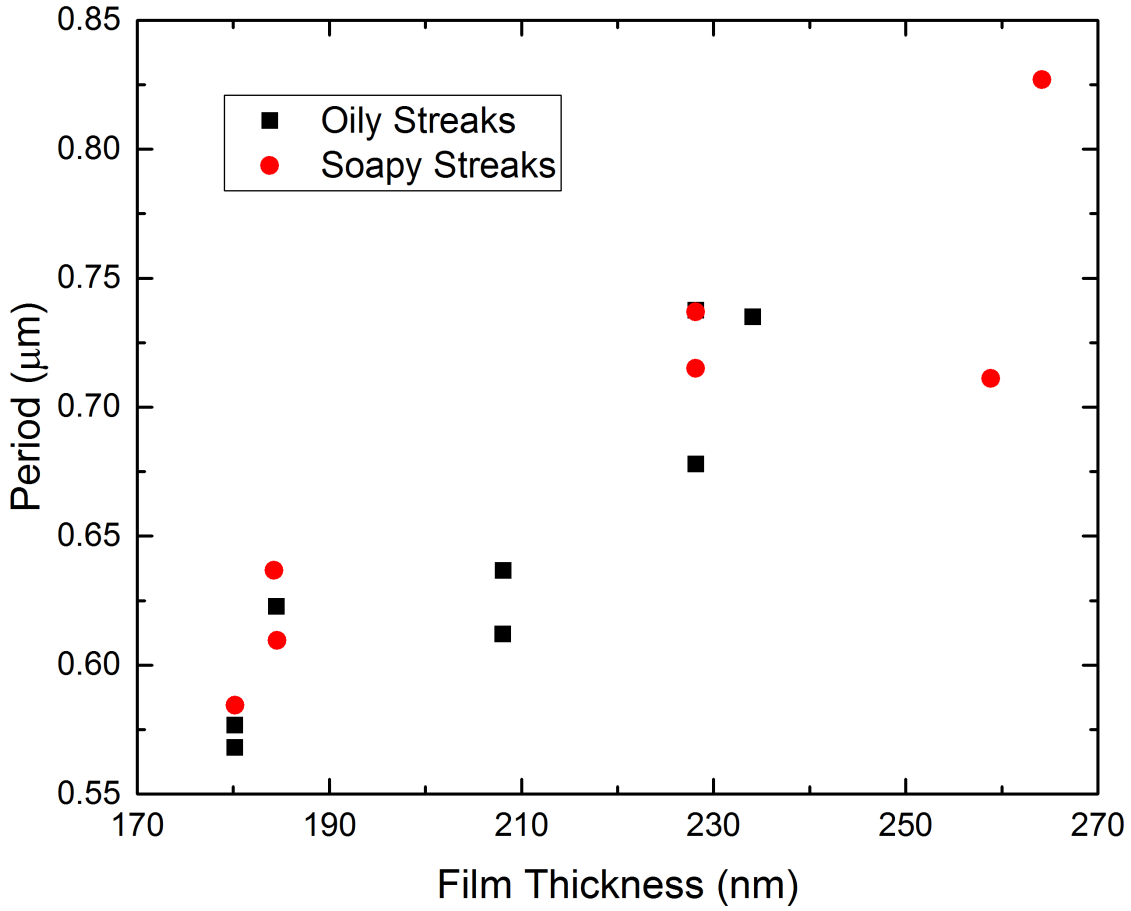

Figure 6.9: Comparison of oily and soapy streak periods. Thin film interference colors using polarized reflection microscopy were used to determine the film thicknesses [148].

Additionally, there appears to be a strong relationship between the period of oily and soapy streaks. In fact, for areas of comparable thickness, the periods of both streaks were nearly the same. This correlation may suggest a relationship between the structure of oily and soapy streaks.

6.3.5 X-ray Measurements

Besides optical experiments, transmission small angle x-ray scattering (TSAXS) measurements were performed by the Lacaze group[2], the results of which are summarized here. Samples of thin 9OO4 films on polyimide coated glass slides were prepared, and confirmed to present with both oily streaks in the Sm-A phase as well as soapy streaks in the Sm-C phase by optical microscopy. Experiments were performed in the ESRF(Grenoble-France) synchrotron on the D2AM beamline. For this set of measurements the beam energy was set to 20 keV and had an incident area of 300 x 300 μm^2. The resulting integrated intensity due to scattering is proportional to the number of layers oriented perpendicular to the incident beam. The orientation of the layers is followed by rotating the sample with respect to the incident beam, and measuring the evolution of the intensity. For this series of experiments, data were taken between the angles of $\alpha = -20^\circ$ and $\alpha = 80^\circ$ in the plane perpendicular to the oily streaks. The resulting data is shown for the Sm-A and Sm-C phases in Figs. 6.10a and b respectively.

Starting with Figs. 6.10a I observe a typical scattering intensity *vs.* incidence angle plot that has been shown in previous works [48, 60] and that is systematically similar for 8CB and 9OO4. The 10° shift of the peak from $\alpha = 0^\circ$ in the Sm-A phase is attributed to a molecular pretilt – and therefore a tilt in the smectic layers – at the polyimide substrate. Moving on to 6.10b, I notice some differences. Most notably, the peak for the Sm-C data set is now centered around 0° rather than 10°. The change

[2]Iryna Gryn, Laurent Pelliser, Bruno Zappone, Michel Goldman, Michel Alba, and Emmanuelle Lacaze.

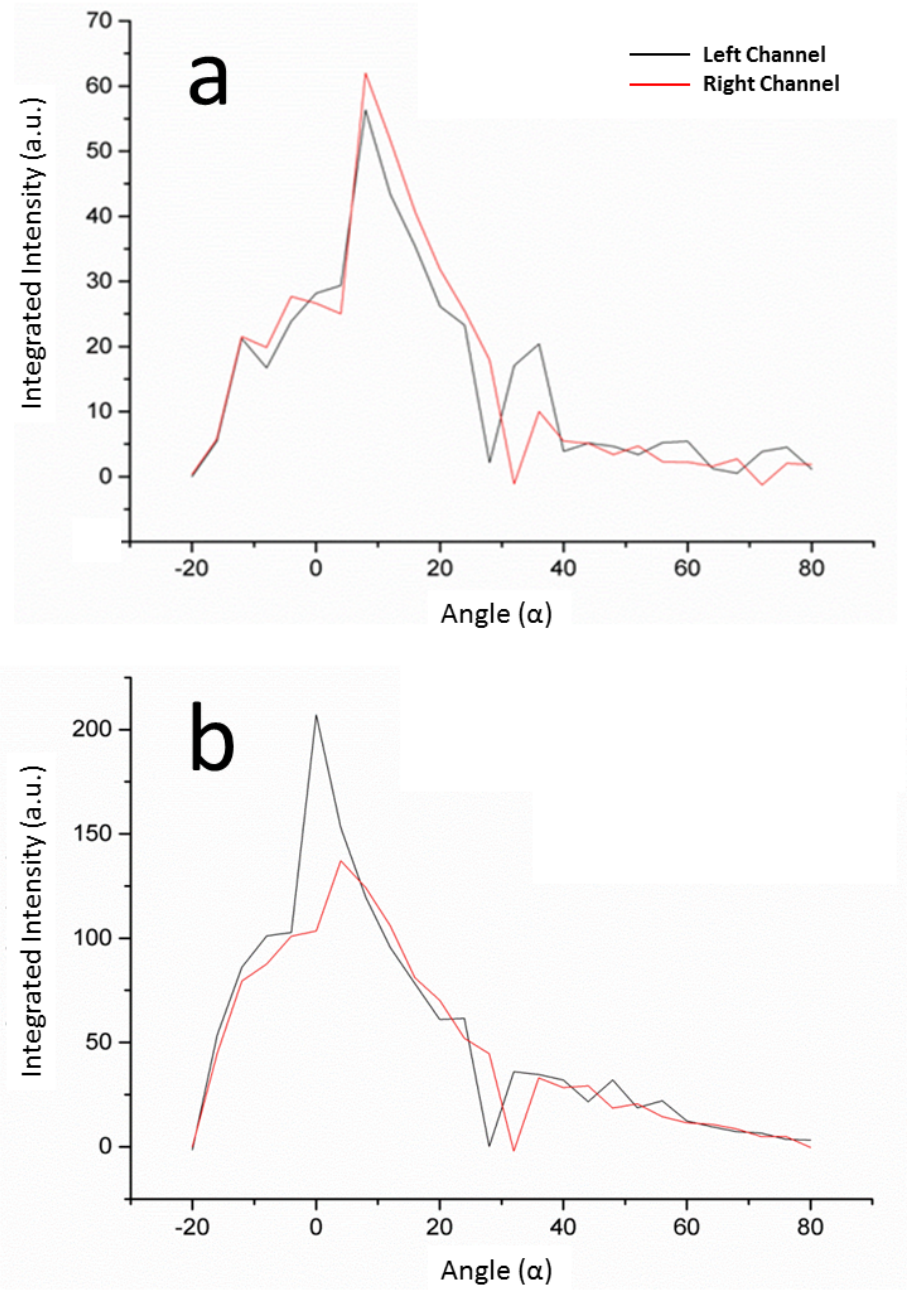

Figure 6.10: X-ray scattering data showing the integrated scattering intensity *vs.* smectic layer angular distribution for a) Sm-A oily streaks in a 100 - 130 nm film and b) Sm-C soapy streaks in a 160 - 180 nm film. Notice the 10° offset in the Sm-A, and the broadening of the angular distribution in the Sm-C.

likely indicates that a transition from one phase to another has occurred. Other than this, at small angles of α the data for the Sm-A and Sm-C phases are quite similar. However, at somewhat larger angles, the data begin to differ. At these larger angles, the Sm-A phase presents with smaller intensities (relative to the maximum value of the peak), which suggest that a large proportion of the smectic layers are parallel – or nearly parallel – to the substrate. This is not the case in the Sm-C phase, where it is apparent that at larger angles the relative intensities are greater. This change in the angular distribution of the layers suggests that there has been a readjustment of the layer orientations. This broadening and more gradual decline of intensity implies that a greater proportion of the layers are no longer planar, and that there is an increase in the density of the curvature walls, as well as a decrease in size (or elimination) of the central defects. This also suggests that the melted nematic (Fig. 6.1 region **B**) between smectic layer orientations is smaller, or simply has transitioned to become a grain boundary.

Due to the nature of the experimental setup used for these measurements, some concessions had to be made. It was necessary to examine different locations on the liquid crystal film in order to probe both the Sm-A and Sm-C phases. Also, due to variations in thickness from area to area, it was not possible to compare the absolute intensities from one data set to another. Additionally, the range of angles ($\alpha = -20^\circ$ and $\alpha = 80^\circ$) does not probe the full array of smectic layer orientations.

6.4 A Basic Model of the Structure

While a great deal of data has been compiled on the nature and appearance of these soapy streaks, a complete description of their structure has remained elusive. Unlike 8CB, which presents with oily streaks in a room temperature Sm-A phase, the liquid crystals studied herein have phase sequences that necessitate the use of thermally

stable insulated heating elements to observe the desired phases. Methods that would yield valuable information about the structure and makeup of the streaks – such as ellipsometry and atomic force microscopy – are relatively difficult to utilize with these restrictions. Many devices cannot handle the high temperatures required by soapy streaks, are not sufficiently thermally stable, or cannot accept the bulk of a heating apparatus. While it is still possible to obtain high resolution photomicrographs and perform general x-ray scattering experiments, these do not yield all of information necessary to develop a complete model. Nevertheless, it is possible to describe a basic model with what data that have been obtained to date. Here I present one possible scenario for the development of the soapy streaks based on the data presented in this chapter.

To begin building a model for soapy streaks, I return to the x-ray results presented in Sec. 6.3.5. For reference, the cartoon of a thin film *oily* streak's cross section with a melted nematic region (Fig. 6.1 item **B**) above the planar transition region (Fig. 6.1 region **E**) in the yz-plane is shown in Fig. 6.11a. This model is based on microscopy, ellipsometry, and x-ray data of 8CB on PVA and MoS_2 [48, 61, 64, 48] and is consistent with the boundary conditions at the two interfaces. While the full extent of the planar alignment just above the substrate is unknown – it depends on the liquid crystal material parameters and the nature of the alignment layer on the substrate – this model agrees with the x-ray data in Fig. 6.10a. The x-ray data indicates a large proportion of smectic layers aligned parallel to the interfaces, and a relatively small proportion of layers that show the presence of curvature walls. While I noted a number of differences between the two sets of x-ray data corresponding to the oily and soapy streaks, they were actually quite similar. This suggests that, rather than transitioning into a completely new structure, the transition from oily to soapy streaks is associated with a modification of the pre-existing structure. This modification is evidenced by the proportional increase in curvature walls, and the

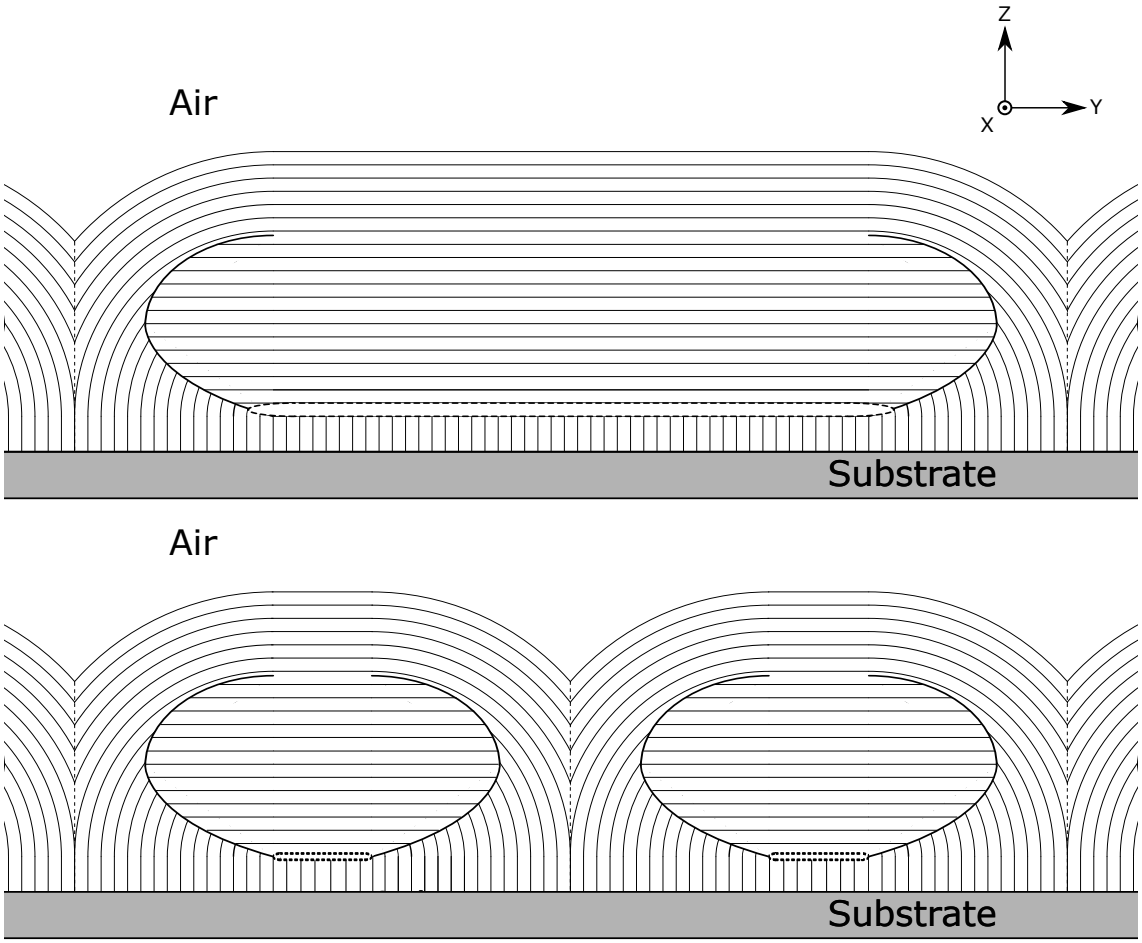

Figure 6.11: Easy axis along ŷ. a) Structure of Sm-A oily streaks and b) a proposed structure of Sm-C soapy streaks, where the periodicity of the oily streaks (running into the page) is greatly reduced while concomitantly soapy streaks (parallel to the y-axis) appear due to Sm-C director tilt and dominate the optical image.

increase in the planar alignment. As the temperature is reduced into the Sm-C phase, the melted nematic boundaries between different smectic layer alignments would likely become more energetically costly. This increased cost would be due to the large temperature difference between the nematic and Sm-C phases. In turn, the curvature walls between the hemicylindrical regions may become less expensive due to the Sm-C tilt allowing for a more favorable rotation. In order to obtain a new energetic equilibrium, the oily streaks could then rearrange in such a way as to decrease their spatial periods. A representation of this is shown if Fig. 6.11b, where the period of the oily streak is shown to have halved (though it may have tripled or more), thereby increasing the amount of curvature walls and decreasing the area of the melted nematic region. This would also be associated with the reduction of homeotropic alignment at the air / liquid crystal interface.

While this is only one scenario capable of explaining the x-ray scattering results associated with the oily streak to soapy streak transition, it further explains a number of the transition's other characteristic properties. First, it gives a reasonable explanation as to why the oily streaks are no longer visible once soapy streaks have formed. If there were no modification of the oily streak structure upon the transition to soapy streaks, then I would expect to see periodic changes in contrast *along* the soapy streaks and parallel to the easy axis. Rather, since the length scale of the oily streaks is already near the visible diffraction limit, a further decrease in their spatial period would render them too small for observation *via* classical optical microscopy. Second, this picture helps to explain the discrete formation of soapy streaks as they progress from the homeotropic region of one oily streak to the next. Because soapy streaks don't form in a continuous manner, it can be assumed that there is an energy barrier that must be overcome in order to progress from one oily streak to the next. This energy barrier can be associated with the grain boundaries between individual oily streaks and the rotating grain boundaries around the central defect. Through

reorientation of the layer structure, it allows for the soapy streaks to progress. In fact, this method of formation itself suggests a change in layer structure – even if it is a small readjustment – and is consistent with the discontinuous progression of the streaks.

In addition to the restructuring of the smectic layers, the optical appearance of the soapy streaks needs to be accounted for, *i.e*, why the soapy streaks appear as linear arrays of light and dark lines *perpendicular* to oily streaks. On cooling from the Sm-A phase into the Sm-C phase it is known from x-ray data that the smectic layer normal near the substrate remains in the plane perpendicular to the oily streaks and the easy axis, but from optical microscopy it is known the liquid crystal director tilts with respect to the smectic layer normal. With smectic layer orientation remaining in the same plane, it can be concluded that it is the molecules that tilt with respect to the easy axis $\hat{e}$. If this tilt were uniform in a single direction, or randomly oriented with respect to $\hat{e}$, there would be uniform contrast throughout the system and no optical evidence of any streaks. From Fig. 6.7, it is known that there is a periodic change in contrast perpendicular to the easy axis, and that it is sinusoid-like. This leads to the conclusion that the molecular tilt with respect to the smectic layers at the liquid crystal / substrate interface – and likely throughout the entire thickness of the film – is rotating. To account for this, I propose a periodic azimuthal rotation of the director at the polar angle θ (the molecular tilt with respect to the smectic layer normal in the Sm-C phase) around $\hat{e}$, parallel to a modified oily streak. While this scenario is reasonable, it isn't the entire picture. Because the tilt needs to stay relatively uniform in the smectic layers at both the substrate and air interfaces, somewhere in the hemicylinder there must be a director mismatch in or between layers. Fig. 6.12 gives a series of schematic drawings for one possible director configuration after the onset of the soapy streaks. In Fig. 6.12, the dotted lines represent individual smectic layers, the bars represent individual molecules in their respective layers, and

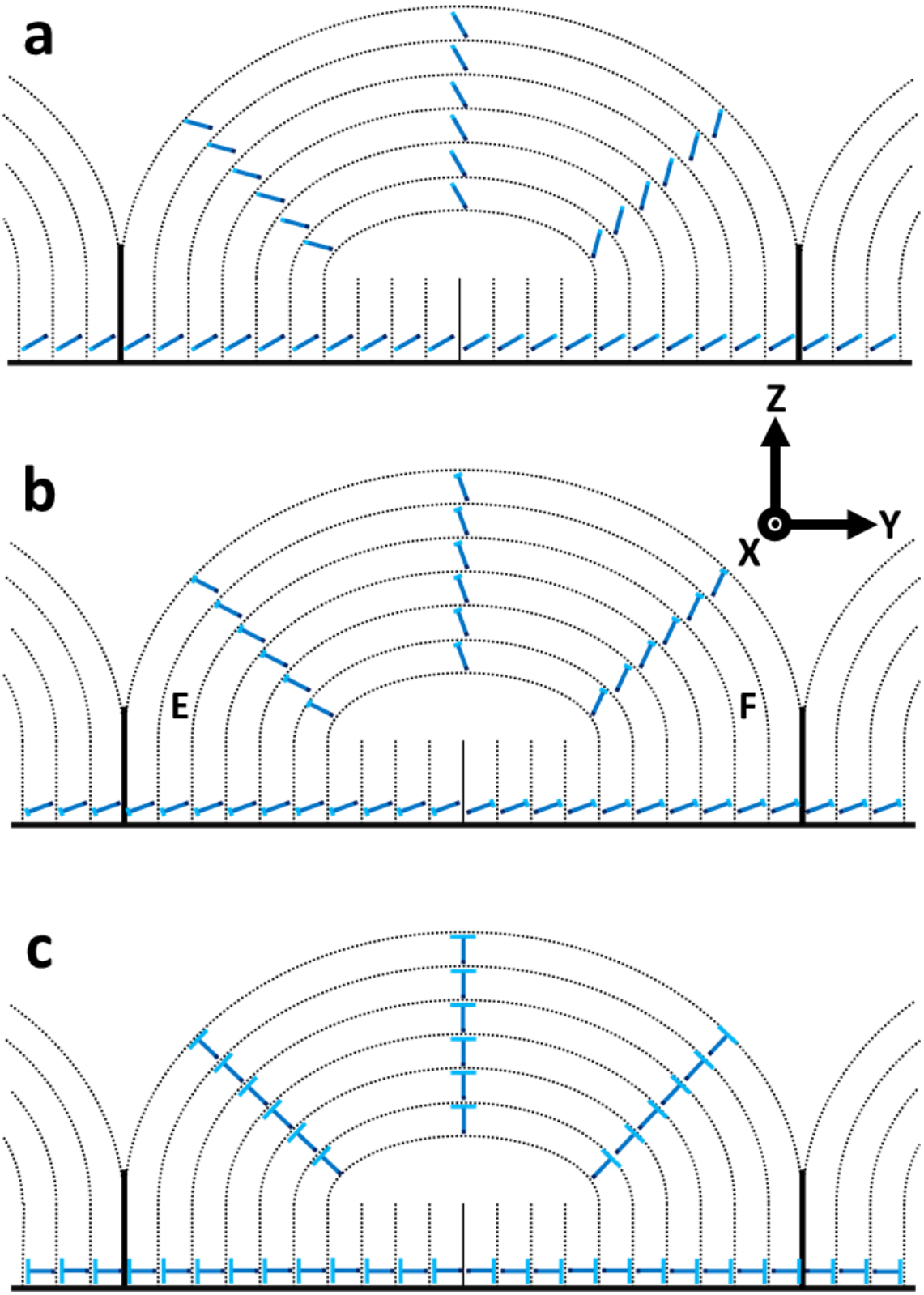

Figure 6.12: Model of molecular liquid crystal rotation through an oily streak for three consecutive locations. The bars represents the molecules, while the crossbar represent the degree of molecular tilt out of the plane. Fig. 6.13 presents the same model, but in the xy-plane. Each successive figure corresponds to a translation along the x-axis, with (a) representing x_0.

the crossbars represent the magnitude of tilt out of the plane, which is proportional to the width of the cross. In Fig. 6.12a, a uniform tilt in the in the yz-plane at position x_0 cna be seen. Relative to the substrate, the molecules are tilted by the polar angle θ, and relative to the yz-plane there is no tilt. If I translate a distance Δx along a streak, the tilt now has a component out of the plane as shown in Fig. 6.12b. While the polar tilt θ and the azimuthal orientation ϕ throughout the smectic layers are maintained from a point on one side of a streak to another on the opposite side (point **E** to point **F** on Fig. 6.12b), the out-of-plane components are rotated in a sense opposite to each other with respect to the z-axis. If I continue to translate along the x-axis perpendicular to the soapy streak, a location can be found where the molecular orientation at the substrate is completely planar. Fig. 6.12c shows that while the tilt in the yz-plane is still constant throughout the streak, at the substrate there is a large director mismatch equal to 2θ due to the mismatched tilt with respect to the yz-plane. For this model, I placed the mismatch in the center of a streak near the substrate (the solid line near the center). There, the region between mismatched layers – this can be thought of as a ribbon of disclination along the x-axis – would be at a minimum energy. This is because the region of oily streaks that presents with vertically aligned smectic layers (the planar transition region) is significantly thinner than the region with horizontal layer alignment (the central defect and the smectic layers near the air interface) [48, 60].

Fig. 6.13 shows the same molecular rotation as Fig.6.12, *but in the xy-plane at the liquid crystal substrate interface.* (Fig. 6.14 is included to aid the reader in comparing Figs. 6.12 and 6.13 by placing them side by side.) In this example, it is easy to see conic-like molecular rotation in individual layers. At the substrate / liquid crystal interface, in the middle of the modified oily streaks, the mismatch in the rotation is apparent. The areas that correspond to the slices in the yz-plane shown in Fig.6.12 are labeled accordingly, the large black lines represent boundaries between *oily* streaks,

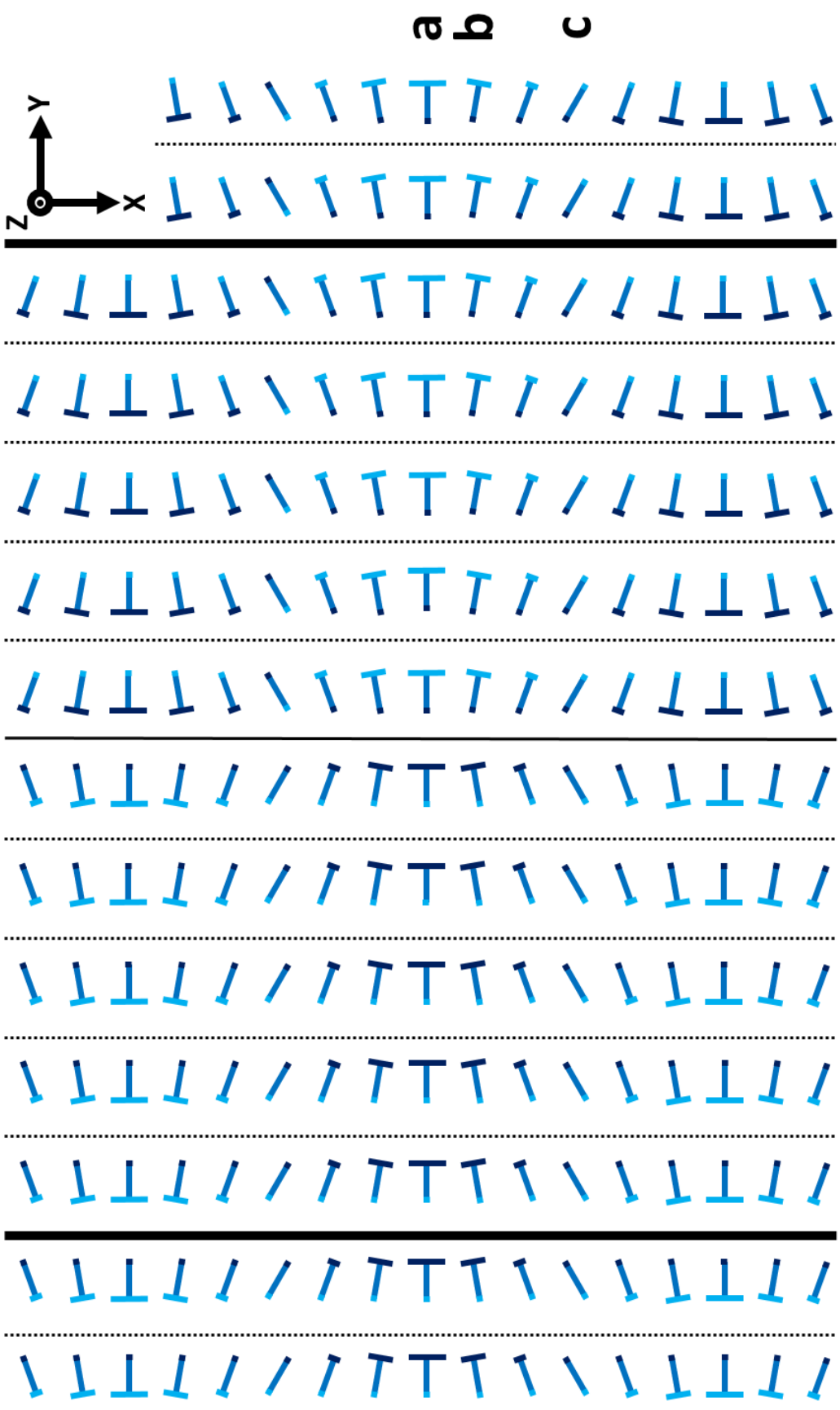

Figure 6.13: Model of liquid crystal molecular alignment in soapy streaks near the liquid crystal / substrate interface. The regions that correspond to the slices in Fig. 6.12 are labeled accordingly. The long lines correspond to smectic layers at the substrate.

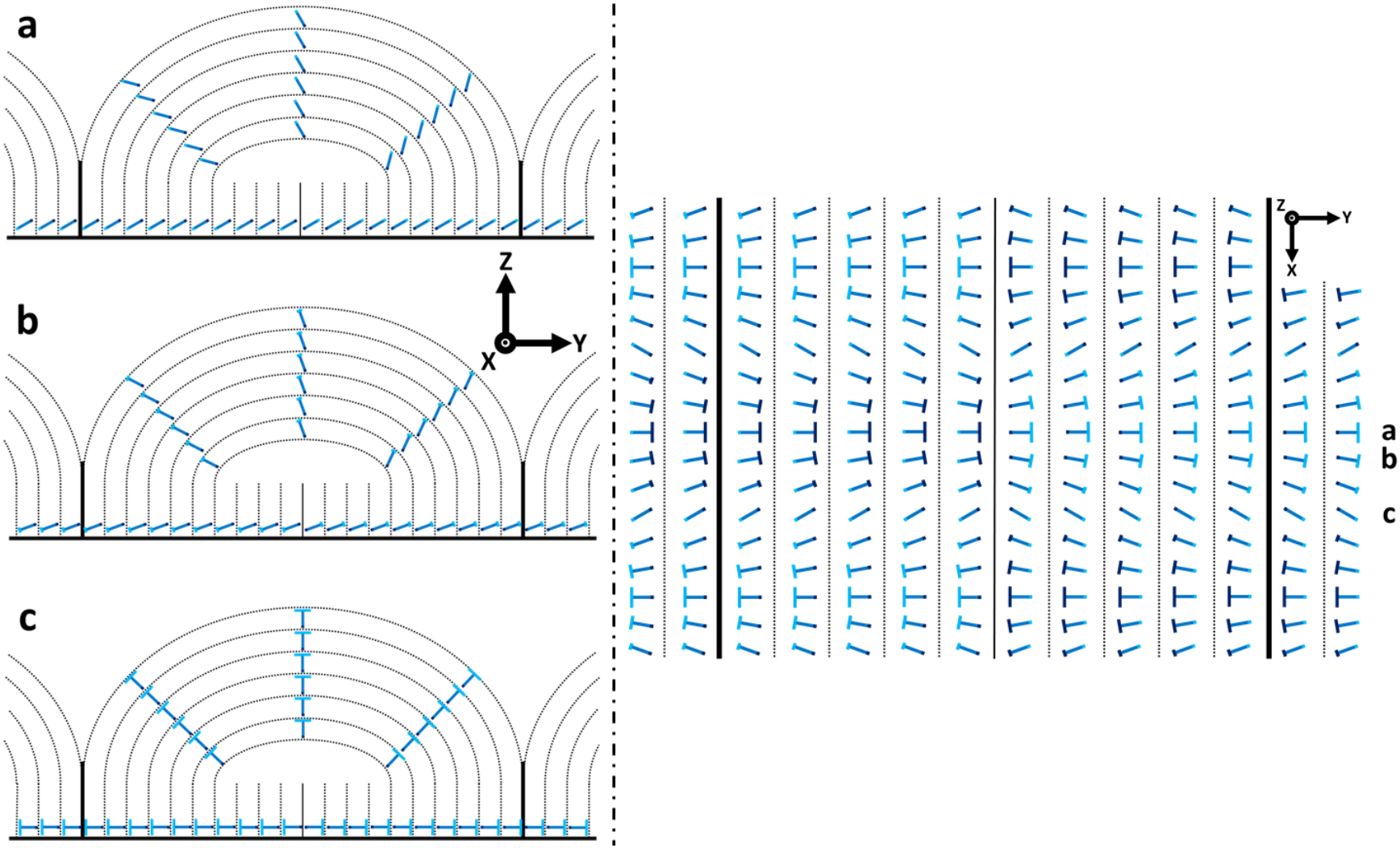

Figure 6.14: Compilation of both Fig. 6.12 and 6.13 to aid the reader for comparison purposes.

and the dotted lines represent individual smectic layers. In this model, the director rotation shown in Figs. 6.12 and 6.13 are the source of the periodic contrast change inherent to soapy streaks. However, using this director field to describe this sinusoidal change in contrast requires some additional explanation. Because the modified oily streaks have the same period as the difference in tilt between the two rotation domains they are both diffraction limited. If the period of the mismatched regions were much larger, hte soapy streaks would no longer be seen as periodic arrays of light and dark regions. Instead, the light regions would show a discrete modulation of lighter and darker striations. If the period of the mismatched domains were much smaller – considerably smaller than optical wavelengths – the average tilt with respect to the smectic layer normal would appear to average to zero. In such a case all optical evidence of both oily and soapy streaks would vanish. For these reasons the areas of mismatched rotational domains must be sub-wavelength of light structures that are still large enough that their intensities are averaged so as to appear as one region.

6.4.1 Chiral Pattern

Finally, the wavy soapy streaks and sawtooth pattern observed on the MoS_2 surface deserves some attention. Scanning tunneling microscopy measurements of 10CB [64] and undecylcyanobiphenyl [164] on MoS_2 reveal an arrangement of the surface layer of liquid crystal molecules that is chiral in two dimensions [57]. (The system, of course is actually three dimensional. Thus the chirality would actually be three-dimensional, but confined very close to – within a few nanometers of – the surface.) Interestingly, the soapy streaks' sawtooth pattern is observable in 9OO4 and $\bar{8}$S5 on the MoS_2, but not the achiral polyimide substrate, also is two-dimensionally chiral [57, 58, 178]. Figure 6.15 presents an image of 9OO4 on MoS_2 where the sawtooth shaped soapy streaks clearly exhibit two distinct chiral domains that are divided by a boundary on a single sample. It is important to note that both 9OO4 and $\bar{8}$S5 are conformationally

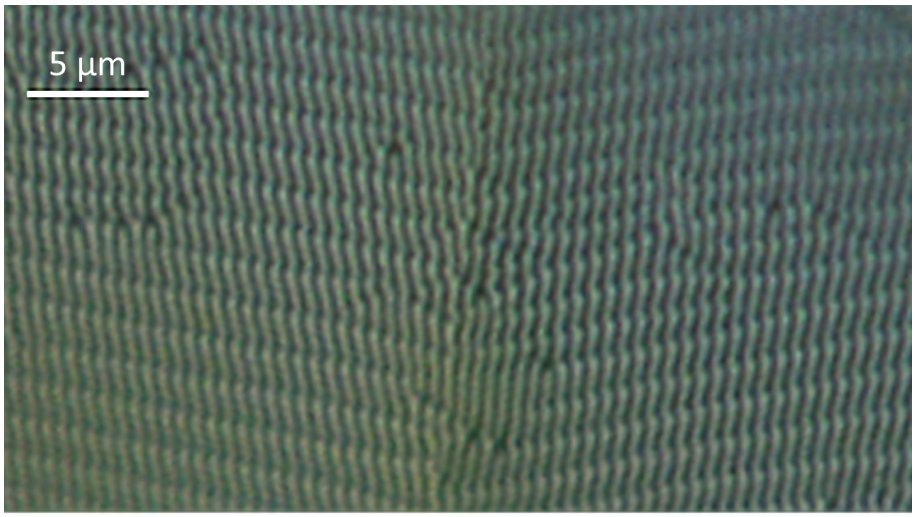

Figure 6.15: Photomicrographs of undulating 9004 soapy streaks on MoS_2 ∼64.5℃ presenting with two distinct chiral domains. This image has been slightly contrast enhanced to aid the reader. The scale bar is oriented perpendicular to the easy axis.

racemic molecules with low energy barriers between left and right handed conformers [179]. This suggests that the surface chirality is being transmitted partially into the bulk, into the macroscopic manifestation of sawtooth-shaped streaks. This is not without merit, as recently Basu *et al* showed that flakes of graphene (which are similar in structure to MoS_2) induced quantifiable chiral signatures when uniformly dispersed into a bulk achiral liquid crystal.

6.5 Summary

To summarize, in this chapter I presented observations of a new type of liquid crystal texture that likely occurs in the Sm-C phase of a liquid crystal with competing homeotropic and planar boundary conditions. Spawning from classical oily streaks in the Sm-A phase, these "soapy streaks" are orthogonal to the oily streaks and appear to elongate discontinuously from one oily streak to the next. At lower temperature the oily streaks begin to undulate and, interestingly, the undulations appear to be two-dimensionally chiral for the MoS_2 substrate. X-ray data were presented that suggest

an increase in the density of curvature walls associated with the flattened hemicylinder oily streak structure, as well as a decrease of the central defect. Combining the x-ray results with the optical microscopy data collected on the soapy streaks, and taking into account the molecular tilt in the Sm-C phase, I present one possible scenario for the formation and structure of soapy streaks.

6.6 Future Work

While I have accrued a great deal of data on these new structures dubbed "soapy streaks", there still remains much that is unknown about their structure and the mechanisms behind their formation. Future work should focus on other methods of characterization, such as ellipsometry, additional x-ray scattering experiments, and atomic force microscopy. In order to ameliorate the need for high temperatures to study these structures, exploration into other viable liquid crystals with near room temperature smectic phases and transitions would be beneficial. Another avenue to explore would be polymerization of soapy streaks, similar to those mentioned in the previous chapter. Additionally, imaging could be done with a near field scanning microscope in order to directly and optically study the possibly diffraction limited structures.

Chapitre 7

Conclusions

The work presented in this dissertation included results from a variety of experiments, and focused primarily on liquid crystal interactions. These interactions, dealing with chirality at surfaces and nanostructures, give better insights into the nature of liquid crystals. By utilizing the chirality-dependent electroclinic effect and optical microscopy, it was possible to observe and measure a number of properties that were previously unknown. Through the experiments presented herein, multiple interesting results have been demonstrated.

The properties of a configurationally achiral liquid crystal in a chiral system were probed. In such a system, applying a macroscopic torsional strain in a nematic twist cell conformationally deracemizes an achiral liquid crystal. Upon the application of an electric field, a surface electroclinic effect was observed. By constructing a cell with a thickness gradient, and filling it with a chirally doped liquid crystal, it was demonstrated that the electroclinic effect disappears in regions where the chiral dopant exactly compensates for the imposed twist. The disappearance of an electroclinic response indicated that a majority of the electrooptic response in a twist cell – utilizing a conformationally deracemizable liquid crystal – occurs near the planar alignment layers. It was also shown that this method is capable of effectively measuring a chiral

dopant's helical twisting power.

Next, the signature of a configurationally achiral liquid crystal doped with chiral periodic mesoporous organosilica (PMO) was explored. Previous research showed that the chirality transfer from the PMO the liquid crystal originates from within the pores. These results suggests that the chiral pores deracemize the liquid crystal in the filled pores, and that chirality is transferred to the bulk of the liquid crystal through interactions with these pores. Again the electroclinic effect was utilized. By comparing a PMO doped system's frequency response in the smectic-A phase near the smectic-A – smectic-C transition to one doped with a chiral molecule, it was possible to determine the origin of the electrooptic response. The contributions of the bulk liquid crystal were separated from that of the liquid crystal within the PMO pores, and it was shown that nearly the entirety of the electrooptic response comes from the liquid crystal *outside* of the PMO pores. This indicates that the contribution from the liquid crystal inside of the pores is negligible or nonexistent.

An electroclinic effect above the bulk chiral nematic – isotropic phase transition was studied. While the existence of an electroclinic effect in both the smectic-A and nematic phases have been extensively researched, there has been little work done on the isotropic electroclinic effect. Previous work has showed that above a direct bulk chiral smectic-A – isotropic phase transition, an electroclinic effect in a thin parasmectic region can be observed. This work explicitly excluded that possibility of nematic order in this thin surface region. The results presented here indicate that an applied electric field induces a director rotation in the very thin *paranematic* layer induced by the system's planar aligning substrates. It was shown that this isotropic electroclinic effect is comparable in magnitude to, and is more than three orders of magnitude slower than, the bulk nematic electroclinic effect. Additionally, the data showed that the electrooptic response in the paranematic region is comparable in magnitude to that of the parasmectic, but that the paranematic response varies

much more slowly with temperature.

Turning to optical microscopy, the interaction of the smectic-A oily streaks with a chiral dopant was reported. It is well known that smectic-A oily streaks in achiral liquid crystals present as flattened hemicylinders oriented perpendicular to the planar easy axis. Upon doping the achiral liquid crystal octylcyanobiphenyl (8CB) with a chiral molecule, a rotation of the oily streaks' orientation was observed. This rotation ϕ, with respect to the orientation of undoped oily streaks, is highly temperature dependent. Experiments show the largest angle of rotation occurs just below the nematic – smectic-A transition temperature, and the angle of rotation relaxes towards zero as the temperature is lowered in the smectic-A phase. These results are consistent with a surface electroclinic effect, and arise due to the large director tilt susceptibility close to the nematic – smectic-A transition temperature where the smectic order parameter is small. In addition to the dependence of ϕ on temperature, preliminary data on the temperature dependence of oily streak periodicity was reported. Extensive suggestions for future work regarding the dependence of oily streak rotation – as well as oily streak periodicity – on temperature were discussed.

Lastly, observation of a novel liquid crystal structure in the smectic-C phase was described. Similar in appearance to oily streaks in the smectic-A phase, slowly reducing the temperature of a liquid crystal system with competing boundary conditions into the smectic-C phase generates linear arrays a light and dark streaks. Unlike oily streaks, these "soapy streaks" form *parallel* to the easy axis, and their contrast can never be completely extinguished when viewed between crossed polarizers. The soapy streaks appear to propagate by discretely jumping form one oily streak to another, and in the process remove optical evidence of the oily streaks. X-ray data show that when the liquid crystal transitions from the smectic-A to the smectic-C phase, there is a reorganization of the smectic layers in the system. The x-ray data, coupled with the optical observations, led to the formation of a basic model that takes into account

the observed phenomenon.

Bibliographie

[1] F. Reinitzer, "Beitrge zur kenntniss des cholesterins," *Monatshefte fr Chemie/-Chemical Monthly*, vol. 9, no. 1, pp. 421–441, 1888.

[2] D. Dunmur and T. Sluckin, *Soapy, Science, and Flat-Screen TVs: A history of liquid crystals*. Oxford University Press, 2011.

[3] O. Lehmann, "ber fliessende krystalle," *Zeitschrift fr Physikalische Chemie*, vol. 4, 1889.

[4] G. H. Heilmeier, J. Castellano, and L. Zanoni, "Guest-host interactions in nematic liquid crystals," *Molecular Crystals and Liquid Crystals*, vol. 8, pp. 293–304, 1969.

[5] G. H. Heilmeir, L. A. Zanoni, and L. A. Barton, "Dynamic scattering: a new electooptic effect in certain classes of nematic liquid crystals," *Proceedings of the IEEE*, vol. 56, pp. 1162 – 1171, 1968.

[6] W. Helfrich and M. Schadt, "Optical device."

[7] "Nobelprize.org: History and properties of liquid crystals," 2014.

[8] V. I. Kopp, B. Fan, H. K. M. Vithana, and A. Z. Genack, "Low-threshold lasing at the edge of a photonic stop band in cholesteric liquid crystals," *Optics Letters*, vol. 23, no. 21, pp. 1707–1709, 1998.

[9] L. Schmidt-Mende, A. Fechtenkotter, K. Mullen, E. Moons, R. Friend, and J. MacKenzie, "Self-organized discotic liquid crystals for high-efficiency organic photovoltaics," *Science*, vol. 293, no. 5532, pp. 119–1122, 2001.

[10] R. J. Bushby and O. Lozman, "Photoconducting liquid crystals," *Current Opinion in Solid State & Material Science*, vol. 6, no. 6, pp. 569–578, 2002.

[11] P. J. Collings and M. Hird, *Introduction to Liquid Crystals*. Taylor & Francis, 1997.

[12] P. de Gennes and J. Gilles de Prost, *The physics of liquid crystals*. Clarendon Press, 1993.

[13] T. A. Strzelecka, M. W. Davidson, and R. L. Rill, "Miltiple liquid crystal phases of dna at high concentrations," *Nature*, vol. 331, pp. 457 – 460, 1988.

[14] J.-C. P. Gabriel, C. Sanches, and P. Davidson, "Observation of nematic liquid-crystal textures in aqueous gels of smectite clays," *Journal of Physical Chemistry*, vol. 100, no. 26, pp. 11139–11143, 1996.

[15] S. Fraden, A. Hurd, R. Meyer, M. Cahoon, and D. Caspar, "Magnetic-field-induced alignment and instabilities in ordered colloids of tobacco mosaic virus," *Journal de Physique*, vol. 46, no. C3, pp. 85–113, 1985.

[16] D. Chapman, "Liquid crystals and cell membranes," *Annals of The New York Academy of Sciences*, vol. 137, pp. 745 – 754, 1966.

[17] M. J. Stepen and J. P. Straley, "Physics of liquid crystals," *Reviews of Modern Physics*, vol. 46, no. 4, pp. 617 – 704, 1974.

[18] L. W. T. Kelvin, *Baltimore lectures on molecular dynamics and the wave theory of light*. C. J. Clay and Sons, 1904.

[19] T. W. G. Solomons and C. B. Fryhle, *Organic Chemistry*. Wiley, 2013.

[20] J. W. Goodby, R. Blinc, N. A. Clark, S. T. Lagerwall, M. A. Osipov, S. A. Pikin, T. Sakurai, K. Yoshino, and Ž. Boštjan, *Ferroelectric Liquid Crystals*. Gordon and Breach Science Publishers, 1991.

[21] I. Dierking, "Chiral liquid crystals: Structures, phases, effects," *Symmetry-Basel*, vol. 6, no. 2, pp. 444–472, 2014.

[22] R. Meyer, L. Liebert, L. Strzelecki, and P. Keller, "Ferroelectric liquid crystals," *Journal de Physique Lettres*, vol. 36, no. 3, pp. 69–71, 1975.

[23] A. Muoz F., P. Palffy-Muhoray, and B. Taheri, "Ultraviolet lasing in cholesteric liquid crystals," *Optics Letters*, vol. 26, no. 11, p. 804, 2001.

[24] M. Ozaki, M. Kasano, D. Ganzke, W. Haase, and K. Yoshino, "Mirrorless lasing in a dye-doped ferroelectric liquid crystal," *Advanced Materials*, vol. 14, no. 4, p. 306, 2002.

[25] W. Cao, A. Muoz, P. Palffy-Muhoray, and B. Taheri, "Lasing in a three-dimensional photonic crystal of the liquid crystal blue phase ii," *Nature Materials*, vol. 1, no. 2, pp. 111–113, 2002.

[26] E. P. Raynes, "The use of bowed reverse twist disclination lines for the measurement of long pitch lengths in chiral nematic liquid crystals," *Liquid Crystals*, vol. 33, no. 10, pp. 1215–1218, 2006.

[27] F. D. Saeva and J. J. Wysocki, "Induced circular dichroism in cholesteric liquid crystals," *Journal of the American Chemical Society*, vol. 93, no. 22, p. 5928, 1971.

[28] A. Mussbaum and R. A. Phillips, *Contemporary Optics for Scientists and Engineers*. Prentice Hall, Inc., 1976.

[29] E. Priestly, *Introduction to Liquid Crystals*. Springer, 1976.

[30] I. R. Nemitz, E. Lacaze, and C. Rosenblatt, "Electroclinic effect in a chiral paranematic liquid-crystal layer above the bulk nematic-to-isotropic transition temperature," *Physical Review E*, vol. 93, no. 2, 2016.

[31] J. Cheng and R. B. Meyer, "Pretransitional optical rotation in the isotropic phase of cholesteric liquid crystals," *Physical Review Letters*, vol. 29, pp. 1240–1243, 1972.

[32] C. Mauguin, "Sur les cristaux liquides de lehman," *Bull. Soc. Fr. Minér. Dristallogr*, vol. 34, no. 3, pp. 71–117, 1911.

[33] M. P. Marder, *Condensced Matter Physics*. Wiley, 2010.

[34] T. C. Renn, S. R.Lubensky, "Abrikosov dislocation lattice in a model of the cholesteric to smectic- a transition," *Physical Review A*, vol. 38, no. 4, pp. 2132–2147, 1988.

[35] K. J. Ihn, J. A. N. Zasadzinski, R. Pindak, A. J. Slaney, and J. Goodby, "Observations of the liquid-crystal analog of the abrikosov phase," *Science*, vol. 258, no. 5080, pp. 275–278, 1992.

[36] D. M. Agra-Kooijiman, H. Yoon, S. Dey, and S. Dumar, "Origin of weak layer contraction in de vries smectic liquid crystals," *Physical Review E*, vol. 89, p. 032506, 2014.

[37] R. B. Meyer, L. Liébert, L. Strzelecki, and P. Keller, "Ferroelectric liquid crystals," *Journal De Physics Lettres*, vol. 36, no. 3, pp. 69–71, 1975.

[38] A. Fukuda, Y. Takanishi, T. Isozaki, K. Ishikawa, and H. Takezoe, "Antiferroelectric chiral smectic liquid crystals," *Journal of Material Chemistry*, vol. 4, pp. 997–1016, 1994.

[39] J. Lee, H. Takezoe, A. Fukuda, and W. J, "Phase transitions among paraelectric, ferroelectric, ferrielectric, and antiferroelectric phases in a chiral smectic liquid crystal," *Journal of Phyiscs: Condensced Matter*, vol. 2, pp. SA271 – SA274, 1990.

[40] S. Chandrasekhar, *Liquid Crystals*. Cambridge University Press, 1992.

[41] J. D. Jackson, *Classical Electrodynamics*. John Wiley & Sons, 1998.

[42] E. Hecht, *Optics*. Pearson, 2002.

[43] K. E. Vaughn, M. Sousa, D. Kang, and C. Rosenblatt, "Continuous control of liquid crystal pretilt angle from homeotropic to planar," *Applied Physics Letters*, vol. 90, 2007.

[44] T. R. N. Kutty, "Planar orientation of nematic liquid crystals by chemisorbed polyvinyl alcohol surface layers," *Molecular Crystals and Liquid Crystals*, vol. 99, no. 1, 1969.

[45] B. Zappone, C. Meyer, L. Bruno, and E. Lacaze, "Periodic lattices of frustrated focal conic defect domains in smectic liquid crystal films," *Soft Matter*, vol. 8, no. 16, p. 4318, 2012.

[46] M. Tokita, O. Sato, Y. Inagaki, A. Nomura, Y. Tsujii, S. Kang, T. Fukuda, and J. Watanabe, "High-density poly(methyl methacrylate) brushes as anchoring surfaces of nematic liquid crystals," *Japanese Journal of Applied Physics*, vol. 50, no. 071701, 2011.

[47] I. Haller, "Elastic constants of the nematic liquid crystalline phase of methoxybenzylindene-p-n-butylaniline (mbba)," *Journal of Chemical Physics*, vol. 57, p. 1400, 1972.

[48] D. Coursault, B. Zappone, A. Coati, A. Boulaoued, L. Pelliser, D. Limagne, N. Boudet, B. H. Ibrahim, A. de Martino, M. Alba, M. Goldmann, Y. Garreau, B. Gallas, and L. Emmanuelle, "Self-organized arrays of dislocations in thin smectic liquid crystal films," *Soft Matter*, vol. 12, no. 3, pp. 678–688, 2016.

[49] S. Garoff and R. B. Meyer, "Electroclinic effect at the a c phase change in a chiral smectic liquid crystal," *Physical Review Letters*, vol. 38, no. 15, pp. 848–851, 1977.

[50] Z. Li, R. G. Petschek, and C. Rosenblatt, "Linear electroclinic effect in a chiral nematic liquid crystal," *Physical Review Letters*, vol. 62, no. 7, pp. 796–799, 1989.

[51] Z. Li, G. A. Di Lisi, R. G. Petschek, and C. Rosenblatt, "Nematic electroclinic effect," *Physical Review A*, vol. 41, no. 4, pp. 1997–2004, 1990.

[52] K. Nakagawa, T. Shinomiya, M. Koden, K. Tsubota, T. Kuratate, Y. Ishii, F. Funada, M. Matsuura, and K. Awane, "Deviation of layer normal from rubbing direction in ssf-lc," *Ferroelectrics*, vol. 85, no. 1, pp. 39–46, 1988.

[53] N. A. Xue, JiuzhiClark, "Surface electroclinic effect in chiral smectic- a liquid crystals," *Physical Review Letters*, vol. 64, no. 3, pp. 307–310, 1990.

[54] S. Tripathi, M.-H. Lu, E. M. Terentjev, R. G. Petschek, and C. Rosenblatt, "Surface-induced polarization at a chiral-nematicsubstrate interface," *Physical Review Letters*, vol. 67, no. 24, pp. 3400–3403, 1991.

[55] J. E. Maclennan, D. Muller, R.-F. Shao, D. Coleman, D. J. Dyer, D. M. Walba, and N. A. Clark, "Field control of the surface electroclinic effect in chiral smectic- a liquid crystals," *Physical Review E*, vol. 69, no. 6, 2004.

[56] R. Basu, I. R. Nemitz, Q. Song, R. P. Lemieux, and C. Rosenblatt, "Surface topography and rotational symmetry breaking," *Physical Reviews E*, vol. 86, no. 011711, 2012.

[57] S. Ferjani, Y. Choi, J. Pendery, R. G. Petschek, and C. Rosenblatt, "Mechanically generated surface chirality at the nanoscale," *Physical Review Letters*, vol. 104, no. 25, 2010.

[58] J. Pendery, S. Ferjani, C. Rosenblatt, and R. G. Petschek, "Spatially controllable surface chirality at the nanoscale," *Europhysics Letters*, vol. 96, no. 2, p. 26001, 2011.

[59] G. Andersson, I. Dahl, P. Keller, W. Kuczynski, S. T. Lagerwall, K. Skarp, and B. Stebler, "Submicrosecond electro-optic switching in the liquid-crystal smectic a phase: The soft-mode ferroelectric effect," *Applied Physics Letters*, vol. 51, no. 9, p. 640, 1987.

[60] J.-P. Michel, E. Lacaze, M. Goldmann, M. Gailhanou, M. de Boissieu, and M. Alba, "Structure of smectic defect cores: X-ray study of 8cb liquid crystal ultrathin films," *Physical Review Letters*, vol. 96, no. 2, 2006.

[61] J.-P. Michel, E. Lacaze, M. Alba, M. de Boissieu, M. Gailhanou, and M. Goldmann, "Optical gratings formed in thin smectic films frustrated on a single crystalline substrate," *Physical Review E*, vol. 70, no. 1, 2004.

[62] E. Zappone, BrunoLacaze, "Surface-frustrated periodic textures of smectic- a liquid crystals on crystalline surfaces," *Physical Review E*, vol. 78, no. 6, 2008.

[63] E. Lacaze, J.-P. Michel, M. Alba, and M. Goldman, "Planar anchoring and surface melting in the smectic-a phase," *Physical Review E*, vol. 76, p. 041702, 2007.

[64] E. Lacaze, J. P. Michel, M. Goldmann, M. Gailhanou, M. d. Boissieu, and M. Alba, "Bistable nematic and smectic anchoring in the liquid crystal octylcyanobiphenyl (8cb) adsorbed on a MoS_2 single crystal," *Physical Review E*, vol. 69, no. 4, 2004.

[65] D. Coursault, B. H. Ibrahim, L. Pelliser, B. Zappone, A. de Martino, E. Lacaze, and B. Gallas, "Modeling the optical properties of self-organized arrays of liquid crystal defects," *Optics Express*, vol. 22, no. 19, pp. 23182–23191, 2014.

[66] N. Katsonis, E. Lacaze, and B. L. Feringa, "Molecular chirality at fluid/solid interfaces: expression of asymmetry in self-organized monolayers," *Journal of Materials Chemistry*, vol. 18, no. 18, 2008.

[67] R. Basu, D. Kinnamon, and A. Garvey, "Detection of graphene chirality using achiral liquid crystalline platforms," *Journal of Applied Physics*, vol. 118, no. 11, 2015.

[68] R. Basu, J. S. Pendery, R. G. Petschek, R. P. Lemieux, and C. Rosenblatt, "Macroscopic torsional strain and induced molecular conformational deracemization," *Physical Review Letters*, vol. 107, no. 23, 2011.

[69] T.-C. Lin, I. R. Nemitz, C. J. McGrath, C. P. J. Schubert, H. Yokoyama, R. P. Lemieux, and C. Rosenblatt, "Nematic molecular core flexibility and chiral induction," *Physical Reviews E*, vol. 88, no. 042501, 2013.

[70] S. Zhang, B. Wen, S. S. Keast, M. E. Neubert, P. L. Taylor, and C. Rosenblatt, "Fredericksz transition in an anticlinic liquid crystal," *Physical Review Letters*, vol. 84, no. 18, pp. 4140–4143, 2000.

[71] J. Vij.

[72] J. Etxebarria and J. Zubia, "Electroclinic effect in a liquid crystal with chiral nematic and smectic- a phases," *Physical Review A*, vol. 44, no. 10, pp. 6626–6631, 1991.

[73] J. W. Goodby, "Twist grain boundary and frustrated liquid crystal phases," *Current Opinion in Colloid and Interface Science*, vol. 7, 2002.

[74] G. P. Crawford and S. Zumer, *Liquid crystals in complex geometries*. Taylor & Francis, 1996.

[75] R. B. Wehrspohn, H.-S. Kitzerow, and K. Busch, *Nanophotonic materials*. Wiley-VCH, 2008.

[76] W. C. Tsoi, M. O'Neill, M. P. Aldred, S. P. Kitney, P. Vlachos, and S. M. Kelly, "Distributed bilayer photovoltaics based on nematic liquid crystal polymer networks," *Chemistry of Materials*, vol. 19, no. 23, pp. 5475–5484, 2007.

[77] I. A. Levitsky, W. B. Euler, N. Tokranova, B. Xu, and J. Castracane, "Hybrid solar cells based on porous si and copper phthalocyanine derivatives," *Applied Physics Letters*, vol. 85, no. 25, p. 6245, 2004.

[78] A. Ide, R. Voss, G. Scholz, G. A. Ozin, M. Antonietti, and A. Thomas, "Organosilicas with chiral bridges and self-generating mesoporosity," *Chemistry of Materials*, vol. 19, no. 10, pp. 2649–2657, 2007.

[79] S. Inagaki, S. Guan, Q. Yang, M. P. Kapoor, and T. Shimada, "Direct synthesis of porous organosilicas containing chiral organic groups within their framework and a new analytical method for enantiomeric purity of organosilicas," *Chemical Communications*, no. 2, pp. 202–204, 2008.

[80] A. Brethon, P. Hesemann, L. Rjaud, J. J. Moreau, and M. Wong Chi Man, "Functional chiral hybrid silica gels prepared from (r)- or (s)-binaphthol derivatives," *Journal of Organometallic Chemistry*, vol. 627, no. 2, pp. 239–248, 2001.

[81] P. Wang, X. Liu, J. Yang, Y. Yang, L. Zhang, Q. Yang, and C. Li, "Chirally functionalized mesoporous organosilicas with built-in binap ligand for asymmetric catalysis," *Journal of Materials Chemistry*, vol. 19, no. 42, p. 8009, 2009.

[82] S. MacQuarrie, M. P. Thompson, A. Blanc, N. J. Mosey, R. P. Lemieux, and C. M. Crudden, "Chiral periodic mesoporous organosilicates based on axially chiral monomers: Transmission of chirality in the solid state," *Journal of the American Chemical Society*, vol. 130, no. 43, pp. 14099–14101, 2008.

[83] M. Giese, J. C. De Witt, K. E. Shopsowitz, A. P. Manning, R. Y. Dong, C. A. Michal, W. Y. Hamad, and M. J. MacLachlan, "Thermal switching of the reflection in chiral nematic mesoporous organosilica films infiltrated with liquid crystals," *ACS Applied Materials & Interfaces*, vol. 5, no. 15, pp. 6854–6859, 2013.

[84] V. Jayalakshmi, T. Wood, R. Basu, J. Du, T. Blackburn, C. Rosenblatt, C. M. Crudden, and R. P. Lemieux, "Probing the pore structure of a chiral periodic mesoporous organosilica using liquid crystals," *Journal of Materials Chemistry*, vol. 22, no. 30, p. 15255, 2012.

[85] M. W. A. MacLean, L. M. Reid, X. Wu, and C. M. Crudden, "Chirality in ordered porous organosilica hybrid materials," *Chemistry - An Asian Journal*, vol. 10, no. 1, pp. 70–82, 2014.

[86] J. Moreau, L. Vellutini, M. Man, and C. Bied, "New hybrid organic inorganic solids with helical morphology via h-bond mediated solgel hydrolysis of silyl

derivatives of chiral (r,r)- or (s,s)-diureidocyclohexane," *Joural of the American Chemical Society*, vol. 123, no. 7, pp. 1509–1510, 2001.

[87] L. Zhang, J. Liu, J. Yang, Q. Yang, and C. Li, "Tartardiamide-functionalized chiral organosilicas with highly ordered mesoporous structure," *Chemistry - An Asian Journal*, vol. 3, no. 10, pp. 1842–1849, 2008.

[88] T. Y. Zhuang, J. Y. Shi, B. C. Ma, and W. Wang, "Chiral norbornane-bridged periodic mesoporous organosilicas," *Journal of Materials Chemistry*, vol. 20, no. 29, p. 6026, 2010.

[89] P. Wang, J. Yang, J. Liu, L. Zhang, and Q. Yang, "Chiral mesoporous organosilicas with r-(+)-binol integrated in the framework," *Microporous and Mesoporous Materials*, vol. 117, no. 1-2, pp. 91–97, 2009.

[90] A. Kuschel, H. Sievers, and S. Polarz, "Amino acid silica hybrid materials with mesoporous structure and enantiopure surfaces," *Angewandte Chemie*, vol. 120, no. 49, pp. 9655–9659, 2008.

[91] J. Tang, D. Li, C. Sun, L. Zheng, and J. Li, "Temperature dependant self-assembly of surfactant brij 76 in room temperature ionic liquid," *Colloids and Surfaces A*, vol. 273, pp. 24–28, 2006.

[92] T. Seki, K. McEleney, and C. M. Crudden, "Enantioselective catalysis with a chiral, phosphane-containing pmo material," *Chemical Communications*, vol. 48, no. 51, p. 6369, 2012.

[93] M. DELAYE, "Coherence length and angular susceptibility divergences above a smectic-a to smectic-c phase transition observed by rayleigh scattering," *Le Journal de Physique Colloques*, vol. 40, no. C3, pp. C3–350–C3–355, 1979.

[94] Z. Li, R. B. Akins, G. A. DiLisi, C. Rosenblatt, and R. G. Petschek, "Anomaly in the dynamic behavior of the electroclinic effect below the nematicsmectic-a phase transition," *Physical Review A*, vol. 43, no. 2, pp. 852–857, 1991.

[95] R. Berardi, H.-G. Kuball, R. Memmer, and C. Zannoni, "Chiral induction in nematics a computer simulation study," *Journal of the Chamical Society, Faraday Transactions*, vol. 94, no. 9, pp. 1229–1234, 1998.

[96] F. Ciesla, UlrikeSchth, "Ordered mesoporous materials," *Microporous and Mesoporous Materials*, vol. 27, no. 2-3, pp. 131–149, 1999.

[97] W. A. Wegene, F. R. M. Dowben, and V. J. Koester, "Time-dependent birefringence, linear dichroism, and optical rotation resulting from rigid-body rotational diffusion," *Journal of Chemical Physics*, vol. 70, no. 2, p. 622, 1979.

[98] P. Sheng, "Phase transition in surfacec-aligned nematic films," *Physical Review Letters*, vol. 37, pp. 1059–1062, 1976.

[99] H. Schröder, "Molecular statistical threory for inhomogeneous nematic liquid crystals with boundary conditions," *Journal of Chemical Phyiscs*, vol. 67, p. 16, 1977.

[100] K. Miyano, "Wall-induced pretransitional birefringence: A new tool to study boundary aligning forces in liquid crystals," *Physical Review Lettersers*, vol. 43, p. 51, 1979.

[101] K. Miyano, "Surface-induced ordering of a liquid crystal in the isotropic phase," *Journal of Chemical Physics*, vol. 71, no. 10, p. 4108, 1979.

[102] K. Tarczon, John C.Miyano, "Surface-induced ordering of a liquid crystal in the isotropic phase. ii. 4-methoxybenzylidene-4-n-butylaniline (mbba)," *Journal of Chemical Physics*, vol. 73, no. 4, p. 1994, 1980.

[103] T. Stinson and J. Listster, "Pretransitional phenomena in the isotropic phase of a nematic liquid crystal," *Physical Review Letters*, vol. 25, no. 8, pp. 503–506, 1970.

[104] P. De Gennes, "Short range order effects in the isotropic phase of nematics and cholesterics," *Molecular Crystals and Liquid Crystals*, vol. 12, no. 3, pp. 193–214, 1970.

[105] A. R. Johnston, "Kerr response of nematic liquids," *Journal of Applied Physics*, vol. 44, no. 7, p. 2971, 1973.

[106] Y. Filippini, J.C.Poggi, "Kerr effect in the isotropic phase of nematic liquid crystals," *Journal de Physique Lettres*, vol. 35, no. 7-8, pp. 99–101, 1974.

[107] T. W. STINSON, J. D. LITSTER, and N. A. CLARK, "Static and dynamic behavior near the order disorder transition of nematic liquid crystals," *Le Journal de Physique Colloques*, vol. 33, no. C1, pp. C1–69–C1–75, 1972.

[108] T. Stinson and J. Listster, "Correlation range of fluctuations of short-range order in the isotropic phase of liquid crystals," *Physical Review Letters*, vol. 30, no. 15, pp. 688–692, 1973.

[109] E. Gulari and B. Chu, "Short-range order fluctuations in the isotropic phase of a liquid crystal mbba," *Journal of Chemical Phyiscs*, vol. 62, p. 195, 1975.

[110] D. W. Allender, G. L. Henderson, and D. L. Johnson, "Landau theory of wall-induced phase nucleation and pretransitional birefringence at the isotropic-nematic transition," *Physical Review A*, vol. 24, no. 2, pp. 1086–1089, 1981.

[111] P. Sheng, "Phase transition in surface-aligned nematic films," *Physical Review Letters*, vol. 37, no. 16, pp. 1059–1062, 1976.

[112] P. Sheng, "Boundary-layer phase transition in nematic liquid crystals," *Physical Review A*, vol. 26, no. 3, pp. 1610–1617, 1982.

[113] H. Hsiung, T. Rasing, and Y. R. Shen, "Wall-induced orientational order of a liquid crystal in the isotropic phasean evanescent-wave-ellipsometry study," *Physical Review Letters*, vol. 57, no. 24, pp. 3065–3068, 1986.

[114] W. Chen, L. J. Martinez-Miranda, H. Hsiung, and Y. R. Shen, "Orientational wetting behavior of a liquid-crystal homologous series," *Physical Review Letters*, vol. 62, no. 16, pp. 1860–1863, 1989.

[115] M. B. Feller, W. Chen, and Y. R. Shen, "Investigation of surface-induced alignment of liquid-crystal molecules by optical second-harmonic generation," *Physical Review A*, vol. 43, no. 12, pp. 6778–6792, 1991.

[116] Y. Moses, T.Shen, "Pretransitional surface ordering and disordering of a liquid crystal," *Physical Review Letters*, vol. 67, no. 15, pp. 2033–2036, 1991.

[117] A. Sluckin, T.J.Ponierwierski, *Fluid Interfactial Phenomena*. Wiley & Sons Ltd, 1986.

[118] T. J. Poniewierski, A.Sluckint, "Theory of the nematic-isotropic transition in a restricted geometry," *Liquid Crystals*, vol. 2, no. 3, pp. 281–311, 1987.

[119] B. Jerome, "Surface effects and anchoring in liquid crystals," *Reports on Progress in Physics*, vol. 54, no. 3, pp. 391–451, 1991.

[120] H. Yokoyama, S. Kobayashi, and H. Kamei, "Boundary dependence of the formation of new phase at the isotropic-nematic transition," *Molecular Crystals and Liquid Crystals*, vol. 99, no. 1, pp. 39–52, 1983.

[121] H. Yokoyama, S. Kobayashi, and H. Kamei, "Temperature dependence of the anchoring strength at a nematic liquid crystal-evaporated sio interface," *Journal of Applied Physics*, vol. 61, no. 9, p. 4501, 1987.

[122] G. Barbero, G.Durand, "Curvature induced quasi-melting from rough surfaces in nematic liquid crystals," *Journal de Physique II France*, vol. 1, no. 6, pp. 651–658, 1991.

[123] G. Barberi, R.Durand, "Order parameter of a nematic liquid crystal on a rough surface," *Physical Review A*, vol. 41, no. 4, pp. 2207–2210, 1990.

[124] U. Wu, Shin-TsonEfron, "Optical properties of thin nematic liquid crystal cells," *Applied Physics Letters*, vol. 48, no. 10, p. 624, 1986.

[125] A. Bortnik Brai, K. Koevar, I. Muevi, and S. umer, "Capillary forces in a confined isotropic-nematic liquid crystal," *Physical Review E*, vol. 68, no. 1, 2003.

[126] K. Koevar, A. Bortnik, I. Muevi, and S. umer, "Capillary condensation of a nematic liquid crystal observed by force spectroscopy," *Physical Review Letters*, vol. 86, no. 26, pp. 5914–5917, 2001.

[127] I. Koevar, K.Muevi, "Forces in the isotropic phase of a confined nematic liquid crystal 5cb," *Physical Review E*, vol. 64, no. 5, 2001.

[128] B. Wen, J.-H. Kim, H. Yokoyama, and C. Rosenblatt, "Depression of the nematic-isotropic phase transition temperature at nanopatterned surfaces," *Physical Review E*, vol. 66, no. 4, 2002.

[129] J.-H. Kim and C. Rosenblatt, "Rubbing strength dependence of surface interaction potential and surface-induced order above the nematicisotropic transition," *Journal of Applied Physics*, vol. 84, no. 11, p. 6027, 1998.

[130] X. Liu, D. W. Allender, and D. Finotello, "Calorimetric study of nematic prewetting," *Europhysics Letters (EPL)*, vol. 59, no. 6, pp. 848–854, 2002.

[131] J.-H. Lee, T. J. Atherton, V. Barna, A. De Luca, E. Bruno, R. G. Petschek, and C. Rosenblatt, "Direct measurement of surface-induced orientational order parameter profile above the nematic-isotropic phase transition temperature," *Physical Review Letters*, vol. 102, no. 16, 2009.

[132] E. Pikina and C. Rosenblatt, "Surface-induced weak orientational order and role of isotropic-nematic interface fluctuations in the appearance of an induced nematic film," *European Physical Journal E*, vol. 35, no. 9, 2012.

[133] S.-D. Lee, J. S. Patel, and J. W. Goodby, "Nature of the surface-induced order above the direct isotropic to chiral-smectic- a transition," *Physical Review A*, vol. 44, no. 4, pp. 2749–2751, 1991.

[134] W. Chen, Y. Ouchi, T. Moses, Y. R. Shen, and K. H. Yang, "Surface electroclinic effect on the layer structure of a ferroelectric liquid crystal," *Physical Review Letters*, vol. 68, no. 10, pp. 1547–1550, 1992.

[135] T. Moses, Y. Ouchi, W. Chen, and Y. R. Shen, "Pretransitional surface phenomena in ferroelectric liquid crystals," *Molecular Crystals and Liquid Crystals Science and Technology. Section A. Molecular Crystals and Liquid Crystals*, vol. 225, no. 1, pp. 55–65, 1993.

[136] S.-D. Lee and J. S. Patel, "Critical behavior of the field-induced molecular tilt near the nematic-chiral-smectic-a transition," *Physical Letters A*, vol. 155, pp. 435–439, 1991.

[137] Z. Li, R. Ambigapathy, R. G. Petschek, and C. Rosenblatt, "Dynamics of the nematic-electroclinic effect," *Physical Review A*, vol. 43, no. 12, pp. 7109–7112, 1991.

[138] I. M. Syed, V. Percec, R. G. Petschek, and C. Rosenblatt, "Apparent tricritical behavior at a nearly second-order nematic-isotropic phase transition of a cyclic liquid crystalline trimer," *Physical Review E*, vol. 67, no. 1, 2003.

[139] O. D. Kleman, MLavrentovich, *Soft Matter Physics*. Spring-Verlag, 2003.

[140] J. Nehring and A. Saupe, "On the schlieren texture in nematic and smectic liquid crystals," *Journal of the Chemical Society, Faraday Transactions 2*, vol. 68, p. 1, 1972.

[141] C. S. Rosenblatt, R. Pindak, N. Clark, and R. Meyer, "The parabolic focal conic : a new smectic a defect," *Journal de Physique France*, vol. 38, no. 9, pp. 1105–1115, 1977.

[142] N. A. Clark, "Strain-induced instability of monodomain smectic a and cholesteric liquid crystals," *Applied Physics Letters*, vol. 22, no. 10, p. 493, 1973.

[143] M. Blanc, C.Kleman, "The confinement of smectics with a strong anchoring," *European Physical Journal E*, vol. 4, no. 2, pp. 241–251, 2001.

[144] Y. H. Kim, D. K. Yoon, H. S. Jeong, O. D. Lavrentovich, and H.-T. Jung, "Smectic liquid crystal defects for self-assembling of building blocks and their lithographic applications," *Advanced Functional Materials*, vol. 21, no. 4, pp. 610–627, 2011.

[145] I. Gryn, E. Lacaze, R. Bartolino, and B. Zappone, "Controlling the self-assembly of periodic defect patterns in smectic liquid crystal films with electric fields," *Advanced Functional Materials*, vol. 25, no. 1, pp. 142–149, 2014.

[146] R. Wang, I. M. Syed, G. Carbone, R. G. Petschek, and C. Rosenblatt, "Bend-induced melting of the smectic- a phase: Analogy to a type-i superconductor," *Physical Review Letters*, vol. 97, no. 16, 2006.

[147] R.-F. Shao, J. E. MacLennan, N. A. Clark, D. J. Dyer, and D. M. Walba, "Giant surface electroclinic effect in a chiral smectic a liquid crystal," *Liquid Crystals*, vol. 28, no. 1, pp. 117–123, 2001.

[148] D. Coursault, *Dcoration de rseaux linaires de dfauts smectiques par des nanoparticules dor*. PhD thesis, Universit Pierre et Marie Curie (U. Paris VI), 2013.

[149] S. Shahini, "Study of oily streaks of 8cb (4'-ictyl-4-biphenylcarbonitrile) liquid crystal," Master's thesis, Universit Pierre et Marie Curie (U. Paris VI), 2013.

[150] T. C. Lubensky, "The nematic-to-smectic- a transition: a theoretical overview," *Journal de Chimie Physique et de Physico-Chimie Biologiqu*, vol. 80, pp. 31–43, 1983.

[151] J. D. LITSTER, J. ALS-NIELSEN, R. J. BIRGENEAU, S. S. DANA, D. DAVIDOV, F. GARCIA-GOLDING, M. KAPLAN, C. R. SAFINYA, and R. SCHAETZING, "High resolution x-ray and light scattering studies of bi-layer smectic a compounds," *le Journal de Physique Colloques*, vol. 40, no. C3, pp. C3–339–C3–344, 1979.

[152] D. Coursault, J. Grand, B. Zappone, H. Ayeb, G. Lvi, N. Flidj, and E. Lacaze, "Linear self-assembly of nanoparticles within liquid crystal defect arrays," *Advanced Materials*, vol. 24, no. 11, pp. 1461–1465, 2012.

[153] D. Coursault, J.-F. Blach, J. Grand, A. Coati, A. Vlad, B. Zappone, D. Babonneau, G. Lvi, N. Flidj, B. Donnio, J.-L. Gallani, M. Alba, Y. Garreau, Y. Boren-

sztein, M. Goldmann, and E. Lacaze, "Tailoring anisotropic interactions between soft nanospheres using dense arrays of smectic liquid crystal edge dislocations," *ACS Nano*, vol. 9, no. 12, pp. 11678–11689, 2015.

[154] L. Pelliser, M. Manceau, C. Lethiec, D. Coursault, S. Vezzoli, G. Lemenager, L. Coolen, M. DeVittorio, F. Pisanello, and L. Carbone, "Alignment of rod-shaped single-photon emmitters driven by line defects in liquid crystals," *Advanced Functional Materials*, vol. 25, no. 11, pp. 1719–1726, 2015.

[155] M. G. Friedel, "Les tats msomorpes de la matire," *B1 Annales de Physique*, vol. 18, pp. 273–474, 1922.

[156] J. B. Fournier, I. Dozov, and G. Durand, "Surface frustration and texture instability in smectic- a liquid crystals," *Physical Review A*, vol. 41, no. 4, pp. 2252–2255, 1990.

[157] M. C. Choi, T. Pfohl, Z. Wen, Y. Li, M. W. Kim, J. N. Israelachvili, and C. R. Safinya, "Ordered patterns of liquid crystal toroidal defects by microchannel confinement," *Proceedings of the National Academy of Sciences*, vol. 101, no. 50, pp. 17340–17344, 2004.

[158] M. Blanc, C.Klman, "Curvature walls and focal conic domains in a lyotropic lamellar phase," *The European Physical Journal B*, vol. 10, no. 1, pp. 53–60, 1999.

[159] L. Z. Ruan, J. R. Sambles, and I. W. Stewart, "Self-organized periodic photonic structure in a nonchiral liquid crystal," *Physical Review Letters*, vol. 91, no. 3, 2003.

[160] M. Kleman, *Points, lines, and walls.* J. Wiley, 1983.

[161] W. Schneider, M.B.Webb, "Undulating paired disclinations (oily streaks) in lyotropic liquid crystals," *Journal de Physique France*, vol. 45, no. 2, pp. 273–281, 1984.

[162] P. Boltenhagen, O. Lavrentovich, and M. Kleman, "Oily streaks and focal conic domains in lyotropic liquid crystals," *Journal de Physique II France*, vol. 1, no. 10, pp. 1233–1252, 1991.

[163] Z. Li and O. D. Lavrentovich, "Surface anchoring and growth pattern of the field-driven first-order transition in a smectic- a liquid crystal," *Physical Review Letters*, vol. 73, no. 2, pp. 280–283, 1994.

[164] E. Lacaze, A. Apicella, M. P. De Santo, D. Coursault, M. Alba, M. Goldmann, and R. Barberi, "Ordered interfaces for dual easy axes in liquid crystals," *Soft Matter*, vol. 7, no. 3, pp. 1078–1083, 2011.

[165] I. R. Nemitz, A. J. Ferris, E. Lacaze, and C. Rosenblatt, "Chiral oily streaks in a smectic-a liquid crystal," *Soft Matter*, vol. 12, pp. 6662–6668, 2016.

[166] D. Johnson and A. Saupe, "Undulation instabilities in smectic c phases," *Physical Review A*, vol. 15, no. 5, pp. 2079–2085, 1977.

[167] K. Harth and R. Stannarius, "Corona patterns around inclusions in freely suspended smectic films," *Eur. Phys. J. European Physical Journal EE*, vol. 28, pp. 265–272, 2009.

[168] J. Loudet, P. V. Dolganov, P. Patricío, H. Saadaoui, and C. P., "Undulation instabilities in the meniscus of smectic membranes," *Physical Review Letters*, vol. 106, p. 117802, 2011.

[169] R. B. Meyer and P. S. Pershan, "Surface polarity induced domains in liquid crystals," *Solid State Communications*, vol. 13, pp. 989–992, 1973.

[170] T. J. Scheffer, H. Gruler, and G. Meier, "Periodic free-surface disclination at nematic to smectic c phase transition," *Solid State Communications*, vol. 11, p. 253, 1972.

[171] J. Fournier and P. Galatola, "Undulation instability of the interface between a smectic-c liquid crystal and its isotropic or nematic melt," *Journal de Physique II France*, vol. 5, no. 9, pp. 1297–1320, 1995.

[172] K. S. Novoselov, A. K. Geim, S. V. Morozov, D. Jiang, Y. Zhang, D. S. V., I. V. Grigorieva, and F. A. A., "Electric field effect in atomically thin carbon films," *Science*, vol. 306, pp. 666–669, 2004.

[173] T. Bartels, W. Bock, J. Braun, C. Busch, W. Buss, W. Dresel, C. Freiler, M. Harperscheid, R.-P. Heckler, D. Hrner, F. Kubicki, G. Lingg, A. Losch, R. Luther, T. Mang, S. Noll, and J. Omeis, *Lubricants and Lubrication.*, ch. 15. Wiley-VCH Verlag GmbH & Co. KGaA, 2000.

[174] H. Yokoyama, "Nematicisotropic transition in bounded thin films," *Journal of the Chemical Society, Faraday Transactions 2*, vol. 84, no. 8, pp. 1023–1040, 1988.

[175] T. J. Poniewierski, A.Sluckint, "Theory of the nematic-isotropic transition in a restricted geometry," *Liquid Crystals*, vol. 2, no. 3, pp. 281–311, 1987.

[176] P. Sheng, "Boundary-layer phase transition in nematic liquid crystals," *Physical Review A*, vol. 26, no. 3, pp. 1610–1617, 1982.

[177] C. Rosenblatt, R. B. Meyer, R. Pindak, and N. A. Clark, "Temperature behavior of ferroelectric liquid-crystal thin films: A classical xy system," *Physical Review A*, vol. 21, no. 1, pp. 140–147, 1980.

[178] Y. Choi, T. Atherton, S. Ferjani, R. G. Petschek, and C. Rosenblatt, "Patterning-induced surface chirality and modulation of director twist in a nematic cell," *Physical Review E*, vol. 80, no. 6, 2009.

[179] R. Basu, C. Rosenblatt, and R. P. Lemieux, "Chiral induction in thioester and oxoester liquid crystals by dispersed carbon nanotubes," *Liquid Crystals*, vol. 39, 2012.

Annexe A

Igor code - Electroclinic Effect

```
// Use modern global access method.
#pragma rtGlobals=1

// Creates the program structure
Macro ECE()
Silent 1
DeclareVariables()
Connect()
TakeTheData()
GotoZero()
SaveTheData()
End

// Connects the computer to the devices
Proc Connect()
FindInstruments()
SetTheInputVoltmeter()
SetTheOutputVoltmeterX()
SetTheoutputVoltmeterX2()
SetTheOutputVoltmeterY()
End

// Declares the variable
Proc DeclareVariables()
Variable/G WorkingFreq = 25 // the Frequency of the individual scan.
Variable/G MinAmplitude =0 // the minimum voltage scanned
Variable/G MaxAmplitude =2 // the maximum voltage scanned
Variable/G Amplifier = 1 // the amplification constant (if amplified)
Variable/G StepAm = 0.05 // the increment the voltage is increasd by
Variable/G Sens = .05 // the sensitivity of the locking
Variable/G Temperature = 60.13 // the temperature of the scan
```

```
Variable/G TC = 10 // the locking time constat setting
Variable/G SleepTime =10 // the time between data points
Variable/G SleepTime2 =.5 // a redundant waittime
Variable/G InputVoltmeter, OutputVoltmeterX,...
OutputVoltmeterX2, OutputVoltmeterY,...
SignalGenerator, n, steps // the variable that will store data
Variable/G Amplitude, Freq // the variable to set the devices
Variable/G NUM=(MaxAmplitude-MinAmplitude)/StepAm + 1 // the number of iterations
// converts the variable to a string for the devices
String/G StringFreq=Num2str(WorkingFreq)
// creates the strings to store data
String/G Input, OutputX, OutputX2, OutputY, StringAmpl
Make/O/N=(NUM) Vgen,VinUp, VoutUpX,...
VoutUpX2, VoutUpY, Temp, Freqs,...
TimeConst, Sensitivity, Root, Radians // array to store data
End

// Finds the devices
Proc FindInstruments()
NI488 ibfind "dev11" InputVoltmeter
NI488 ibfind "dev2", OutputVoltmeterX
NI488 ibfind "dev7", OutputVoltmeterX2
NI488 ibfind "dev12", OutputVoltmeterY
NI488 ibfind "dev9", SignalGenerator
End

// Initializes the devices
Proc SetTheInputVoltmeter()
GPIB device InputVoltmeter
GPIBWrite "F1T4G1Y2X"
End
Proc SetTheOutputVoltmeterX()
GPIB device OutputVoltmeterX
GPIBWrite "F0R3T4G1Y2X"
End
Proc SetTheOutputVoltmeterX2()
GPIB device OutputVoltmeterX2
GPIBWrite "F0R3T4G1Y2X"
End
Proc SetTheOutputVoltmeterY()
GPIB device OutputVoltmeterY
GPIBWrite "F0R3T4G1Y2X"

// Initializes data aquisition
Proc TakeTheData()
GPIB device SignalGenerator
GPIBWrite "FREQ"+StringFreq
```

```
// Sets the voltage to its minimum value.
Amplitude=MinAmplitude
StringAmpl=num2str(Amplitude)
GPIB device SignalGenerator
GPIBWrite "AMPL"+StringAmpl+"VP"
Sleep/S StartSleepTime
n=0

// Creates the loop to aquire the data.
do

// Loop counter
n+=1

// Increments the voltage
Amplitude += StepAm
StringAmpl=num2str(Amplitude)
GPIB device SignalGenerator
GPIBWrite "AMPL"+StringAmpl+"VR"

// Reads and stores the input voltage.
GPIB device InputVoltmeter
GPIBRead Input
VinUp[n]=str2num(Input)
VGen[n]= (MinAmplitude + n*StepAm)*Amplifier

// Pauses to allow device equilibration
Sleep/S SleepTime

// Calls devices to collect data and stores data
GPIB device OutputVoltmeterX
GPIBRead OutputX
VoutUpX[n]=str2num(OutputX)
GPIB device OutputVoltmeterX2
GPIBRead OutputX2
VoutUpX2[n]=str2num(OutputX2)
GPIB device OutputVoltmeterY
GPIBRead OutputY
VoutUpY[n]=str2num(OutputY)
TimeConst[n]= TC
Sensitivity[n] = Sens
Temp[n]= Temperature
Freqs[n]= WorkingFreq
Root[n] = ((VoutUpX[n])^2 + (VoutUpX2[n])^2)^(1/2)
Radians[n] = Root[n] /4/ VoutUpY[n] /10 * Sens
```

```
while(n<NUM)
End

//Sets the input voltage to zero
Proc GotoZero()
GPIB device SignalGenerator
GPIBWrite "AMPL0.00VP"
End

// Saves the final data
Proc  SaveTheData()
Save/J/M="\r\n"/W VinUp,Vgen,Temp,Freqs,TimeConst,...
Sensitivity,VoutUpX,VoutUpX2,VoutUpY,Root,Radians as "ECE.dat"
End
```

Annexe B

Matlab code - Electroclinic Effect

B.1 Voltage Scan Code

```
% Electroclinic voltage scan program using a lockin amplifier
% a dmm, and a function generator (feline optional).
% Assuming that a sine wave is being used.

amp22=1; % the maximum voltage applied
step22=0.01; % the incremental increase in voltage
freq22=100; % the frequency of this individual scan
wait22=5; % the time between data points
sens22=.02; % the sensitivity of the lockin amplifier
temp22=87; % the temperature the scan is supposedly taken at
file22 = 'meow'; % the file name prefix

% Creates the dmm, lockin amp and function generator objects
% Set up the session
lock=gpib('ni',0,8);
func=gpib('ni',0,15);
involt=gpib('ni',0,11);
tempres=gpib('ni',0,10);
dcvolt=gpib('ni',0,5);

% Opens communication with the devices
fopen(lock);
fopen(func);
fopen(involt);
fopen(tempres);
fopen(dcvolt);
```

```
% Sets the function generator to sine wave
fprintf(func,'FUNC0');
% Sets the dmm to correct units, and forces unitless values
fprintf(involt,':FORM:ELEM READ');
fprintf(involt,':SENS:FUNC "VOLT:AC"');
%fprintf(dcvolt,':FORM:ELEM READ');
%fprintf(dcvolt,':SENS:FUNC "VOLT[:DC]"');
fprintf(tempres,'F2R0T4G1X');

% Creates location for data storage
final=[];

% Sets the initial frequency and amplitude
fprintf(func,cat(2,'FREQ',num2str(freq22)));
fprintf(func,cat(2,'AMPL',num2str(0),'VR'));

% Inserts a wait bar with cancel feature
h = waitbar(0,'Starting Program...
','Name','Scanning Voltages...',...
'CreateCancelBtn',...
'setappdata(gcbf,''canceling'',1)');
setappdata(h,'canceling',0)

% Creates a loop counter
i=0;

% Loops the program to incrase voltage
% and take data with each iteration
for genvolt = 0.0: step22: amp22

% Checks for cancellation
if getappdata(h,'canceling')
break
end

% Sets the voltage of current iteration
fprintf(func,cat(2,'AMPL',num2str(genvolt),'VR'));

% Pauses while devices equilibrate
pause(wait22);

% Collects temperature data
resfin = str2double(query(tempres,'DATA?'));
%temp22 = -2.7447*((log10(resfin))^3)+34.9511*((log10(resfin))^2)...
-196.54*(log10(resfin))+401.247;

% Collects X, Y, R and Phase from the lockin
```

```
ac=str2num(query(lock,'SNAP?1,2,3,4')); %#ok<*ST2NM>
acx=ac(1);
acy=ac(2);
R=ac(3);
phase=ac(4);

% Collects the input voltage and the dc voltage.
vin = str2double(query(involt,'DATA?'));
dcs = query(dcvolt,'DATA?');
dc = str2double(dcs(5:end));

% Calculates Theta for the ECE
ecefinal=(R/(dc))/4;

data=[genvolt,vin,freq22,resfin,temp22,sens22,acx,acy,dc,R,phase,ecefinal];
final=[final;data]; %#ok<AGROW>

%update waitbar
waitbar(genvolt/amp22,h,sprintf('%12.9f',genvolt))

end

fprintf(func,cat(2,'AMPL',num2str(0),'VR'));

% Closes the devices
fclose(lock);
fclose(func);
fclose(involt);
fclose(tempres);
fclose(dcvolt);

% Deletes the devices
delete(lock);
delete(func);
delete(involt);
delete(tempres);
delete(dcvolt);

% Deletes waitbar
delete(h);

% Converts and writes the data to file with time and date
final=final';
fulltime = clock;
year = num2str(fulltime(1));
month = num2str(fulltime(2));
day = num2str(fulltime(3));
```

```
hour = num2str(fulltime(4));
minute = num2str(fulltime(5));
filename = cat(2,file22,'_',hour,'_',minute,'_',month,'_',day,'_',year);
fileID = fopen(cat(2,filename,'.txt'),'w');
fprintf(fileID,..
'%15s %15s %15s %15s %15s %15s %20s %20s %20s %20s %20s %20s\r\n',...
'genvolt','vin','freq','res','temp','sens','acx','acy','dc','R',...
'phase','ecefinal');
fprintf(fileID,...
'%15s %15f %15f %15f %15f %15f %20.15f %20.15f...
%20.15f %20.15f %20.15f %20.15f\r\n',final);
fclose(fileID);

% Plots and returns slope of the best fit line.
hplot = figure;
x1=final(2,:);
y1=final(12,:);
z1=final(11,:);
subplot(2,1,1); plot(x1,y1,'.')
title('ECE vs Voltage')
xlabel('Volts');
ylabel('ECE');
subplot(2,1,2);plot(x1,z1,'.')
title('Phase vs Voltage')
xlabel('Volts');
ylabel('Phase');

% Save the plot
saveas(hplot, filename,'fig');

% Save the workspace
save(filename);
```

B.2 Frequency Scan Code

```
% Electroclinic frequency scan program using a lockin amplifier
% a dmm, and a function generator.
% Assuming that a sine wave is being used, and that cats are awesome (they are).

amp22=3; % the maximum voltage applied
genfreq=10; % the initial generator frequency
i = .02;             % the initial exponential for frequency
step22=.02;    % the exponential increment for the frequency scan
```

```
maxfreq=100000; % the maximum frequency of the scan
wait22=12; % amount of time between data points
sens22=0.0010; % the sensitivity setting on the locking amplifier
cellThick = (0.00000756);  % thickness of the cell in meters
tempSet=95; % the temperature the scan is supposedly taken at
file22 = 'purr'; % the file name prefix

% Turn the initial conditions into strings for the devices.
amp22txttemp=cat(2,num2str(amp22),'V');
amp22txt=strrep(amp22txttemp,'.','_');
temptxttemp=cat(2,num2str(tempSet),'C');
temptxt=strrep(temptxttemp,'.','_');

% Creates the dmm, lockin amp and function generator objects
% set up the session
involt=gpib('ni',0,12);
tempres=gpib('ni',0,10);
dcvolt=gpib('ni',0,9);
lock=gpib('ni',0,2);


% Opens communication with the devices
fopen(involt);
fopen(tempres);
fopen(dcvolt);
fopen(lock);

% Sets the dmm to correct units, and set them to return unitless values.
fprintf(involt,':FORM:ELEM READ');
fprintf(involt,':SENS:FUNC "VOLT:AC"');
fprintf(dcvolt,':FORM:ELEM READ');
fprintf(dcvolt,':SENS:FUNC "VOLT[:DC]"');
fprintf(tempres,'F2R0T4G1X');

% Creates location for data storage
final=[];

% Sets the initial frequency and amplitude as a sine wave.
fprintf(lock,'OUTX1');
fprintf(lock,'FMOD1');
fprintf(lock,cat(2,'FREQ',num2str(genfreq)));
fprintf(lock,'RSLP0');
fprintf(lock,cat(2,'SLVL',num2str(amp22)));

% Inserts a wait bar with cancel feature
h = waitbar(0,'Starting Program...','Name','Scanning Frequencies...',...
'CreateCancelBtn',...
```

```
'setappdata(gcbf,''canceling'',1)');
setappdata(h,'canceling',0)

% Creates a loop counter
j=0;

% Checks initial temperature
resfin = str2double(query(tempres,'DATA?'));
temp22 = -2.7447*((log10(resfin))^3)+34.9511*((log10(resfin))^2)...
-196.54*(log10(resfin))+401.247

% Initializes plot
tempplot = figure;

% Allows the setup to activate
pause(1);

% Calculates initial frequency
freq = genfreq^i;

% Loops the program  to increase frequency and take data with each iteration.
while freq <= (maxfreq+1);

% Checks for a cancelation
if getappdata(h,'canceling')
break
end

$ Sets the frequency of current iteration
fprintf(lock,cat(2,'FREQ',num2str(freq)));

% Update waitbar
waitbar(log(freq)/log(maxfreq),h,sprintf('%12.9f',freq))

% Pauses while devices equilibrate
pause(wait22);

% Breaks loop if there was a cancelation
if j < 1
if getappdata(h,'canceling')
break
end

% Loop counter
j=j+1;

% Collects temperature data
```

```
resfin = str2double(query(tempres,'DATA?'));
temp22 = -2.7447*((log10(resfin))^3)+34.9511*((log10(resfin))^2)...
-196.54*(log10(resfin))+401.247;

% Collects X, Y, R and Phase from the lockin, as well as the DC
% and input voltage.
ac=str2num(query(lock,'SNAP?1,2,3,4'));
acx=ac(1);
acy=ac(2);
R=ac(3);
phase=ac(4);
dc=str2double(query(dcvolt,'DATA?'));
vin=str2double(query(involt,'DATA?'));

% Calculates the electric field and theta for the ECE
efield = vin/cellThick;
ecetheta=(R/(dc))/4;

% Calculates the electroclinic coefficient
ec=ecetheta/efield;

$ Stores the data
data=[i,vin,efield,freq,resfin,temp22,sens22,acx,acy,...
dc,R,phase,ecetheta,ec];
final=[final;data]; %#ok<AGROW>

% Updates the plots
x1=final(:,4);
y1=final(:,14);
z1=final(:,12);
d1=final(:,10);
r1=final(:,11);
acx1=final(:,8);
acy1=final(:,9);
subplot(3,2,1); semilogx(x1,y1,'.')
title('Ec vs Freq')
xlabel('Freq');
ylabel('ECE');
subplot(3,2,5); semilogx(x1,z1,'.')
title('Phase vs Freq')
xlabel('Freq');
ylabel('Phase');
subplot(3,2,6); semilogx(x1,d1,'.')
title('Freq vs DC output');
xlabel('Freq');
ylabel('DC Output (Volts)')
subplot(3,2,2); semilogx(x1,r1,'.')
```

```
title('R vs Freq')
xlabel('Freq');
ylabel('R');
subplot(3,2,3); semilogx(x1,acx1,'.');
title('X signal vs Freq');
xlabel('Freq');
ylabel('X Signal');
subplot(3,2,4); semilogx(x1,acy1,'.');
title('Y signal vs Freq');
xlabel('Freq');
ylabel('Y Signal');

% Creates frequency for the next iteration
i = i + step22;
freq = genfreq^i;


% Ends the loop
end

% Sets the frequency and voltage to minimum values.
fprintf(lock,cat(2,'FREQ',num2str(genfreq)));
fprintf(lock,cat(2,'SLVL0.004'));

% Closes the devices
fclose(involt);
fclose(tempres);
fclose(dcvolt);
fclose(lock);

% Deletes the devices
delete(involt);
delete(tempres);
delete(dcvolt);
delete(lock);

% Deletes the waitbar and the plots
delete(h);
delete(tempplot);

% Converts and writes the data to file with time and date.
final=final';
fulltime = clock;
year = num2str(fulltime(1));
month = num2str(fulltime(2));
day = num2str(fulltime(3));
hour = num2str(fulltime(4));
```

```
minute = num2str(fulltime(5));

filename = cat(2,file22,'_',temptxt,'_',amp22txt,'_',...
hour,'_',minute,'_',month,'_',day,'_',year);

fileID = fopen(cat(2,filename,'.txt'),'w');
fprintf(fileID,...
'%15s %15s %15s %15s %15s %15s %15s %20s %20s %20s %20s %20s %20s %20s\r\n',...
'counter','vin','efield','freq','res','temp','sens','acx','acy','dc','R',...
'phase','ecetheta','ec');
fprintf(fileID,...
'%15s %15f %15f %15f %15f %15s %15f %20.15f %20.15f...
%20.15f %20.15f %20.15f %20.15f %20.15f\r\n',final);
fclose(fileID);

% Plots the data and returns the slope of the best line fit for the scan.
hplot = figure;
x1=final(4,:);
y1=final(14,:);
z1=final(12,:);
d1=final(10,:);
r1=final(11,:);
acx1=final(8,:);
acy1=final(9,:);
subplot(3,2,1); semilogx(x1,y1,'.')
title('Ec vs Freq')
xlabel('Freq');
ylabel('Ec');
subplot(3,2,5); semilogx(x1,z1,'.')
title('Phase vs Freq')
xlabel('Freq');
ylabel('Phase');
subplot(3,2,6); semilogx(x1,d1,'.')
title('Freq vs DC output');
xlabel('Freq');
ylabel('DC Output (Volts)')
subplot(3,2,2); semilogx(x1,r1,'.')
title('R vs Freq')
xlabel('Freq');
ylabel('R');
subplot(3,2,3); semilogx(x1,acx1,'.');
title('X signal vs Freq');
xlabel('Freq');
ylabel('X Signal');
subplot(3,2,4); semilogx(x1,acy1,'.');
title('Y signal vs Freq');
xlabel('Freq');
```

```
ylabel('Y Signal');

% Saves the plot
saveas(hplot, filename,'fig');

% Save the entire workspace
save(filename);
```

Annexe C

Image-J macro - Oily Streak and Soapy Streak Analysis

C.1 Stack FFT Code

```
// StackFFTCode
// This ImageJ macro gets runs a FFT on all availabe slices
// in an image stack.

setBatchMode(true);
stack = getImageID;
newImage("FFT Stack of "+getTitle, "8-bit", getWidth, getHeight,
nSlices);
stack2 = getImageID;
for (i=1; i<=nSlices; i++) {
showProgress(i, nSlices);
selectImage(stack);
setSlice(i);
run("FFT");
run("Copy");
close;
selectImage(stack2);
setSlice(i);
run("Paste");
}
setBatchMode(false);
```

C.2 Stack Profile Data Code

```
// StackProfileData
// This ImageJ macro gets the profile of all slices in a stack
// and writes the data to the Results table, one column per slice.

macro "Stack profile Data" {
if (!(selectionType()==0 || selectionType==5 || selectionType==6))
exit("Line or Rectangle Selection Required");
setBatchMode(true);

run("Plot Profile");
Plot.getValues(x, y);
run("Clear Results");
for (i=0; i<x.length; i++)
setResult("x", i, x[i]);
close();

n = nSlices;
for (slice=1; slice<=n; slice++) {
showProgress(slice, n);
setSlice(slice);
profile = getProfile();
sliceLabel = toString(slice);
sliceData = split(getMetadata("Label"),"\n");
if (sliceData.length>0) {
line0 = sliceData[0];
if (lengthOf(sliceLabel) > 0)
sliceLabel = sliceLabel+ " ("+ line0 + ")";
}
for (i=0; i<profile.length; i++)
setResult(sliceLabel, i, profile[i]);
}
setBatchMode(false);
updateResults;
}
```

C.3 Stack Profile Plot Code

```
// StackProfilePlot
// This macro generates profile plots of all the images
// in a stack and stores then in another stack.

macro "Stack profile Plot" {
ymin = 0;
ymax = 255;
saveSettings();
```

```
if (nSlices==1)
exit("Stack required");
run("Profile Plot Options...",
"width=400 height=200 minimum="+ymin+" maximum="+ymax+" fixed");
setBatchMode(true);
stack1 = getImageID;
stack2 = 0;
n = nSlices;
for (i=1; i<n; i++) {
showProgress(i, n);
selectImage(stack1);
setSlice(i);
run("Plot Profile");
run("Copy");
w = getWidth; h = getHeight;
close();
if (stack2==0) {
newImage("Plots", "8-bit", w, h, 1);
stack2 = getImageID;
} else {
selectImage(stack2);
run("Add Slice");
}
run("Paste");
}
setSlice(1);
setBatchMode(false);
restoreSettings();
}
```

Table des Figures

Liste des Tableaux

Résumé

Cette thèse se concentre sur les cristaux liquides (CLs), en particulier leurs propriétés chirales et leurs interactions avec des surfaces et des nanostructures. Des cellules nématiques torsadées ont été remplies d'un CL dopé avec la molécule chirale CB15, qui compense la torsion imposée. Les résultats indiquent qu'un effet électroclinique (ECE) existe toujours près de la surface dans les cellules torsadées contenant des molécules déracémisables conformes. Des mesures ECE ont aussi été réalisées afin de déterminer la réponse en ECE dans un CL dopé avec des organosilicates mésoporeux périodiques (OMP) chiraux. Les données montrent que la source principale du signal émane de l'extérieur des OMP plutôt que de leurs curs. Un ECE est aussi mesuré pour des CLs chiraux au-del de leur température de transition de phase nématique/isotrope chirale de bulk, et est observable dans les couches paranématiques induites par les substrats causant un alignement planaire. Des mesures de microscopie optique ont été réalisées sur des stries huileuses de smectique A dopées avec du CB15. Lors d'un dopage chiral, l'orientation des stries a tourné d'un angle dépendant de la température: cet angle augmente avec la concentration et est maximum juste en-dessous de la température de transition smectique A/nématique, se stabilisant aux alentours de zéro moins d'un degré en-dessous de T_{NA}. Ceci est expliqué comme une manifestation de l'ECE de surface sous la structure de strie huileuse permettant une rotation de cette dernier. Enfin, une structure innovante dans un système hybride aligné a été observée en-dessous de la température de transition Smectique-A/Smectique-C. Cette structure est apparue comme des stries périodiques sombres et claires perpendiculaires aux stries huileuses, formées par l'extension individuelle d'une strie la suivante, éliminant les traces optiques des stries huileuses. A des températures plus faibles, les stries ondulent suivant un schéma chiral en 2D. Une origine possible de ces stries est présentée.

Mots-cles: [Cristaux Liquides; Chiralité; Electroclinic; Surface Ordre Induit; Transition de Phase; Défauts]

Abstract

This dissertation focuses on liquid crystals (LCs), specifically their chiral properties and interactions with surfaces and nanostructures. Nematic twist cells were filled with a LC doped with the chiral molecule CB15, which compensates for the imposed twist. Using the electroclinic effect (ECE), results indicate that an ECE always exists near the surface in twist cells containing conformationally deracemizable molecules. ECE measurements were also performed to determine the source of the ECE response in a LC doped with chiral periodic mesoporous organosilica (PMO). The data show that the main source of the signal emanates from outside the PMO, and not inside the PMO pores. An ECE also is reported for chiral LCs above their bulk chiral isotropic-nematic phase transition, and is observable in the paranematic layers induced by the planar-aligning substrates. Optical microscopy measurements were performed on smectic-A oily streaks doped with CB15. When chirally doped, the stripe orientation rotated by a temperature dependent angle: This angle increased with concentration, was largest just below the nematic - smectic-A transition, and stabilized to near zero within $\sim$ 1°C below T_{NA}. This is explained as a manifestation of a surface ECE. Finally, a novel structure in a hybrid aligned system was observed below the Smectic-A - Smectic-C transition. The structure appeared as periodic dark and light streaks running perpendicular to the oily streaks, and formed by extending discretely from one oily streak to the next, eliminating optical evidence of the oily streaks. At lower temperatures the streaks undulated in a 2D chiral pattern. A possible origin of these streaks is presented.

Key words: [Liquid Crystals; Chirality; Electroclinic; Induced Surface Order; Phase Transitions; Defects]